THE UNIVERSITY OF CALGARY

Modelling Buried Pipelines in Freezing Soils using Non-linear Fourier Finite Elements

by

Rong You

A THESIS

SUBMITTED TO THE FACULTY OF GRADUATE STUDIES

IN PARTIAL FULFILLMENT OF THE REQUIREMENTS FOR THE DEGREE OF MASTER OF SCIENCE

DEPARTMENT OF CIVIL ENGINEERING

CALGARY, ALBERTA

October, 1997

Abstract

The study of frost heave and soil-structure interaction of pipelines in permafrost is a challenging task. There exists a large number of theories ranging from simple Winkler's models to more sophisticated ones based on continuum mechanics.

This thesis considers the continuum approach in which the pipeline is regarded as an axi-symmetric structure upon which non-axisymmetric loads resulting from heat processes are being applied. The Fourier finite element method is known to be very efficient for solving this problem. The time dependent load induced by thermal processes are first obtained by solving the coupled heat transfer-moisture migration equations using Galerkin's method. Then, stresses and deformations are computed from Fourier finite elements incorporating material non-linearity.

Numerical results obtained were in good agreement with the Caen pipe-freezing soil experimental data. Comparisons of results to ABAQUS revealed that the Fourier finite element formulation produced a more efficient program.

Acknowledgements

I have to express my sincere thanks to my supervisor, Dr. Richard Wan, for his considerate and patient guidance throughout the whole time of my graduate studies, especially during the period of completing this thesis. I also thank Drs. Ron Wong and Ramesh Joshi for their great help during my graduate studies.

Funding provided by The National Energy Board of Canada and the Department of Civil Engineering of The University of Calgary to complete this thesis is greatly appreciated.

Particularly, I have to thank my wife, Min Jin, for her support during my study and her taking care of our daughter and most of the housework. At the same time, I thank my sweet four and a half year old daughter, Jing-Ya You, because she always brings me happiness after my busy work. I thank my friends Dr. Peijun Guo, Dr. Xiaodong Wang, Dr. Changqing Wang, Jianing Ju, Bahaa Mekalled, Dale Walters, Xuefeng Pan, Tristan Spronken, Ed Choi, Peter Chan, and Richard Smith for their help. My thanks also go to Tracia Veer, Tracy Harris, Susan Anand, and other secretaries in the Department of Civil Engineering of The University of Calgary. Lastly, but not least, Drs. Doug Phillips and Bryan Gooding of Academic Computer Services (ACS) at The University of Calgary were very helpful in teaching me how to use visualization softwares and ABAQUS.

Finally, I must thank my deceased father for providing me an invaluable early education. Especially, I thank my mother, my parents-in-law, my sisters, brothers-in-law, and other relatives for their consistent help and continuing support.

Table of Contents

List of Tables

List of Figures

List of Symbols

δ – Kronecker symbol

ε – strain or tolerance of iteration

θ – angle measured counterclockwise along circumferential direction

θ_i/θ_l – ice/liquid fraction

λ – thermal conductivity

μ – chemical potential

ν – Poisson's ratio

π – constant (3.14159265)

ρ – density

$\boldsymbol{\sigma}$ – stress tensor

φ – friction angle

Γ – boundary

Ω – domain of interest

b – body force

c – cohesion

$\mathbf{e}$ – deviatoric strain tensor

k – hydraulic conductivity

l – direction cosine or length

n_0 – initial porosity

p – harmonic number or mean pressure

q – heat flux

r – radius

$\mathbf{s}$ – deviatoric stress tensor

t – time

u, v, w, U – displacements

x, y, z – coordinates

$\mathbf{B}$ – geometric matrix

$\mathbf{C}_{n+1}^{k}$ – consistent tangent operator

C – heat capacity

C_{ijkl} – constitutive matrix

E – Young's modulus

F – force or yield function

G – shear modulus

H' – hardening parameter

$\mathbf{K}$ – stiffness matrix

K – bulk modulus

L – latent heat of fusion or length

N_i – interpolation function

P – pressure

Q – plastic potential or mass flux

S – entropy or surface

T – temperature or traction

V – volume

Chapter 1

INTRODUCTION

1.1 Background

Pipelines, mainly made of cast iron, ductile iron, steel and polyethylene, are widely used infra-structures for transporting oil, natural gas, water, or sewage materials. Usually, pipelines can either be buried underground, off-shore, or placed above ground. While underground pipelines have better stability and longer service life than above ground pipelines, they also take less land use. However, one major issue for considering underground pipelines is the need for major ground excavation works and maintenance.

During their service life, buried pipelines can experience damage due to a variety of reasons such as frost heave, loss of soil strength due to thawing, landslides, buckling, leaking, corrosion, and creeping movements of slopes. Frost heave is a very common problem when the pipeline is buried in cold regions of Northern Canada. Sometimes, frost may cause so much heave that large deformations in the pipeline ultimately result in its failure. On the other hand, lateral loads can be induced by landslides due to generation of high pore pressures in unstable slopes. In that case, the loads are so huge that a long flexible pipeline is subjected to large bending with the adjacent soil failing in both active and passive modes. Another aspect of failure

can result from a loss of soil strength when the surrounding frozen soil thaws. Again, this type of failure may cause large displacement of the pipeline. In some cases there have been reports of buried pipelines buckling and being uprooted from the ground due to the development of large thermally induced axial forces.

Most of Canada's pipelines are mainly used to transport oil or natural gas from cold northern regions to the south of Canada or the United States. Some pipelines are buried in permafrost while others are located in the seasonal freezing and thawing zone. The latter pipelines are in particular subjected to freezing and/or thawing load cycles. In this thesis, the study of underground pipelines and the surrounding soil undergoing freezing will be the main focus of research since it presents special and interesting soil-structure modelling aspects.

1.2 Objectives

A proper understanding of the mechanics of buried pipelines in freezing soils involves the study of displacement, strain, and stress fields developed in both the soil and pipeline as they are subjected to mechanical and thermal loads. Also, considerations have to be made to the interaction of the buried pipeline and the surrounding soils as well. Usually, the analysis leads to solving a complicated system of equilibrium equations, together with other equations describing thermal and mechanical loads, fluid flow, phase change, and creep.

The main objectives of this thesis are as follows:

- develop a special numerical procedure so that a three-dimensional stress analy-

sis of soil-pipeline systems can be undertaken in an efficient manner,

- perform a coupled heat transfer-moisture migration analysis of the freezing soil so that the temperature field, and hence frost bulb development, can be computed in time,
- couple the above thermal analysis with the stress analysis mentioned in the first point, and
- validate the model by referring to bench mark problems.

It is worth mentioning that this research is probably first in its kind since it attempts to apply Fourier finite element techniques to the analysis of soil-pipeline problems.

1.3 Methods

The finite element method is a well established theory which is commonly used in a lot of engineering applications. There are also numerous commercial finite element codes which permit the analysis of structures in either two or three dimensions, with different constitutive models describing the material. The most complete analyses are three-dimensional in nature, but they require rather heavy computational effort especially in non-linear cases. In this respect, solving realistic three-dimensional finite element problems is probably limited to workstations. On the other hand, two-dimensional analyses, which involve much less computational effort, are normally

found to suit most engineering applications except the more complicated ones such as soil-pipelines systems.

Other aspects which need to be considered in the analysis are non-linearities (either materially or geometrically related) which appear in the solution of the problem. Linear models are fairly simple in physical concept and are only good as a preliminary solution to most engineering problems. However, most realistic constitutive models are non-linear in nature and require an iterative based solution strategy.

Turning to a typical analysis of soil-pipeline problems, the domain of interest can be restricted to the immediate vicinity of the pipeline and advantage can be taken from the axi-symmetrical nature of the geometry. However, the load induced by the surrounding frozen soils on the pipeline usually has a non-axisymmetric or arbitrary spatial distribution. This type of three-dimensional structure can be efficiently analyzed by using Fourier series based finite element methods. Sometimes, these methods are also called semi-analytical or quasi-analytical finite element methods. In this thesis, the Fourier finite element method will be used because it can be a viable analysis tool. This method uses classical two-dimensional finite elements in one plane of the geometry and expands all variables into a Fourier series in the third direction, thus leading to a system of decoupled equations which correspond to a series of 2-D analyses. Therefore lots of computational work can be saved while retaining all of the 3-D nature of the principal field variables. Depending upon the formulation, the resulting Fourier finite element can be classified as being continuous or discrete. Further details will be provided in subsequent chapters. This thesis will focus on continuous Fourier finite element method unless stated otherwise.

1.4 Organization of this Thesis

Chapter one begins with an introduction of the subject and deals with general information on the thesis. Chapter two follows with a literature review on soil-pipeline systems and their numerical modelling. Chapter three presents the formulation of the proposed Fourier finite element method which deals with non-linearities. The coupled non-linear problem of heat transfer and moisture migration, relevant to the freezing soil, is then described in Chapter four. Chapter five demonstrates the validity of the developed model by comparing results to ABAQUS, a commercial finite element code. Application of the Fourier finite element method to the computation of ice pressure and liquid pressure development as a result of heat transfer and moisture migration is described in Chapter six. The numerical solutions are compared to the results obtained from the well-known Caen experiment which deals with a pipe buried in two different freezing soils. Finally, Chapter seven discusses the findings of this research including conclusions and recommendations for further studies.

Chapter 2

LITERATURE REVIEW

2.1 Introduction

There has been a lot of interest in the analysis of underground soil-pipeline systems, particularly in the case of the surrounding soil being subjected to freezing. In this latter case, the soil heaves at ground surface (frost heave problem) due to freezing, and at the same time induces mechanical loads which can be detrimental to the pipeline. For analyzing such a problem, there exists a variety of methods which range from simple one-dimensional elastic models to complicated ones in which both the soil and pipeline, treated as solid continua, deform plastically.

The freezing of the soil, as well as its evolution, is an important issue to consider in the analysis. This can only be achieved by a proper understanding of soil freezing and the characterization of the different governing thermal processes.

The following sections discuss issues of frost heave, moisture migration, heat transfer, and also the different methods of analysis available in the current literature. This literature review will indeed lead to a better understanding of the current issues in soil-pipeline modelling while also providing a guideline for the development of the thesis model.

2.2 Winkler Model

The simplest method of analysis for soil-pipeline frost heave problems is based on the Winkler model which has been classically used in elastic foundation engineering, see reference [1]. The concept is to isolate the pipeline from the soil and model the soil-pipeline interaction by means of a series of individual supporting springs.

Rajani and Morgenstern [2] [3] [4] successfully used the above concept in a 1-D case to pipeline problems, and incorporated creep behaviour as a result of ice in the surrounding soils by using Winkler "creep" springs. They adopted the Norton creep relationships written in the generalized form as proposed by Ladanyi [5]

$$\dot{\varepsilon} = B\sigma^n \tag{2.1}$$

where

$\dot{\varepsilon}$ is the axial strain rate;

σ is the axial stress;

B and n are the creep constants. Typically, n is about 3 for ice at low stresses and icy silts. B is both temperature and material dependent.

The comparisons between the results predicted by their model and measurements in the Caen experiment [6] were made and concluded to be satisfactory. Along the same line of thought, Ng, Pyrah, and Anderson [7] simulated a pipeline as an elastic beam under lateral load and also regarded the supporting soils as a series of elastic Winkler springs. Other applications of Winkler model can be found in the work by Rajani, Zhan, and Kuraoka [8].

Although all the above works seem to give good predictions for soil-pipeline behaviour, the major shortcomings and challenges still lie in the modelling of the surrounding soil which is altogether precluded. While the Winkler type model has been preferred to other methods for analysis due to its inherent simplicity, its capabilities are still fairly limited as it applies only to simple configurations. There is major contention about the true physical meaning of the spring constants and which values to adopt for different soils.

Perhaps it is also of interest to mention that various modifications to Winkler's model have been attempted in the past. As cited in Selvadurai [9], these include: (1) Filonenko-Borodich model which acquires continuity between the individual spring elements by connecting them to a thin elastic membrane under a constant tension T, (2) Hetényi model which accounts for the interaction between the independent spring elements by incorporating an elastic plate, (3) Pasternak model which assumes the existence of shear interaction between the spring elements by connecting them to a layer of incompressible vertical elements deforming in transverse shear only, and (4) Vlazov model which introduces displacement constraints that simplify the basic equations for a linear elastic isotropic continuum.

2.3 Continuum Model

Contrary to the Winkler model, continuum based models treat the surrounding soil as a continuum and the pipeline as a shell structure. Hence, the behaviour of the surrounding soils, the pipeline, and the interaction of soil-pipeline can be readily

modelled. A proper analysis should ideally include the computation of stress and deformation fields in the soil-pipeline system which undergoes both mechanical and thermal loading such as that induced by freezing.

Nixon *et al.* [10] applied a continuum model to analyze frost heave-pipeline interaction. They found that, when a chilled gas pipeline crosses a transition from frozen to unfrozen ground, the stiff layer of the frozen ground between the pipe and the heaving soil will attenuate or dampen the sudden differential movements. By contrast, the Winkler model assumes that the differential movements are transmitted almost directly onto the pipeline without the benefit of any smoothing effect from the surrounding frozen soils. They demonstrated the performance of their model in the elastic and viscous (creep) behavioural regimes of the soil, but did not include any three-dimensional or thermal effects due to freezing. The following sub-sections investigate the thermal problem and numerical methods available for conducting a stress-deformation analysis of a continuum.

2.4 Thermal Aspects

2.4.1 The Formation and Growth of an Ice Lens

Lewis and Sze [11] applied the principles of irreversible thermodynamics to describe the freezing of soil, and thus derived a system of coupled heat and mass transfer partial differential non-linear equations. They have ideally classified frost heave models into two categories:

1. *Primary heave model* which is characterized by the existence of sharp freezing front that separates the frozen and unfrozen zones of the soil system.

2. *Secondary heave model* which extends the sharp freezing front into a region called the frozen "fringe", where the ice and liquid water are in a state of thermodynamics equilibrium.

Their models not only treat the surrounding soils as continuum media, but also take the coupled heat and mass (liquid water) transfer into account.

A more elaborate concept of frost-heave characteristics of soils has been proposed by Svec [12]. It is known that the frost heave is caused not only by freezing of in-situ pore water, but also by the migratory water. The latter process is known as ice segregation and is characterized by the growth of ice lenses at the "segregation" freezing temperature, which is a few tenths of a degree below the freezing point. The water flowing towards an ice lens is induced by suction pressures developed within the freezing "fringe". This fringe is a partly frozen zone between the zero-degree isotherm and the growing ice lens.

The process of ice segregation in soils is reasonably well understood now, but its quantitative description and prediction is not yet possible. This is mainly due to difficulties in obtaining adequate experimental measurements and verification. The following description gives some insight into this problem.

It has been demonstrated that pore water migration depends on the capillary characteristics of a particular soil, its chemical potential, pneumatic and elevation heads, and overburden pressure. The main agent generating the suction potential is the change in the adsorbed water layer surrounding the soil particles. As this water

layer freezes and becomes thinner, a negative pressure within the layer is generated. It has been commonly assumed that the water content, suction pressure and soil hydraulic conductivity vary exponentially in the freezing fringe. During the growth of an ice lens, the segregation temperature as well as the ice lens location remain constant due to the release of latent heat. The zero-degree isotherm, however, moves as continuous cooling takes place. Consequently, the width of the freezing fringe increases and, therefore, the overall "effective" hydraulic conductivity decreases. The water flow towards the ice lens can be calculated as a product of the hydraulic conductivity and the suction potential. Since the suction potential remains more or less constant, it is the low hydraulic conductivity and the "long" path through the freezing fringe that will eventually retard the water movement. At such a time, the lack of latent heat at the ice lens surface will result in fast freezing. During this process, only the in-situ water will change phase. This is possible because the cold part of the freezing fringe has been partially depleted of water. The entire fringe then moves further with continuing cooling until a new segregation location, with suitable thermal and hydraulic conditions, develops.

An experiment on ice lens growth has been conducted by Penner [13] . He found that the growth rate rises rapidly when a lens has been initiated. Then a protracted period of decreasing growth follows. The measured temperature of the growing face of the ice lens decreases continuously until the next lens starts to form. The rapid increase in latent heat released in the period following lens initiation can be seen on plots of isotherms. It is thought to be partly due to intra-lens freezing combined with much higher rate of growth during the early period of lens growth.

Konrad and Morgenstern [14] [15] investigated the effects of applied pressure on freezing soils and the influence of cooling rate on the temperature of ice lens formation in clayey silts. They found that when external loads are applied to soils subjected to open-system freezing, segregational frost heave will be inhibited. The temperature of ice lens initiation is not a constant for a given soil. The temperature at a newly formed ice lens is warmer with smaller rates of cooling of the frozen fringe. They also found that the velocity $v(t)$ of pore water arrival at the freezing point can be predicted from:

$$v(t) = SP\text{grad}(T) \tag{2.2}$$

where

SP is the segregation potential ($mm^2s^{-1\circ}C^{-1}$);

grad(T) is the thermal gradient (mm/s).

The segregational heave increment, Δh_s, which corresponds to the arrival of pore water over a time interval Δt can be obtained from

$$\Delta h_s = 1.09v(t)\Delta t \tag{2.3}$$

and the frost heave increment resulting from the freezing of in-situ pore water, Δh_p, is given by

$$\Delta h_i = 0.09\varepsilon n\left(1 - \frac{w_{uf}}{n}\right)\Delta z \tag{2.4}$$

where

ε is a factor taking into account the proportion of unfrozen water remaining in the frozen sample;

n is the porosity;

0.09 represents the volumetric expansion of water when it freezes;

w_{uf} is the volumetric unfrozen moisture content;

Δz is the increase in frozen depth.

Thus, the total frost heave during a time period, Δt, is given by

$$\Delta h = \Delta h_s + \Delta h_i \tag{2.5}$$

Other works regarding ice lens formation and growth can be found in Smith and Williams [16].

2.4.2 Heat-Moisture-Frost Heave Description

Frost heave, generally, is caused by the moisture migration from unfrozen to frozen soils. Up to now, there seems to be no complete model to simulate this process despite the numerous experimental and numerical studies cited in the literature. The main reason is that there are too many factors which are involved, such as soil type, permeability, degree of saturation, void ratio, temperature, heat characteristics, creep properties of soil, ice/water pressure, and external loads.

Shen and Ladanyi [17] [18] [19] proposed a numerical model to deal with the coupled heat, moisture and stress field including creep effects in the freezing soil.

Sheppard, Kay, and Loch [20] developed a similar computer model to Shen and Ladanyi's for heat and mass flow in freezing soils. They also tested their model against data generated from laboratory studies and field data, and identified the limitations in applying such a model to the field situation.

In both Shen and Sheppard's formulations, the ice and liquid pressures along with the temperature relations are described by the Clapeyron equation [21] which takes the general form

$$\frac{P_l}{\rho_l} - \frac{P_i}{\rho_i} = L \ln \frac{T_k}{T_0} \tag{2.6}$$

where

P_l and P_i are the liquid and ice pressure (Pa);

ρ_l and ρ_i are the liquid and ice density (kg/m^3);

L is the latent heat of fusion (J/kg);

T_k and T_0 are the temperature and freezing point of pure water at atmospheric pressure, i.e. 273.16 $(°K)$;

$°K =° C + 273.16$.

A detailed derivation for Eq. (2.6) based on the principle of thermodynamics can be found in Kay and Groenevelt [21]. They basically investigated the chemical potential equilibrium between water and ice in the porous medium and described it by using Gibbs-Duhem equation. A more detailed explanation will be given in Chapter four of this thesis. Similar model describing the water and heat transport and the frost heave can also be found in the work by Fremond and Mikkola [22].

Computational modelling of pipelines in discontinuous frost heave zones can be also found in the works of Selvadurai [23]. He examined the flexural interaction of a long distance pipeline with the surrounding soils and attributed it to differential ground heave due to frost heave. Beam elements were also used in his model to simulate pipeline and the frozen soil was considered a creeping material.

Nixon [24] established an analytical method for predicting the build up of ice due to thermally induced water flow in frozen soil initially near its melting point beneath a chilled pipeline. The method requires a steady state temperature field that can be obtained from relatively straightforward closed-form analysis. In addition, a function describing the hydraulic conductivity gradient with temperature is required to complete an estimate of long-term or steady heave rate. He suggested an expression of power law in the form

$$\frac{dk}{dT} = CT^{-n} \tag{2.7}$$

where k is the hydraulic conductivity in cm/s, T is the temperature in $°C$ below freezing, C is a constant dependent on soil type, and n is an exponent having a value of about 2.5. Equation (2.7) appears to be valid in the range of temperatures from about $-0.2°C$ to about $-2°C$. The long-term frost after many years of operation of a chilled pipe in previously frozen ground can be expected to be in the range of a few centimeters.

The consequence of soil freezing is due to the action of frost loads. Rajani and Zhan [25] developed a model based on the estimation of frost loads. They indicated

that vertical force equilibrium is satisfied throughout the trench and sidefill prior to the setup of the freezing front. Thus, frost load is an additional stress generated load as a consequence of net upward movement at the freezing front, i.e. soil expansion. Therefore, if the frozen soil above the freezing front were to behave as a Mohr-Coulomb type material, frost load is a consequence of "negative arching". This situation is contrasted with "positive arching" where trench backfill settlement mobilizes the soil stresses at the backfill-sidefill interface with a concurrent reduction in earth pressure. It is also assumed that the shear resistance at the trench backfill-sidefill interface is less than that at the soil-soil interface. Concurrently, a reaction force will be generated by the mass of unfrozen soil beneath the freezing front in response to the frost heave at the freezing front.

Other investigations on heat and moisture transfer and frost heave can be found in the works by Williams [26] [27] [28] [29] [30] [31].

2.5 Numerical Modelling

2.5.1 Finite Element Method

Most of the finite element analysis relating to soil-pipeline systems have been carried out in two dimensions, even though three-dimensional computations have also been attempted, see [23]. In fact, three-dimensional finite element models are well established now, but one drawback is that they are computationally intensive, especially in the non-linear case where solutions must be searched iteratively. In this situation,

an efficient and yet simple method is highly desired. Also, the method should be able to capture most of the constitutive features of the soil and the pipeline. The Fourier finite element method theory seems to provide the required efficiency by using an alternative formulation. The method and its application to pipeline engineering will be developed in details in the following sections.

2.5.2 Fourier FEM Theory and its Applications

As discussed in the previous chapter, when a structure reveals periodicity in one of its dimensions even if the load is non-symmetric, the Fourier finite element method can be employed. In this method, all the variables in the periodic direction will be expanded into a Fourier series and the classical finite element can be used in the other directions. Upon certain conditions of linearity, the global system of equations referring to the three-dimensional problem reduces to perfectly decoupled blocks of equations, of which each refers to a classical two-dimensional finite element case. Hence, efficiency in computations stems from the fact that the solution of the complete three-dimensional problem can be carried out from a series of independent classical two-dimensional finite element analyses.

As early as in 1965, Wilson [32] had already developed a Fourier finite element method in the context of linear structural analysis of axisymmetric solids. Later on, Percy *et al.* [33] and Stricklin *et al.* [34] also used the Fourier series decomposition technique to analyze linear elastic deformation of shells of revolution subjected to non-axisymmetric loads. A few years later, the method was extended to a geometrically non-linear analysis of shells of revolution under non-axisymmetric loading in

both static and dynamic regimes, see Stricklin *et al.* [35] and Wunferlich *et al.* [36].

Geometrically non-linear problems which involve large deformations have also been solved by Danielson and Tielking [37] using Fourier continuum finite elements. Their study showed that although the Fourier harmonics resulting from the equilibrium equations are coupled, the computational effort can still be much less than that required for an analysis based on traditional 3-D brick elements. The first step in their proposed solution involves the use of a decoupled stiffness matrix to precondition the coupled system of linear simultaneous equations. Then the solution as obtained from the decoupled system is used as first estimate into the coupled system for achieving a better solution. In fact, the scheme basically involves an iterative process in which the solution is being constantly updated until an acceptable level of error tolerance is reached.

With regards to addressing materially non-linear structural problems within Fourier finite element context, the basic theory of the method and its application can be found in the work by Winnicki and Zienkiewicz [38]. They judiciously introduced elasto-visco-plastic behavior in their model in order to solve elasto-plastic problems, and found that their approach is 6-10 times cheaper than the true three-dimensional case. In fact, it is well known that the elasto-visco-plastic solution will tend towards the non-viscid solution corresponding to the original elasto-plastic problem when time reaches infinity. Also, by explicitly integrating the elasto-visco-plasticity equations and treating the resulting unbalanced forces due to visco-plasticity as initial strains, the elastic stiffness which is constant can be used during each step of the solution, see Owen and Hinton [39]. Hence, the resulting Fourier harmonics are still

decoupled so that a series of independent two-dimensional finite element analyses can be carried out.

Kay and Griffiths [40] successfully used the above method to solve the structural response of a concrete skirt structure of geometric revolution axisymmetry under conventional horizontal, vertical, and moment loads which result into a non-axisymmetric load effect. The concrete skirt structure is embedded in a normally consolidated clay which follows plastic deformation.

The Fourier finite element method was also used in heat transfer problems by Hinton and Owen [41]. Heat transfer is investigated in a rectangular plane with the uniform temperature distribution on two opposing sides. The method here takes a special form known as the finite strip method, a semi-analytical finite element process, in which a rectangular plate is discretized by using different interpolation functions in different directions of space so that the resulting equations can be solved in a decoupled manner. Each decoupled system of equations then correspond to a problem with reduced dimension in space; in the case of the plate they would be one-dimensional. Further details with regard to the exact form and properties of the interpolation functions can be found in Cheung [42].

2.5.3 Discrete Fourier FEM

The literature suggests that Fourier finite element methods of the continuous type is the most commonly used approach. There is, however, another approach which uses discrete Fourier series expansion in the finite element method. Runesson and Booker [43] [44] used a discrete Fourier finite element approach in elasto-plastic

layered soil and in consolidation problems. A circular boundary element technique of discrete Fourier finite element approach has also been adopted by Moore and Booker [45] in solving deep underground tunnel problems. The discrete Fourier finite element method works with variables defined in discrete domains while its continuous counterpart deals with variables in continuous domains. This can be regarded as the major difference between these two branches of the Fourier finite element method and their choice in analysis is based on their relative ease and flexibility in mathematical formulation.

Lai and Brooker [46] presented detailed formulation of this discrete method in their paper. They found that discrete method can overcome Gibb 's phenomenon which is inherent in the Fourier series approximation. Basically Gibb's phenomenon refers to an oscillation or offset which might always exist no matter how many Fourier terms are employed for some particular problem when the continuous method is used. Using complex function decomposition, they derived their equilibrium equations which are decoupled from each mode (wedge, or slice). To illustrate their method, a rigid caisson founded in both elastic and elasto-plastic soils was presented. They also concluded that no special joint or interface element is needed when shear failure, slip, or breakaway is encountered. This is probably because the variables are dealt with in discrete domains with orthogonality conditions still prevalent.

The commercial finite element code ABAQUS [47] offers the possibility of using the discrete Fourier finite element method. However, only up to four Fourier modes are allowed in ABAQUS, which is usually not accurate enough for complicated load conditions.

2.5.4 Consistent Tangent Operator

This section describes a general method for solving non-linear problems with particular reference to plasticity which will be later used in the Fourier finite element method developed in this thesis.

Simo and Taylor [48] were first to introduce the concept of consistent tangent operator in 1985. This method uses a closest-point-projection algorithm to return the yielded stress state onto the yield surface, and the tangent operator which is consistent with this algorithm can be developed accordingly. It has been proven in their paper that the resulting iterative procedure for the linearization of the equilibrium equation will preserve the quadratic convergence nature of Newton's method. However, the so called elasto-plastic tangent modulus derived from the continuum elasto-plastic equations with a radial return integration algorithm has been used for more than a decade now. It is found that this modulus results into a loss of quadratic convergence characteristic which is particularly important for large time step problems.

An implicit integration algorithm for Hoek-Brown elastic-plastic model for rocks with consistent tangent modulus has been investigated by Wan [49] in 1992. It was demonstrated that formulation of such consistent tangent modulus results in accurate and rapid convergence of the displacement finite element scheme during the search for equilibrium, even for complicated yield surfaces in non-associated plasticity calculations.

2.5.5 Contact Element

Due to the disparity in the soil and pipe material properties, their respective deformations will be largely different. Discontinuities in displacement fields in the form of a slip may take place between these two different materials. The contact problem which arises is of a complex nature because the contacting surfaces may change in size and shape with load conditions. This may result in changes in friction conditions between the contacting bodies. Consequently, the contact problem is highly non-linear and remains one of the most challenging problems in computational mechanics.

Literature which deals with direct application of contact elements to soil-pipeline is scarce. However, contact elements have been profusely used in other engineering problems such as in the mechanical, civil, structural, and geotechnical areas. One of the early applications was by Wilson and Parsons [50] who used an indirect approach where contact conditions were treated as subsidiary equations. Another classical application of contact elements was used Goodman *et al.* [51] for simulating slippage in jointed rocks. Extension of this method to include friction was presented by Chan and Tuba [52] [53]. A formulation based on flexibility matrices for contact problems was introduced by Francavilla and Zienkiewicz [54]. More recent applications of finite element method to contact problems can be divided into three major approaches: the Lagrange multiplier method; the Penalty method; and the Mixed (or Hybrid) method.

Bathe and Chaudhary [55] made efforts to develop an algorithm for analyzing planar and axisymmetric contact problems. They included the possibilities to analyze contact between flexible-flexible and rigid-flexible bodies under various conditions

such as

(1) sticking or sliding conditions (with or without friction);

(2) large relative motions between bodies;

(3) repeated contact and separation between the bodies.

The solution procedure uses a Lagrange multiplier technique to incrementally impose the deformation constraints along the contact surfaces. The contact forces are evaluated from distributed tractions that act on the contactors. The friction condition is based upon the Coulomb's law.

Peric and Owen [56] used penalty method in 3-D contact problems with friction. The friction forces are assumed to follow the Coulomb's law. Plastic flow obeys a non-associated frictional contact law, with a slip criterion treated in the context of a standard return mapping algorithm. Consistent linearization, used for the field equations, leads to a fully implicit scheme with non-symmetric tangent stiffness. This stiffness preserves asymptotic quadratic convergence of the Newton-Raphson method. Their model is suitable for simulating problems not involving high normal forces.

For frictionless contact problems, the contact element stiffness matrices are symmetric. However, for friction contact problems, a shear force should be included and consequently the stiffness matrices become unsymmetrical. Generally, an analysis which involves unsymmetrical matrices requires about twice the amount of storage space and twice the amount of calculation time as those with symmetric matrices. To overcome the solution of non-symmetric system of equations Ju and Rowlands [57] proposed a new contact element for frictional contact problems based on the

penalty method. The unique feature of this approach is that the contact element stiffness matrix is symmetrical, even for frictional contact problems with a large sliding mode. This element can be used to simulate sticking, sliding, and separation modes in frictional contact analysis. Finite element analysis that uses this new contact element requires only half the computing time and half the storage space of those using unsymmetrical contact elements.

In the frictional type of contact finite elements Cescotto and Charlier [58] developed mixed contact finite elements based on mixed variational principles. The displacement field and the contact stress field are discretized independently. The basic advantage of using such mixed contact elements is that the contact condition is naturally smoother than with the displacement type approach. Discretizing the contact stress field alone basically ensures stress compatibility at the interface just in the same way as what is done for stress type finite element formulations. However, displacement compatibility is not ensured which is suitable for describing the interface slip.

Joint element is another type of contact element. Lee, Pande, and Pietruszczak [59] developed a joint element method based on a homogenization technique for the finite element analysis of jointed rock masses. In fact, the homogenization technique uses an averaging rule by which the influence of the joint is smeared into a small region of the adjacent intact rock based on energy principles. The constitutive matrix in this region is defined in terms of properties of both the intact rock and the joint as well as the geometry of the homogenized domain. The stiffness matrix does not depend on the thickness of the joint, which is the main advantage over other joint

elements. And the position of the joint within the element can be arbitrary since the homogenization technique is performed according to the volume fractions of the materials.

2.6 Conclusion

From the above literature review, it appears that the continuum approach is the most flexible method of analysis despite the mathematical complexity involved. On the other hand, in terms of numerical modelling, most previous works have focussed on two-dimensional finite elements for simplicity while limiting true three-dimensional finite elements to only specialized cases. It seems that more efficient calculations may be achieved by the Fourier finite element method which has been used for different applications as described in the previous sections. In this thesis, a numerical model based on Fourier finite elements and elasto-plasticity will be developed. Also, for solving the complete stress-moisture migration-thermal problem, it is proposed to perform a separate thermal analysis which will then be explicitly coupled to the Fourier finite element model.

Chapter 3

DESCRIPTION OF MODEL

3.1 Formulation of Continuous Fourier FEM

3.1.1 Background

The Fourier finite element theory is based on the judicious use of trigonometric functions for discretizing field variables which appear in the finite element equations. For structures which reveal a periodicity in one of their dimensions, the efficiency of the finite element analysis can be improved. It is natural to assume these structures as geometrically axisymmetric, but loaded non-axisymmetrically. For a pipeline, some degree of periodicity can also be established in its circumferential direction.

The technique involves developing two-dimensional finite elements in one plane of the structure and expressing the main field variable by a Fourier series in the periodic direction. In the literature, these elements have been often referred to as Fourier expansion or semi-analytic elements, see Winnicki and Zienkiewiczs [38] and Kay and Griffiths [40] . Here, Fourier series could be written in either continuous or discrete form. In this thesis, the continuous scheme is utilized unless noted explicitly.

The Fourier series involves trigonometric functions such as cosine and sine which are endowed with the orthogonality property. In this respect, advantage is taken

from this property in an analysis where the deformational displacement fields can be superimposed from each harmonic load component. It will be demonstrated in this thesis that the superposition of harmonics is still legitimate for the case of non-linear constitutive behaviour. This observation can interestingly produce several beneficial effects, the major one being the reduction of a three-dimensional model to a two-dimensional one. Furthermore, this advantage is accentuated by the fact that in some cases the loading can be represented by only a few harmonics.

In one longitudinal plane of the pipeline, the space is discretized by standard finite elements, while in the periodic direction, one has the choice between a Fourier expansion or a series of discrete finite elements using polynomials. It is clearly desirable to use Fourier series in the periodic direction due to the orthogonality property of trigonometric functions. The resulting stiffness matrices of each harmonic will be decoupled from the other one. Hence, modelling can be greatly simplified by the analysis of a series of decoupled two-dimensional finite element problems.

3.1.2 Principle of Virtual Work

The equilibrium equations for a deforming solid, irrespective of the nature of its constitutive behaviour, can be expressed by the virtual work statement in which all quantities are expressed with respect to a global cylindrical coordinate system:

$$\int_{\Omega} \sigma_{ij}\delta\varepsilon_{ij}\, r\, dr\, dz\, d\theta - \int_{\Omega} b_i \delta u_i\, r dr\, dz\, d\theta - \int_{\Gamma_g} T_i \delta u_i\, r\, dg\, d\theta = 0 \qquad (3.1)$$

The above equation basically indicates that the internal work done by Cauchy

stresses σ_{ij} during virtual infinitesimal strains $\delta\varepsilon_{ij}$ must be equal to the external work done by surface tractions, T_i during virtual displacements δu_i. Subscripts i and j vary from 1 to 3 referring to radial, axial and circumferential directions r, z and θ respectively. Here, $\delta u, \delta v$ and δw are virtual displacements in radial, axial and circumferential directions respectively, and g is a coordinate along the loaded edge in the $r-z$ plane.

In general terms, the deformable body could be subjected to an initial stress and/or initial strain field denoted by σ^0_{ij} and ε^0_{ij} respectively. For example, the initial stresses may originate from in-situ stress in the soil while initial strains may be due to thermal loads. Hence, the virtual work equation in Eq. (3.1) must be amended by considering the following:

$$\sigma_{ij} = C_{ijkl}(\varepsilon_{kl} - \varepsilon^0_{kl}) + \sigma^0_{ij} \tag{3.2}$$

where C_{ijkl} is the constitutive tensor of the material.

3.1.3 Fourier Discretization of Field Variables

Figure 3.1 shows a typical pipeline embedded in the ground with reference to a cylindrical system axes. The radial, axial, and circumferential axes of the pipeline are represented by axes r, z, and θ.

During the discretization of Eq. (3.1), the displacement field variable is expanded using both polynomial and trigonometric functions. In precise terms, isoparametric quadrilateral finite element interpolation is used in the $r-z$ plane, while interpolation

in the circumferential direction θ is represented by a trigonometric series generally in cosine and sine functions. Depending on the degree of symmetry about the axis of the pipeline, the series can be simplified accordingly. Herein, both cosine and sine components are included in the formulation for the sake of generality. Each trigonometric series is truncated after the mth harmonic and each $r-z$ plane is discretized using n nodes. Within each plane, the coordinates (r, z) of any point are given as

$$\begin{aligned} r &= \sum_{i=1}^{n} N_i(r,z)\,\bar{r}_i \\ z &= \sum_{i=1}^{n} N_i(r,z)\,\bar{z}_i \end{aligned} \tag{3.3}$$

whereas displacements for a given reference plane oriented at θ are expanded as

$$\begin{aligned} u(r,\,z,\,\theta) &= \sum_{p=0}^{m}\left(\sum_{i=1}^{n} N_i(r,\,z)\,\overline{u}_i^p\,\cos(p\theta) + \sum_{i=1}^{n} N_i(r,\,z)\,\overline{\overline{u}}_i^p\,\sin(p\theta)\right) \\ v(r,\,z,\,\theta) &= \sum_{p=0}^{m}\left(\sum_{i=1}^{n} N_i(r,\,z)\,\overline{v}_i^p\,\cos(p\theta) + \sum_{i=1}^{n} N_i(r,\,z)\,\overline{\overline{v}}_i^p\,\sin(p\theta)\right) \\ w(r,\,z,\,\theta) &= \sum_{p=0}^{m}\left(\sum_{i=1}^{n} N_i(r,\,z)\,\overline{w}_i^p\,\cos(p\theta) + \sum_{i=1}^{n} N_i(r,\,z)\,\overline{\overline{w}}_i^p\,\sin(p\theta)\right) \end{aligned} \tag{3.4}$$

The discretization in the $r-z$ plane is typically done by means of isoparametric

finite elements whose shape functions are $N_i(r, z)$. In the coordinate interpolation given in Eq. (3.3) barred variables refer to nodal values. For the discretization of displacements in Eq. (3.4) single and double barred variables stand for cosine and sine components respectively.

The external load terms which appear in Eq. (3.1) can also be expanded similarly as displacements

$$\begin{aligned} T_s &= \sum_{p=0}^{m} \left(\sum_{i=1}^{n} N_i(r,z)\, \overline{T}^{p}_{s,i}\, \cos(p\theta) + \sum_{i=1}^{n} N_i(r,z)\, \overline{\overline{T}}^{p}_{s,i}\, \sin(p\theta) \right) \\ b_s &= \sum_{p=0}^{m} \left(\sum_{i=1}^{n} N_i(r,z)\, \overline{b}^{p}_{s,i}\, \cos(p\theta) + \sum_{i=1}^{n} N_i(r,z)\, \overline{\overline{b}}^{p}_{s,i}\, \sin(p\theta) \right) \\ & (s = r,\ z,\ \text{and}\ \theta) \end{aligned} \tag{3.5}$$

3.1.4 Discretization of Virtual Strains

The small strain components are typically given in terms of displacement derivatives obtained from strain-displacement compatibility equations, i.e.

$$\varepsilon = \left\{ \begin{array}{c} \varepsilon_{rr} \\ \varepsilon_{zz} \\ \varepsilon_{\theta\theta} \\ \gamma_{rz} \\ \gamma_{r\theta} \\ \gamma_{z\theta} \end{array} \right\} = \left\{ \begin{array}{c} \frac{\partial u}{\partial r} \\ \frac{\partial v}{\partial z} \\ \frac{u}{r} + \frac{1}{r}\frac{\partial w}{\partial \theta} \\ \frac{\partial u}{\partial z} + \frac{\partial v}{\partial r} \\ \frac{1}{r}\frac{\partial u}{\partial \theta} + \frac{\partial w}{\partial r} - \frac{w}{r} \\ \frac{1}{r}\frac{\partial v}{\partial \theta} + \frac{\partial w}{\partial z} \end{array} \right\} \tag{3.6}$$

The interpolation scheme given in Eq. (3.4) can be readily replaced into the expression of strains in Eq. (3.6).

$$\varepsilon_{rr} = \frac{\partial u}{\partial r} = \sum_{p=0}^{m} \left(\sum_{i=1}^{n} \frac{\partial N_i}{\partial r} \overline{\overline{u}}_i^p \cos p\theta + \sum_{i=1}^{n} \frac{\partial N_i}{\partial r} \overline{\overline{u}}_i^p \sin p\theta \right)$$

$$\varepsilon_{zz} = \frac{\partial v}{\partial z} = \sum_{p=0}^{m} \left(\sum_{i=1}^{n} \frac{\partial N_i}{\partial z} \overline{\overline{v}}_i^p \cos p\theta + \sum_{i=1}^{n} \frac{\partial N_i}{\partial z} \overline{\overline{v}}_i^p \sin p\theta \right)$$

$$\varepsilon_{\theta\theta} = \frac{u}{r} + \frac{1}{r}\frac{\partial w}{\partial \theta} = \sum_{p=0}^{m} \left(\sum_{i=1}^{n} \frac{N_i}{r} \overline{\overline{u}}_i^p \cos p\theta + \sum_{i=1}^{n} \frac{N_i}{r} \overline{\overline{u}}_i^p \sin p\theta \right) + \sum_{p=0}^{m} \left(-p \sum_{i=1}^{n} \frac{N_i}{r} \overline{\overline{w}}_i^p \sin p\theta + p \sum_{i=1}^{n} \frac{N_i}{r} \overline{\overline{w}}_i^p \cos p\theta \right)$$

$$\gamma_{rz} = \frac{\partial u}{\partial z} + \frac{\partial v}{\partial r} = \sum_{p=0}^{m} \left(\sum_{i=1}^{n} \frac{\partial N_i}{\partial z} \overline{\overline{u}}_i^p \cos p\theta + \sum_{i=1}^{n} \frac{\partial N_i}{\partial z} \overline{\overline{u}}_i^p \sin p\theta \right) + \sum_{p=0}^{m} \left(\sum_{i=1}^{n} \frac{\partial N_i}{\partial r} \overline{\overline{v}}_i^p \cos p\theta + \sum_{i=1}^{n} \frac{\partial N_i}{\partial r} \overline{\overline{v}}_i^p \sin p\theta \right)$$

$$\gamma_{r\theta} = \frac{1}{r}\frac{\partial u}{\partial \theta} + \frac{\partial w}{\partial r} - \frac{w}{r} = \sum_{p=0}^{m} \left(-p \sum_{i=1}^{n} \frac{N_i}{r} \overline{\overline{u}}_i^p \sin p\theta + p \sum_{i=1}^{n} \frac{N_i}{r} \overline{\overline{u}}_i^p \cos p\theta \right) +$$

$$\sum_{p=0}^{m}\left[\sum_{i=1}^{n}\left(\frac{\partial N_i}{\partial r}-\frac{N_i}{r}\right)\overline{w}_i^p\cos p\theta+\sum_{i=1}^{n}\left(\frac{\partial N_i}{\partial r}-\frac{N_i}{r}\right)\overline{\overline{w}}_i^p\sin p\theta\right]$$

$$\gamma_{z\theta} = \frac{1}{r}\frac{\partial v}{\partial \theta}+\frac{\partial w}{\partial z}=\sum_{p=0}^{m}\left(-p\sum_{i=1}^{n}\frac{N_i}{r}\overline{v}_i^p\sin p\theta+p\sum_{i=1}^{n}\frac{N_i}{r}\overline{\overline{v}}_i^p\cos p\theta\right)+$$

$$\sum_{p=0}^{m}\left(\sum_{i=1}^{n}\frac{\partial N_i}{\partial z}\overline{w}_i^p\cos p\theta+\sum_{i=1}^{n}\frac{\partial N_i}{\partial z}\overline{\overline{w}}_i^p\sin p\theta\right) \tag{3.7}$$

After considerable algebraic manipulations the strain vector ε can be written in a matrix form. This matrix expression involves cosine and sine components of displacements for all nodes contained in a typical plane in (r, z) and for all harmonics.

$$\varepsilon = \mathbf{B} : \mathbf{u} = [\mathbf{B}_1\ \mathbf{B}_2\ \mathbf{B}_3\ \ldots\ \mathbf{B}_p\ \ldots\ \mathbf{B}_m]\begin{Bmatrix}\mathbf{u}_1\\ \mathbf{u}_2\\ \mathbf{u}_3\\ .\\ .\\ \mathbf{u}_p\\ .\\ .\\ \mathbf{u}_m\end{Bmatrix} \tag{3.8}$$

m = total number of harmonics.

The structure for the matrix $\mathbf{B}_p$ at a particular harmonic p contains terms in partial derivatives of shape functions $N_i(r, z)$ and cosine and sine components for the entire plane in (r, z).

$$\mathbf{B}_p = \left[\mathbf{B}_p^1\, \mathbf{B}_p^2 \,....\, \mathbf{B}_p^i \,....\, \mathbf{B}_p^n\right] \text{ and } \mathbf{B}_p^i = \left[\overline{\mathbf{B}}_p^i \mid \overline{\overline{\mathbf{B}}}_p^i\right] \tag{3.9}$$

The single barred and double barred matrices $\overline{\mathbf{B}}_p^i$ and $\overline{\overline{\mathbf{B}}}_p^i$ corresponding to the ith node and pth harmonic are indeed given as:

$$\overline{\mathbf{B}}_p^i = \begin{bmatrix} \frac{\partial N_i}{\partial r}\cos p\theta & 0 & 0 \\ 0 & \frac{\partial N_i}{\partial z}\cos p\theta & 0 \\ \frac{N_i}{r}\cos p\theta & 0 & -p\frac{N_i}{r}\sin p\theta \\ \frac{\partial N_i}{\partial z}\cos p\theta & \frac{\partial N_i}{\partial r}\cos p\theta & 0 \\ -p\frac{N_i}{r}\sin p\theta & 0 & \left(\frac{\partial N_i}{\partial r} - \frac{N_i}{r}\right)\cos p\theta \\ 0 & -p\frac{N_i}{r}\sin p\theta & \frac{\partial N_i}{\partial z}\cos p\theta \end{bmatrix}$$

$$\overline{\overline{\mathbf{B}}}_p^i = \begin{bmatrix} \frac{\partial N_i}{\partial r}\sin p\theta & 0 & 0 \\ 0 & \frac{\partial N_i}{\partial z}\sin p\theta & 0 \\ \frac{N_i}{r}\sin p\theta & 0 & p\frac{N_i}{r}\cos p\theta \\ \frac{\partial N_i}{\partial z}\sin p\theta & \frac{\partial N_i}{\partial r}\sin p\theta & 0 \\ p\frac{N_i}{r}\cos p\theta & 0 & \left(\frac{\partial N_i}{\partial r} - \frac{N_i}{r}\right)\sin p\theta \\ 0 & p\frac{N_i}{r}\cos p\theta & \frac{\partial N_i}{\partial z}\sin p\theta \end{bmatrix} \tag{3.10}$$

or written in a more abbreviated way:

$$\begin{aligned}\overline{\mathbf{B}}_p^i &= \mathbf{B}^r \cos p\theta - \mathbf{B}^s \sin p\theta \\ \overline{\overline{\mathbf{B}}}_p^i &= \mathbf{B}^r \sin p\theta - \mathbf{B}^s \cos p\theta \end{aligned} \tag{3.11}$$

in which

$$\mathbf{B}^r = \begin{bmatrix} \frac{\partial N_i}{\partial r} & 0 & 0 \\ 0 & \frac{\partial N_i}{\partial z} & 0 \\ \frac{N_i}{r} & 0 & 0 \\ \frac{\partial N_i}{\partial z} & \frac{\partial N_i}{\partial r} & 0 \\ 0 & 0 & \left(\frac{\partial N_i}{\partial r} - \frac{N_i}{r}\right) \\ 0 & 0 & \frac{\partial N_i}{\partial z} \end{bmatrix}; \qquad \mathbf{B}^s = \frac{pN_i}{r} \begin{bmatrix} 0 & 0 & 0 \\ 0 & 0 & 0 \\ 0 & 0 & 1 \\ 0 & 0 & 0 \\ 1 & 0 & 0 \\ 0 & 1 & 0 \end{bmatrix} \tag{3.12}$$

The displacement vector $\mathbf{u}$ given in Eq. (3.8) contains all the degrees of freedom including the sine and cosine components for each harmonic. In precise terms, the vector $\mathbf{u}_p$ at the pth harmonic has the following structure in which single and double barred degrees of freedom are grouped per node contained in the plane $r - z$, i.e.

$$\begin{aligned}\mathbf{u}_p^T = \{&\overline{u}_1^p, \overline{v}_1^p, \overline{w}_1^p, \overline{\overline{u}}_1^p, \overline{\overline{v}}_1^p, \overline{\overline{w}}_1^p | \ \overline{u}_2^p, \overline{v}_2^p, \overline{w}_2^p, \overline{\overline{u}}_2^p, \overline{\overline{v}}_2^p, \overline{\overline{w}}_2^p | \ \ldots | \\ &\overline{u}_i^p, \overline{v}_i^p, \overline{w}_i^p, \overline{\overline{u}}_i^p, \overline{\overline{v}}_i^p, \overline{\overline{w}}_i^p | \ \ldots | \ \overline{u}_n^p, \overline{v}_n^p, \overline{w}_n^p, \overline{\overline{u}}_n^p, \overline{\overline{v}}_n^p, \overline{\overline{w}}_n^p\} \\ &(p = 1, 2, 3, \ldots, m)\end{aligned} \tag{3.13}$$

Finally, the virtual strain vector $\delta\boldsymbol{\varepsilon}$ can be obtained by taking the virtual form of Eq. (3.6), i.e.

$$\delta\boldsymbol{\varepsilon} = \mathbf{B} : \delta\,\mathbf{u} \tag{3.14}$$

3.1.5 Discretization of Displacements

The displacements δu, δv, δw which appear in Eq. (3.1) can be written in terms of cosine and sine components by using Eq. (3.4). After rearranging terms the same way as was done for strains in the previous section, one gets

$$\begin{Bmatrix} \delta u \\ \delta v \\ \delta w \end{Bmatrix} = [\mathbf{A}_1\ \mathbf{A}_2\ \mathbf{A}_3\ ....\ \mathbf{A}_p\ ....\ \mathbf{A}_m] \begin{Bmatrix} \delta\mathbf{u}_1 \\ \delta\mathbf{u}_2 \\ \delta\mathbf{u}_3 \\ . \\ . \\ \delta\mathbf{u}_p \\ . \\ . \\ \delta\mathbf{u}_m \end{Bmatrix} \tag{3.15}$$

m = total number of harmonics, in which a typical submatrix $\mathbf{A}_p$ for the pth harmonic is given by

$$\begin{aligned} \mathbf{A}_p &= \left[\mathbf{A}_p^1\, \mathbf{A}_p^2 \,....\, \mathbf{A}_p^i \,....\, \mathbf{A}_p^n\right] \\ \mathbf{A}_p^i &= \left[\bar{\mathbf{A}}_p^i \mid \overline{\overline{\mathbf{A}}}_p^i\right] \end{aligned} \tag{3.16}$$

and

$$\begin{aligned} \bar{\mathbf{A}}_p^i &= N_i \cos p\theta\, \mathbf{I}_3 \\ \overline{\overline{\mathbf{A}}}_p^i &= N_i \sin p\theta\, \mathbf{I}_3; \qquad \mathbf{I}_3 = \begin{bmatrix} 1 & 0 & 0 \\ 0 & 1 & 0 \\ 0 & 0 & 1 \end{bmatrix} \end{aligned} \tag{3.17}$$

or written in explicit expression, Eq. (3.16) becomes

$$\mathbf{A}_p = \begin{bmatrix} N_i \cos p\theta & 0 & 0 & N_i \sin p\theta & 0 & 0 \\ 0 & N_i \cos p\theta & 0 & 0 & N_i \sin p\theta & 0 \\ 0 & 0 & N_i \cos p\theta & 0 & 0 & N_i \sin p\theta \end{bmatrix} \tag{3.18}$$

A typical expression of $\delta \mathbf{u}_p$ in Eq.(3.15) can be easily obtained by taking the virtual form of Eq. (3.13). This virtual form is just by putting a δ symbol in Eq. (3.13).

3.1.6 Discretization of External Load Terms

The tractions and body forces given in Eq. (3.5) have three components, i.e. radial, axial and circumferential directions. For example, the discretized form of traction forces can be given as

$$\mathbf{T} = \begin{Bmatrix} \sum_{p=0}^{m}\left(\sum_{i=1}^{n} N_i(r,z)\,\overline{T}^{p}_{r,i}\cos(p\theta) + \sum_{i=1}^{n} N_i(r,z)\,\overline{\overline{T}}^{p}_{r,i}\sin(p\theta)\right) \\ \sum_{p=0}^{m}\left(\sum_{i=1}^{n} N_i(r,z)\,\overline{T}^{p}_{z,i}\cos(p\theta) + \sum_{i=1}^{n} N_i(r,z)\,\overline{\overline{T}}^{p}_{z,i}\sin(p\theta)\right) \\ \sum_{p=0}^{m}\left(\sum_{i=1}^{n} N_i(r,z)\,\overline{T}^{p}_{\theta,i}\cos(p\theta) + \sum_{i=1}^{n} N_i(r,z)\,\overline{\overline{T}}^{p}_{\theta,i}\sin(p\theta)\right) \end{Bmatrix}$$

$$= [\mathbf{P}_1\ \mathbf{P}_2 ... \mathbf{P}_p ... \mathbf{P}_m] \begin{Bmatrix} \mathbf{T}_1 \\ \mathbf{T}_2 \\ . \\ \mathbf{T}_p \\ . \\ \mathbf{T}_m \end{Bmatrix} \tag{3.19}$$

in which

$$\mathbf{P}_p = \begin{bmatrix} \mathbf{P}_p^1 & \mathbf{P}_p^2 & .... & \mathbf{P}_p^i & ... & \mathbf{P}_p^n \end{bmatrix}$$

$$\mathbf{P}_p^i = \begin{bmatrix} \overline{\mathbf{P}}_p^i \mid \overline{\overline{\mathbf{P}}}_p^i \end{bmatrix} \tag{3.20}$$

and

$$\begin{aligned} \overline{\overline{\mathbf{P}}}_p^i &= N_i \cos p\theta \, \mathbf{I}_3; \\ \overline{\overline{\overline{\mathbf{P}}}}_p^i &= N_i \sin p\theta \, \mathbf{I}_3 \end{aligned} \tag{3.21}$$

or written in explicit expression, Eq. (3.20) becomes

$$\mathbf{P}_p = \begin{bmatrix} N_i \cos p\theta & 0 & 0 & N_i \sin p\theta & 0 & 0 \\ 0 & N_i \cos p\theta & 0 & 0 & N_i \sin p\theta & 0 \\ 0 & 0 & N_i \cos p\theta & 0 & 0 & N_i \sin p\theta \end{bmatrix} \tag{3.22}$$

A typical submatrix in Eq. (3.19) is as follows

$$\begin{aligned} \mathbf{T}_p^T = \{ & \overline{T}_{r,1}^p, \overline{T}_{z,1}^p, \overline{T}_{\theta,1}^p, \overline{\overline{T}}_{r,1}^p, \overline{\overline{T}}_{z,1}^p, \overline{\overline{T}}_{\theta,1}^p | \, \overline{T}_{r,2}^p, \overline{T}_{z,2}^p, \overline{T}_{\theta,2}^p, \overline{\overline{T}}_{r,2}^p, \overline{\overline{T}}_{z,2}^p, \overline{\overline{T}}_{\theta,2}^p | \, \ldots | \\ & \overline{T}_{r,i}^p, \overline{T}_{z,i}^p, \overline{T}_{\theta,i}^p, \overline{\overline{T}}_{r,i}^p, \overline{\overline{T}}_{z,i}^p, \overline{\overline{T}}_{\theta,i}^p | \, \ldots | \, \overline{T}_{r,n}^p, \overline{T}_{z,n}^p, \overline{T}_{\theta,n}^p, \overline{\overline{T}}_{r,n}^p, \overline{\overline{T}}_{z,n}^p, \overline{\overline{T}}_{\theta,n}^p \} \\ & (p = 1, 2, 3, \ldots, m) \end{aligned}$$

For body forces $\mathbf{b}$, the Fourier expansion has the same form as above for traction forces, except that $\mathbf{T}_i$ are substituted by $\mathbf{b}_i$.

3.1.7 Finite Element Equations

The displacement based Fourier finite elements equations can be readily obtained by substituting Eqs. (3.14), (3.15), and (3.19) and invoking a stress-strain matrix **C**. It is noted that the constitutive matrix **C** is not restricted to elasticity but can represent any material non-linearity or time dependency behaviour. Thus, the equation of equilibrium is

$$\begin{aligned}\int_{\Omega} \mathbf{B}^T \;\; &: \;\; \mathbf{C} : \mathbf{B}\, r\, dr\, dz\, d\theta : \mathbf{u} \\ &= \int_{\Omega} \mathbf{A}^T : \mathbf{b}\, r\, dr\, dz\, d\theta + \int_{\Gamma_g} \mathbf{A}^T : \mathbf{T}\, r\, dg\, d\theta \end{aligned} \tag{3.23}$$

The above integration has the contribution of displacement from each harmonic. It also involves each element in the mesh.

It should be also noted that if initial strain ε_{ij}^0 is involved, Eq. (3.23) must include another term in the right hand side to represent the equivalent initial strain load. For example, temperature loads induce strains which can be treated as initial strains.

One typically obtains the following global system of equilibrium to solve simultaneously, i.e.

$$\begin{bmatrix} \mathbf{K}^{11} & \mathbf{K}^{12} & .. & .. & \mathbf{K}^{1m} \\ \mathbf{K}^{21} & \mathbf{K}^{22} & .. & .. & \mathbf{K}^{2m} \\ . & . & . & \mathbf{K}^{pq} & . \\ . & . & . & . & . \\ \mathbf{K}^{m1} & \mathbf{K}^{m2} & . & . & \mathbf{K}^{mm} \end{bmatrix} \begin{Bmatrix} \mathbf{u}_1 \\ \mathbf{u}_2 \\ . \\ . \\ \mathbf{u}_m \end{Bmatrix} = \begin{Bmatrix} \mathbf{b}_1 \\ \mathbf{b}_2 \\ . \\ . \\ \mathbf{b}_m \end{Bmatrix} + \begin{Bmatrix} \mathbf{T}_1 \\ \mathbf{T}_2 \\ . \\ . \\ \mathbf{T}_m \end{Bmatrix} \tag{3.24}$$

3.1.8 Stiffness Matrix

A typical submatrix $\mathbf{K}^{pq}$ found in the global stiffness matrix of Eq. (3.24) represents the coupling of harmonic p with harmonic q. Hence $\mathbf{K}^{pq}$ is formed by $\mathbf{B}$ matrices introduced in Eq. (3.8) and constitutive matrix $\mathbf{C}$, i.e.

$$\mathbf{K}^{pq} = \int_{\Omega} \mathbf{B}_p^T : \mathbf{C} : \mathbf{B}_q \, r \, dr \, dz \, d\theta$$

$$= \int_{\Omega} \begin{bmatrix} \mathbf{B}_p^{1\mathbf{T}} \\ \mathbf{B}_p^{2\mathbf{T}} \\ \cdot \\ \cdot \\ \mathbf{B}_p^{i\mathbf{T}} \\ \cdot \\ \cdot \\ \mathbf{B}_p^{n\mathbf{T}} \end{bmatrix} : \mathbf{C} : \left[\mathbf{B}_q^1,\ \mathbf{B}_q^2,\ ...,\ \mathbf{B}_q^j,\ ...,\ \mathbf{B}_q^n\right]\ r\,dr\,dz\,d\theta$$

$$= \begin{bmatrix} \mathbf{K}_{pq}^{11} & \mathbf{K}_{pq}^{12} & ... & \mathbf{K}_{pq}^{1n} \\ ... & ... & ... & ... \\ ... & \mathbf{K}_{pq}^{ij} & ... & ... \\ ... & ... & ... & ... \\ \mathbf{K}_{pq}^{n1} & \mathbf{K}_{pq}^{n2} & ... & \mathbf{K}_{pq}^{nn} \end{bmatrix} \tag{3.25}$$

Introducing Eqs. (3.9) and (3.11), a typical inner submatrix of the above equation can be written as

$$\mathbf{K}_{pq}^{ij} = \int_{\Omega} \mathbf{B}_p^{i\,\mathbf{T}} : \mathbf{C} : \mathbf{B}_q^j\ r\,dr\,dz\,d\theta$$

$$= \int_{\Omega} \begin{bmatrix} \overline{\overline{\mathbf{B}}}_p^{i\mathbf{T}} \\ \overline{\overline{\mathbf{B}}}_p^{i\mathbf{T}} \end{bmatrix} : \mathbf{C} : \left[\overline{\overline{\mathbf{B}}}_q^j \vdots \overline{\overline{\mathbf{B}}}_q^j\right]\ r\,dr\,dz\,d\theta$$

$$
\begin{aligned}
&= \int_{\Omega} \begin{bmatrix} \mathbf{B}_i^{r\mathbf{T}} \cos p\theta - \mathbf{B}_i^{s\mathbf{T}} \sin p\theta \\ \mathbf{B}_i^{r\mathbf{T}} \sin p\theta + \mathbf{B}_i^{s\mathbf{T}} \cos p\theta \end{bmatrix} : \mathbf{C} \\
&\quad \left[\mathbf{B}_j^r \cos q\theta - \mathbf{B}_j^s \sin q\theta \;\vdots\; \mathbf{B}_j^r \sin q\theta + \mathbf{B}_j^s \cos q\theta \right] \, r\, dr\, dz\, d\theta \\
&= \begin{bmatrix} \mathbf{k}_{11} & \mathbf{k}_{12} \\ \mathbf{k}_{21} & \mathbf{k}_{22} \end{bmatrix}
\end{aligned} \tag{3.26}
$$

where

$$
\begin{aligned}
\mathbf{k}_{11} &= \int_{\Omega} (\mathbf{B}_i^{r\,\mathbf{T}} : \mathbf{C} : \mathbf{B}_j^r \cos p\theta \cos q\theta - \mathbf{B}_i^{r\,\mathbf{T}} : \mathbf{C} : \mathbf{B}_j^s \cos p\theta \sin q\theta \\
&\quad - \mathbf{B}_i^{s\,\mathbf{T}} : \mathbf{C} : \mathbf{B}_j^r \sin p\theta \cos q\theta + \mathbf{B}_i^{s\,\mathbf{T}} : \mathbf{C} : \mathbf{B}_j^s \sin p\theta \sin q\theta)\, d\theta \cdot r\, dr\, dz \\
\mathbf{k}_{12} &= \int_{\Omega} (\mathbf{B}_i^{r\,\mathbf{T}} : \mathbf{C} : \mathbf{B}_j^r \cos p\theta \sin q\theta + \mathbf{B}_i^{r\,\mathbf{T}} : \mathbf{C} : \mathbf{B}_j^s \cos p\theta \cos q\theta \\
&\quad - \mathbf{B}_i^{s\,\mathbf{T}} : \mathbf{C} : \mathbf{B}_j^r \sin p\theta \sin q\theta - \mathbf{B}_i^{s\mathbf{T}} : \mathbf{C} : \mathbf{B}_j^s \sin p\theta \cos q\theta)\, d\theta \cdot r\, dr\, dz \\
\mathbf{k}_{21} &= \int_{\Omega} (\mathbf{B}_i^{r\,\mathbf{T}} : \mathbf{C} : \mathbf{B}_j^r \sin p\theta \cos q\theta - \mathbf{B}_i^{r\,\mathbf{T}} : \mathbf{C} : \mathbf{B}_j^s \sin p\theta \sin q\theta \\
&\quad + \mathbf{B}_i^{s\,\mathbf{T}} : \mathbf{C} : \mathbf{B}_j^r \cos p\theta \cos q\theta - \mathbf{B}_i^{s\,\mathbf{T}} : \mathbf{C} : \mathbf{B}_j^s \cos p\theta \sin q\theta)\, d\theta \cdot r\, dr\, dz \\
\mathbf{k}_{22} &= \int_{\Omega} (\mathbf{B}_i^{r\,\mathbf{T}} : \mathbf{C} : \mathbf{B}_j^r \sin p\theta \sin q\theta + \mathbf{B}_i^{r\,\mathbf{T}} : \mathbf{C} : \mathbf{B}_j^s \sin p\theta \cos q\theta \\
&\quad + \mathbf{B}_i^{s\,\mathbf{T}} : \mathbf{C} : \mathbf{B}_j^r \cos p\theta \sin q\theta - \mathbf{B}_i^{s\,\mathbf{T}} : \mathbf{C} : \mathbf{B}_j^s \cos p\theta \cos q\theta)\, d\theta \cdot r\, dr\, dz
\end{aligned} \tag{3.27}
$$

3.1.9 Orthogonality Conditions

When calculating the stiffness matrices in Eq. (3.27), the orthogonality property of trigonometric series can be applied provided that the constitutive matrix $\mathbf{C}$ is independent of the circumferential direction θ. The orthogonality relationships can be expressed as follows

$$\int_{-\pi}^{\pi} \cos p\theta \, \sin q\theta \, d\theta = 0 \text{ for all } p \text{ and } q \tag{3.28}$$

$$\int_{-\pi}^{\pi} \cos p\theta \, \cos q\theta \, d\theta = \begin{cases} 0 & \text{for } p \neq q \\ \pi & p = q \neq 0 \\ 2\pi & p = q = 0 \end{cases} \tag{3.29}$$

$$\int_{-\pi}^{\pi} \sin p\theta \, \sin q\theta \, d\theta = \begin{cases} 0 & \text{for } p \neq q \text{ and } p = q = 0 \\ \pi & p = q \neq 0 \end{cases} \tag{3.30}$$

When the above orthogonality conditions are applied to Eq. (3.27), one can easily get the following only if p is not equal to q ($p \neq q$),

$$\begin{aligned} \mathbf{k}_{11} &= \mathbf{k}_{12} = \mathbf{k}_{21} = \mathbf{k}_{22} = \mathbf{0} \\ (\text{if } p &\neq q) \end{aligned} \tag{3.31}$$

This means that off-diagonal terms in Eq. (3.24) are all zero. Thus, the equilib-

rium equations take a decoupled form, i.e.

$$\begin{bmatrix} \mathbf{K}^{11} & \mathbf{0} & .. & .. & \mathbf{0} \\ \mathbf{0} & \mathbf{K}^{22} & .. & .. & \mathbf{0} \\ . & . & . & \mathbf{K}^{pp} & . \\ . & . & . & . & . \\ \mathbf{0} & \mathbf{0} & . & . & \mathbf{K}^{mm} \end{bmatrix} \begin{Bmatrix} \mathbf{u}_1 \\ \mathbf{u}_2 \\ . \\ . \\ \mathbf{u}_m \end{Bmatrix} = \begin{Bmatrix} \mathbf{b}_1 \\ \mathbf{b}_2 \\ . \\ . \\ \mathbf{b}_m \end{Bmatrix} + \begin{Bmatrix} \mathbf{T}_1 \\ \mathbf{T}_2 \\ . \\ . \\ \mathbf{T}_m \end{Bmatrix} \tag{3.32}$$

For diagonal terms such as matrix $\mathbf{K}^{pp}(q = p)$, the four submatrices of which it is composed are given as

$$\mathbf{k}_{11} = \int_r \int_z \pi \cdot \left(\mathbf{B}_i^{r\mathbf{T}} : \mathbf{C} : \mathbf{B}_j^r + \mathbf{B}_i^{s\mathbf{T}} : \mathbf{C} : \mathbf{B}_j^s \right) r \, dr \, dz \tag{3.33}$$

$$\mathbf{k}_{12} = \int_r \int_z \pi \cdot \left(\mathbf{B}_i^{r\mathbf{T}} : \mathbf{C} : \mathbf{B}_j^s - \mathbf{B}_i^{s\mathbf{T}} : \mathbf{C} : \mathbf{B}_j^r \right) r \, dr \, dz \tag{3.34}$$

$$\mathbf{k}_{21} = \int_r \int_z \pi \cdot \left(-\mathbf{B}_i^{r\mathbf{T}} : \mathbf{C} : \mathbf{B}_j^s + \mathbf{B}_i^{s\mathbf{T}} : \mathbf{C} : \mathbf{B}_j^r \right) r \, dr \, dz \tag{3.35}$$

$$\mathbf{k}_{22} = \int_r \int_z \pi \cdot \left(\mathbf{B}_i^{r\mathbf{T}} : \mathbf{C} : \mathbf{B}_j^r + \mathbf{B}_i^{s\mathbf{T}} : \mathbf{C} : \mathbf{B}_j^s \right) r \, dr \, dz \tag{3.36}$$

$$(q = p \neq 0, \text{ diagonal terms})$$

A special case arises for the 0th harmonic, i.e. $q = p = 0$. The term π in Eqs. (3.33) and (3.36) should be replaced by 2π and 0 respectively.

Written in a concise form, the diagonal terms in Eq. (3.32) are as follows

$$\mathbf{K}^{pp} = \begin{bmatrix} \tilde{\mathbf{K}}^{pp}_{rr} & \tilde{\mathbf{K}}^{pp}_{rs} \\ \tilde{\mathbf{K}}^{pp}_{sr} & \tilde{\mathbf{K}}^{pp}_{ss} \end{bmatrix} \tag{3.37}$$

where inner submatrices are given by

$$\begin{aligned} \tilde{\mathbf{K}}^{pp}_{IJ} &= \int_r \int_z \mathbf{B}_i^{I\mathbf{T}} : \mathbf{C} : \mathbf{B}_j^J \, r \, dr \, dz \\ I, J &= r, s \text{ and } i, j = 1, 2, 3...n; \; p = 1, 2, ...m \end{aligned} \tag{3.38}$$

in which I, J refer to cosine and sine components as shown in Eqs. (3.11) and (3.12) while i and j identify the nodes contained in the $r-z$ plane. The superscript p refers to the pth harmonic.

The procedures for calculating stiffness matrix $\mathbf{K}^{pp}$ in Eq. (3.32) can be pseudo-coded in Table 3.1.

3.1.10 Body Force

The body force term $\mathbf{b}$ which appears in Eq. (3.23) can be discretized in the same fashion as shown in Eq. (3.19). Thus,

Table 3.1: Procedures for Calculating Stiffness Matrix

1. Calculate $\mathbf{B}$ by Eq. (3.12)

$$\mathbf{B}^r = \begin{bmatrix} \frac{\partial N_i}{\partial r} & 0 & 0 \\ 0 & \frac{\partial N_i}{\partial z} & 0 \\ \frac{N_i}{r} & 0 & 0 \\ \frac{\partial N_i}{\partial z} & \frac{\partial N_i}{\partial r} & 0 \\ 0 & 0 & \left(\frac{\partial N_i}{\partial r} - \frac{N_i}{r}\right) \\ 0 & 0 & \frac{\partial N_i}{\partial z} \end{bmatrix}; \qquad \mathbf{B}^s = \frac{pN_i}{r} \begin{bmatrix} 0 & 0 & 0 \\ 0 & 0 & 0 \\ 0 & 0 & 1 \\ 0 & 0 & 0 \\ 1 & 0 & 0 \\ 0 & 1 & 0 \end{bmatrix}$$

2. Calculate submatrices $\tilde{\mathbf{K}}_{IJ}^{pp}$ by Eq. (3.38)

$$\tilde{\mathbf{K}}_{IJ}^{pp} = \int_r \int_z \mathbf{B}_i^{IT} : \mathbf{C} : \mathbf{B}_j^J \, r \, dr \, dz$$

3. Assemble $\mathbf{K}^{pp}$ by Eq. (3.37)

$$\mathbf{K}^{pp} = \begin{bmatrix} \tilde{\mathbf{K}}_{rr}^{pp} & \tilde{\mathbf{K}}_{rs}^{pp} \\ \tilde{\mathbf{K}}_{sr}^{pp} & \tilde{\mathbf{K}}_{ss}^{pp} \end{bmatrix}$$

$$\int_\Omega \mathbf{A}^T : \mathbf{b} \; r \, dr \, dz \, d\theta = \int_\Omega \mathbf{A}^T : \mathbf{P} \; r \, dr \, dz \, d\theta \begin{Bmatrix} \bar{b}_r \\ \bar{b}_z \\ \bar{b}_\theta \\ \bar{\bar{b}}_r \\ \bar{\bar{b}}_z \\ \bar{\bar{b}}_\theta \end{Bmatrix} \tag{3.39}$$

The single and double barred terms refer to cosine and sine components of body forces $\mathbf{b}$ when expanded into Fourier series. The integral which appears in Eq. (3.39) can be expressed as

$$\int_{\Omega} \mathbf{A}^T : \mathbf{P}\ r\,dr\,dz\,d\theta = \begin{bmatrix} \hat{\mathbf{A}}_{11} & \hat{\mathbf{A}}_{12} & .... & .... & \hat{\mathbf{A}}_{1m} \\ . & . & .... & .... & . \\ . & \hat{\mathbf{A}}_{pq} & .... & .... & . \\ . & . & .... & .... & . \\ \hat{\mathbf{A}}_{m1} & \hat{\mathbf{A}}_{m2} & .... & .... & \hat{\mathbf{A}}_{mm} \end{bmatrix} \tag{3.40}$$

where typically

$$\hat{\mathbf{A}}_{pq} = \int_{\Omega} \begin{Bmatrix} \mathbf{A}_p^{1\mathrm{T}} \\ \mathbf{A}_p^{2\mathrm{T}} \\ . \\ . \\ . \\ \mathbf{A}_p^{i\mathrm{T}} \\ . \\ . \\ . \\ \mathbf{A}_p^{n\mathrm{T}} \end{Bmatrix} \begin{bmatrix} \mathbf{P}_q^1 & \mathbf{P}_q^2 & ... & \mathbf{P}_q^i & ... & \mathbf{P}_q^n \end{bmatrix} r\,dr\,dz\,d\theta$$

$$= \begin{bmatrix} \mathbf{Q}_{11} & \mathbf{Q}_{12} & \cdots & \cdots & \mathbf{Q}_{1n} \\ . & . & \cdots & \cdots & . \\ . & \mathbf{Q}_{ij} & \cdots & \cdots & . \\ . & . & \cdots & \cdots & . \\ \mathbf{Q}_{n1} & \mathbf{Q}_{n2} & \cdots & \cdots & \mathbf{Q}_{nn} \end{bmatrix} \tag{3.41}$$

Introducing Eqs. (3.17) and (3.21), $\mathbf{Q}_{ij}$ in the above equation becomes

$$\begin{aligned} \mathbf{Q}_{ij} &= \int_{\Omega} \mathbf{A}_p^{i^T} : \mathbf{P}_q^j \, r \, dr \, dz \, d\theta \\ &= \int_{\Omega} \begin{bmatrix} N_i \cos p\theta \, \mathbf{I}_3 \\ N_i \sin p\theta \, \mathbf{I}_3 \end{bmatrix} \begin{bmatrix} N_j \cos q\theta \, \mathbf{I}_3 & N_j \sin q\theta \, \mathbf{I}_3 \end{bmatrix} r \, dr \, d\theta \, dz \\ &= \int_{\Omega} N_i N_j \begin{bmatrix} \cos p\theta \cos q\theta \, \mathbf{I}_3 & \cos p\theta \sin q\theta \, \mathbf{I}_3 \\ \sin p\theta \cos q\theta \, \mathbf{I}_3 & \sin p\theta \sin q\theta \, \mathbf{I}_3 \end{bmatrix} r \, dr \, d\theta \, dz \end{aligned}$$

If p is different from q, i.e. if found off-diagonal in Eq. (3.41), due to the orthogonality conditions given in Eqs. (3.28), (3.29), and (3.30), all the off-diagonal terms are zero.

The non-zero matrix $\hat{\mathbf{A}}_{pq}$ $(p = q \neq 0)$ of diagonal terms contains typical terms such as

$$\mathbf{Q}_{ij} = \int_{\Omega} \mathbf{A}_p^{i^T} : \mathbf{P}_q^j \, r \, dr \, dz \, d\theta = \int_r \int_z N_i N_j \begin{bmatrix} \pi \ \mathbf{I}_3 & 0 \\ 0 & \pi \ \mathbf{I}_3 \end{bmatrix} r \, dr \, dz \qquad (3.42)$$

If p equals to 0, the upper-left π should be replaced with 2π and the lower-right π should be replaced with 0.

Further back referring to Eq.(3.39), the Fourier cosine and sine components of the body force need to be calculated as follows

$$\left.\begin{aligned} \overline{b}_s^p &= \tfrac{1}{\pi} \int_{-\pi}^{\pi} b_s \cos p\theta \, d\theta \\ \overline{\overline{b}}_s^p &= \tfrac{1}{\pi} \int_{-\pi}^{\pi} b_s \sin p\theta \, d\theta \end{aligned}\right\} \quad p = 1, 2, ..., m; \quad s = r, \ z, \ \theta \qquad (3.43)$$

For the zero harmonic, the single and double barred coefficients are given by

$$\left.\begin{aligned} \overline{b}_s^0 &= \tfrac{1}{2\pi} \int_{-\pi}^{\pi} b_s \, d\theta \\ \overline{\overline{b}}_s^0 &= 0 \end{aligned}\right\} \quad p = 0; \quad s = r, \ z, \ \theta \qquad (3.44)$$

3.1.11 Traction Force

The calculation of the traction force $\mathbf{T}$ which appears in Eq. (3.23) can be obtained following the same developments outlined for the body forces in the previous sections except that

$$\int_{\Gamma_g} \mathbf{A}^T : \mathbf{T}\; r\, dg\, d\theta$$

$$= \begin{cases} \mathbf{0} & \text{for off-diagonal terms, i.e. } p \neq q \\ \displaystyle\int_{\Gamma_g} N_i N_j \begin{bmatrix} \pi\, \mathbf{I}_3 & \mathbf{0} \\ \mathbf{0} & \pi\, \mathbf{I}_3 \end{bmatrix} r\, dg & \text{for diagonal terms, i.e. } p = q \neq 0 \end{cases} \tag{3.45a}$$

The traction force $\mathbf{T}$ is applied along Γ_g, which is a boundary curve in $r - z$ plane. Thus, dg can be expressed as

$$dg = \sqrt{(dr)^2 + (dz)^2} \tag{3.46}$$

Introducing geometric interpolation Eq. (3.3), one gets

$$\begin{aligned} dr &= \sum_{i=1}^{n} \left(\frac{\partial N_i}{\partial \xi} d\xi + \frac{\partial N_i}{\partial \eta} d\eta \right) \bar{r}_i \\ dz &= \sum_{i=1}^{n} \left(\frac{\partial N_i}{\partial \xi} d\xi + \frac{\partial N_i}{\partial \eta} d\eta \right) \bar{z}_i \end{aligned} \tag{3.47}$$

Then, Eq. (3.46) can be easily written as

$$dg = \sqrt{\left[\sum_{i=1}^{n}\left(\frac{\partial N_i}{\partial \xi}\,d\xi + \frac{\partial N_i}{\partial \eta}\,d\eta\right)\,\bar{r}_i\right]^2 + \left[\sum_{i=1}^{n}\left(\frac{\partial N_i}{\partial \xi}\,d\xi + \frac{\partial N_i}{\partial \eta}\,d\eta\right)\,\bar{z}_i\right]^2} \tag{3.48}$$

3.1.12 Initial Stress and Strain Loads

The principle of virtual work given in Eq. (3.1) can take an alternate and compact form when considering equilibrium of the system,

$$\int_\Omega \boldsymbol{\sigma} : \delta\boldsymbol{\varepsilon}\; d\Omega - \int_\Omega \mathbf{b} : \delta\mathbf{u}\; d\Omega - \int_{\Gamma_g} \mathbf{T} : \delta\mathbf{u}\; d\Gamma_g = \mathbf{0} \tag{3.49}$$

When the body has initial strains $\boldsymbol{\varepsilon}_0$ and initial stresses $\boldsymbol{\sigma}_0$, the stress-strain relationship is given as

$$\boldsymbol{\sigma} = \mathbf{C}\,(\boldsymbol{\varepsilon} - \boldsymbol{\varepsilon}_0) + \boldsymbol{\sigma}_0 \tag{3.50}$$

Substituting Eq. (3.50) into (3.49) and noticing Eq. (3.14), one gets

$$\begin{aligned}
&\int_\Omega \mathbf{C}\,(\boldsymbol{\varepsilon} - \boldsymbol{\varepsilon}_0) + \boldsymbol{\sigma}_0 : \delta\boldsymbol{\varepsilon}\; d\Omega \\
= &\int_\Omega \mathbf{C} : \boldsymbol{\varepsilon} : \delta\boldsymbol{\varepsilon}\; d\Omega - \int_\Omega \mathbf{C} : \boldsymbol{\varepsilon}_0 : \delta\boldsymbol{\varepsilon}\; d\Omega + \int_\Omega \boldsymbol{\sigma}_0\, \delta\boldsymbol{\varepsilon}\; d\Omega \\
= &\int_\Omega \mathbf{B}^T : \mathbf{C} : \mathbf{B} : \delta\mathbf{u}\; d\Omega - \int_\Omega \mathbf{B}^T : \mathbf{C} : \boldsymbol{\varepsilon}_0 : \delta\mathbf{u}\; d\Omega + \int_\Omega \mathbf{B}^T\boldsymbol{\sigma}_0 : \delta\mathbf{u}\; d\Omega
\end{aligned} \tag{3.51}$$

Using Eqs. (3.14), (3.15), and (3.19), then Eq. (3.49) can be further written as

$$\int_\Omega \mathbf{B}^T : \mathbf{C} : \mathbf{B}\, d\Omega : \mathbf{u} = \int_\Omega \mathbf{A}^T : \mathbf{b}\, d\Omega + \int_{\Gamma_g} \mathbf{A}^T : \mathbf{T}\, d\Gamma_g + \int_\Omega \mathbf{B}^T : \mathbf{C} : \boldsymbol{\varepsilon}_0\, d\Omega - \int_\Omega \mathbf{B}^T : \boldsymbol{\sigma}_0\, d\Omega \tag{3.52}$$

Comparing Eq. (3.52) with Eq. (3.23), one finds that the only difference is that on the right-hand side there are two more terms. These terms are $\int_\Omega \mathbf{B}^T : \mathbf{C} : \boldsymbol{\varepsilon}_0\, d\Omega$ and $\left(-\int_\Omega \mathbf{B}^T : \boldsymbol{\sigma}_0\, d\Omega\right)$ which represent the initial strain load and initial stress load, respectively.

It is noted that the $\mathbf{B}$ matrix contains submatrices relating strains to displacements for each harmonic, just like in Eq. (3.12). Furthermore for the calculation of the term $\int_\Omega \mathbf{B}^T : \mathbf{C} : \boldsymbol{\varepsilon}_0\, d\Omega$ and $\int_\Omega \mathbf{B}^T : \boldsymbol{\sigma}_0\, d\Omega$, the integration can be performed as

$$\begin{aligned}
\int_\Omega \mathbf{B}^T : \mathbf{C} : \boldsymbol{\varepsilon}_0\, d\Omega &= \int_0^{2\pi} \int_r \int_z \mathbf{B}^T : \mathbf{C} : \boldsymbol{\varepsilon}_0\, r\, dz\, dr\, d\theta \\
&\cong \sum_{L=1}^{np} \left(\int_r \int_z \mathbf{B}^T : \mathbf{C} : \boldsymbol{\varepsilon}_0\, r\, dz\, dr \right) \Delta\theta_L \qquad (3.53) \\
\int_\Omega \mathbf{B}^T \boldsymbol{\sigma}_0\, d\Omega &= \int_0^{2\pi} \int_r \int_z \mathbf{B}^T : \boldsymbol{\sigma}_0\, r\, dz\, dr\, d\theta \\
&\cong \sum_{L=1}^{np} \left(\int_r \int_z \mathbf{B}^T : \boldsymbol{\sigma}_0\, r\, dz\, dr \right) \Delta\theta_L \qquad (3.54)
\end{aligned}$$

where np is the number of planes used to discretize the temperature distribution.

Equation (3.52) is a general expression which includes body force, traction, initial strain load, and initial stress load. However, if a structure undergoes any particular load condition, only the corresponding load term will be considered and the other load terms will be discarded.

The coupled temperature distribution with water pressure and ice pressure will be elaborated in the next chapter. Both the water and ice pressures will be simply considered as initial stress loads exerted to the soil-pipeline system.

3.1.13 Boundary Conditions

The finite element formulations derived in the previous sections will have to be completed with appropriate boundary conditions which will adequately reflect the three-dimensional nature of the pipeline problem shown in Fig. 3.2.

Due to the nature of the finite element approximation which involves the discretization of field variables in a $r - z$ plane and the use of Fourier expansion for variables in the circumferential direction θ , the boundary of interest for computations is a circle of radius R as shown in dotted lines in Fig. 3.2 (b).

To simulate a long enough pipeline, all the end nodes for the concerned cylinder are restrained in the longitudinal direction. This means that all the end nodes in $r - z$ plane are restrained in the z direction. To simulate volumetric expansion due to frost heave, all the nodes are free in their r degree of freedom. This treatment is a necessary approximation to meet the geometric symmetry requirement of this method. But the restriction conditions for the real case will be dependent upon the

depth from the ground surface. For example, in Fig. 3.2 (b), at three locations, point B, C, and D should have different restriction conditions.

3.2 Numerical Solution of Equilibrium Equations

In considering a general boundary value problem, the static equilibrium equations derived from the previous sections must be solved together with the constitutive equations and appropriate static or kinematic boundary conditions. The following derivations are meant to be applied to the Fourier finite elements equations derived in the last sections. The elementary volume of interest will be generically denoted by $d\Omega$ instead of specifically alluding to a cylindrical reference which includes dr, dz and $d\theta$.

3.2.1 Discrete Equilibrium Equations

The condition of static equilibrium can be generically stated through an integral equation representing the principle of virtual work shown in Eq. (3.49). From the finite element view point, one needs to advance the solution from t_n at which principal field variables such as $\mathbf{u}_n$, $\boldsymbol{\varepsilon}_n$ and $\boldsymbol{\sigma}_n$ are known to time t_{n+1}. The finite element equilibrium equation at time t_{n+1} is thus written as

$$\mathbf{F}_{\text{int}}(\mathbf{u}_{n+1}) = \int_{\Omega} \mathbf{B}^T : \boldsymbol{\sigma}_{n+1}\, d\Omega = (\mathbf{F}_{ext})_{n+1} \tag{3.55}$$

in which $\mathbf{F}_{\text{int}}$ is the vector of internal nodal force and $\mathbf{B}$ is the strain-displacement transformation matrix. Since the internal force vector $\mathbf{F}_{\text{int}}$ depends on the final stresses, strains, and displacements which are unknowns an iterative process must be adopted for finding the solution. Setting up the iterative process, at the kth iteration, the equilibrium conditions can be written as

$$\mathbf{F}_{\text{int}}(\mathbf{u}_{n+1}^{k} + \Delta\mathbf{u}_{n+1}^{k}) = \mathbf{F}_{ext} \tag{3.56}$$

By using a Taylor expansion about the kth iteration, one gets

$$\mathbf{F}_{\text{int}}(\mathbf{u}_{n+1}^{k}) + \left.\frac{\partial \mathbf{F}_{\text{int}}}{\partial \mathbf{u}}\right|_{n+1}^{k} \Delta\mathbf{u}_{n+1}^{k} + 0(\Delta\mathbf{u}_{n+1}^{k})^2 = \mathbf{F}_{ext} \tag{3.57}$$

Hence, the increment of displacement at the end of iteration k is

$$\Delta\mathbf{u}_{n+1}^{k} = \left[\mathbf{K}_{n+1}^{k}\right]^{-1} \left[\mathbf{F}_{ext} - \mathbf{F}_{\text{int}}(\mathbf{u}_{n+1}^{k})\right] \tag{3.58}$$

in which $\mathbf{K}_{n+1}^{k}$ is the Jacobian of the linearized system, whose expression is

$$\mathbf{K}_{n+1}^{k} = \left.\frac{\partial \mathbf{F}_{\text{int}}}{\partial \mathbf{u}}\right|_{n+1}^{k} \tag{3.59}$$

Finally, the displacement at the end of the kth iteration becomes

$$\mathbf{u}_{n+1}^{k+1} = \mathbf{u}_{n+1}^{k} + \Delta\mathbf{u}_{n+1}^{k} \tag{3.60}$$

The expression of $\mathbf{K}_{n+1}^{k}$ can be further developed by combining Eqs. (3.55) and

(3.59). Thus,

$$\mathbf{K}^k_{n+1} = \int_\Omega \mathbf{B}^T : \frac{\partial \boldsymbol{\sigma}^k_{n+1}}{\partial \mathbf{u}^k_{n+1}} \, d\Omega = \int_\Omega \mathbf{B}^T : \mathbf{C}^k_{n+1} : \mathbf{B} \, d\Omega \tag{3.61}$$

in which

$$\mathbf{C}^k_{n+1} = \frac{\partial \boldsymbol{\sigma}^k_{n+1}}{\partial \boldsymbol{\varepsilon}^k_{n+1}} \tag{3.62}$$

is the material stress-strain matrix or the so called consistent tangent modulus introduced by Simo and Taylor [48].

When formulating the problem from a finite element view point, non-linear equations arise. These must be linearized and solved within a Newton-Raphson scheme. The algorithm presented herein distinguishes itself from the conventional methods in that the global equilibrium equations and the constitutive stress integrations are intimately linked during the Newton-Raphson iterations. By virtue of this, the quadratic rate of convergence of the Newton method is preserved.

3.2.2 Non-linear Fourier Finite Elements

The Fourier finite element model hinges on orthogonality conditions. Within this model complications arise when the consistent tangent modulus in Eq. (3.62) is used in the integrals of Eq. (3.38). This is because $\mathbf{C}^k_{n+1}$ is no longer constant as it varies with the circumferential direction θ . Hence, the orthogonality conditions cannot be applied explicitly and thus destroys the decoupled nature of the harmonics. In order

to retain the decoupled nature of all the harmonics, the orthogonality conditions must be made to hold even in the non-linear case. In this thesis, the mean of the consistent tangent modulus $\mathbf{C}^k_{n+1}$ will be taken in the circumferential direction so that it can be separated out of the integral involving θ. By virtue of this approximation, the orthogonality relations can still be applied. The numerical example described in the next sections shows that the technique proves to be very effective. This is because the Newtonian equilibrium iterations retain a quadratic convergence despite of the averaging of $\mathbf{C}^k_{n+1}$ in the circumferential direction.

3.2.3 Stress Return Algorithm

The elasto-plastic formulation is cast into the stress return mapping algorithm which basically results from the discretization of a set of evolution equations as obtained from a strain driven framework. Typically, for a given incremental strain history, new values of state variables $\{\boldsymbol{\sigma},\, \boldsymbol{\varepsilon}^p,\, \bar{\varepsilon}^p\}$ must be determined from the constitutive equations. In precise terms, let the total and plastic strain tensors, as well as the effective plastic strains be known at state t_n, i.e. $\{\, \boldsymbol{\varepsilon}_n,\, \boldsymbol{\varepsilon}^p_n,\, \bar{\varepsilon}^p_n\}$.

The incremental stresses which result from the change of state from time t_n to t_{n+1}, due to an increment of total strain $\Delta\, \boldsymbol{\varepsilon}_{n+1}$, can be calculated based on the additivity of elastic and plastic strains, and the flow rule of plasticity, i.e.

$$\Delta\boldsymbol{\sigma}_{n+1} = \mathbf{C}^e : (\Delta\boldsymbol{\varepsilon}_{n+1} - \Delta\boldsymbol{\varepsilon}^p_{n+1}); \quad \Delta\boldsymbol{\varepsilon}^p_{n+1} = \Delta\lambda_{n+1}\frac{\partial Q_{n+1}}{\partial\boldsymbol{\sigma}_{n+1}} \tag{3.63}$$

where the elasticity tensor is denoted by $\mathbf{C}^e$, λ is a plastic multiplier, and Q is

a plastic potential. When the stress increment $\Delta\boldsymbol{\sigma}_{n+1}$ is added to the previous converged stress $\boldsymbol{\sigma}_n$, the total stress $\boldsymbol{\sigma}_{n+1}$ emerges as

$$\boldsymbol{\sigma}_{n+1} = \boldsymbol{\sigma}_n + \Delta\boldsymbol{\sigma}_{n+1} = \boldsymbol{\sigma}^{tr}_{n+1} - \mathbf{C}^e :< \Delta\boldsymbol{\varepsilon}^p_{n+1} > \tag{3.64}$$

where the so called trial ($.^{tr}$) stress $\boldsymbol{\sigma}^{tr}_{n+1}$ which represents an elastic stress predictor is given as

$$\boldsymbol{\sigma}^{tr}_{n+1} = \boldsymbol{\sigma}_n + \mathbf{C}^e : \Delta\boldsymbol{\varepsilon}_{n+1} \tag{3.65}$$

The operator $< . >$ is defined as follows. If the elastic trial stress $\boldsymbol{\sigma}^{tr}_{n+1}$ falls beyond the elastic region, which is defined by an appropriate yield surface in the stress space, the incremental plastic strains are non-zero and $< \Delta\boldsymbol{\varepsilon}^p_{n+1} >= \Delta \quad \boldsymbol{\varepsilon}^p_{n+1}$; otherwise $< \Delta\boldsymbol{\varepsilon}^p_{n+1} >= 0$. The implication of Eq. (3.64) is that the elastic stress predictor is being corrected by a term which depends on the amount of plastic strains $\Delta\boldsymbol{\varepsilon}^p_{n+1}$ produced during times t_n and t_{n+1}. This corrector term can be viewed as a stress return of the trial stress to the yield surface. To satisfy the consistency conditions, the final stress $\boldsymbol{\sigma}_{n+1}$ must lie on the yield surface.

The procedure of tracking down the evolution of the stresses within the stress return framework proves to be very simple, yet accurate and stable. References of such methods can be found in Simo and Taylor [48]. These methods deviate from other incremental techniques used by Owen and Hinton [39].

3.2.4 Equilibrium Iteration

Equation (3.32) represents the equilibrium of the structure written in an decoupled form which can be easily solved. However, for an elasto-plastic analysis, the equilibrium equations are in fact coupled since the constitutive matrix $\mathbf{C}$ is function of circumferential direction θ and orthogonality relations cannot be applied. In order to circumvent this problem, a homogenized matrix $\mathbf{C}$ based on taking the mean of all values of $\mathbf{C}$ along direction θ is used instead. Hence, using such an approximation, the decoupled form of the equilibrium equations can be regained.

Special care has to be exercised for solving Eq. (3.32) in the elasto-plastic case. Within each load step, for each harmonic starting from the $0th$, one should solve that only harmonic and accumulate the stress, strain, and displacement to the total targeted value. For each harmonic, the yield criterion is then checked using values accumulated for the stress. If the accumulated stress state is found beyond the yield surface, then plastic deformations take place and the stress state has to be brought back onto the yield surface.

The equilibrium iteration procedure can be explained by referring to the pseudo-code shown in Table 3.2.

3.3 Algorithm for Solving the Coupled Equations

For sake of completeness, an alternative algorithm is herein proposed to solve the coupled equilibrium equation system. Let's assume that three harmonics are involved for the purpose of illustration. The fully coupled equations take the following form:

Table 3.2: Procedures for Solving Equilibrium Equations

1. Loop over each load step

2. Loop over each harmonic (starting from $0th$), solve Eq. (3.32);

$$\begin{bmatrix} \mathbf{K}^{11} & \mathbf{0} & .. & .. & \mathbf{0} \\ \mathbf{0} & \mathbf{K}^{22} & .. & .. & \mathbf{0} \\ . & . & . & \mathbf{K}^{pp} & . \\ . & . & . & . & . \\ \mathbf{0} & \mathbf{0} & . & . & \mathbf{K}^{mm} \end{bmatrix} \begin{Bmatrix} \mathbf{u}_1 \\ \mathbf{u}_2 \\ . \\ . \\ \mathbf{u}_m \end{Bmatrix} = \begin{Bmatrix} \mathbf{b}_1 \\ \mathbf{b}_2 \\ . \\ . \\ \mathbf{b}_m \end{Bmatrix} + \begin{Bmatrix} \mathbf{T}_1 \\ \mathbf{T}_2 \\ . \\ . \\ \mathbf{T}_m \end{Bmatrix}$$

3. Loop over each Gauss point and calculate stress state

4. Check for yielding
   IF (total stress is beyond the yield surface) THEN
      bring this total stress back
   ENDIF

5. Check for equilibrium
   IF $\mathbf{F}_{\text{int}} = \mathbf{F}_{ext}$ THEN
      goto 3 for the next Gauss point
   ELSE
      goto 3 for the same Gauss point
   ENDIF

6. Next harmonic

7. Next load step

$$\begin{bmatrix} K_{11} & K_{12} & K_{13} \\ K_{21} & K_{22} & K_{23} \\ K_{31} & K_{32} & K_{33} \end{bmatrix} \begin{Bmatrix} U_1 \\ U_2 \\ U_3 \end{Bmatrix} = \begin{Bmatrix} F_1 \\ F_2 \\ F_3 \end{Bmatrix} \tag{3.66}$$

If all off-diagonal terms K_{ij} $(i \neq j)$ are equal to 0 , the above equation obviously collapses into the decoupled case. The algorithm for solving decoupled equations has been discussed in previous sections.

Let's split the stiffness matrix **K** into two parts: decoupled and coupled terms. Equation (3.66) can be written as

$$\begin{bmatrix} K_{11} & 0 & 0 \\ 0 & K_{22} & 0 \\ 0 & 0 & K_{33} \end{bmatrix} \begin{Bmatrix} U_1 \\ U_2 \\ U_3 \end{Bmatrix} + \begin{bmatrix} 0 & K_{12} & K_{13} \\ K_{21} & 0 & K_{23} \\ K_{31} & K_{32} & 0 \end{bmatrix} \begin{Bmatrix} U_1 \\ U_2 \\ U_3 \end{Bmatrix} = \begin{Bmatrix} F_1 \\ F_2 \\ F_3 \end{Bmatrix} \tag{3.67}$$

Rearranging Eq. (3.67), one gets

$$\begin{bmatrix} K_{11} & 0 & 0 \\ 0 & K_{22} & 0 \\ 0 & 0 & K_{33} \end{bmatrix} \begin{Bmatrix} U_1 \\ U_2 \\ U_3 \end{Bmatrix} = \begin{Bmatrix} F_1 \\ F_2 \\ F_3 \end{Bmatrix} - \begin{bmatrix} 0 & K_{12} & K_{13} \\ K_{21} & 0 & K_{23} \\ K_{31} & K_{32} & 0 \end{bmatrix} \begin{Bmatrix} U_1 \\ U_2 \\ U_3 \end{Bmatrix} \tag{3.68}$$

Equation (3.68) can be written in a concise form

$$\mathbf{K}^0 : \mathbf{U}^{i+1} = \mathbf{F} - \mathbf{K}^* : \mathbf{U}^i \qquad (i = 0, 1, 2, 3, \ldots) \tag{3.69}$$

where

$$\mathbf{K}^0 = \begin{bmatrix} K_{11} & 0 & 0 \\ 0 & K_{22} & 0 \\ 0 & 0 & K_{33} \end{bmatrix} \quad \text{and} \quad \mathbf{K}^* = \begin{bmatrix} 0 & K_{12} & K_{13} \\ K_{21} & 0 & K_{23} \\ K_{31} & K_{32} & 0 \end{bmatrix} \tag{3.70}$$

$$\mathbf{F} = \begin{Bmatrix} F_1 \\ F_2 \\ F_3 \end{Bmatrix} \quad \text{and} \quad \mathbf{U} = \begin{Bmatrix} U_1 \\ U_2 \\ U_3 \end{Bmatrix} \tag{3.71}$$

Actually, Eq. (3.69) refers to an iterative formula for solving $\mathbf{U}$. In Eq. (3.69), $\mathbf{U}^i$ is the estimate for $\mathbf{U}$ iteration i, while $\mathbf{U}^{i+1}$ the updated estimate at $i+1$ is to be solved iteratively.

To solve Eq. (3.69), we set the first estimation $\mathbf{U}^0 = \mathbf{0}$. Then, Eq. (3.69) becomes

$$\mathbf{K}^0 : \mathbf{U}^1 = \mathbf{F} \tag{3.72}$$

Let's write Eq. (3.72) in a clear expression

$$\begin{bmatrix} K_{11} & 0 & 0 \\ 0 & K_{22} & 0 \\ 0 & 0 & K_{33} \end{bmatrix} \begin{Bmatrix} U_1^1 \\ U_2^1 \\ U_3^1 \end{Bmatrix} = \begin{Bmatrix} F_1 \\ F_2 \\ F_3 \end{Bmatrix} \tag{3.73}$$

Equation (3.73) is in a decoupled form which can be solved easily using the algorithm previously discussed. Once $\{U^1\}$ is obtained from Eq. (3.72), one can easily solve for $\{U^2\}$ by substituting $\{U^1\}$ into Eq. (3.69) and setting $i = 2$. In this way, once $\|\{U^{i+1}\} - \{U^i\}\| < \varepsilon$ (a given tolerance for iteration), convergence of the iterative scheme towards the solution is assumed to be reached.

The proposed algorithm for solving coupled equations can be summarized as follows in Table 3.3.

3.4 Plasticity Models

3.4.1 von Mises Model

The von Mises model is one of the simplest models ever used in the constitutive modelling of materials. Here for the soil-pipeline problem, it can be well applied to model the constitutive behaviour of steel pipeline.

In connection with the subsequent developments, let the following stress invariants be defined as

Table 3.3: Procedures for Solving Coupled Equilibrium Equations

1. Set the initial iteration value
   $i = 0$, $\mathbf{U}^0 = \mathbf{0}$

2. Calculate the first estimation
   $\mathbf{K}^0 : \mathbf{U}^1 = \mathbf{F}$

3. Calculate the current corrector in Eq. (3.69)
   $\mathbf{K}^* : \mathbf{U}^i$

4. Compute the right hand side of Eq. (3.69)
   $\mathbf{F} - \mathbf{K}^* : \mathbf{U}^i$

5. Sovle for new value
   $\mathbf{K}^0 : \mathbf{U}^{i+1} = \mathbf{F} - \mathbf{K}^* : \mathbf{U}^i$

6. Check for convergence
   IF: $\|\mathbf{U}^{i+1} - \mathbf{U}^i\| < \varepsilon$ THEN:
   exit
   ELSE
   goto 3
   ENDIF

$$p = \frac{1}{3} trace\,(\boldsymbol{\sigma}_{n+1}); \qquad p^{tr} = \frac{1}{3} trace\,(\boldsymbol{\sigma}^{tr}_{n+1}) \tag{3.74}$$

$$\mathbf{s} = \boldsymbol{\sigma}_{n+1} - p\,\mathbf{1}; \qquad \mathbf{s}^{tr} = \boldsymbol{\sigma}^{tr}_{n+1} - p^{tr}\,\mathbf{1} \tag{3.75}$$

where p represents the mean stress; $\mathbf{s}$ is the deviatoric stress tensor; $\mathbf{1}$ is the Kronecker delta tensor; and *trace* operator corresponds to the sum of all diagonal terms of a tensor.

The yield criterion used for von Mises material is mean stress insensitive as shown in the following yield function F,

$$F = F(\mathbf{s},\ \bar{\varepsilon}^p) = \|\mathbf{s}\| - \sqrt{\frac{2}{3}}\ \left(\bar{\sigma}_0 + H'\ \bar{\varepsilon}^p\right) = 0; \qquad \|\mathbf{s}\| = \sqrt{s_{ij}\,s_{ij}} \tag{3.76}$$

where $\bar{\sigma}_0$ is the uniaxial yield stress, H' is the hardening parameter and $\bar{\varepsilon}^p$ is the effective plastic strain calculated from the following equation

$$\bar{\varepsilon}^p = \int_0^t \sqrt{\frac{2}{3}}\ \|\dot{\mathbf{e}}^p(\tau)\|\ d\tau; \qquad \tau = \text{ pseudo time} \tag{3.77}$$

where the deviatoric strain tensor is defined as $\mathbf{e} = \boldsymbol{\varepsilon} - \frac{1}{3} tr\,(\boldsymbol{\varepsilon})\ \mathbf{1}$.

In writing the incremental constitutive equations in terms of elastic strain components, one gets

$$\dot{p} = K\ trace\,(\dot{\boldsymbol{\varepsilon}})\,; \qquad \dot{\mathbf{s}} = 2G\,(\dot{\mathbf{e}} - \dot{\mathbf{e}}^{p}) \tag{3.78}$$

in which K and G are bulk and shear modulus.

Furthermore, if associated plastic flow rule is assumed, we have

$$\dot{\mathbf{e}}^{p} = \lambda \frac{\partial F}{\partial \mathbf{s}} = \lambda\, \hat{\mathbf{n}} \tag{3.79}$$

where $\hat{\mathbf{n}}$ is the direction of plastic strain and has a radial direction when looking in the deviatoric plane. $\hat{\mathbf{n}}$ can be obtained from

$$\hat{\mathbf{n}} = \frac{\partial F}{\partial \mathbf{s}} = \frac{\partial \|\mathbf{s}\|}{\partial \mathbf{s}} = \frac{\partial \sqrt{s_{ij}\, s_{ij}}}{\partial s_{kl}} \mathbf{g}_k\, \mathbf{g}_l = \frac{s_{ij}\, \delta_{kl}}{\sqrt{s_{ij}\, s_{ij}}} \mathbf{g}_k\, \mathbf{g}_l = \frac{\mathbf{s}}{\|\mathbf{s}\|} \tag{3.80}$$

The normal at trial stress $\mathbf{s}^{tr}$ is the same as that at final stress $\mathbf{s}_{n+1}$ found on the yield surface, i.e.

$$\hat{\mathbf{n}} = \frac{\mathbf{s}^{tr}}{\|\mathbf{s}^{tr}\|} = \frac{\mathbf{s}_{n+1}}{\|\mathbf{s}_{n+1}\|} \tag{3.81}$$

The stress update equation can be readily obtained by splitting the total stress into deviatoric and spherical parts, i.e., $\boldsymbol{\sigma} = \mathbf{s}^{tr} + \mathbf{1}\ trace(\boldsymbol{\sigma})/3$, and noting Eqs. (3.76), (3.78) and (3.81) one finally gets

$$\boldsymbol{\sigma}_{n+1} \;=\; K\ trace(\boldsymbol{\varepsilon}_{n+1})\ \mathbf{1} + \mathbf{s}_{n+1} = K\ trace(\boldsymbol{\varepsilon}_{n+1})\ \mathbf{1} + \|\mathbf{s}_{n+1}\|\ \hat{\mathbf{n}}$$

$$= K\ trace(\boldsymbol{\varepsilon}_{n+1})\ \mathbf{1} + \sqrt{\frac{2}{3}}\left(\bar{\sigma}_0 + H'\ \bar{\varepsilon}^p_{n+1}\right)\hat{\mathbf{n}} \tag{3.82}$$

Figure 3.3 illustrates the stress return scheme as the trial stress is pulled back to the expanding yield surface in the stress space.

The consistent tangent modulus emerges when the stress $\boldsymbol{\sigma}_{n+1}$ is differentiated with respect to strains $\boldsymbol{\varepsilon}_{n+1}$. After numerous algebraic manipulations, the final expression for $\mathbf{C}^k_{n+1}$ at the kth iteration is

$$\begin{aligned}\mathbf{C}^k_{n+1} &= K\mathbf{1}\otimes\mathbf{1} + \sqrt{\frac{2}{3}}\left(\bar{\sigma}_0 + H'\ \bar{\varepsilon}^p_{n+1}\right)\frac{2G}{\|\mathbf{s}_{n+1}\|}\left[(\mathbf{I} - \frac{1}{3}\mathbf{1}\otimes\mathbf{1}) - \hat{\mathbf{n}}\otimes\hat{\mathbf{n}}\right] \\ &\quad + \frac{2GH'}{H' + 3G}\,\hat{\mathbf{n}}\otimes\hat{\mathbf{n}}\end{aligned} \tag{3.83}$$

Comprehensive derivations of the above can be found in Simo and Taylor [48].

3.4.2 Drucker-Prager Model

The constitutive modelling of the soil can be approximated by a model based on Mohr-Coulomb failure criterion. The Drucker-Prager model a simplified version of Mohr-Coulomb model in the sense that the yield function represents a cone instead of a pyramidal surface in the stress space. The expression of the yield surface F here is

$$F = F(\boldsymbol{\sigma},\ p) = \|\mathbf{s}\| - \sqrt{\frac{2}{3}}\,\kappa(p) = 0; \quad \kappa(p) = \frac{6}{3-\sin\varphi}\,(c\cos\varphi + p\sin\varphi) \quad (3.84)$$

where c and φ represent cohesion and friction angle respectively.

Here, adopting an associated flow rule, the incremental stress-strain relations can be set up just like in Eqs. (3.78), (3.79) and (3.81). The stress return equation is readily obtained by using Eq. (3.64) and applying consistency conditions such that the final stress lies on the yield surface given in Eq. (3.84). Thus, one finally gets

$$p^k_{n+1} = p^{tr}_{n+1} - \lambda_{n+1}\frac{6\sin\varphi}{3-\sin\varphi}K; \quad \mathbf{s}^k_{n+1} = \mathbf{s}^{tr}_{n+1} - 2G\sqrt{\frac{3}{2}}\,\lambda_{n+1}\frac{\mathbf{s}^{tr}_{n+1}}{\|\mathbf{s}^{tr}_{n+1}\|} \quad (3.85)$$

$$\lambda_{n+1} = \frac{1}{3G + K\left(\dfrac{6\sin\varphi}{3-\sin\varphi}\right)^2} \cdot \left\{\sqrt{\frac{3}{2}}\,\|\mathbf{s}^{tr}_{n+1}\| - \frac{6\sin\varphi}{3-\sin\varphi}(c\cos\varphi - p^{tr}_{n+1}\sin\varphi)\right\} \quad (3.86)$$

Figure 3.4 shows the Drucker-Prager yield surface and the stress return algorithm.

The consistent tangent modulus is obtained by differentiating stress $\boldsymbol{\sigma}_{n+1}$ with respect to strains $\boldsymbol{\varepsilon}_{n+1}$. Thus,

$$\mathbf{C}^{k}_{n+1} = \left[K - \left(\frac{6\sin\varphi}{3-\sin\varphi}K\right)^{2}\eta\right]\mathbf{1}\otimes\mathbf{1}$$
$$+2G\left(\mathbf{I} - \frac{1}{3}\mathbf{1}\otimes\mathbf{1} - \hat{\mathbf{n}}\otimes\hat{\mathbf{n}}\right)\left(1 - 3G\eta + \frac{\sqrt{6}G\eta\,\kappa(p^{k}_{n+1})}{\left\|\mathbf{s}^{tr}_{n+1}\right\|}\right)$$
$$+2G(1-3G\eta)\,\hat{\mathbf{n}}\otimes\hat{\mathbf{n}} - \sqrt{6}G\eta\frac{6\sin\varphi}{3-\sin\varphi}K\,(\mathbf{1}\otimes\hat{\mathbf{n}} + \hat{\mathbf{n}}\otimes\mathbf{1}) \qquad (3.87)$$

in which

$$1/\eta = 3G + K\left(\frac{6}{3-\sin\varphi}\right)^{2} \qquad (3.88)$$

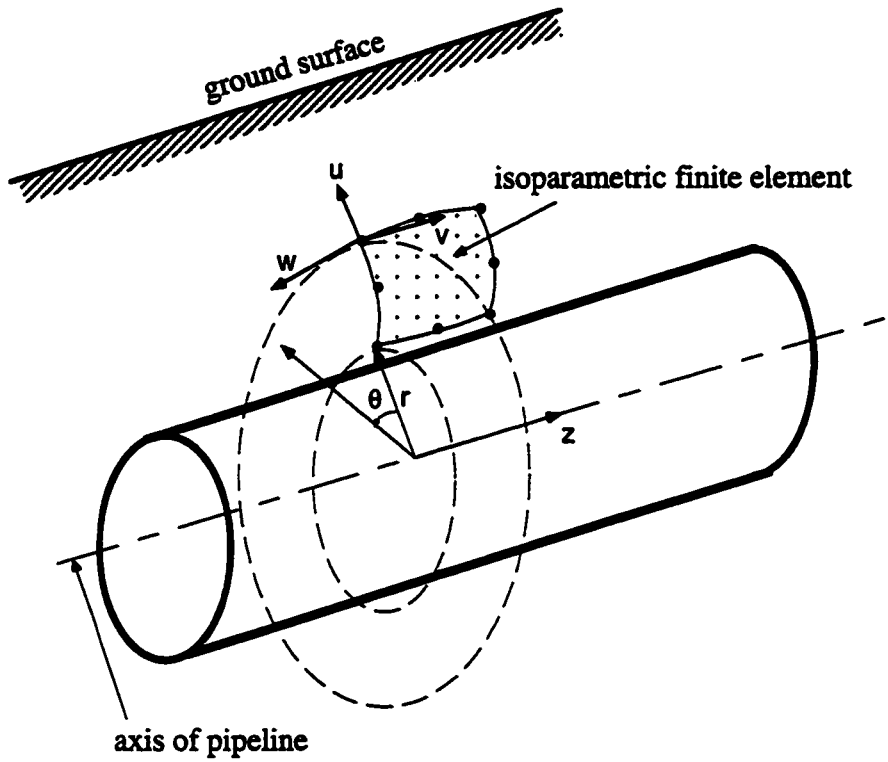

Fig. 3.1 Fourier Discretization of Soil Around Pipeline

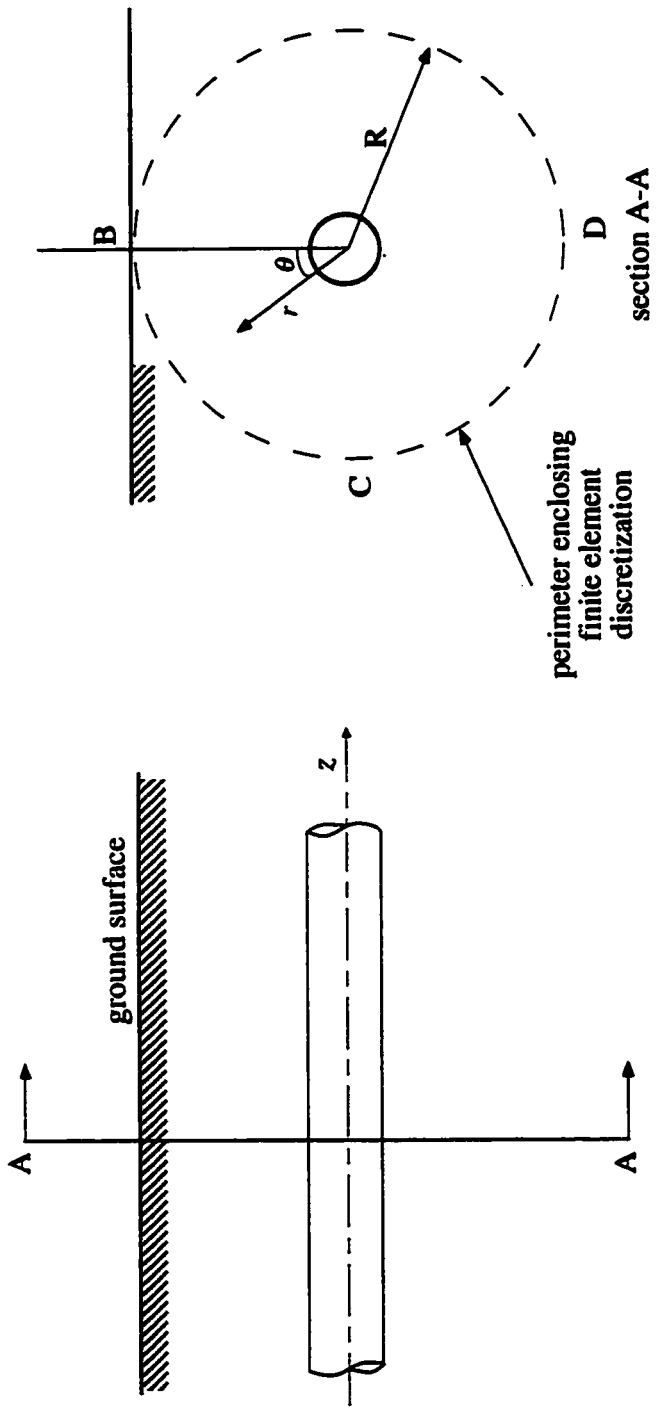

Fig. 3.2 Longitudinal and Sectional Views of Buried Pipeline

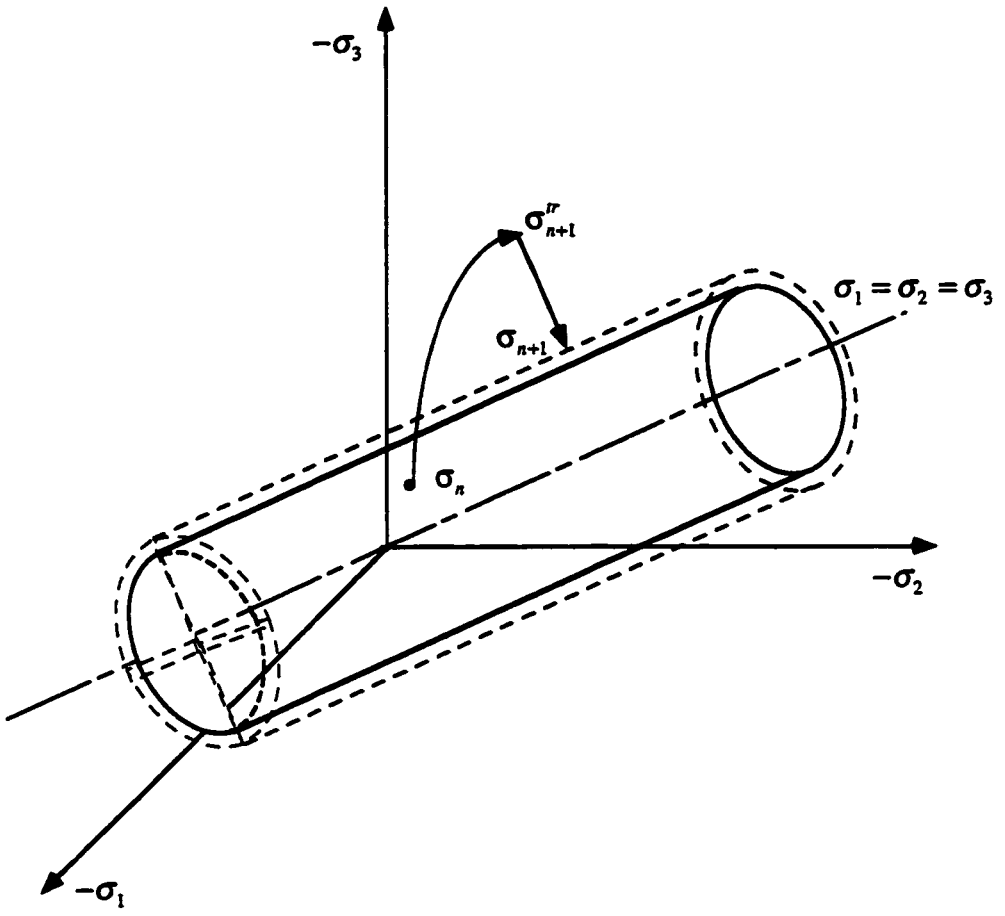

Fig. 3.3 Stress Return Algorithm for the Hardening von-Mises Model

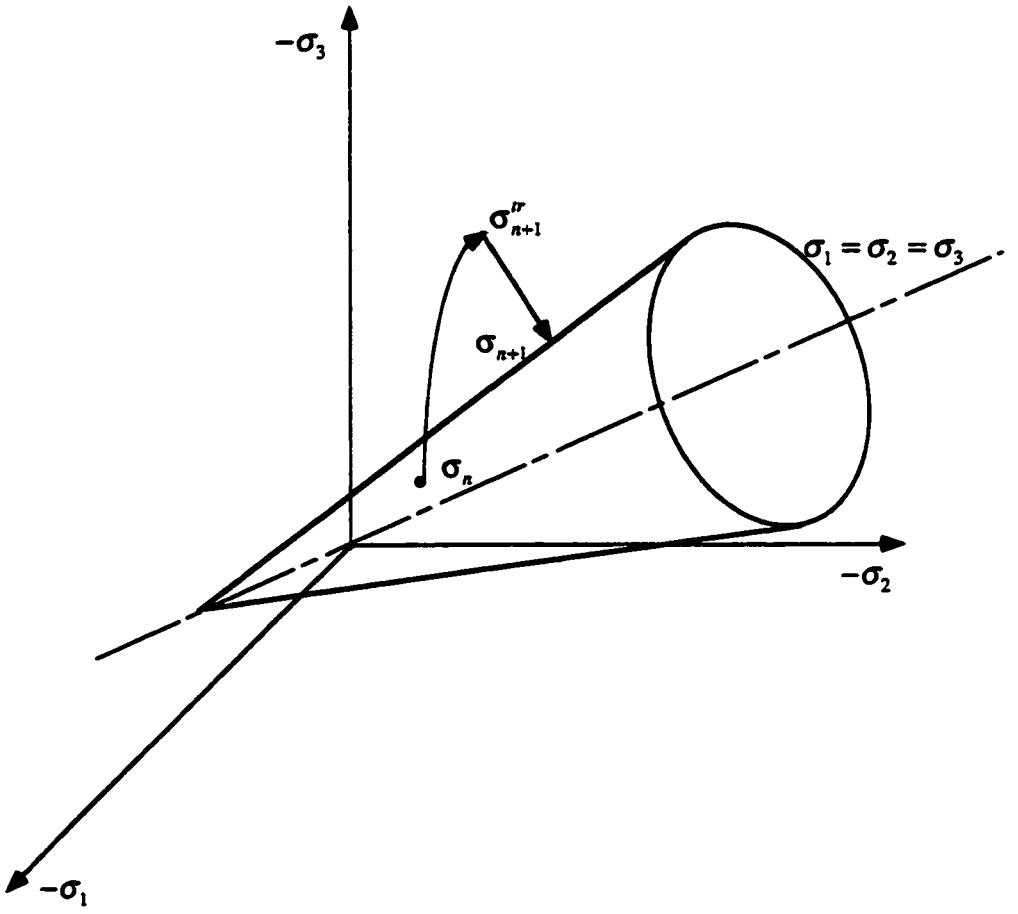

Fig. 3.4 Stress Return Algorithm for Drucker-Prager Model

Chapter 4

HEAT TRANSFER/MOISTURE MIGRATION

4.1 Introduction

The processes taking place in the freezing of fine-grained soil are first identified before introducing the basic equations of physics. When a saturated fine-grained soil such as silt is subjected to freezing temperature, part of the water in the pores can solidify into ice, i.e. pore ice particles. Close to the soil particles, a film of unfrozen water remains since it is more tightly bound to them. According to thermodynamics, this adsorbed water film has lower free energy at a lower negative temperature. Thus, a potential gradient can develop along with the existing temperature gradient. Chemical potentials of water due to gradients of hydrostatic pressure, solute concentration and temperature interact additively to create a strong thermodynamic sink. This water is basically sucked from the warm portion to replace the water lost during freezing and to feed the accumulation of pore ice. As the pore ice particles grow, they can finally contact each other and form an ice lens oriented perpendicular to the direction of heat and water flow. Solutes are largely excluded in the freezing process, and maximum solute concentration in the medium thus establishes an osmotic pressure gradient which also helps the movement of water.

The freezing in a capillary-porous medium described in the above is essentially a

process coupling heat and mass transfer. Also, the understanding of the movement of water into the freezing and frozen zones through the capillaries, and factors governing it, is of critical importance in order to understand the freezing and thawing phenomena. From a thermodynamic point of view, a capillary porous medium will involve heat, water, solute and electric fluxes when subjected to physico-chemico-electro environment. For example, water moves in response to gradients in temperature (thermal), hydrostatic pressure (Darcy's law), solute concentration (capillary osmosis) and electric potential (electro osmosis).

Amongst other things during the freezing process, the solute will also lower the freezing point of water. For dilute solutions, Van't Hoff equation in reference [60] may be used to quantity the freezing point depression.

The mathematical description of the freezing-thaw processes in capillary-porous systems will normally involve the assumption that the medium is a continuum. The writing of (a) the mass balance equations in terms of the fluxes described above, (b) the heat transfer equations with mostly conduction, and (c) the pressure equations supplemented with the relevant boundary conditions will lead to a set of governing equations from which the principal unknowns will be solved numerically in most of the times.

Governing equations presented in this chapter will be expressed in Cartesian coordinates (x, y, z). Here, directions x, y, z correspond to directions r, z and θ respectively which were previously defined in Chapter 3.

4.2 Governing Equations

4.2.1 Assumptions

The basic assumptions made in the derivation of the model are as follows:

- Moisture transport in frozen and unfrozen zones occurs only by the liquid water form. The air phase and vapor transfer have negligible effects in net water transfer.
- The freezing of the soil is considered to be mainly controlled by heat conduction and convection is neglected.
- The freezing point depression of ice in the soil under loading is negligible.
- The soil is consolidated under external pressure before freezing, and the effect of consolidation in the unfrozen zone is negligible during the freezing process.
- The volume of the soil particles remains constant in the freezing process.
- Both unfrozen and frozen soil are isotropic bodies.
- The sign rule is that all tensile stresses and strains are positive.
- Gravitational pressure on water flow in the frozen zone is negligible.

4.2.2 Heat Transfer

To investigate the heat transfer in a water saturated soil, an elemental volume (dx, dy, dz) shown in Fig. 4.1 is considered. Neglecting heat convection during the

freezing of the soil, the net heat flux q_i (i=1, 2, 3) generated by pure conduction must be equal to the heat flux associated to the cooling of the water (heat capacity C) and phase change (latent heat L) as part of the water turns into ice. In the following developments, the balance equations will be written in rate form with "energy rate" expressed in *joule/sec* due to the evolutionary nature of the of cooling process.

Referring to Fig. 4.1, the rate of heat flux balance in the direction x (i=1) can be described as follows:

$$\frac{\partial q_x}{\partial x} \cdot dx\,dy\,dz = -L\rho_i \frac{\partial \theta_i}{\partial t} \cdot dx\,dy\,dz + C\frac{\partial T}{\partial t} \cdot dx\,dy\,dz \tag{4.1}$$

in which the term on the left hand side corresponds to net rate of energy flux passing through the cube, while the first and second terms on the right hand side refer to rate of energy changes associated to phase change and heat capacity respectively. The temperature is denoted by T while ice fraction and ice density are given by θ_i and ρ_i respectively.

Furthermore, the process of heat conduction can be described by Fourier's Law which states that the heat flux is proportional to the temperature gradient through the thermal conductivity λ. Therefore, in direction x, the heat flux q_x is

$$q_x = -\lambda \frac{\partial T}{\partial x} \tag{4.2}$$

Writing rate of heat balance in all three directions x, y, z and considering Eq. (4.2), one finally arrives at the three-dimensional heat transport equation

$$C\frac{\partial T}{\partial t} = \frac{\partial}{\partial x}\left(\lambda\frac{\partial T}{\partial x}\right) + \frac{\partial}{\partial y}\left(\lambda\frac{\partial T}{\partial y}\right) + \frac{\partial}{\partial z}\left(\lambda\frac{\partial T}{\partial z}\right) + L\rho_i\frac{\partial \theta_i}{\partial t} \tag{4.3}$$

In the above Eq. (4.3), C : heat capacity of material $(J\,m^{-3}\,{}^{\circ}C^{-1})$, T : temperature $({}^{\circ}C)$, t : time (sec), x, y : coordinates (m), λ : thermal conductivity of material $(W\,m^{-1}\,{}^{\circ}C^{-1})$, isotropic case here, L : latent heat of fusion $(J\,kg^{-1})$, i.e. the heat extracted from 0 $^{\circ}C$ of water to 0 $^{\circ}C$ of ice, $L = 333.7 \times 10^3\ (J\,kg^{-1})$, ρ_i : density of ice $0.9\,Mg\ m^{-3}$, and finally, θ_i : fraction of ice $(m^3\ m^{-3})$.

4.2.3 Mass Transfer

In order to investigate mass transfer phenomena in the freezing soil, an elemental volume $(dx, dy.dz)$ is again considered as shown in Fig. 4.2. Aspects such as the effect of gravitational potential on moisture flow and vapour phase transfer as the soil freezes can be neglected in the derivation as the unfrozen water movement is mainly driven by pressure gradients. As the soil freezes, mass must be conserved as the liquid water flows out of the pores due to a combination of pressure gradient build up and ice formation. Looking at mass transfer balance across a face of area $(dy.dz)$ along the x direction, one gets

$$\rho_l\frac{\partial Q_x}{\partial x}\,dx\,dy\,dz = \rho_l\frac{\partial \theta_l}{\partial t}\cdot dx\,dy\,dz + \rho_i\frac{\partial \theta_i}{\partial t}\cdot dx\,dy\,dz \tag{4.4}$$

in which new variables ρ_l, θ_l and Q_x refer to unfrozen water (liquid) density, volume fraction and flux respectively. The left hand side of Eq. (4.4) represents the net

mass flux across two faces of the cube in the x direction, while the right hand side refers to mass flux due to unfrozen water and ice generation.

Further assuming that the liquid water flux Q_x is governed mainly by a diffusion process, Fick's Law can be introduced, i.e.

$$Q_x = -k\frac{\partial P_l}{\partial x} \tag{4.5}$$

in which P_l (Pa) is the pressure in the unfrozen water (liquid) pressure and k $(m^2\ \sec^{-1}\ Pa^{-1})$ is its hydraulic conductivity.

Inserting Eq. (4.5) into Eq. (4.4) and writing the mass balance in all directions x, y, z, the generalized moisture transport equation for steady state or unsteady state emerges as

$$\frac{\partial \theta_l}{\partial t} + \frac{\rho_i}{\rho_l}\frac{\partial \theta_i}{\partial t} = \frac{\partial}{\partial x}\left(k\frac{\partial P_l}{\partial x}\right) + \frac{\partial}{\partial y}\left(k\frac{\partial P_l}{\partial y}\right) + \frac{\partial}{\partial z}\left(k\frac{\partial P_l}{\partial z}\right) \tag{4.6}$$

4.2.4 Clapeyron Equation

In this section, the relationship of liquid pressure, ice pressure, and temperature will be investigated. Frozen soil can be regarded as porous medium with the mixture of liquid, ice, air, and solid skeleton, as shown in Fig. 4.3.

From Fig. 4.3, when equilibrium is reached, at any point of the porous medium, the chemical potential of ice μ_i must be equal to the chemical potential of liquid μ_l, i.e.

$$\mu_i = \mu_l \quad \text{or} \quad d\mu_i = d\mu_l$$

Applying Gibbs-Duhem (energy dissipation) equation for liquid and ice separately,

$$d\mu_i = -S_i\, dT_k + V_i\, dP_i \quad \text{and} \quad d\mu_l = -S_l\, dT_k + V_l\, dP_l$$

one gets

$$V_i\, dP_i - V_l\, dP_l + (S_l - S_i)\; dT_k = 0$$

$$\Longrightarrow \qquad V_l\, dP_l - V_i\, dP_i = (S_l - S_i)\; dT_k$$

By definition the difference of the liquid entropy and the ice entropy must be equal the latent heat of that liquid per unit temperature in Kelvin, i.e.

$$(S_l - S_i) = \frac{L}{T_k}$$

Hence,

$$V_l\,dP_l - V_i\,dP_i = \frac{L}{T_k}\,dT_k$$

Integrating the above equation, one gets

$$V_l \int_0^{P_l} dP_l - V_i \int_0^{P_i} dP_i = L \int_{T_0}^{T_k} \frac{dT_k}{T_k}$$
$$V_l P_l - V_i P_i = L \ln\left(\frac{T_k}{T_0}\right)$$

or

$$\frac{P_l}{\rho_l} - \frac{P_i}{\rho_i} = L \ln\left(\frac{T_k}{T_0}\right) \tag{4.7}$$

In the above equation, μ : chemical potential ($J\,kg^{-1}$), S : specific entropy ($J\,kg^{-1}\,K^{-1}$), V : specific volume ($m\ kg^{-1}$), P_i : ice pressure (Pa), P_l : liquid pressure (Pa), T_k : temperature in Kelvin ($K =^{\circ} C + 273.16$), T_0 : reference temperature ($273.16\,K$).

4.2.5 Liquid Fraction and Temperature Relations

A certain amount of liquid water remains unfrozen in the pores due to several factors, freezing point depression being a major one. The relationship between the amount of unfrozen liquid and temperature has been determined experimentally for many

different soils by Anderson and Morgenstern [61] and Fortier *et al.* [62] . Based on these experimental data, it is found that the best fit would be described by an exponential function. However, due to the complexity of the problem addressed herein, a linear relationship is chosen for sake of simplicity. Thus, assuming that at zero degree Celsius there is no ice and all the pores are occupied by unfrozen water, the linear relationship can be written as

$$\theta_l = f(T) = n_0 (0.3 + \frac{T}{30}) \times 100 \tag{4.8}$$

in which, n_0 is the initial porosity of the frozen soil.

Figure 4.4 shows a comparison of the assumed linear relationship for a soil such as Caen silt ($n_0 = 0.3808$) with the experimental data given by Fortier *et al.* [62]. At this point, it is important to note that the hypothesis of linearity has to be still verified.

4.2.6 Ice Pressure Relations

The generation of ice pressures in frozen soils is probably the most poorly understood topic in soil mechanics. In order to numerically simulate the nature of frozen soil, some assumptions must be introduced according to the experimental work done by other researchers. In this thesis, the author borrows Shen and Ladanyi's suggestion for ice pressure distribution [17] because of its simplicity. In their suggestion, the ice pressure distributed linearly within the freezing fringe, as shown in Fig. 4.5.

Thus, in two dimensions, we have

$$\frac{\partial}{\partial x}\left(k\frac{\partial P_i}{\partial x}\right)+\frac{\partial}{\partial y}\left(k\frac{\partial P_i}{\partial y}\right)=0 \tag{4.9}$$

It is important to emphasize that in general, Eq. (4.9) does not imply a linear distribution of ice pressures.

Eqs. (4.3), (4.6), (4.7), (4.8), and (4.9) reveal that there are five unknowns, namely T, θ_l, θ_i, P_l, and P_i.Once these are solved, the resulting ice and liquid pressures P_i and P_l can be considers as initial stresses in a finite element type of stress analysis which involves only mechanical processes, i.e.

$$\boldsymbol{\sigma}_0=(P_i+P_l)\boldsymbol{\delta} \tag{4.10}$$

in which $\boldsymbol{\delta}$ is the Kronecker delta symbol used to imply that the ice and liquid pressures are being applied to the soil grains isotropic.

Then work equivalent mechanical load terms $\mathbf{F}_{\sigma_0}$ which enter the Fourier finite element equations can be simply calculated as

$$\mathbf{F}_{\sigma_0}=\int_{\Omega}\mathbf{B}^T:\boldsymbol{\sigma}_0\,d\Omega \tag{4.11}$$

which will be used in the Fourier finite element model developed in the previous chapter.

4.3 Derivation of General Controlling Equation

The following derivations will be carried out in two dimensions as a result of a reduction in dimensions due to the use of Fourier finite elements. The five principal unknowns are T, θ_l, θ_i, P_l, and P_i have been derived according to the physical nature of the frozen soil in the previous section. In this thesis, the temperature, T , will be solved first. Then, the liquid and the ice pressure, P_l and P_i, will be employed as the initial stress load in the mechanical analysis of a numerical example. So, P_l and P_i will also be solved explicitly. The liquid and ice fractions, θ_l and θ_i, will be treated as intermediate variables in the following derivations, because they cannot be solved explicitly based on the above mentioned assumptions unless some other conditions are introduced.

From Eq. (4.6), one can get

$$\rho_i L\frac{\partial \theta_i}{\partial t} = \rho_l L\left[\frac{\partial}{\partial x}\left(k\frac{\partial P_l}{\partial x}\right)+\frac{\partial}{\partial y}\left(k\frac{\partial P_l}{\partial y}\right)\right]-\rho_l L\frac{\partial \theta_l}{\partial t}$$

Substituting the above equation into Eq. (4.3) leads to

$$C\frac{\partial T}{\partial t}+\rho_l L\frac{\partial \theta_l}{\partial t}=\frac{\partial}{\partial x}\left(\lambda\frac{\partial T}{\partial x}\right)+\frac{\partial}{\partial y}\left(\lambda\frac{\partial T}{\partial y}\right)+\rho_l L\left[\frac{\partial}{\partial x}\left(k\frac{\partial P_l}{\partial x}\right)+\frac{\partial}{\partial y}\left(k\frac{\partial P_l}{\partial y}\right)\right] \tag{4.12}$$

From Eq. (4.7), one can derive the following

$$
\begin{aligned}
P_l &= \frac{\rho_l}{\rho_i} P_i + \rho_l L \left(\ln T_k - \ln T_0\right) \\
\frac{\partial P_l}{\partial x} &= \frac{\rho_l}{\rho_i} \frac{\partial P_i}{\partial x} + \rho_l L \left(\frac{1}{T_k}\right) \left(\frac{\partial T_k}{\partial x}\right) \\
\frac{\partial}{\partial x}\left(k \frac{\partial P_l}{\partial x}\right) &= \frac{\rho_l}{\rho_i} \frac{\partial}{\partial x}\left(k \frac{\partial P_i}{\partial x}\right) + \rho_l L \left[-\frac{1}{T_k^2} k \left(\frac{\partial T_k}{\partial x}\right)^2 + \frac{1}{T_k} \frac{\partial}{\partial x}\left(k \frac{\partial T_k}{\partial x}\right)\right] \\
&= \frac{\rho_l}{\rho_i} \frac{\partial}{\partial x}\left(k \frac{\partial P_i}{\partial x}\right) - \frac{\rho_l L}{T_k^2} k \left(\frac{\partial T_k}{\partial x}\right)^2 + \frac{\rho_l L}{T_k} \frac{\partial}{\partial x}\left(k \frac{\partial T_k}{\partial x}\right)
\end{aligned}
$$

Similarly,

$$
\frac{\partial}{\partial y}\left(k \frac{\partial P_l}{\partial y}\right) = \frac{\rho_l}{\rho_i} \frac{\partial}{\partial y}\left(k \frac{\partial P_i}{\partial y}\right) - \frac{\rho_l L}{T_k^2} k \left(\frac{\partial T_k}{\partial y}\right)^2 + \frac{\rho_l L}{T_k} \frac{\partial}{\partial y}\left(k \frac{\partial T_k}{\partial y}\right)
$$

and

$$
\begin{aligned}
&\frac{\partial}{\partial x}\left(k \frac{\partial P_l}{\partial x}\right) + \frac{\partial}{\partial y}\left(k \frac{\partial P_l}{\partial y}\right) = \frac{\rho_l}{\rho_i} \left[\frac{\partial}{\partial x}\left(k \frac{\partial P_i}{\partial x}\right) + \frac{\partial}{\partial y}\left(k \frac{\partial P_i}{\partial y}\right)\right] - \\
&\frac{\rho_l L}{T_k^2} \left[k \left(\frac{\partial T_k}{\partial x}\right)^2 + k \left(\frac{\partial T_k}{\partial y}\right)^2\right] + \frac{\rho_l L}{T_k} \left[\frac{\partial}{\partial x}\left(k \frac{\partial T_k}{\partial x}\right) + \frac{\partial}{\partial y}\left(k \frac{\partial T_k}{\partial y}\right)\right] \quad (4.13)
\end{aligned}
$$

Substituting Eq. (4.13) into (4.12), and noting that $\frac{\partial \theta_l}{\partial t} = \frac{\partial \theta_l}{\partial T} \frac{\partial T}{\partial t}$, one gets

$$\left(C+\rho_l L\frac{\partial\theta_l}{\partial T}\right)\frac{\partial T}{\partial t}=\frac{\partial}{\partial x}\left(\lambda\frac{\partial T}{\partial x}\right)+\frac{\partial}{\partial y}\left(\lambda\frac{\partial T}{\partial y}\right)+\frac{L\rho_l^2}{\rho_i}\left[\frac{\partial}{\partial x}\left(k\frac{\partial P_i}{\partial x}\right)+\frac{\partial}{\partial y}\left(k\frac{\partial P_i}{\partial y}\right)\right]$$
$$-\frac{k\,L^2\rho_l^2}{T_k^2}\left[\left(\frac{\partial T_k}{\partial x}\right)^2+\left(\frac{\partial T_k}{\partial y}\right)^2\right]+\frac{L^2\rho_l^2}{T_k}\left[\frac{\partial}{\partial x}\left(k\frac{\partial T_k}{\partial x}\right)+\frac{\partial}{\partial y}\left(k\frac{\partial T_k}{\partial y}\right)\right] \tag{4.14}$$

Furthermore, assuming that the temperature change within an element is small, i.e.,

$$\frac{\partial T}{\partial x}=\frac{\partial T_k}{\partial x}=\frac{\partial T}{\partial y}=\frac{\partial T_k}{\partial y}=small$$

so that higher order terms are negligible, i.e.

$$\left(\frac{\partial T}{\partial x}\right)^2=\left(\frac{\partial T}{\partial y}\right)^2=0$$

then, Eq. (4.12) becomes

$$\overline{C}\frac{\partial T}{\partial t}=\frac{\partial}{\partial x}\left(\overline{\lambda}\frac{\partial T}{\partial x}\right)+\frac{\partial}{\partial y}\left(\overline{\lambda}\frac{\partial T}{\partial y}\right)+\frac{\rho_l^2}{\rho_i}L\left[\frac{\partial}{\partial x}\left(k\frac{\partial P_i}{\partial x}\right)+\frac{\partial}{\partial y}\left(k\frac{\partial P_i}{\partial y}\right)\right] \tag{4.15}$$

in which

$$\begin{aligned} \overline{C} &= C + \rho_l L \frac{\partial \theta_l}{\partial T} \\ \overline{\lambda} &= \lambda + \frac{k \rho_l^2 L^2}{T_k} = \lambda + \frac{k \rho_l^2 L^2}{T + 273.16} \end{aligned} \tag{4.16}$$

Finally, assuming a linear distribution of ice pressures, as a first approximation, which results into Eq. (4.9), Eq. (4.15) reduces to

$$\overline{C} \frac{\partial T}{\partial t} = \frac{\partial}{\partial x}\left(\overline{\lambda} \frac{\partial T}{\partial x}\right) + \frac{\partial}{\partial y}\left(\overline{\lambda} \frac{\partial T}{\partial y}\right) = \overline{\lambda}\left(\frac{\partial^2 T}{\partial x^2} + \frac{\partial^2 T}{\partial y^2}\right) \tag{4.17}$$

Equation (4.17) contains parameters $\overline{C}$ and $\overline{\lambda}$ which are function of unknowns such as temperature T and liquid volume fraction θ_l. Noting Eq. (4.16) and also realizing that θ_l is a function of T by virtue of Eq. (4.8), Eq. (4.17) turns out to be non-linear with respect to temperature. An iterative scheme is devised based on Newton's method.

The author wants to highlight that the developments described in reference [17] contain minor errors. For example, referring to Eq. (8) of [17], i.e.

$$\overline{C} \frac{\partial T}{\partial \tau} = \frac{\partial}{\partial x}\left(\overline{\lambda} \frac{\partial T}{\partial x}\right) + \frac{\partial}{\partial z}\left(\overline{\lambda} \frac{\partial T}{\partial z}\right) + \rho_l L \left[\frac{\partial}{\partial x}\left(k \frac{\partial P_i}{\partial x}\right) + \frac{\partial}{\partial z}\left(k \frac{\partial P_i}{\partial z}\right)\right]$$

the multiplier $\rho_l L$, in the right hand side, should be $\frac{\rho_l^2 L}{\rho_i}$. Instead, their basic governing equation for heat and moisture transfer should be Eq. (10) only, not including

(3) and (7), because (10) is derived from (3) and (7). The same relationship should also be imposed on their Eqs. (21) and (22), which means that only Eq. (21) is the controlling equation for one-dimensional case. The principal unknown should be temperature, T, in Eq. (10) or (21) for one-dimensional case. The other unknowns can only be solved by "back-substitution" based on that T is known, instead of solving Eqs. (21) and (22) for one-dimensional case.

4.4 Finite Element Discretization

Consider a domain of volume Ω bounded by a contour Γ subjected to initial and boundary conditions as shown in Fig. 4.6. Galerkin's method is used to discretize Eq. (4.17) for finite element calculations. Thus, the temperature field $T(x, y, t)$ can be discretized using interpolation functions $N(x, y)$, i.e.

$$T(x, y, t) = \sum_{k=1}^{N} N_k(x, y)\, T_k(t) = \sum_{k=1}^{N} N_k T_k \tag{4.18}$$

where T_k is the nodal temperature and N is the order of interpolation.

As a result of the above discretization, Galerkin's method requires that the weighted residual over volume of interest Ω to be zero. Hence,

$$\int_{\Omega} N_i \left[\overline{\lambda} \left(\frac{\partial^2 T}{\partial x^2} + \frac{\partial^2 T}{\partial y^2} \right) - \overline{C} \frac{\partial T}{\partial t} \right] d\Omega = 0 \tag{4.19}$$

Let's apply Gauss integral theorem to Eq. (4.19) so that the volume integral converts into a surface integral along contour Γ, i.e.

$$\int_\Omega N_i \left[\overline{\lambda}\left(\frac{\partial^2 T}{\partial x^2}+\frac{\partial^2 T}{\partial y^2}\right)\right] d\Omega$$
$$= \oint_\Gamma N_i \overline{\lambda}\left(\frac{\partial T}{\partial x} l_x + \frac{\partial T}{\partial y} l_y\right) d\Gamma - \int_\Omega \overline{\lambda}\left(\frac{\partial N_i}{\partial x}\frac{\partial T}{\partial x}+\frac{\partial N_i}{\partial y}\frac{\partial T}{\partial y}\right) d\Omega$$

Substituting the above into Eq. (4.19), one gets

$$\int_\Omega \left[\overline{\lambda}\left(\frac{\partial N_i}{\partial x}\frac{\partial T}{\partial x}+\frac{\partial N_i}{\partial y}\frac{\partial T}{\partial y}\right) + N_i \overline{C}\frac{\partial T}{\partial t}\right] d\Omega$$
$$= \oint_\Gamma N_i \overline{\lambda}\left(\frac{\partial T}{\partial x} l_x + \frac{\partial T}{\partial y} l_y\right) d\Gamma \qquad (4.20)$$

At this point, let's recall the following conditions:

Initial condition: $t = 0$, $T(x, y, 0) = T^0(x, y, 0)$

Boundary condition:

(1) along Γ_1 : $T(x, y, t) = T^*(x, y, t)$ given

(2) along Γ_2 :

$$\overline{\lambda}\left(\frac{\partial T}{\partial x} l_x + \frac{\partial T}{\partial y} l_y\right) = -\beta(T - T_c)$$

in which, β is a surface dissipation factor, and T_c is a reference temperature.

In Eq. (4.20), let the right hand side

$$\oint_{\Gamma} N_i \overline{\lambda} \left(\frac{\partial T}{\partial x} l_x + \frac{\partial T}{\partial y} l_y \right) d\Gamma$$

$$= \int_{\Gamma_1} N_i \overline{\lambda} \left(\frac{\partial T}{\partial x} l_x + \frac{\partial T}{\partial y} l_y \right) d\Gamma_1 + \int_{\Gamma_2} N_i \overline{\lambda} \left(\frac{\partial T}{\partial x} l_x + \frac{\partial T}{\partial y} l_y \right) d\Gamma_2 \quad (4.21)$$

When calculating the temperature along the elements of boundary Γ_1 , e.g. j, k, the temperature at i and m are known while N_i along $\overline{im}$ is 0, see Fig. 4.6. Hence,

$$\int_{\Gamma_1} N_i \overline{\lambda} \left(\frac{\partial T}{\partial x} l_x + \frac{\partial T}{\partial y} l_y \right) d\Gamma_1 = 0 \quad (4.22)$$

Accumulating Eq. (4.20) for each element, one gets

$$\sum_e \int_{\Omega^e} \left[\overline{\lambda} \left(\frac{\partial N_i}{\partial x} \frac{\partial T}{\partial x} + \frac{\partial N_i}{\partial y} \frac{\partial T}{\partial y} \right) + N_i \overline{C} \frac{\partial T}{\partial t} \right] d\Omega$$

$$= \sum_e \int_{\Gamma_2^e} \overline{\lambda} \left(\frac{\partial T}{\partial x} l_x + \frac{\partial T}{\partial y} l_y \right) d\Gamma_2$$

$$= -\sum_e \int_{\Gamma_2^e} N_i \beta (T - T_c) \, d\Gamma_2 \quad (4.23)$$

Introducing an interpolation function (4.18), one gets

$$\sum_e \int_{\Omega^e} \left\{ \overline{\lambda} \left[\frac{\partial N_i}{\partial x} \left(\sum \frac{\partial N_k}{\partial x} T_k \right) + \frac{\partial N_i}{\partial y} \left(\sum \frac{\partial N_k}{\partial y} T_k \right) \right] + N_i \overline{C} \left(\sum N_k \frac{\partial T_k}{\partial t} \right) \right\} d\Omega^e$$

$$= -\sum_e \int_{\Gamma_2^e} N_i \beta (\sum N_k T_k - T_c)\, d\Gamma_2^e$$

Rearranging the above gives rise to

$$\begin{aligned} &\sum_e \int_{\Omega^e} \left\{ \overline{\lambda} \left[\frac{\partial N_i}{\partial x} (\sum \frac{\partial N_k}{\partial x} T_k) + \frac{\partial N_i}{\partial y} (\sum \frac{\partial N_k}{\partial y} T_k) \right] \right\} d\Omega^e \\ &+ \sum_e \int_{\Gamma_2^e} N_i \beta \left(\sum N_k T_k \right) d\Gamma_2^e + \sum_e \int_{\Omega^e} N_i \overline{C} (\sum N_k \frac{\partial T_k}{\partial t}) \, d\Omega^e \\ = &\sum_e \int_{\Gamma_2^e} N_i \beta T_c \, d\Gamma_2^e \end{aligned} \tag{4.24}$$

which can be written in matrix form,

$$\mathbf{K}(\mathbf{T}) : \mathbf{T} + \mathbf{M}(\mathbf{T}) : \frac{\partial \mathbf{T}}{\partial t} = \mathbf{P} \tag{4.25}$$

$$K_{ij}(T) = \sum_e K_{ij}^e(T), \quad M_{ij}(T) = \sum_e M_{ij}^e(T), \quad P_i = \sum_e P_i^e$$

For each element,

$$\begin{aligned} K_{ij}^e(T) &= \int_{\Omega^e} \left(\frac{\partial N_i}{\partial x} \frac{\partial N_j}{\partial x} + \frac{\partial N_i}{\partial y} \frac{\partial N_j}{\partial y} \right) d\Omega^e + \int_{\Gamma_2^e} \beta \, N_i \, N_j \, d\Gamma_2^e \\ M_{ij}^e(T) &= \int_{\Omega^e} \overline{C} \, N_i \, N_j \, d\Omega^e, \qquad P_i^e = \int_{\Gamma_2^e} \beta \, N_i \, T_c \, d\Gamma_2^e \end{aligned} \tag{4.26}$$

Equation (4.25) is nonlinear and has to be solved by an iteration scheme, say Newton's method.

In this study, the dissipation factor β is equal to 0 since the boundaries are insulated. Therefore,the term $\mathbf{P}$ can be discarded so that the finite element equations simplify into

$$\mathbf{F}(\mathbf{T}) = \Delta t\ \mathbf{K}(\mathbf{T}) : \mathbf{T} + \mathbf{M}(\mathbf{T}) : \Delta\mathbf{T} = \mathbf{0} \tag{4.27}$$

The above equation is function of both space (x, y) and time t. Let's consider a time interval Δt taken between time stations t_n and t_{n+1} at which the temperature fields are $\mathbf{T}_n$ and $\mathbf{T}_{n+1}$ respectively. Equation (4.27) can be written at a time $t_{n\theta} \in [t_n,\ t_{n+1}]$ by using an average scheme controlled by a parameter $\Theta \in [0,\ 1]$, i.e.

$$\begin{aligned}\mathbf{F}(\mathbf{T}_{n+\theta}) &= (1-\Theta)\cdot\Delta t\cdot\mathbf{K}(\mathbf{T}_n) : \mathbf{T}_n + \Theta\cdot\Delta t\cdot\mathbf{K}(\mathbf{T}_{n+1}) : \mathbf{T}_{n+1} \\ &\quad + \mathbf{M}(\mathbf{T}_{n+1}) : (\mathbf{T}_{n+1} - \mathbf{T}_n)\end{aligned}$$

Values of $\Theta = 0$ and $\Theta = 1$ correspond to explicit and implicit schemes respectively.

Rearranging the above equation, one gets

$$\begin{aligned}\mathbf{F}(\mathbf{T}_{n+\theta}) &= [\Theta\cdot\Delta t\cdot\mathbf{K}(\mathbf{T}_{n+1}) + \mathbf{M}(\mathbf{T}_{n+1})] : \mathbf{T}_{n+1} \\ &\quad + [(1-\Theta)\cdot\Delta t\cdot\mathbf{K}(\mathbf{T}_n) - \mathbf{M}(\mathbf{T}_{n+1})] : \mathbf{T}_n\end{aligned} \tag{4.28}$$

The non-linear character of the above Eq. (4.28) can be dealt with by expanding it into Taylor's series about the kth iteration, i.e.

$$\begin{aligned}\mathbf{F}\left(\mathbf{T}_{n+\theta}\right) &= \mathbf{F}\left(\mathbf{T}_{n+1}^{k}\right)+\mathbf{F}'\left(\mathbf{T}_{n+1}^{k}\right):\left(\mathbf{T}_{n+1}-\mathbf{T}_{n+1}^{k}\right)+\mathbf{0}^{2}=0 \text{ or}\\ &\mathbf{F}'\left(\mathbf{T}_{n+1}^{k}\right):\Delta\mathbf{T}_{n+1}^{k+1}=-\mathbf{F}\left(\mathbf{T}_{n+1}^{k}\right) \qquad (4.29)\end{aligned}$$

in which

$$\Delta\mathbf{T}_{n+1}^{k+1}=\mathbf{T}_{n+1}^{k+1}-\mathbf{T}_{n+1}^{k} \qquad (4.30)$$

By virtue of Eq. (4.28), the right hand side of Eq. (4.29) becomes

$$\begin{aligned}\mathbf{F}\left(\mathbf{T}_{n+\theta}^{k}\right) &= \left[\Theta\cdot\Delta t\cdot\mathbf{K}\left(\mathbf{T}_{n+1}^{k}\right)+\mathbf{M}\left(\mathbf{T}_{n+1}^{k}\right)\right]:\mathbf{T}_{n+1}^{k}\\ &\quad+\left[(1-\Theta)\cdot\Delta t\cdot\mathbf{K}\left(\mathbf{T}_{n}\right)-\mathbf{M}\left(\mathbf{T}_{n+1}^{k}\right)\right]:\mathbf{T}_{n}\\ &= \mathbf{F}_{\text{int}}\left(\mathbf{T}_{n+1}^{k}\right) \qquad (4.31)\end{aligned}$$

Also, making use of Eq. (4.28) one gets

$$\mathbf{F}'(\mathbf{T}_{n+1}^{k}) = \left(\frac{\partial\mathbf{F}}{\partial\mathbf{T}_{n+1}}\right)^{k}=\left(\Theta\cdot\Delta t\cdot\left.\frac{\partial\mathbf{K}\left(\mathbf{T}_{n+1}\right)}{\partial\mathbf{T}_{n+1}}\right|^{k}+\left.\frac{\partial\mathbf{M}\left(\mathbf{T}_{n+1}\right)}{\partial\mathbf{T}_{n+1}}\right|^{k}\right):\mathbf{T}_{n+1}^{k}$$

$$+\left[\Theta\cdot\Delta t\cdot\mathbf{K}\left(\mathbf{T}_{n+1}^{k}\right)+\mathbf{M}\left(\mathbf{T}_{n+1}^{k}\right)\right]-\left.\frac{\partial\mathbf{M}\left(\mathbf{T}_{n+1}\right)}{\partial\mathbf{T}_{n+1}}\right|^{k}:\mathbf{T}_{n} \quad (4.32)$$

Substituting Eqs. (4.31) and (4.32) into (4.29), $\Delta\mathbf{T}_{n+1}^{k+1}$ can be solved. Finally, the temperature distribution $\mathbf{T}$ can be obtained from Eq. (4.30). Equation (4.31) will be used to check convergence. If $\mathbf{F}_{\text{int}}\left(\mathbf{T}_{n+1}^{k}\right)=\mathbf{0}$ or $\leq$ *tolerance* , convergence is reached.

The procedures for solving the temperature field can be summarized in Table 4.1.

4.5 Liquid Pressure Field

Once the temperature field $T(x,y,t)$ is found at a given time t, the liquid pressure field P_l and ice pressure field P_i can be calculated. Let's recall Eq. (4.3) which is now written in two dimensions, i.e.

$$\rho_i\frac{\partial\theta_i}{\partial t}=\frac{C}{L}\frac{\partial T}{\partial t}-\frac{\lambda}{L}\left(\frac{\partial^2 T}{\partial x^2}+\frac{\partial^2 T}{\partial y^2}\right) \quad (4.33)$$

Substituting Eq. (4.33) into (4.6) and after some rearranging one ultimately gets

$$\frac{\lambda}{\rho_l L}\left(\frac{\partial^2 T}{\partial x^2}+\frac{\partial^2 T}{\partial y^2}\right)-\left(\frac{\partial\theta_l}{\partial T}+\frac{C}{\rho_l L}\right)\frac{\partial T}{\partial t}+\frac{\partial}{\partial x}\left(k\frac{\partial P_l}{\partial x}\right)+\frac{\partial}{\partial y}\left(k\frac{\partial P_l}{\partial y}\right)=0 \quad (4.34)$$

Applying Galerkin's Method to Eq. (4.34) to get the finite element equations

Table 4.1: Procedures for Solving Temperature Field

1. Start from time step 1 and iteration step 1, introduceing initial value and boundary conditions

2. Compute $\mathbf{F}\left(\mathbf{T}_{n+1}^{k}\right)$ by Eq. (4.31)
$$\mathbf{F}\left(\mathbf{T}_{n+1}^{k}\right) = \left[\Theta \cdot \Delta t \cdot \mathbf{K}\left(\mathbf{T}_{n+1}^{k}\right) + \mathbf{M}\left(\mathbf{T}_{n+1}^{k}\right)\right] : \mathbf{T}_{n+1}^{k} + \left[(1-\Theta) \cdot \Delta t \cdot \mathbf{K}\left(\mathbf{T}_{n}\right) - \mathbf{M}\left(\mathbf{T}_{n+1}^{k}\right)\right] : \mathbf{T}_{n}$$

3. Calculate $\mathbf{F}'(\mathbf{T}_{n+1}^{k})$ by Eq. (4.32)
$$\mathbf{F}'(\mathbf{T}_{n+1}^{k}) = \left(\Theta \cdot \Delta t \cdot \left.\frac{\partial \mathbf{K}(\mathbf{T}_{n+1})}{\partial \mathbf{T}_{n+1}}\right|^{k} + \left.\frac{\partial \mathbf{M}(\mathbf{T}_{n+1})}{\partial \mathbf{T}_{n+1}}\right|^{k}\right) : \mathbf{T}_{n+1}^{k} + \left[\Theta \cdot \Delta t \cdot \mathbf{K}\left(\mathbf{T}_{n+1}^{k}\right) + \mathbf{M}\left(\mathbf{T}_{n+1}^{k}\right)\right] - \left.\frac{\partial \mathbf{M}(\mathbf{T}_{n+1})}{\partial \mathbf{T}_{n+1}}\right|^{k} : \mathbf{T}_{n}$$

4. Calculate temperature increment $\Delta \mathbf{T}_{n+1}^{k+1}$ by Eq. (4.29)
$$\mathbf{F}'\left(\mathbf{T}_{n+1}^{k}\right) : \Delta \mathbf{T}_{n+1}^{k+1} = -\mathbf{F}\left(\mathbf{T}_{n+1}^{k}\right)$$

5. Calculate current temperature field by Eq. (4.30)
$$\Delta \mathbf{T}_{n+1}^{k+1} = \mathbf{T}_{n+1}^{k+1} - \mathbf{T}_{n+1}^{k} \quad \text{or} \quad \mathbf{T}_{n+1}^{k+1} = \mathbf{T}_{n+1}^{k} + \Delta \mathbf{T}_{n+1}^{k+1}$$

6. Check for convergence by Eq. (4.31)
   IF $\mathbf{F}_{\text{int}}\left(\mathbf{T}_{n+1}^{k}\right) \leq$ *tolerance* THEN
      calculate liquid pressure and ice pressure described in the next sections
      proceed to next time step
   ELSE
      goto 2
   ENDIF

leads to

$$\int_{\Omega} N_i \left[\frac{\lambda}{\rho_l L} \left(\frac{\partial^2 T}{\partial x^2} + \frac{\partial^2 T}{\partial y^2} \right) - \left(\frac{\partial \theta_l}{\partial T} + \frac{C}{\rho_l L} \right) \frac{\partial T}{\partial t} + k \left(\frac{\partial^2 P_l}{\partial x^2} + \frac{\partial^2 P_l}{\partial y^2} \right) \right] d\Omega = 0 \tag{4.35}$$

Gauss integral theorem can again be used towards converting volume integrals into surface integrals the above equation, one gets

$$\begin{aligned} \int_{\Omega} N_i \frac{\lambda}{\rho_l L} \left(\frac{\partial^2 T}{\partial x^2} + \frac{\partial^2 T}{\partial y^2} \right) d\Omega &= \oint_{\Gamma} N_i \frac{\lambda}{\rho_l L} \left(\frac{\partial T}{\partial x} \cdot l_x + \frac{\partial T}{\partial y} \cdot l_y \right) d\Gamma \\ &- \int_{\Omega} \frac{\lambda}{\rho_l L} \left(\frac{\partial N_i}{\partial x} \frac{\partial T}{\partial x} + \frac{\partial N_i}{\partial y} \frac{\partial T}{\partial y} \right) d\Omega \end{aligned} \tag{4.36}$$

and

$$\begin{aligned} \int_{\Omega} N_i k \left(\frac{\partial^2 P_l}{\partial x^2} + \frac{\partial^2 P_l}{\partial y^2} \right) d\Omega &= \oint_{S} N_i \, k \left(\frac{\partial P_l}{\partial x} \cdot l_x + \frac{\partial P_l}{\partial y} \cdot l_y \right) dS \\ &- \int_{\Omega} k \left(\frac{\partial N_i}{\partial x} \frac{\partial P_l}{\partial x} + \frac{\partial N_i}{\partial y} \frac{\partial P_l}{\partial y} \right) d\Omega \end{aligned} \tag{4.37}$$

Substituting (4.36) and (4.37) into Eq. (4.35), one gets

$$\int_\Omega \frac{\lambda}{\rho_l L}\left(\frac{\partial N_i}{\partial x}\frac{\partial T}{\partial x}+\frac{\partial N_i}{\partial y}\frac{\partial T}{\partial y}\right)d\Omega+\int_\Omega k\left(\frac{\partial N_i}{\partial x}\frac{\partial P_l}{\partial x}+\frac{\partial N_i}{\partial y}\frac{\partial P_l}{\partial y}\right)d\Omega$$
$$+\int_\Omega N_i\left(\frac{\partial \theta_l}{\partial T}+\frac{C}{\rho_l L}\right)\frac{\partial T}{\partial t}d\Omega \qquad (4.38)$$
$$=\oint_\Gamma N_i\frac{\lambda}{\rho_l L}\left(\frac{\partial T}{\partial x}\cdot l_x+\frac{\partial T}{\partial y}\cdot l_y\right)d\Gamma+\oint_S N_i k\left(\frac{\partial P_l}{\partial x}\cdot l_x+\frac{\partial P_l}{\partial y}\cdot l_y\right)dS$$

Γ is the same boundary which relates to temperature T as described in the previous section while S is the boundary relating to liquid pressure in the following manner:

Initial conditions: when $t=0,\ P_l=P_l^0$

Boundary conditions:

(1) along S_1 : $P_l=P_l^*(t)$ given

(2) along S_2 :

$$k\left(\frac{\partial P_l}{\partial x}\cdot l_x+\frac{\partial P_l}{\partial y}\cdot l_y\right)=0$$

under the conditions set in the previous section of the basic equations for P_l .

Note, S_1 and S_2 could be different from Γ_1 and Γ_2 respectively.

Introducing interpolation function for the temperature T and liquid pressure P_l

such that

$$T(x,y,t) = \sum N_k(x,y)\, T_k(t) = \sum N_k T_k$$
$$P_l(x,y,t) = \sum N_k(x,y)\, P_{lk}(t) = \sum N_k P_{lk}$$

the discrete form of Eq. (4.38) becomes

$$\sum_e \int_{\Omega^e} \frac{\lambda}{\rho_l L}\left[\frac{\partial N_i}{\partial x}\left(\sum \frac{\partial N_k}{\partial x} T_k\right) + \frac{\partial N_i}{\partial y}\left(\sum \frac{\partial N_k}{\partial y} T_k\right)\right]$$
$$+k\left[\frac{\partial N_i}{\partial x}\left(\sum \frac{\partial N_k}{\partial x} P_{lk}\right) + \frac{\partial N_i}{\partial y}\left(\sum \frac{\partial N_k}{\partial y} P_{lk}\right)\right] + N_i\left(\frac{\partial \theta_l}{\partial T} + \frac{C}{\rho_l L}\right)\left(\sum N_k \frac{\partial T_k}{\partial t}\right) d\Omega^e$$
$$= -\sum_e \int_{\Gamma_2^e} N_i \beta\left[\left(\sum N_k T_k\right) - T_c\right] d\Gamma_2^e \qquad (4.39)$$

Again, for an insulated temperature boundary, i.e. $\beta = 0$, the right hand side of the above equation reduces to zero. Equation (4.39) re-written in matrix form becomes

$$\mathbf{U}:\mathbf{T} + \mathbf{Q}:\mathbf{P}_l + \mathbf{R}:\frac{\partial \mathbf{T}}{\partial t} = \mathbf{0} \quad \text{or} \quad \mathbf{Q}:\mathbf{P}_l = -\left(\mathbf{U}:\mathbf{T} + \mathbf{R}:\frac{\partial \mathbf{T}}{\partial t}\right)$$

or in discrete form

$$\Delta t\, \mathbf{Q}:\mathbf{P}_l = -\left(\Delta t\, \mathbf{U}:\mathbf{T} + \mathbf{R}:\Delta \mathbf{T}\right) \qquad (4.40)$$

in which

$$\begin{aligned}
\mathbf{q}_{ij}^{e} &= \int_{\Omega^e} k \left(\frac{\partial N_i}{\partial x}\frac{\partial N_j}{\partial x} + \frac{\partial N_i}{\partial y}\frac{\partial N_j}{\partial y} \right) d\Omega^e \\
\mathbf{u}_{ij}^{e} &= \int_{\Omega^e} \frac{\lambda}{\rho_l L} \left(\frac{\partial N_i}{\partial x}\frac{\partial N_j}{\partial x} + \frac{\partial N_i}{\partial y}\frac{\partial N_j}{\partial y} \right) d\Omega^e \\
\mathbf{r}_{ij}^{e} &= \int_{\Omega^e} N_i N_j \left(\frac{\partial \theta_l}{\partial T} + \frac{C}{\rho_l L} \right) d\Omega^e
\end{aligned} \tag{4.41}$$

The liquid pressure P_l can thus be calculated from Eq. (4.40) .

4.6 Ice Pressure Field

It has been found in this study that the original Clapeyron Eq. (4.7) tends to overestimate the ice pressure, especially for a temperature of $-5°C$ for which an ice pressure of $P_i = 5.5\,MPa$ is obtained. In order to obtain more realistic values, a modified Clapeyron equation as suggested by [63] will be adopted, i.e. $\mathbf{P}_l = 1.091\mathbf{P}_i$ or $\mathbf{P}_i = 0.9166\mathbf{P}_l$.

Referring back to Eqs. (4.10) and (4.11), the load induced by ice/liquid pressure can be finally obtained. If one applies this load to the Fourier finite element model the displacement and stress field corresponding to the heat conduction-moisture migration problem can be obtained.

The procedures of solving for liquid pressure and ice pressure can be summarized by Table 4.2.

Table 4.2: Procedures for Solving Liquid and Ice Pressure

1. Calculate $\mathbf{Q}$, $\mathbf{U}$, and $\mathbf{R}$ by Eq. (4.41)

$$\mathbf{q}_{ij}^{e} = \int_{\Omega^e} k \left(\frac{\partial N_i}{\partial x}\frac{\partial N_j}{\partial x} + \frac{\partial N_i}{\partial y}\frac{\partial N_j}{\partial y} \right) d\Omega^e$$

$$\mathbf{u}_{ij}^{e} = \int_{\Omega^e} \frac{\lambda}{\rho_l L} \left(\frac{\partial N_i}{\partial x}\frac{\partial N_j}{\partial x} + \frac{\partial N_i}{\partial y}\frac{\partial N_j}{\partial y} \right) d\Omega^e$$

$$\mathbf{r}_{ij}^{e} = \int_{\Omega^e} N_i N_j \left(\frac{\partial \theta_l}{\partial T} + \frac{C}{\rho_l L} \right) d\Omega^e$$

2. Calculate $\mathbf{P}_l$ by Eq. (4.40) for the current time step

$$\Delta t\,\mathbf{Q} : \mathbf{P}_l = -\left(\Delta t\,\mathbf{U} : \mathbf{T} + \mathbf{R} : \Delta \mathbf{T}\right)$$

3. Calculate $\mathbf{P}_i$ by equation

$$\mathbf{P}_l = 1.091\mathbf{P}_i \quad \text{or} \quad \mathbf{P}_i = 0.9166\mathbf{P}_l$$

4. Proceed to the next time step

4.7 Conclusion

The model described in this chapter presents the solution of a sequence of equations, which govern the coupled heat transfer-moisture migration in a freezing soil. The key field variable is temperature which is solved from a non-linear set of differential equations. Once temperature is calculated, the determination of ice and liquid pressures becomes an easy task.

In the freezing soil-pipeline problem which is the main subject of this thesis, the heat transfer-moisture migration induced thermal stress $\boldsymbol{\sigma}^{th}$ can hence be computed as $\boldsymbol{\sigma}^{th} = (P_i + P_l)\,\boldsymbol{\delta}$ with $\boldsymbol{\delta}$ being the Kronecker delta symbol. It is herein assumed that both ice and liquid pressures are isotropic. These stresses will enter as work equivalent loads in the Fourier finite element model described in the previous chapter.

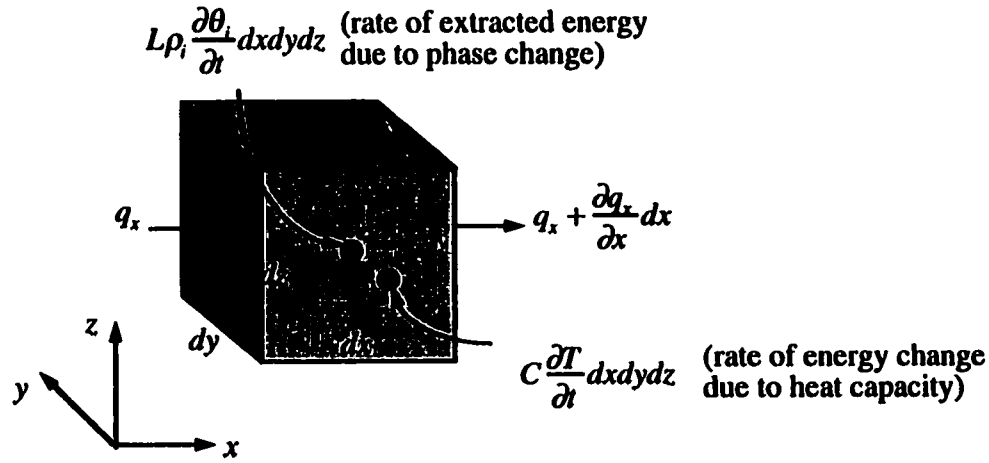

Fig. 4.1 Heat Transfer in an Element Volume

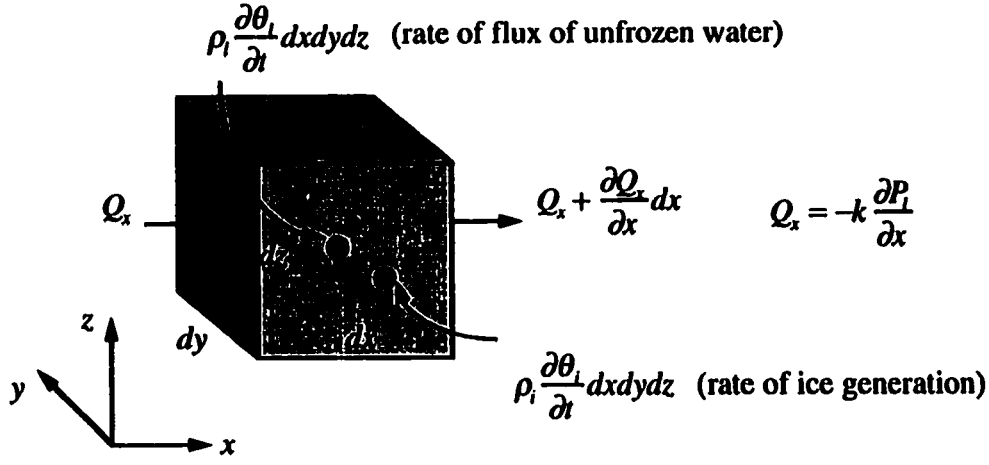

Fig. 4.2 Mass Transfer in an Element Volume

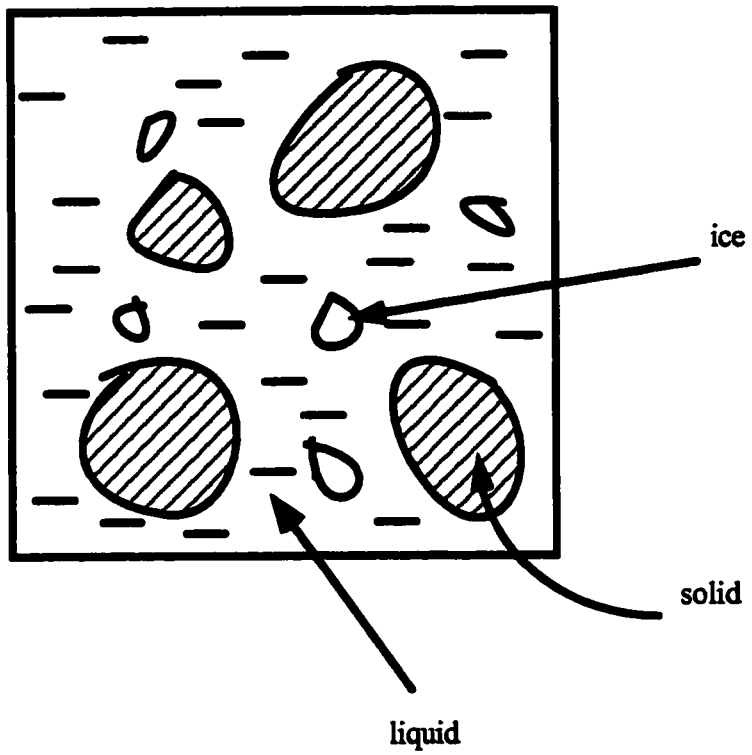

Fig. 4.3 Equilibrium of Ice and Water

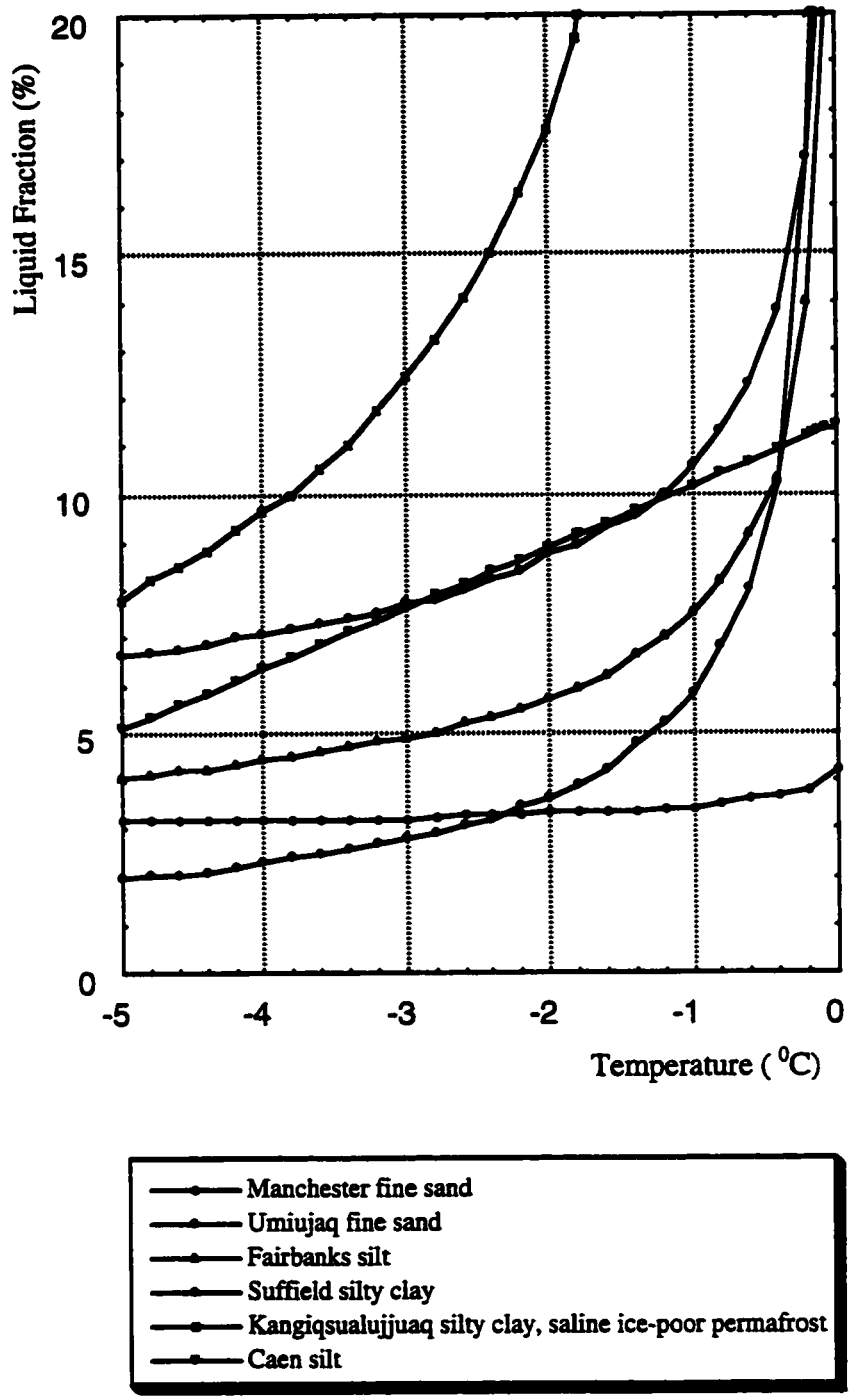

Fig. 4.4 Liquid Fraction vs. Temperature Relations

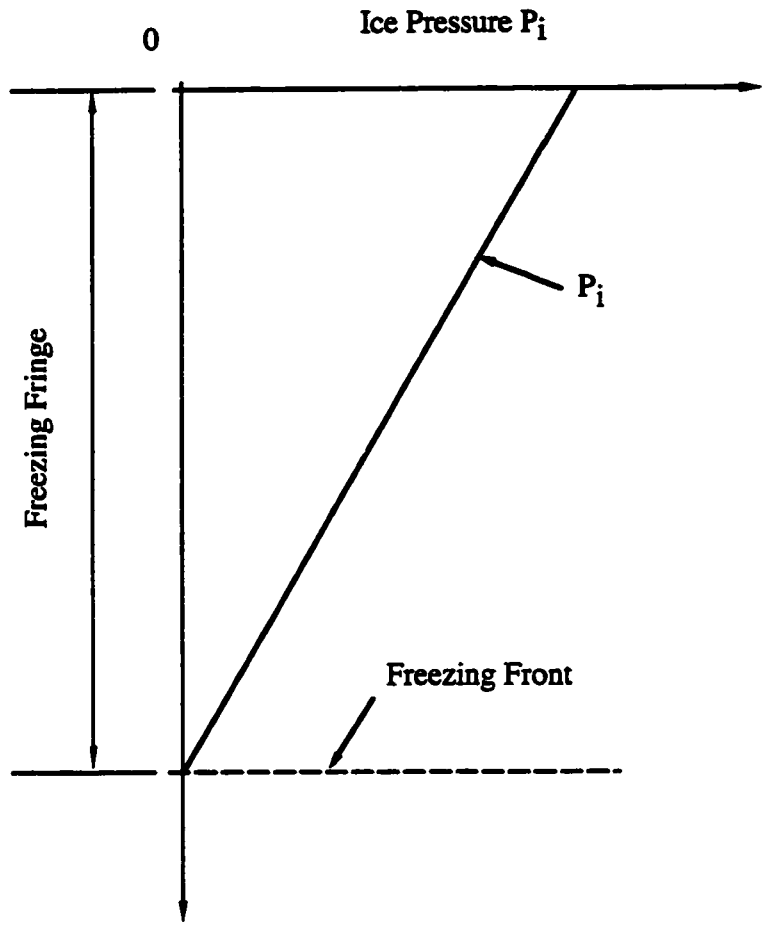

Fig. 4.5 Distribution of Ice Pressure

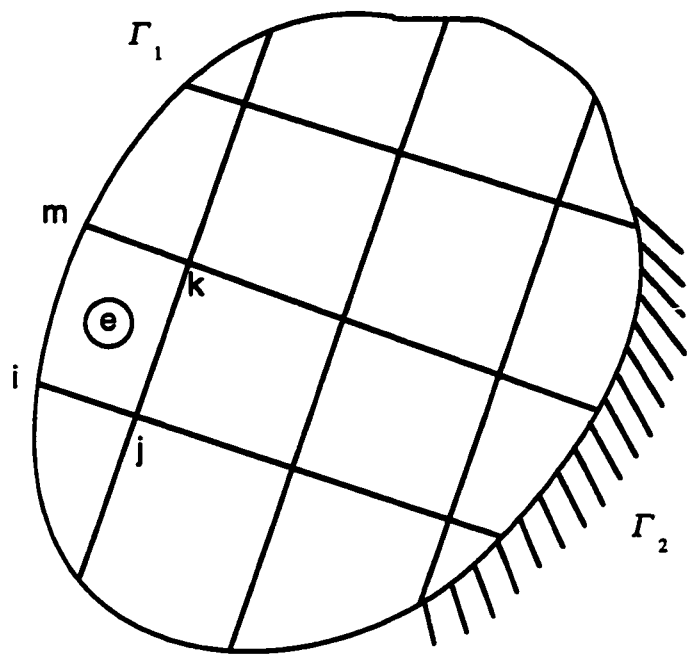

Fig. 4.6 Boundary Conditions

Chapter 5

VALIDATION OF THE MODEL

5.1 Introduction

The purpose of developing the Fourier finite element model is to solve problems with axisymmetric geometry under arbitrary loading conditions by a series of 2-D problems. The Fourier finite element theory was presented in Chapters 2 and 3 with reference to both linear and non-linear cases. It was found in particular, that the decoupling of harmonics was destroyed as soon as material non-linearity was introduced. Amongst strategies which were proposed to circumvent this problem, the method which replaces the variation of the constitutive matrix C in the circumferential direction θ with a mean value $\bar{\mathbf{C}}$ was retained. This was found to preserve the decoupling nature of the equilibrium equations at the expense of approximations. In this chapter, the algorithm proposed for non-linear Fourier finite elements is verified and approximations made evaluated.

5.2 Validation of Algorithm

There are no closed form solutions available to verify the model, especially in the non-linear regime. However one can compare the Fourier finite element results to

Table 5.1: Material Properties

Young's modulus	Poisson's ratio	Cohesion	Friction angle
$E = 2 \times 10^8\, kPa$	$\nu = 0.3$	$c = 2 \times 10^5\, kPa$	$\varphi = 30°$

those obtained from a classical three-dimensional finite element program such as ABAQUS [47]. It is particularly interesting to make the comparisons in the non-linear regime. To this end, benchmark problems which refer to the elastic and elasto-plastic responses of a thick-walled cylinder subjected to uniform internal pressure have been considered since closed form solutions are available. Furthermore, the case of a thick-walled cylinder subjected to an arbitrary internal loading was examined. The latter is intended to illustrate the performance of the model in the case of material non-linearity and arbitrary loading conditions in three dimensions.

5.2.1 Finite Element Mesh and Material Properties

The thick-walled cylinder selected for analysis has an internal radius of $a = 1.0m$, outer radius of $b = 1.5m$, and length of $L = 2.0m$ with one of its ends fixed, see Fig. 5.1. The finite element mesh used in ABAQUS is shown in Fig. 5.2 where 3456 nodes and 576 elements are used, while in the Fourier finite element analysis, only 16 elements and 69 nodes are needed, see Fig. 5.3. The elastic and elasto-plastic parameters used in this analysis are shown in Table 5.1.

5.2.2 Under Uniform Pressure

Elastic Analysis

A uniform pressure of $1.0 \times 10^5 kPa$ is applied at the internal wall of the cylinder in the elastic analysis. Figure 5.4 shows the radial, tangential, and longitudinal stress distributions along the radial distance for any given section along the circumference since a uniform pressure is applied. As far as displacements are concerned, the two models basically give identical results. In this simple case, which actually corresponds to the axi-symmetric problem, it is not surprising that good agreement is obtained between ABAQUS and the Fourier finite element model.

Elasto-Plastic Analysis

It is more interesting to turn to the elasto-plastic case which involves a thick-walled soil cylinder subjected to uniform internal pressure. There exists a closed form solution for the case the material follows a Drucker-Prager failure criterion governed by cohesion c and friction angle φ. The elastic limiting pressure p_{lm} is found to be

$$p_{lm} = \frac{6\,c\,(b^2 - a^2)\cos\varphi}{6\,a^2 \sin\varphi + \sqrt{3}\,b^2\,(3 - \sin\varphi)} \tag{5.1}$$

where a, b are the inner and outer radii respectively.

Using the set of parameters in Table 5.1, one finds an elastic limiting pressure of $1.17 \times 10^5 kPa$ for an internal pressure of $1.3 \times 10^5 kPa$. Figure 5.5 shows the radial, tangential, and longitudinal stress distributions along radial distance. It is again seen that the Fourier finite element model agrees very well with the ABAQUS

results, even in the non-linear material regime.

5.2.3 Mildly Non-symmetric Internal Loading

From the previous section, it can be seen that the Fourier finite element model agrees perfectly with ABAQUS for both elastic and elasto-plastic thick-walled cylinder under uniform internal pressure. Tests still need to be passed for cases of arbitrary loads in both elasticity and elasto-plasticity. The same thick-walled cylinder is now subjected to an arbitrary internal loading described by a radial pressure variation along circumferential direction, i.e.

$$p_r = p_0 + p_1 \cos\theta + p_2 \sin\theta + p_3 \cos 2\theta + p_4 \sin 2\theta \tag{5.2}$$

where $\sin\theta = \frac{z}{\sqrt{x^2+z^2}}$ and $\cos\theta = \frac{x}{\sqrt{x^2+z^2}}$; x, y, z being given in Fig. 5.1. In order to complicate the loading, the radial pressure also varies linearly along the longitudinal direction according to $p = p_0(L-y)/L$. As such, one can say that the load distribution is truly three-dimensional in nature.

Elastic Analysis

The load for the elastic analysis was chosen such that the coefficients that appear in Eq. (5.2) are $p_0 = 19200kPa$, $p_1 = 320kPa$, $p_2 = -160kPa$, $p_3 = 640kPa$ and $p_4 = 480kPa$. The load distribution which emerges from such choice of values is illustrated in Fig. 5.6 in a cross-sectional plane.

Figure 5.7 shows the load vs. displacement relations and the comparison between

the Fourier FEM and ABAQUS results. The four locations at sections 0°, 90°, 180°, and 270° were previously defined in Fig. 5.1. Very good agreement between the two methods is hence obtained.

The following sets of Figs. 5.8 to 5.15 show the radial, tangential, and longitudinal stress distributions along radial distance at the free end and middle sections of the pipe at sections 0°, 90°, 180°, and 270°. It is observed that the agreement between the Fourier FEM and ABAQUS calculations is very satisfactory.

Elasto-Plastic Analysis

In the plastic analysis, the load coefficients used were $p_0 = 192000kPa$, $p_1 = 3200kPa$, $p_2 = -1600kPa$, $p_3 = 6400kPa$ and $p_4 = 4800kPa$ so that the load magnitude was substantially increased to make the material yield plastically. The load distribution which emerges from such choice of values is illustrated in Fig. 5.16 in a typical cross-sectional plane.

Figure 5.17 shows the deformed shape of the cylinder under the mildly non-symmetric load distribution. It can be seen that the deformations are truly three-dimensional and there is no axis of symmetry.

The yield zone results of the Fourier FEM and ABAQUS comparison are very close, see Figs. 5.18 and 5.19.

The load vs. displacement curves are shown in Figs. 5.20 to 5.23. These four figures also show good agreement between the Fourier FEM and ABAQUS computations.

Finally, figures 5.24 to 5.31 show the radial, tangential, and longitudinal stress

distributions along radial distance at the end and middle sections of the pipe at four locations at 0°, 90°, 180°, and 270°. It is observed that the overall agreement between the Fourier FEM and ABAQUS results are again satisfactory.

5.2.4 Extremely Non-symmetric Internal Loading

In the previous sections, the Fourier FEM and ABAQUS results agreed very well for the elastic loading case because no plasticity occurred. For the extremely non-symmetric loading case, only the elasto-plastic analysis was attempted for reason of interest.

Elasto-Plastic Analysis

In this analysis, the load coefficients used were $p_0 = 103680kPa$, $p_1 = 48000kPa$, $p_2 = -24000kPa$, $p_3 = 96000kPa$ and $p_4 = 72000kPa$ so that the load magnitude was substantially increased in order to achieve a more profuse yielding state. The load distribution which emerges from such choice of values is very non-symmetric as illustrated in Fig. 5.32 for a typical cross-sectional plane. The geometric description of the problem can be found in Fig. 5.1.

Figure 5.33 shows the deformed shape of the cylinder under this extremely non-symmetric load distribution. It is obvious that the deformations are three-dimensional and there is no axis of symmetry.

The comparisons of yield zone results bewteen the Fourier FEM and ABAQUS are very close, see Figs. 5.34 to 5.37. Figures 5.34 and 5.35 show comparisons of the yield zones at the free end while Figs. 5.36 and 5.37 refer to the yield zones at the

fixed end.

The load vs. displacement curves are shown in Figs. 5.38 to 5.41 which reveal a relatively good agreement between the Fourier FEM and ABAQUS computations. However, some problems arise at 0° and 90° locations where the Fourier FEM load-displacement curve seems to be stiffer than the ones generated by ABAQUS due to mainly two reasons. Firstly, the mean consistent tangent operator made the cylinder appear to be stiffer than in the real case. Secondly, the yield zone near 0° and 90° sections is more severe than in the other sections, which can be found in Figs. 5.34 and 5.35. On the other hand, at the 180° section where the yield zone is not well developed, the results given by the two methods agreed very well again.

Figures 5.42 to 5.53 show the radial, longitudinal, and tangential stress distributions along radial distance at the free end section of the cylinder at 0°, 90°, 180°, and 270° locations. It is observed that the results given by the two methods do not agree well as in the mildly non-symmetric load case. This is largely due to the yield zone being quite localized and confined within a small area. Consequently, the mean consistent tangent operator technique does not apply very well in this case.

The effective plastic strain results of these two methods are compared in Figs. 5.54 to 5.57. It can be seen that the overall trend still shows very good agreement. However, one can see that the Fourier FEM computation gives smaller effective plastic strain values than those of ABAQUS. The use of a mean consistent tangent operator obviously led to stiffer results in this case.

5.3 Limitations

The above verifications indicate that the Fourier finite element model predicts the stress and deformation behaviour of an elastic material accurately as shown in Figs. 5.7 to 5.15. However, great caution should be exercised when applying the Fourier finite element model to elasto-plastic materials under non-axisymmetric loading conditions. Referring to the treatment of the consistent tangent operator $\mathbf{C}^k_{n+1}$ as presented in the previous sections, a mean value $\overline{\mathbf{C}}^k_{n+1}$ in the circumferential direction was proposed. As a result, this mean value of $\overline{\mathbf{C}}^k_{n+1}$ can be taken out of the integral involving θ, thus retaining the orthogonality condition in the integral and the decoupled nature of all the harmonics.

Figures 5.58(a), (b), and (c) show graphically the process of taking the mean consistent tangent operator at different radii. If the materials at a certain radius are all in the elastic state as shown in Fig. 5.58(a), the mean stiffness is the same as the elastic stiffness. Thus, this technique would accurately predict the correct results. However, if the materials at a certain radius are all in the plastic state as shown in Fig. 5.58(b), the mean stiffness would approximately predict the solution with good accuracy. The reason for this is that the variation of the plastic stiffness may not be very significantly different. However, if at certain radius, the plastic zone occurs in one section and the rest is in an elastic state as shown in Fig. 5.58(c), this technique would not be recommended. The applicability of this technique is questionable because the material with the mean stiffness would behave quite differently to the real case.

Figures 5.59(a) and (b) show a schematic view of a pipe subjected to non-

axisymmetric internal pressures with different degrees of non-axisymmetry. Figure 5.59(a) is subjected to a mildly non-axisymmetric pressure and the plastic zone developed under this pressure tends to be also mildly non-axisymmetric. If one takes a radius in the plastic zone, the soils in the circumferential direction would be in the plastic state and the mean stiffness would be very close to the actual plastic stiffness as illustrated in Fig. 5.59(a). Therefore this technique would provide a reasonably good solution to the problem. In the case of a uniform internal pressure, the solution is accurate as shown in Figs. 5.4 and 5.5, regardless of the elastic or plastic state.

However, under extremely non-symmetric loading conditions, the plastic zone will also be severely non-axisymmetric as shown in Fig. 5.59(b). The plastic zone occurs in one part of the cylinder while the remainder is still in elastic state. It can be easily noted that the mean of the consistent tangent operator would not predict accurate results. As such, the strength of the structure would be overestimated as the elastic zone contributes significantly to the plastic zone.

5.4 Conclusion

The above discussion indicates that the mean of consistent tangent operator technique is computationally advantageous. However, this technique should be used with caution. In general, the load should be mildly non-symmetric such that the plastic zone development follows the same trend. Although that the displacements in the plastic zone would be smaller than in the true solution, the stress distribution tendencies would be the same as shown in Figs. 5.42 –5.53. This technique can be used in

the preliminary study of axisymmetric structures subjected to mildly non-symmetric loading. An example would be the case of soil-pipeline systems where soil pressure, ice pressure, water pressure, and thermal loading are mildly non-symmetric.

Under an extremely non-symmetric loading condition, the mean consistent tangent operator technique should not be recommended. The actual stiffness of soils in the circumferential direction should be employed which would involve much more computational effort due to the coupled nature of the harmonics. In such a situation, the advantage of the Fourier finite element method may not be very significant. An alternative solution is to use the algorithm described in section 3.3 which accounts for the coupling nature of the harmonics.

Finally, it is interesting to note that for extremely non-symmetric loadings, the computing time for ABAQUS was 125 minutes while the Fourier FEM needed only 2 minutes on a RISC 6000 IBM Workstation at The University of Calgary.

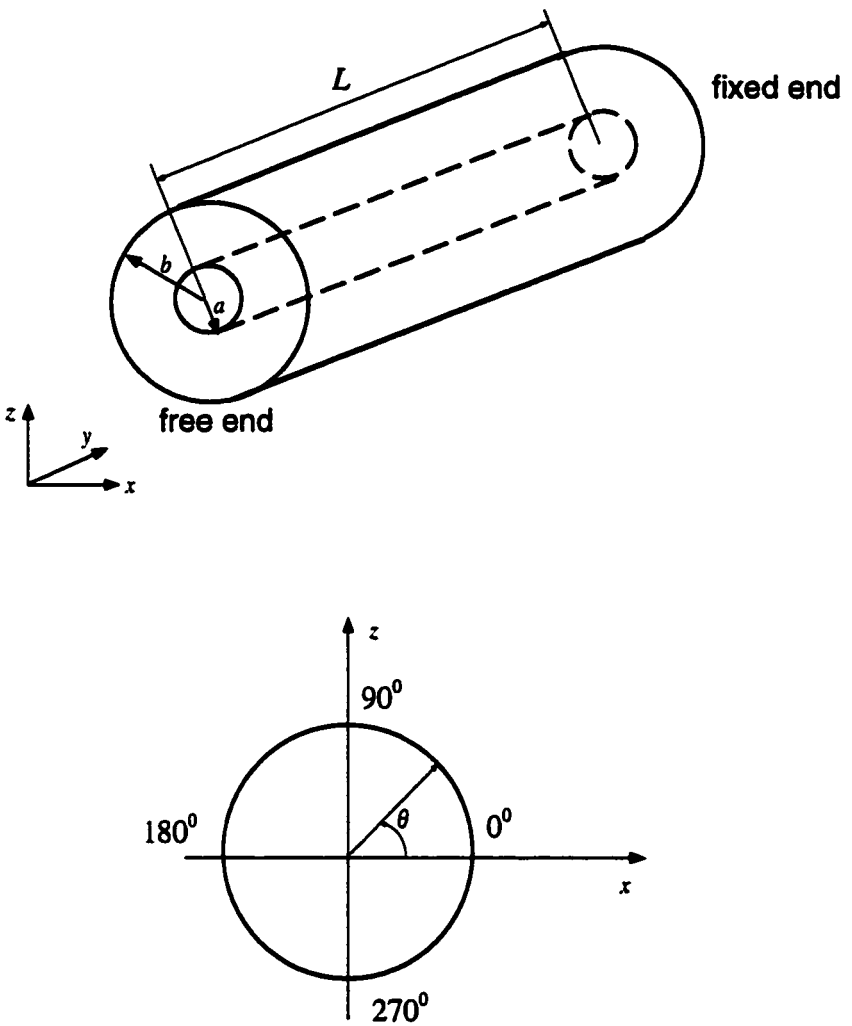

Fig. 5.1 Geometric Definition

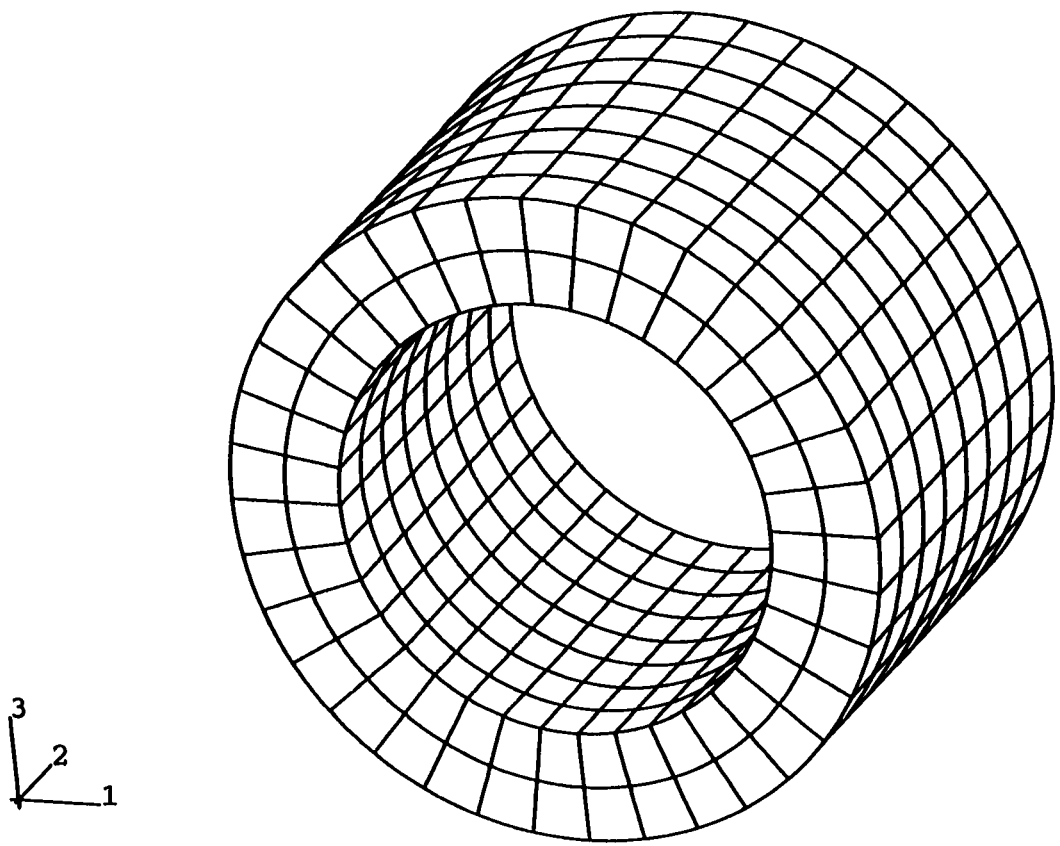

Fig. 5.2 ABAQUS 3-D Mesh

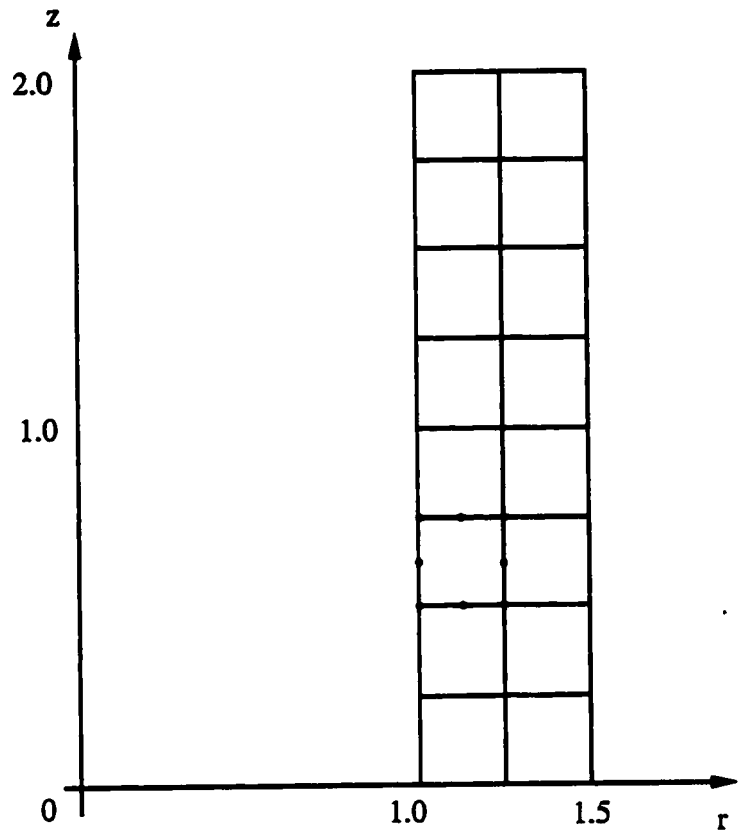

2-D Fourier FEM Mesh

Fig. 5.3 Fourier Finite Element Mesh

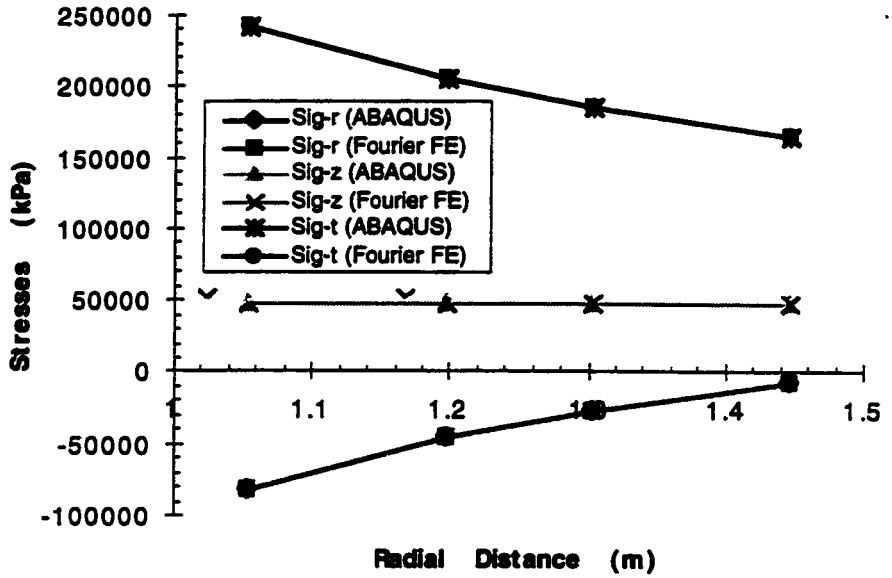

Fig. 5.4 Radial Direction Stress Comparison for Uniform Elastic Load

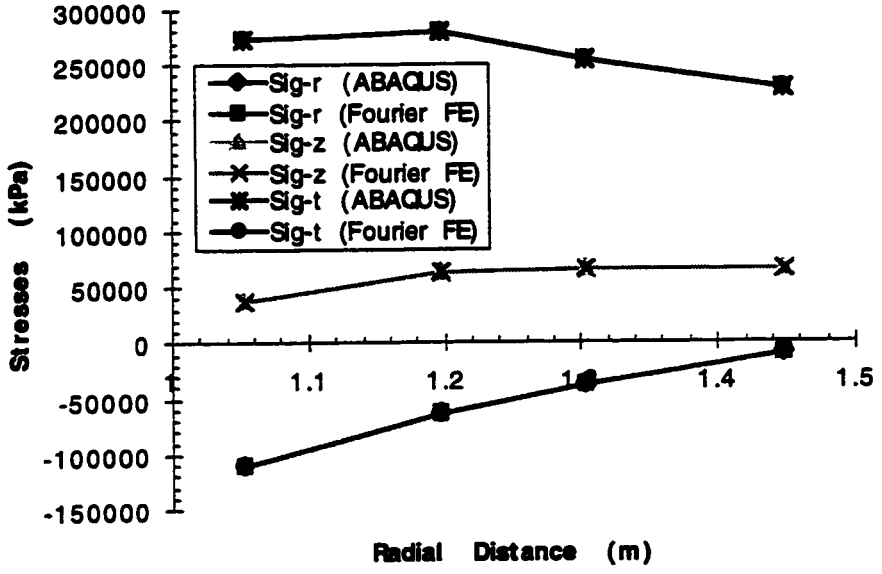

Fig. 5.5 Radial Direction Stress Comparison for Uniform Elasto-Plastic Load

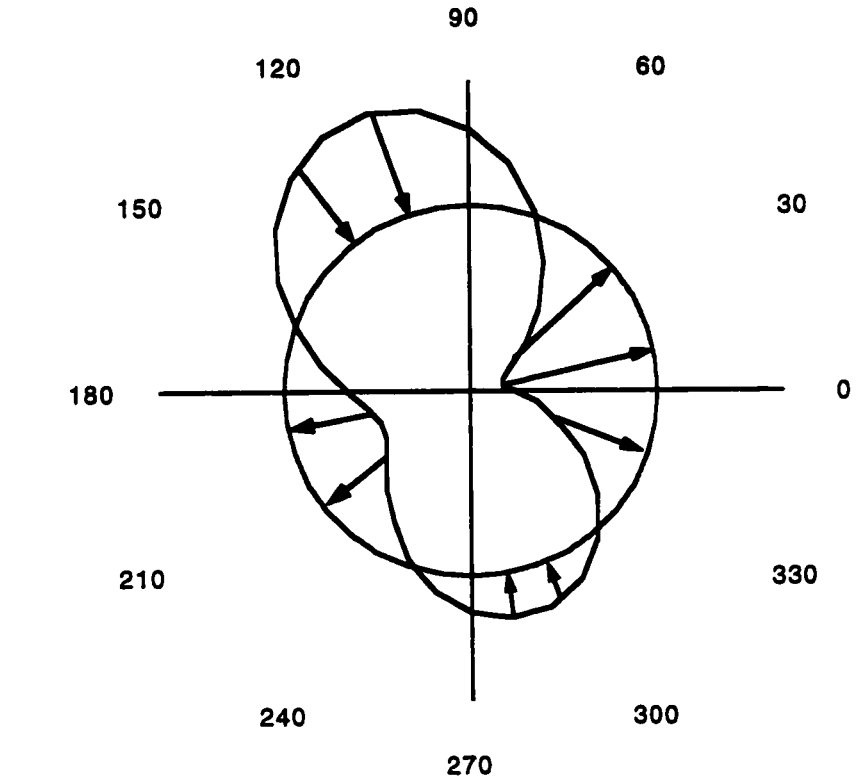

Fig. 5.6 Load Distribution for Mildly Non-symmetric Elastic Case

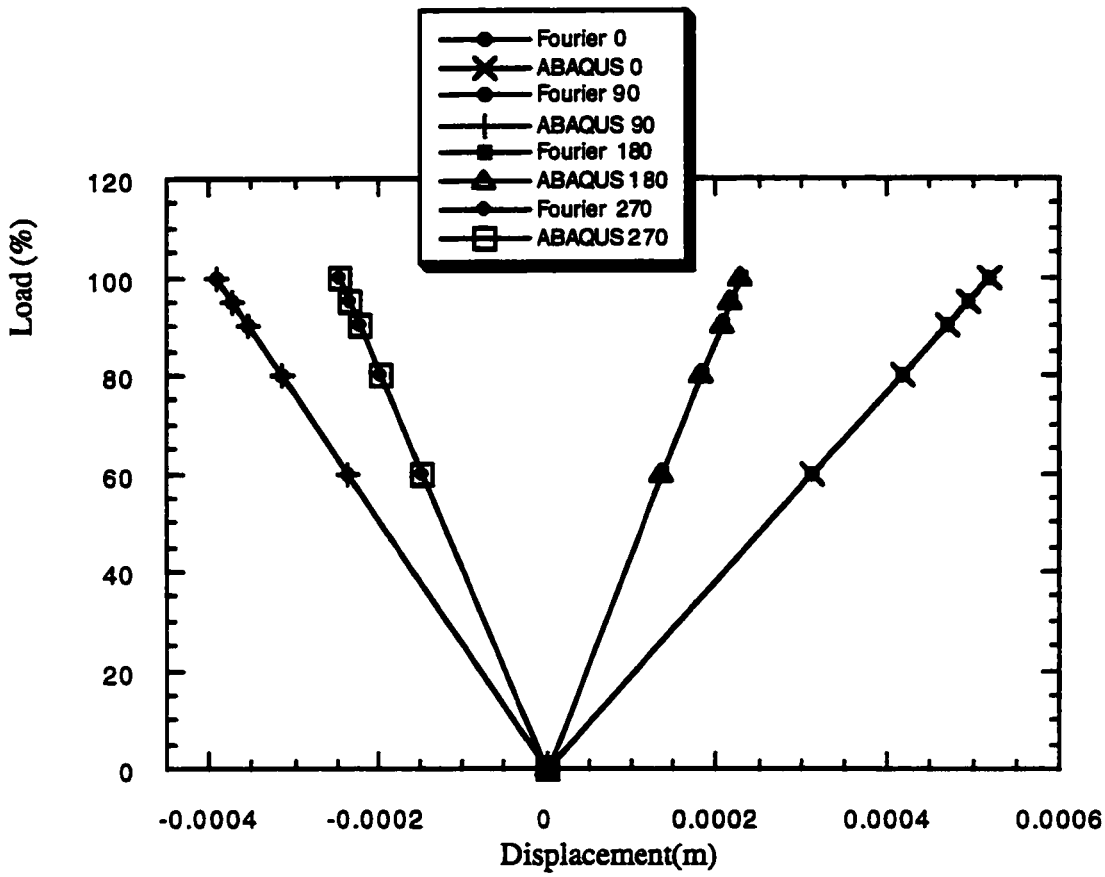

Fig. 5.7 Load vs. Displacement for Mildly Non-symmetric Elastic Case

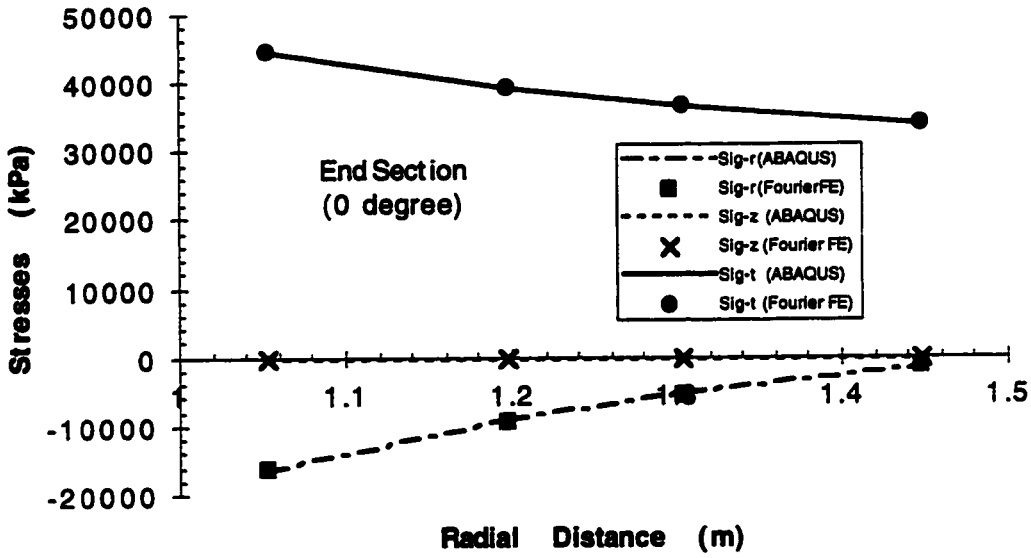

Fig. 5.8 Radial Direction Stress Comparison for Non-uniform Elastic Load
(Free End 0 Degree Location)

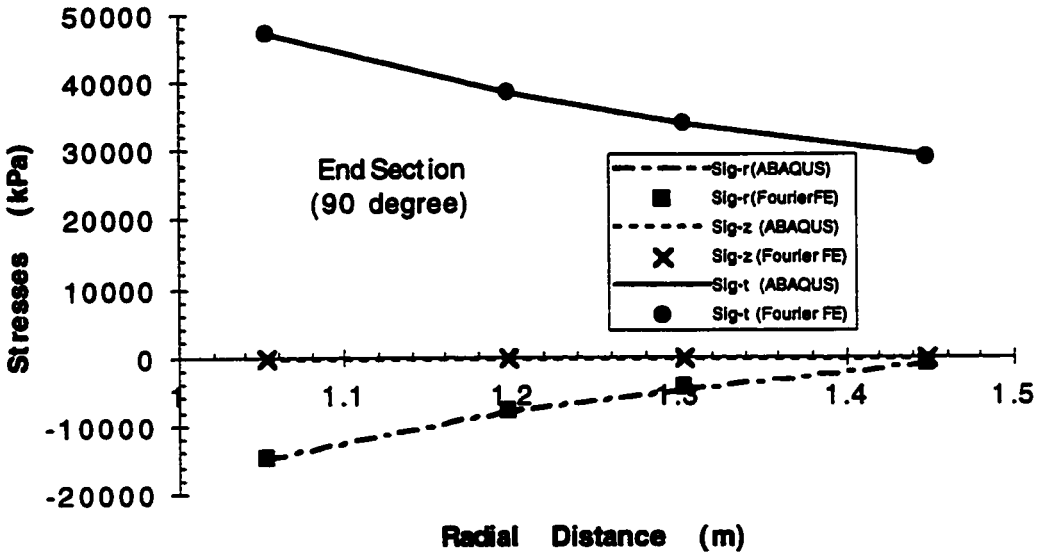

Fig. 5.9 Radial Direction Stress Comparison for Non-uniform Elastic Load (Free End 90 Degree Location)

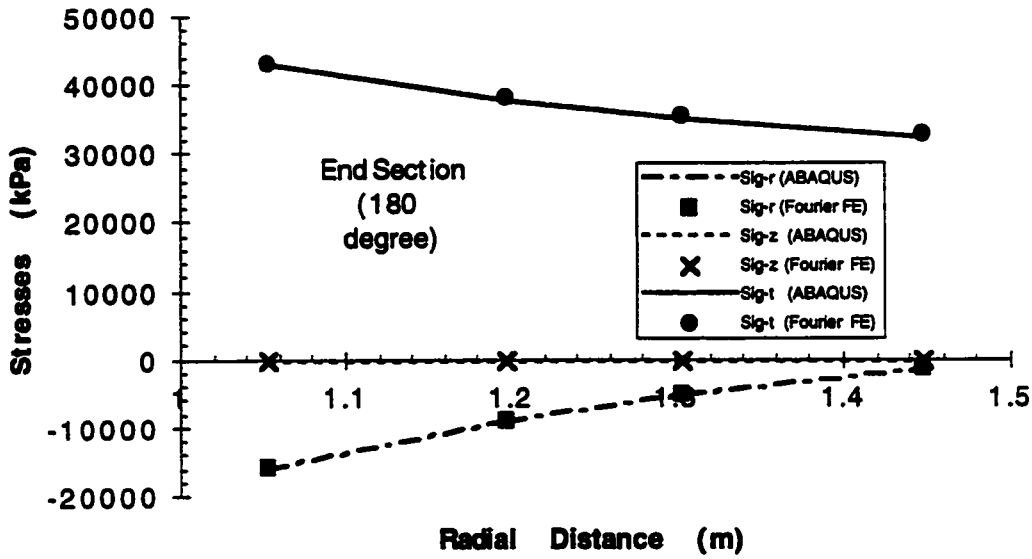

Fig. 5.10 Radial Direction Stress Comparison for Non-uniform Elastic Load
(Free End 180 Degree Location)

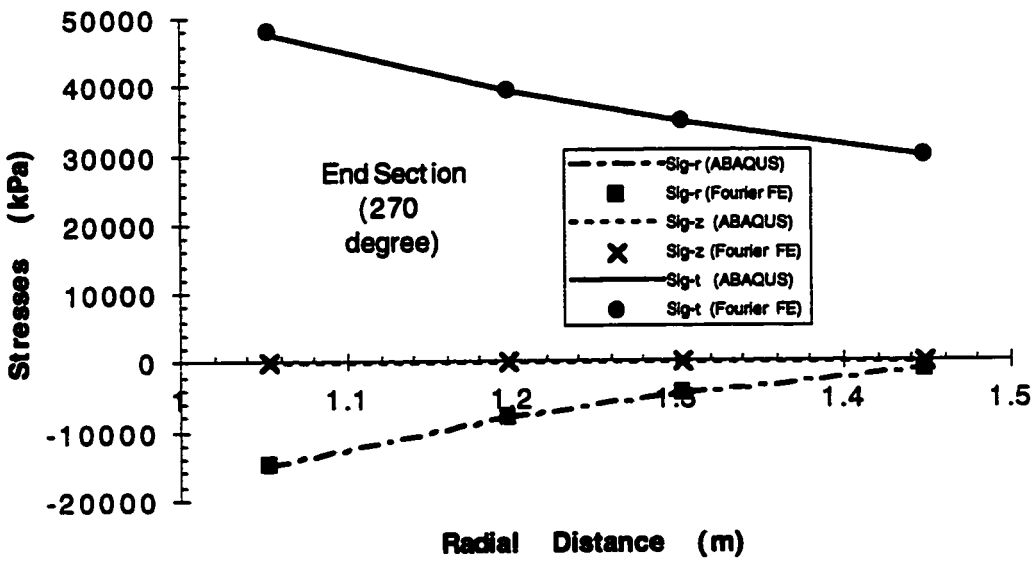

Fig 5.11 Radial Direction Stress Comparison for Non-uniform Elastic Load
(Free End 270 Degree Location)

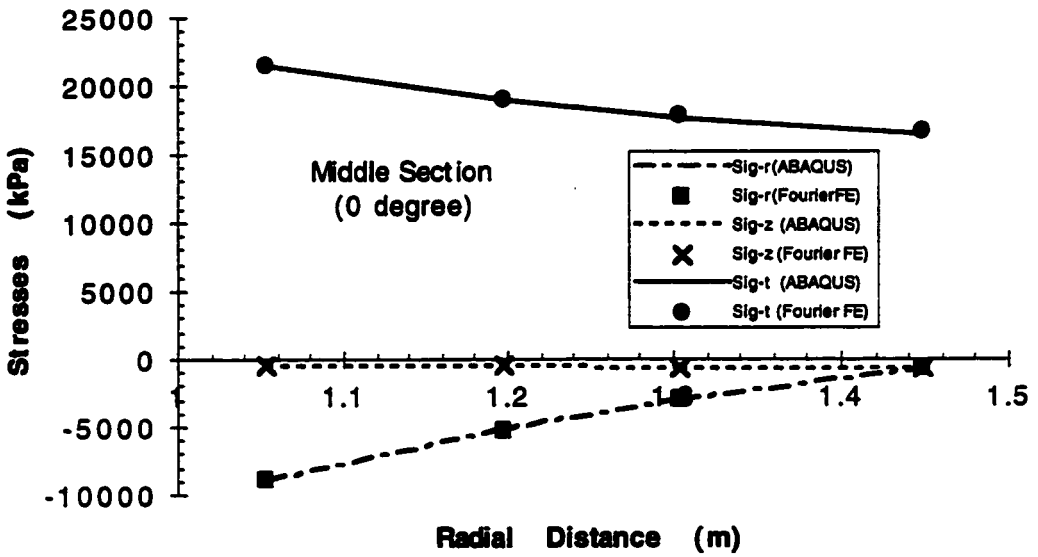

Fig. 5.12 Radial Direction Stress Comparison for Non-uniform Elastic Load
(Mid Section 0 Degree Location)

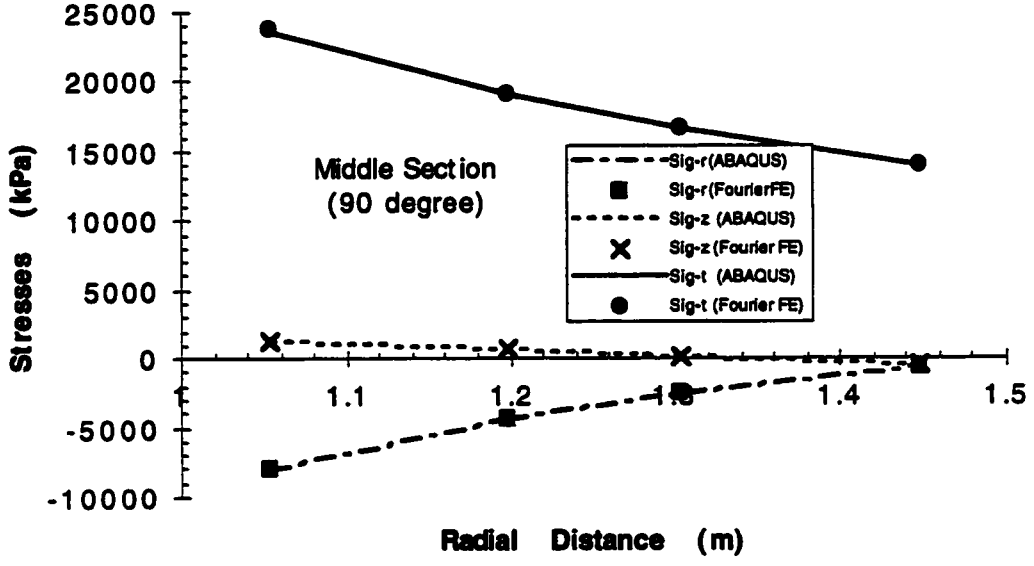

Fig. 5.13 Radial Direction Stress Comparison for Non-uniform Elastic Load
(Mid Section 90 Degree Location)

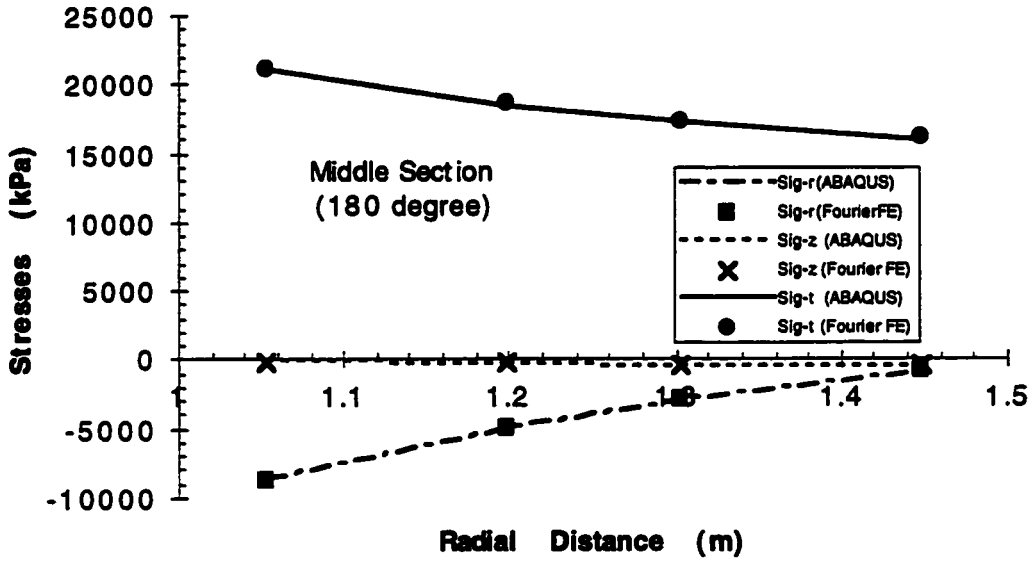

Fig. 5.14 Radial Direction Stress Comparison for Non-uniform Elastic Load
(Mid Section 180 Degree Location)

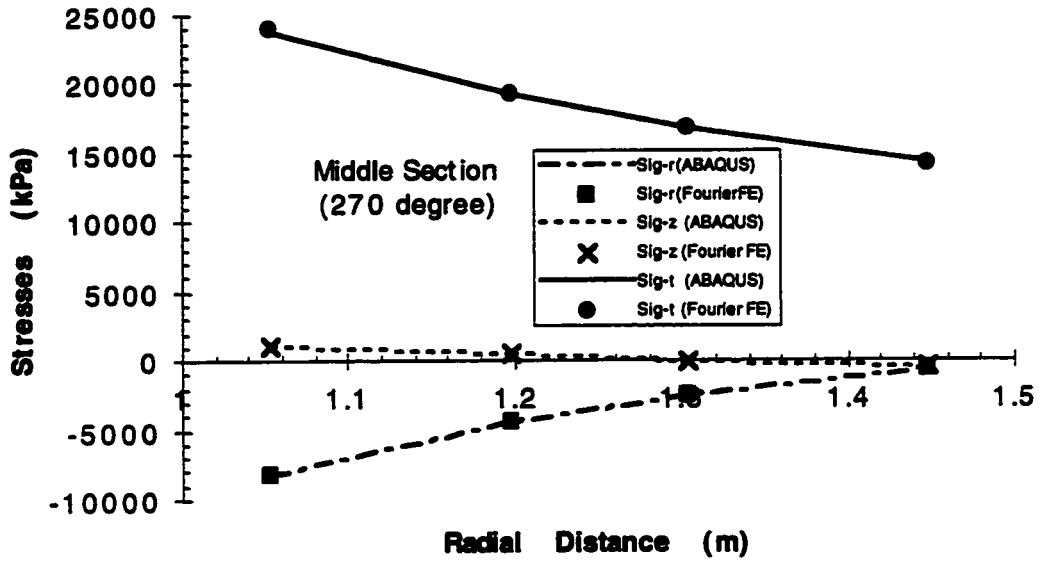

Fig. 5.15 Radial Direction Stress Comparison for Non-uniform Elastic Load
(Mid Section 270 Degree Location)

Mildly non-symmetric (for Drucker-Prager), load distribution

$$P_r = [192+3.2\cos(t)-1.6\sin(t)+6.4\cos(2t)+4.8\sin(2t)]*10^3$$

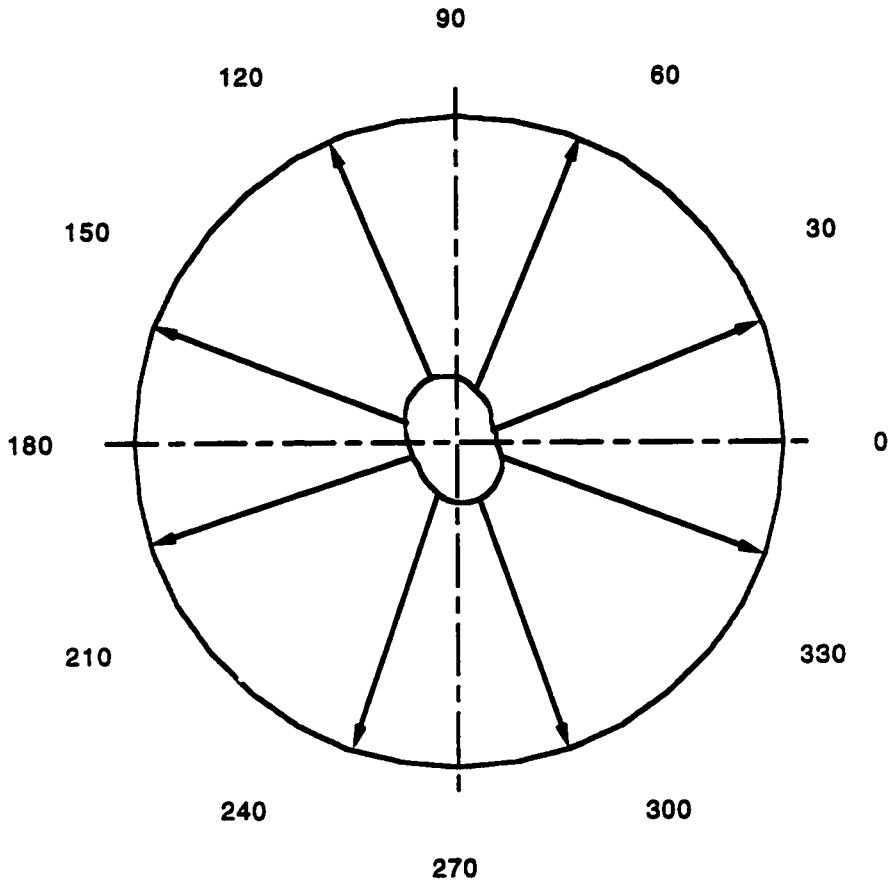

Fig. 5.16 Load Distribution for Mildly Non-symmetric Plastic Case

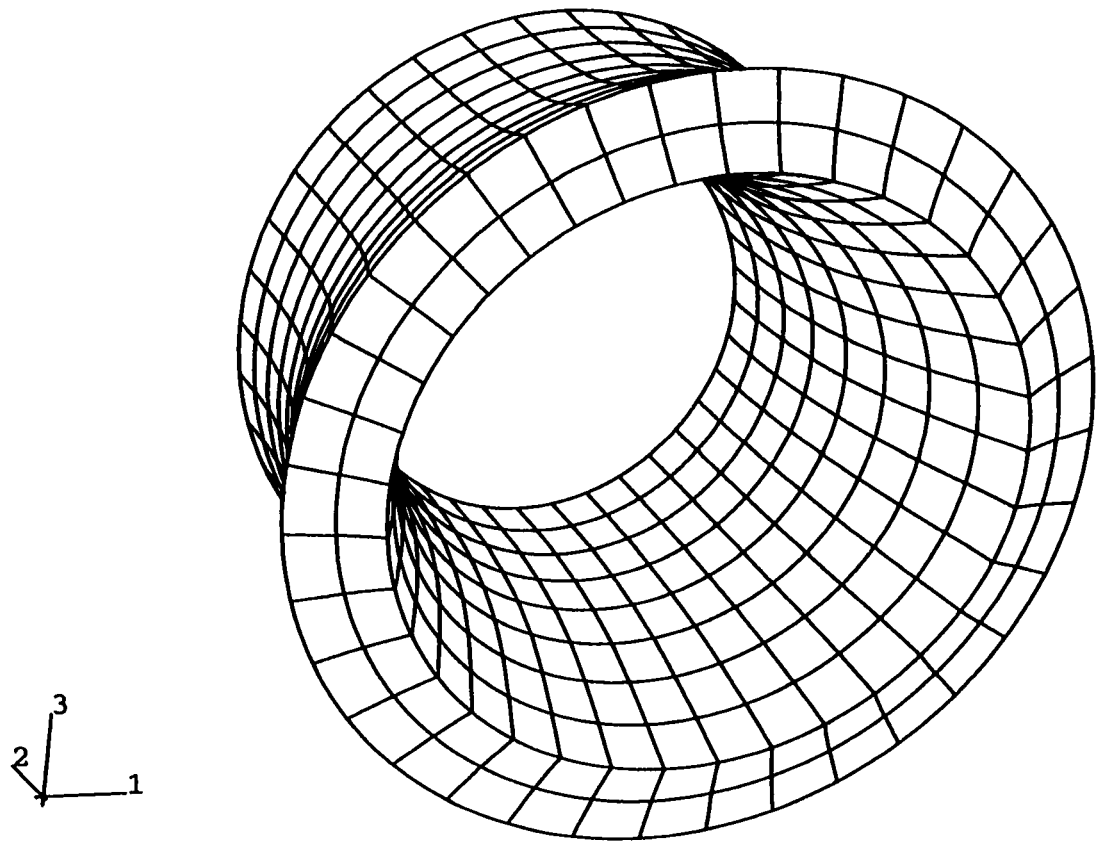

Fig. 5.17 Deformed Mesh under Mildly Non-axisymmetric Plastic Load

Fig. 5.18 Yield Zone under Mildly Non-symmetric Plastic Load
(Free End, Fourier FEM)

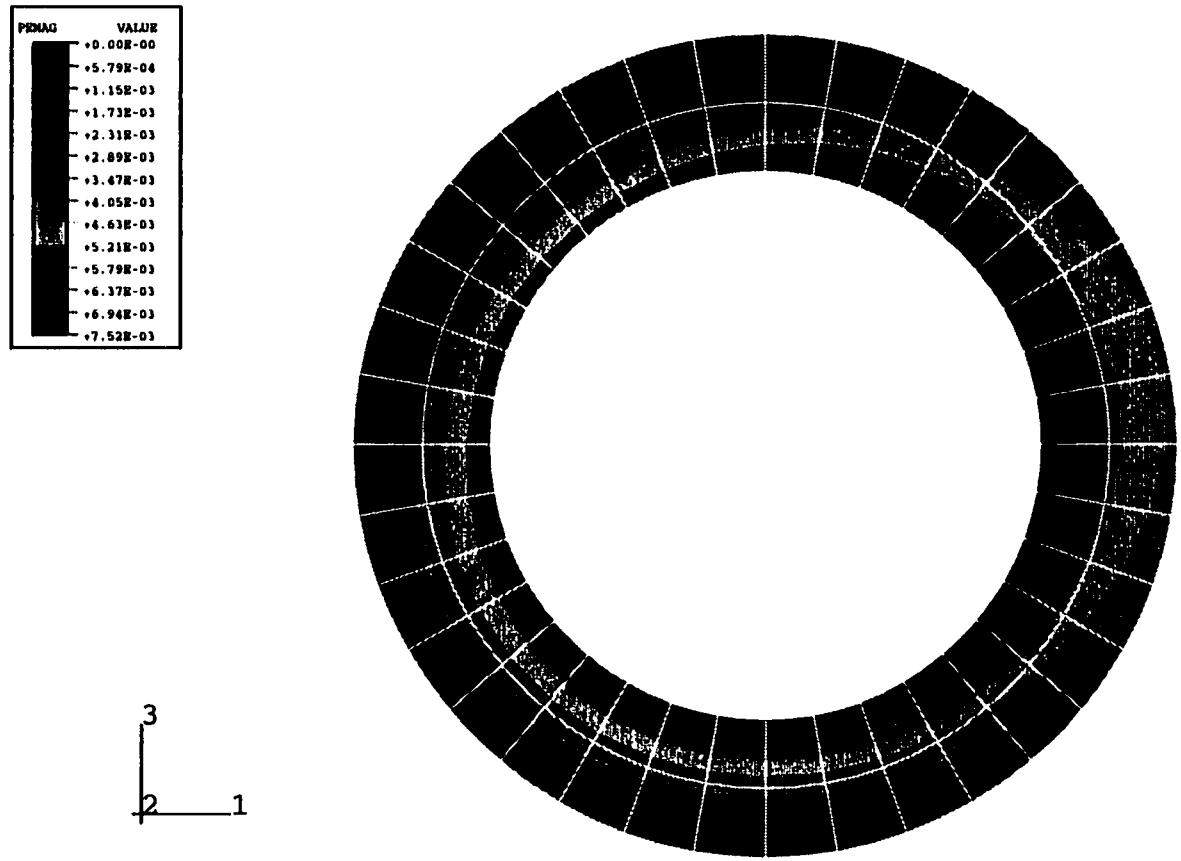

Fig. 5.19 Yield Zone under Mildly Non-symmetric Plastic Load
(Free End, ABAQUS)

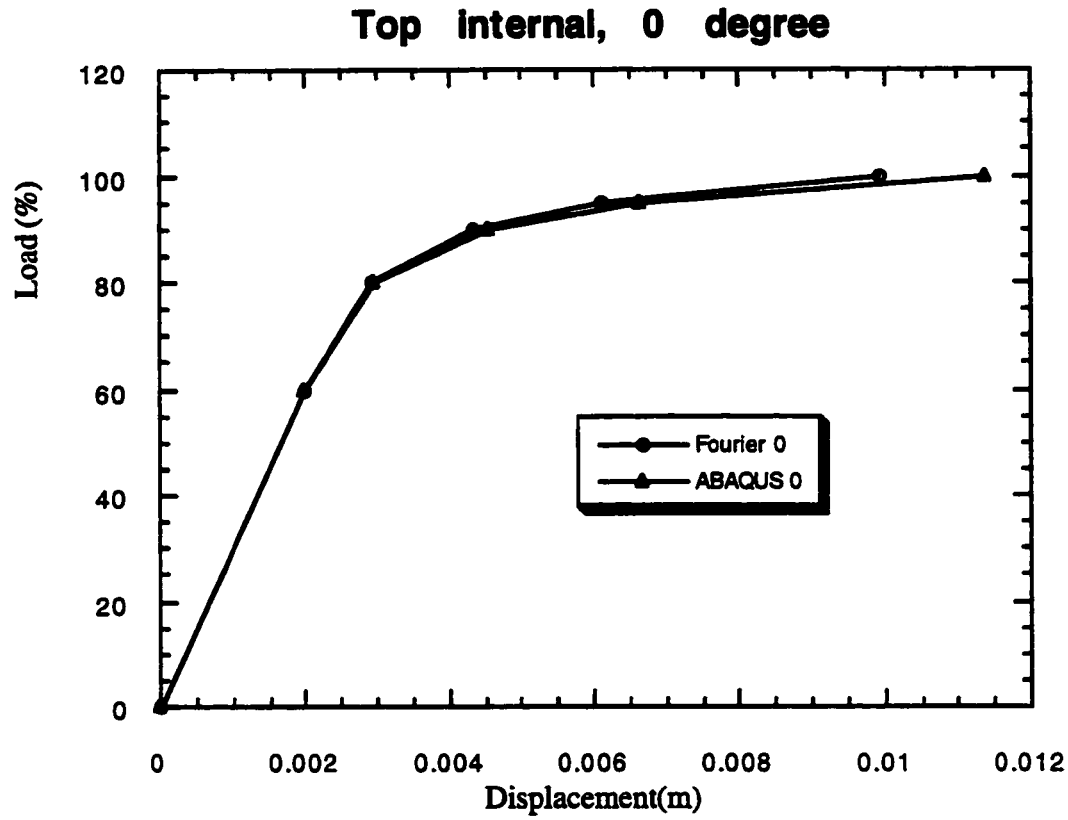

Fig. 5.20 Load vs. Displacement for Mildly Non-symmetric Plastic Case at 0° Location of Free End

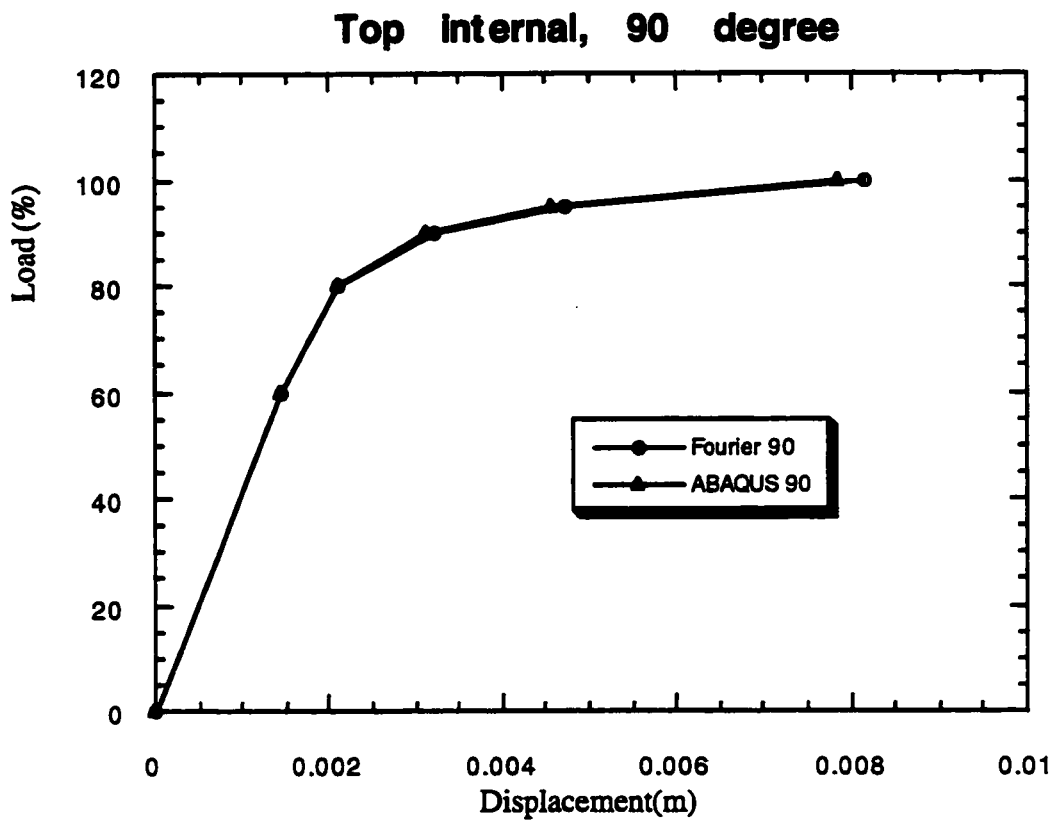

Fig. 5.21 Load vs. Displacement for Mildly Non-symmetric Plastic Case at 90° Location of Free End

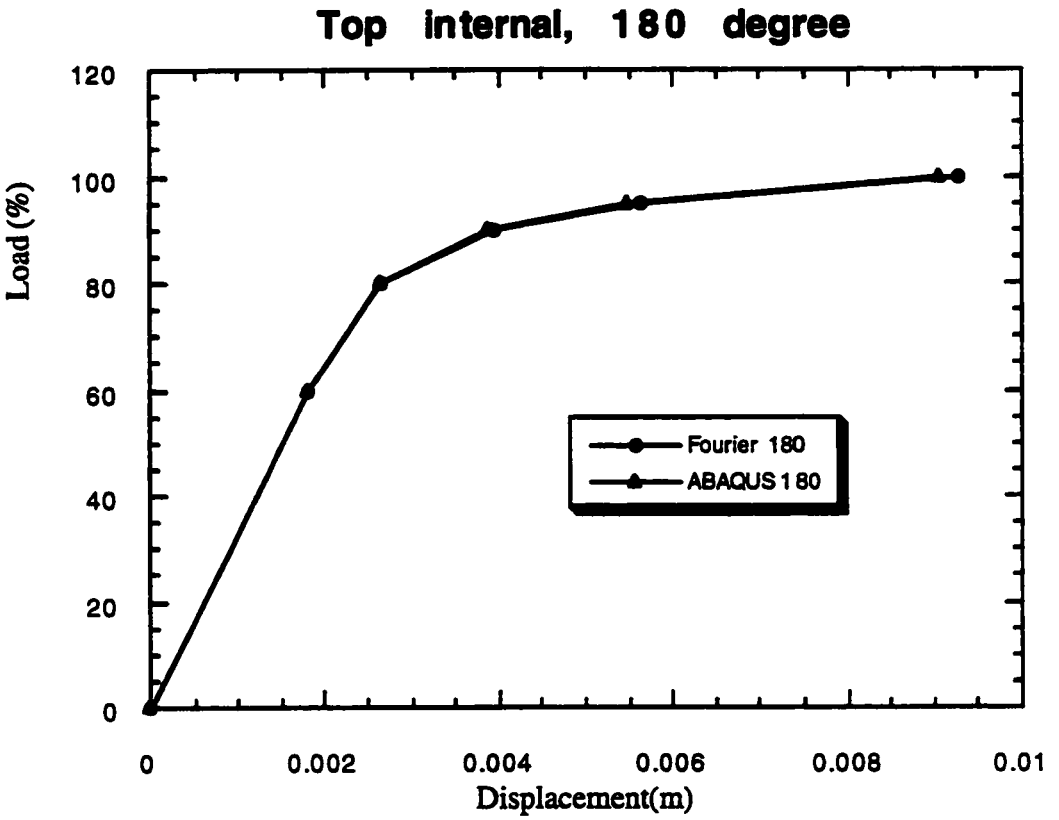

Fig. 5.22 Load vs. Displacement for Mildly Non-symmetric Plastic Case at 180° Location of Free End

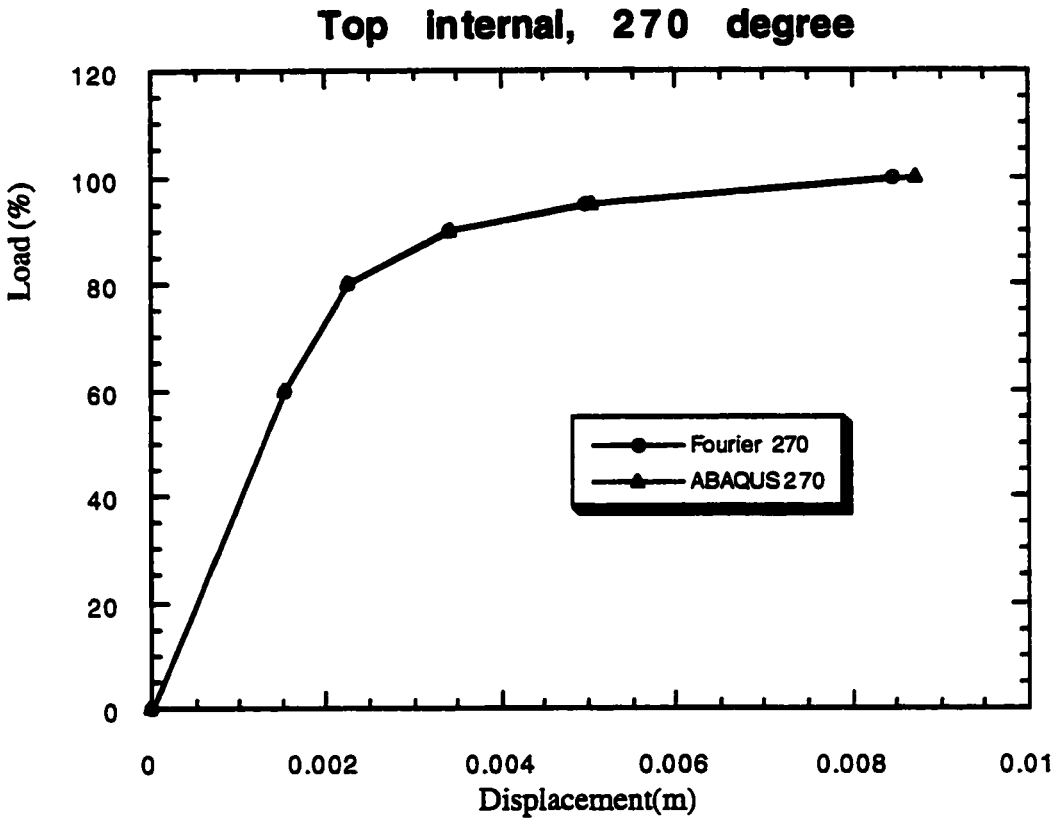

Fig. 5.23 Load vs. Displacement for Mildly Non-symmetric Plastic Case at 270° Location of Free End

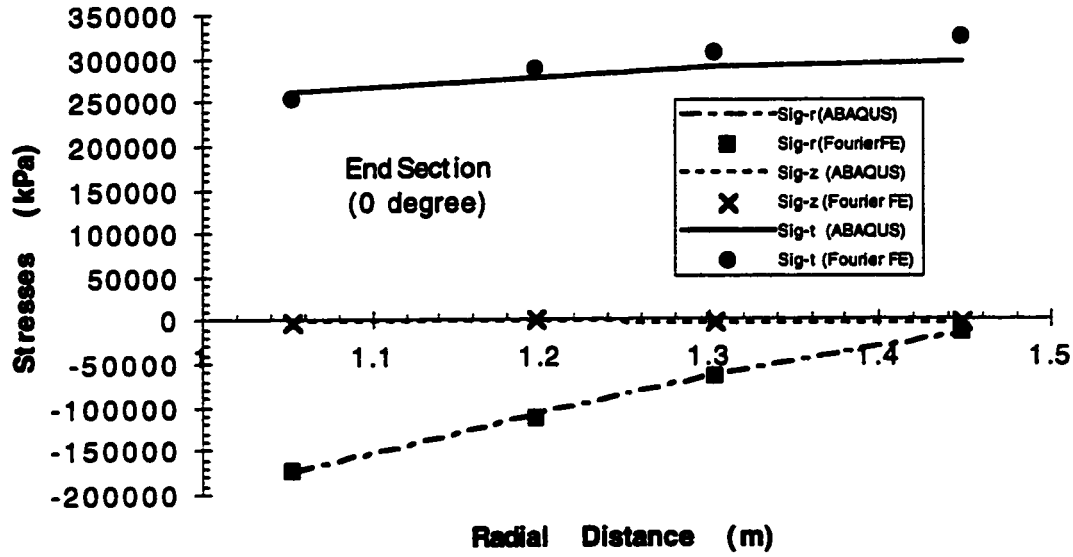

Fig. 5.24 Radial Direction Stress Comparison for Mildly Non-symmetric Plastic Load (Free End 0 degree Location)

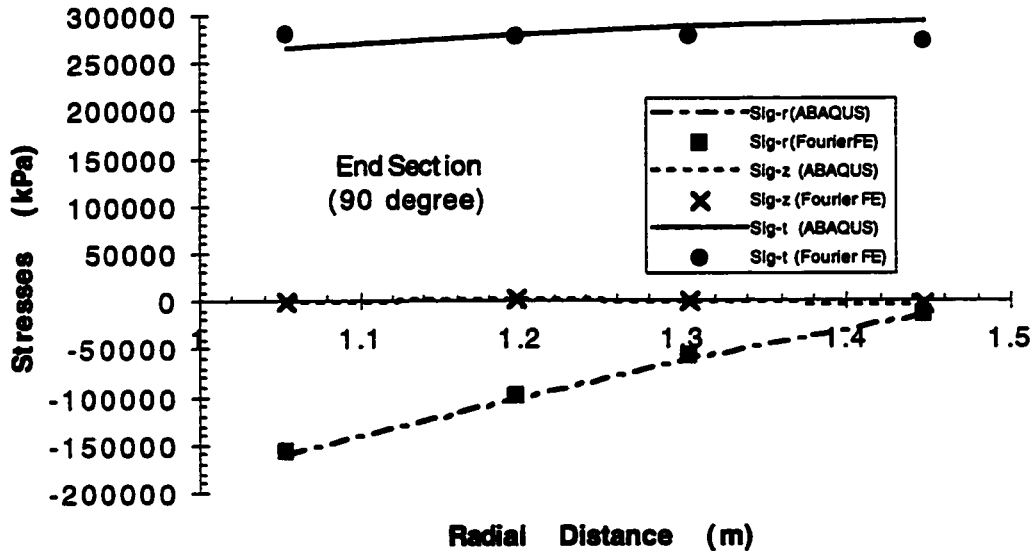

Fig. 5.25 Radial Direction Stress Comparison for Mildly Non-symmetric Plastic Load (Free End 90 Degree Location)

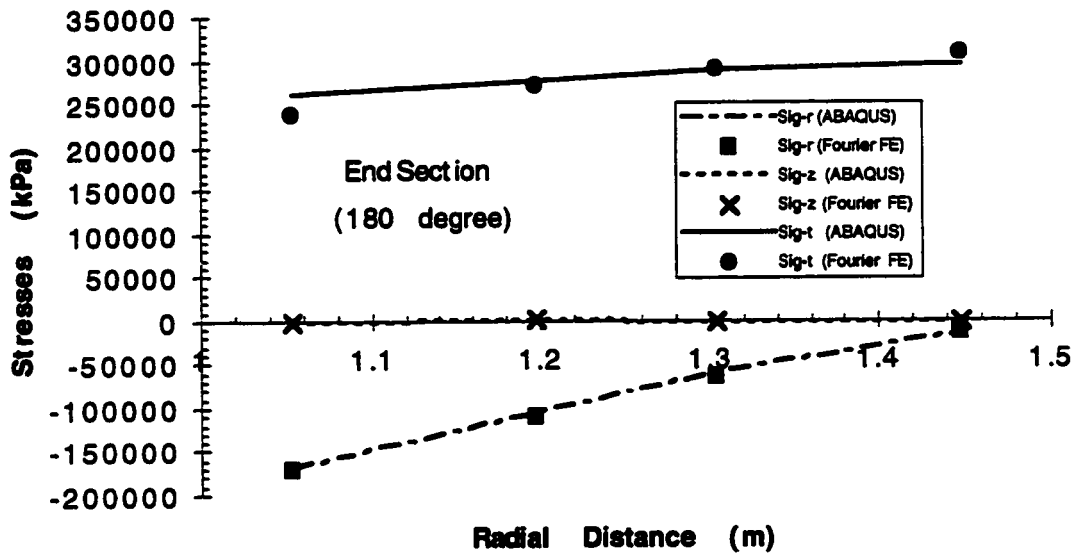

Fig. 5.26 Radial Direction Stress Comparison for Mildly Non-symmetric Plastic Load (Free End 180 Degree Location)

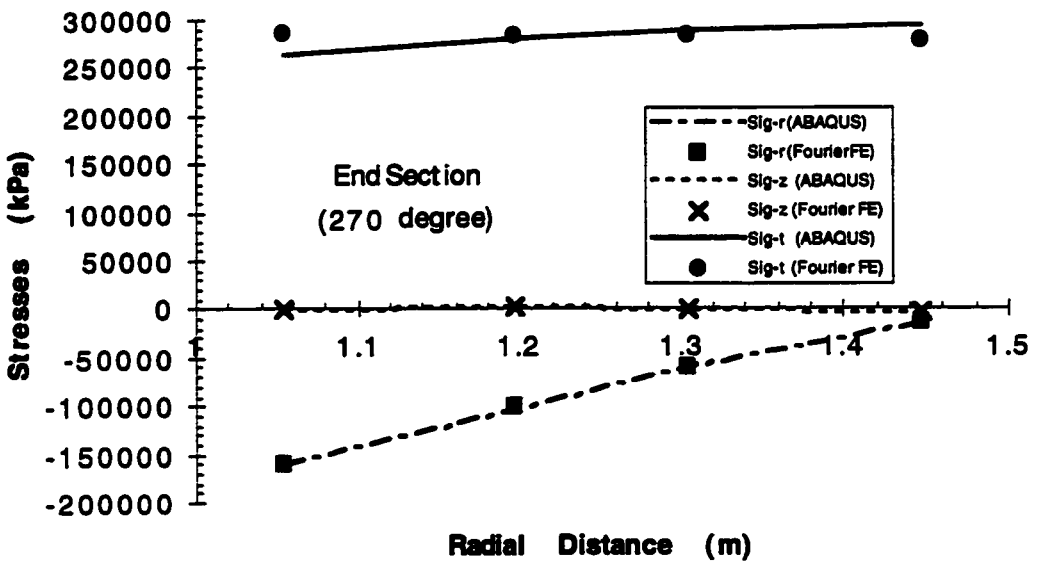

Fig. 5.27 Radial Direction Stress Comparison for Mildly Non-symmetric Plastic Load (Free End 270 Degree Location)

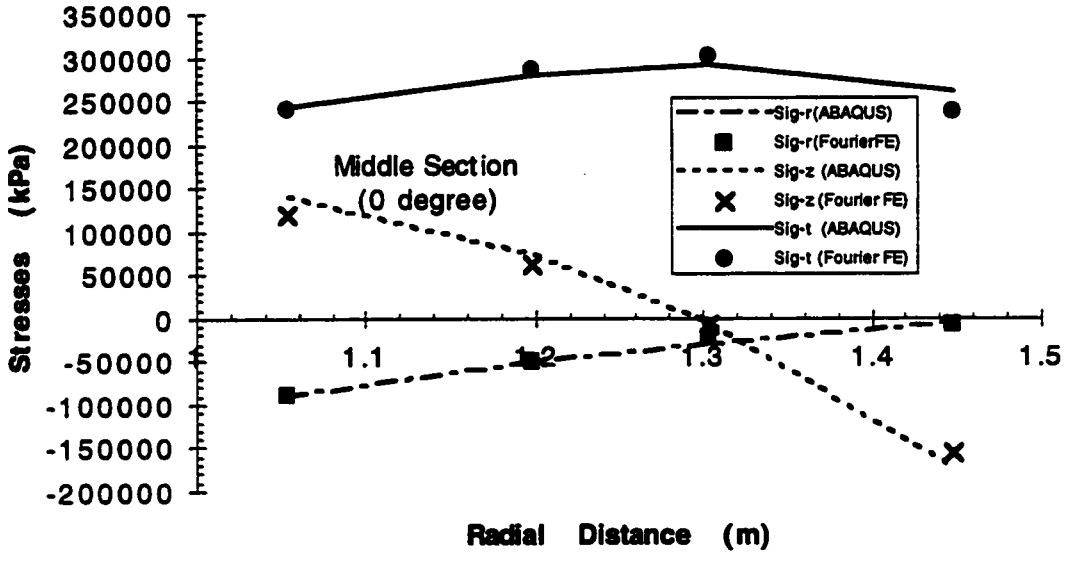

Fig. 5.28 Radial Direction Stress Comparison for Mildly Non-symmetric Plastic Load (Mid Section 0 Degree Location)

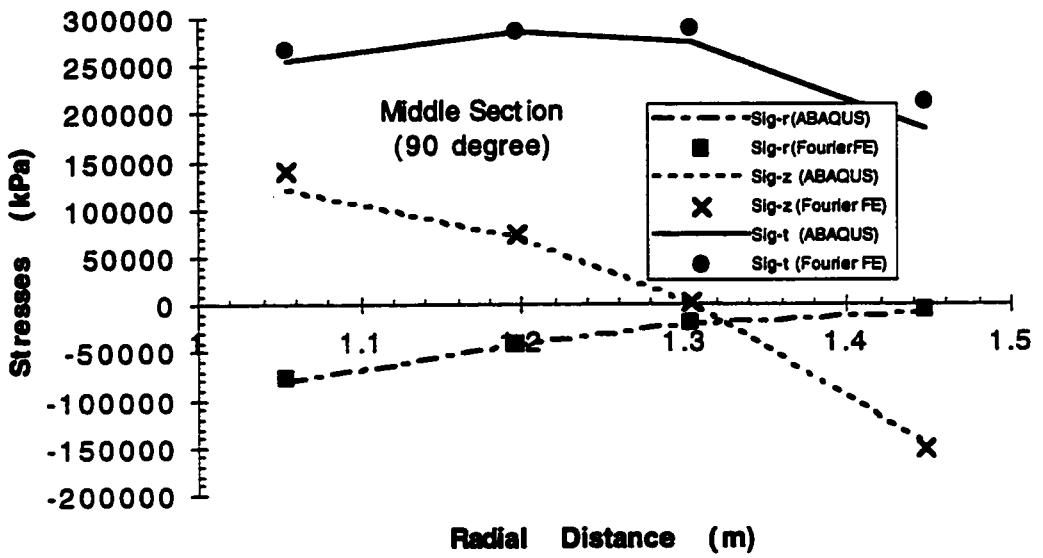

Fig. 5.29 Radial Direction Stress Comparison for Mildly Non-symmetric Plastic Load (Mid Section 90 Degree Location)

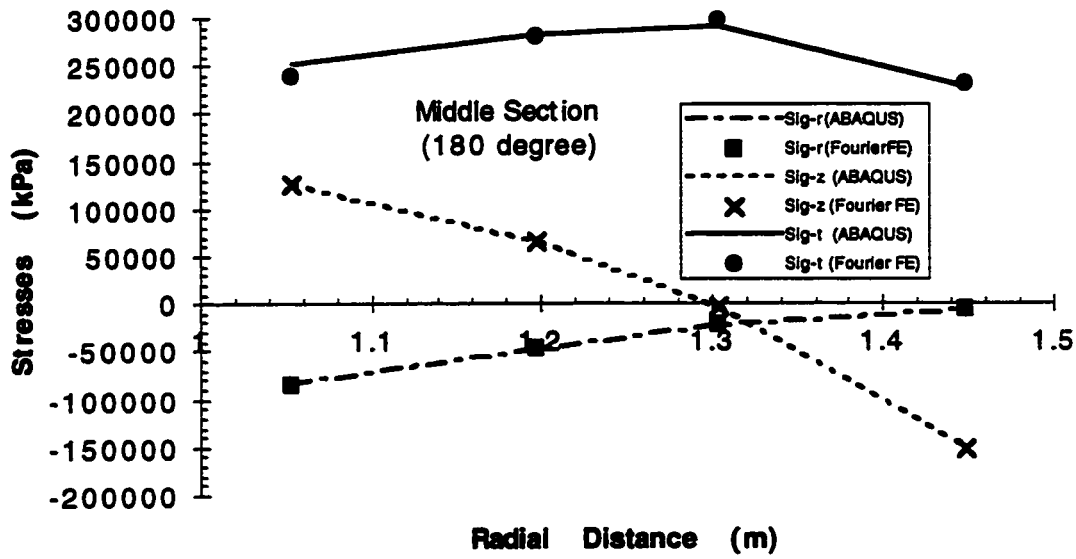

Fig. 5.30 Radial Direction Stress Comparison for Mildly Non-symmetric Plastic Load (Mid Section 180 Degree Location)

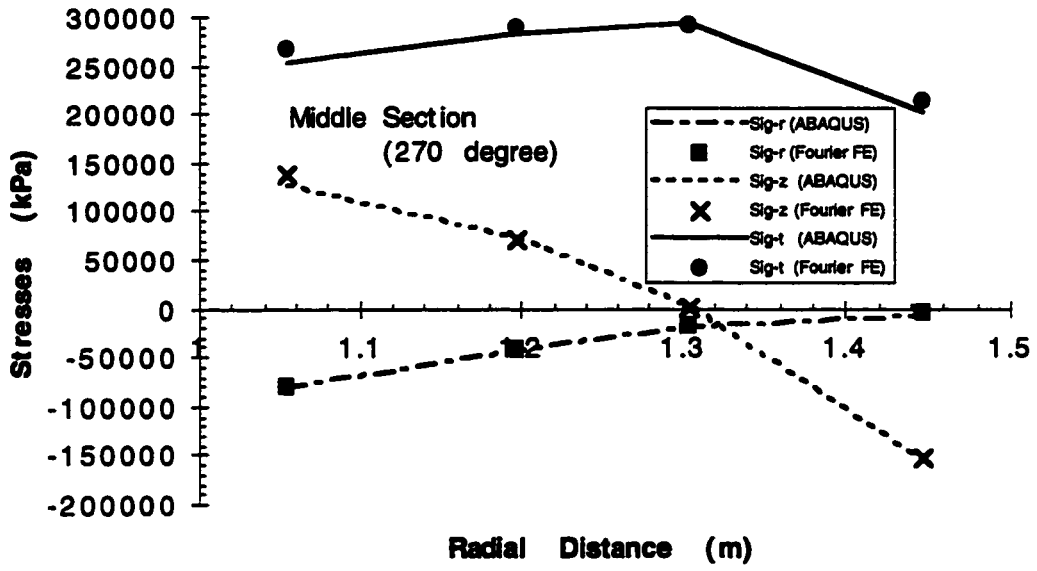

Fig. 5.31 Radial Direction Stress Comparison for Mildly Non-symmetric Plastic Load (Mid Section 270 Degree Location)

Extremely non-symmetric (for Drucker-Prager), load distribution

$$P_r = [10.368+4.8\cos(t)-2.4\sin(t)+9.6\cos(2t)+7.2\sin(2t)]*10^4$$

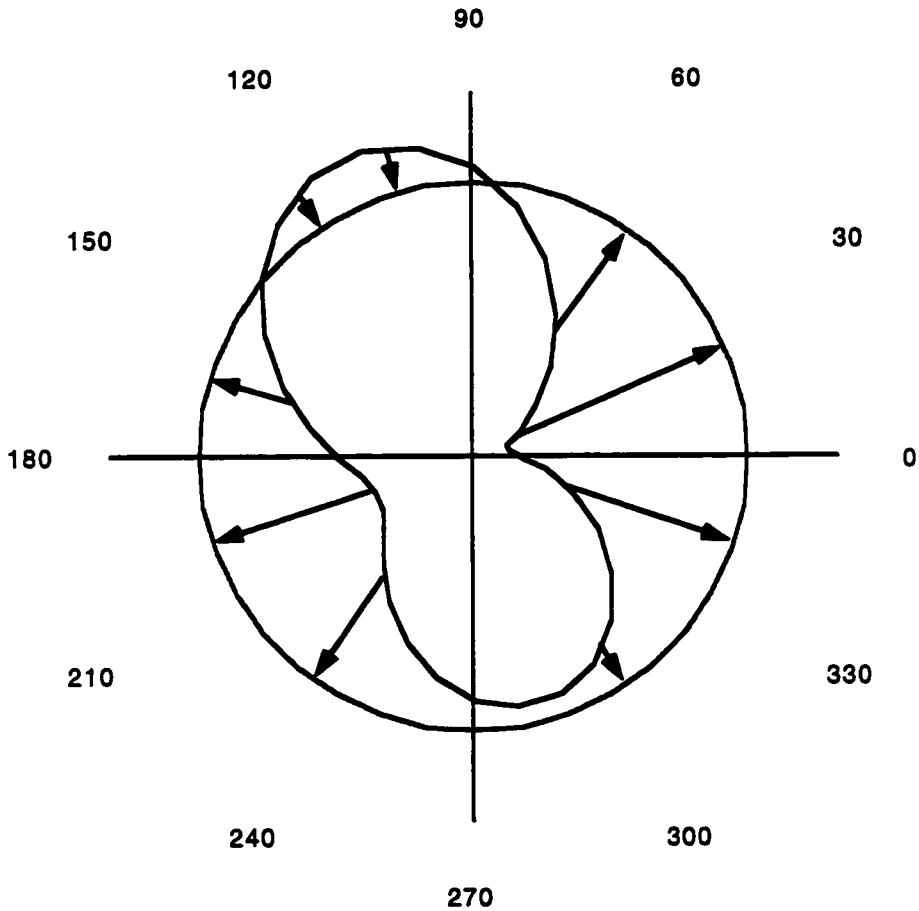

Fig. 5.32 Load Distribution for Extremely Non-symmetric Case

ABAQUS

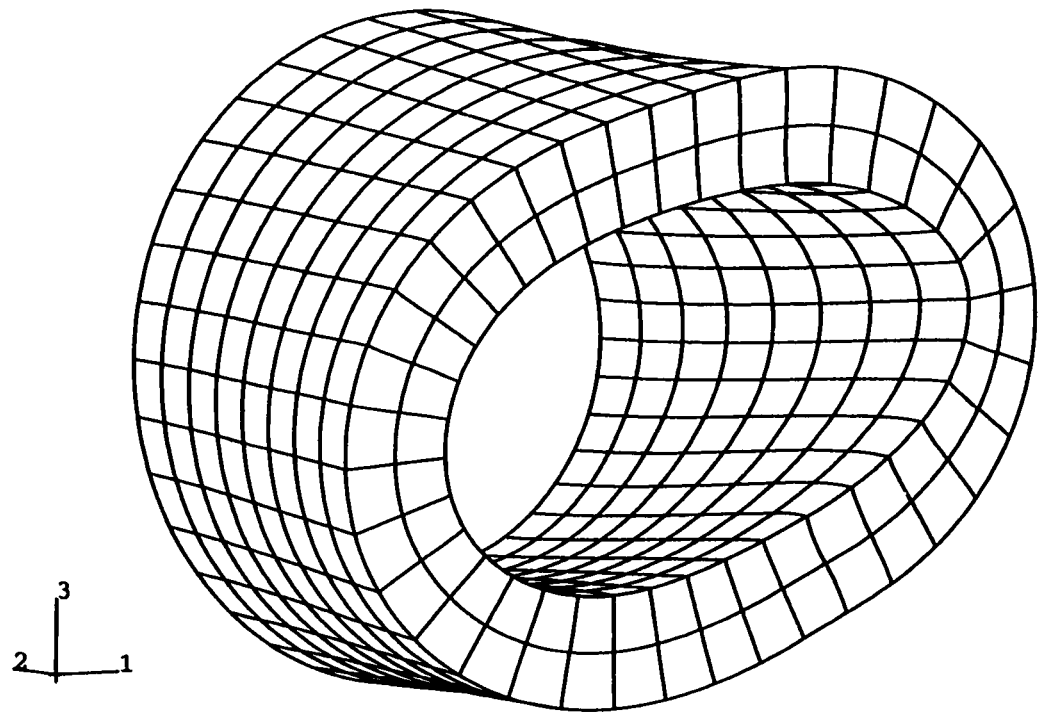

Fig. 5.33 Deformed Mesh under Extremely Non-symmetric Plastic Load

Fig. 5.34 Yield Zone under Extremely Non-symmetric Plastic Load
(Free End, Fourier FEM)

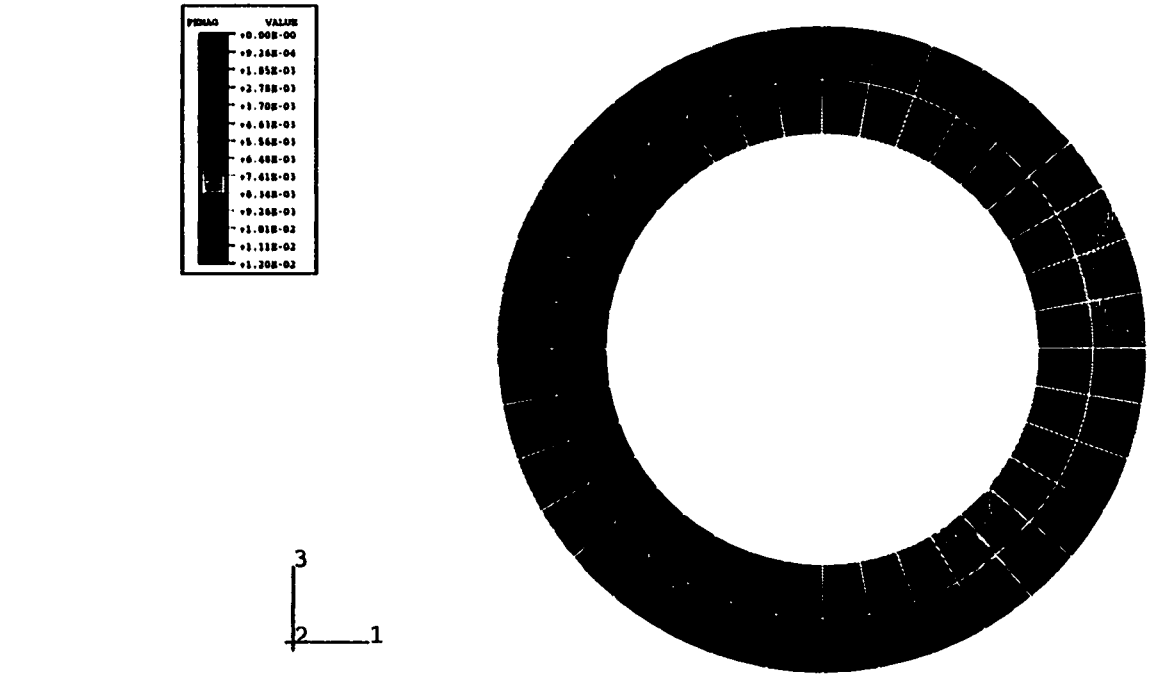

Fig. 5.35 Yield Zone under Extremely Non-symmetric Plastic Load
(Free End, ABAQUS)

Fig. 5.36 Yield Zone under Extremely Non-symmetric Plastic Load
(Fixed End, Fourier FEM)

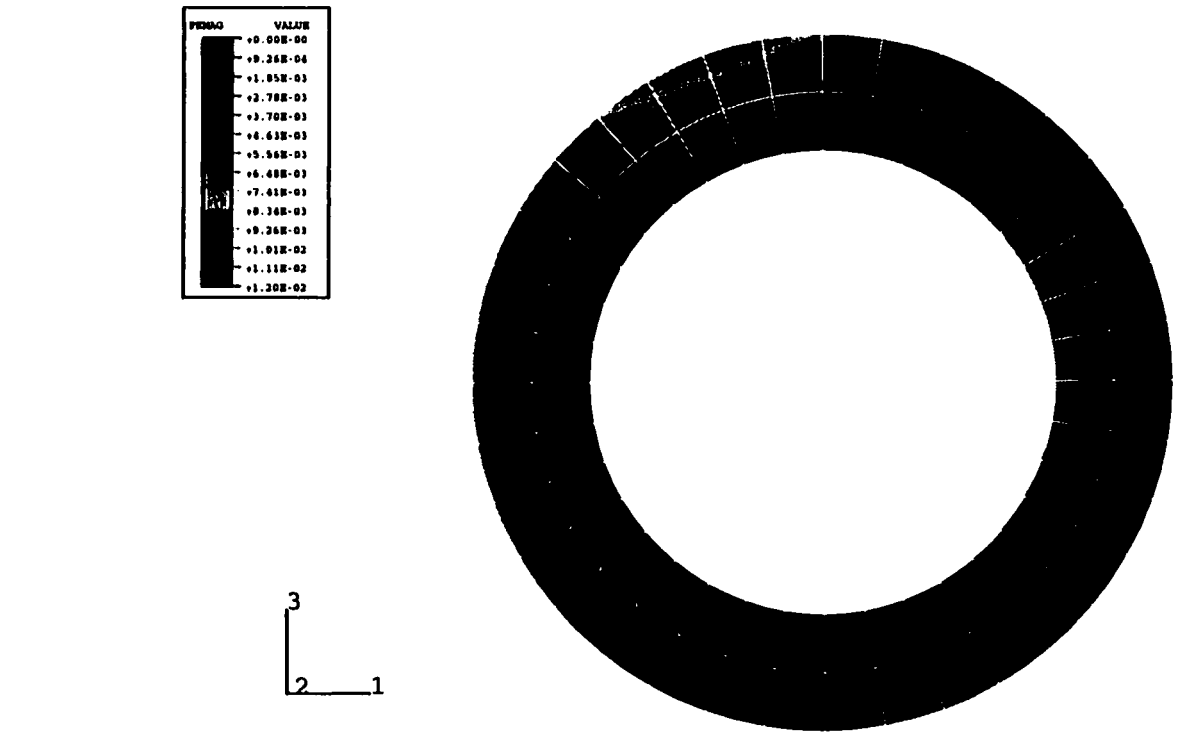

Fig. 5.37 Yield Zone under Extremely Non-symmetric Plastic Load
(Fixed End, ABAQUS)

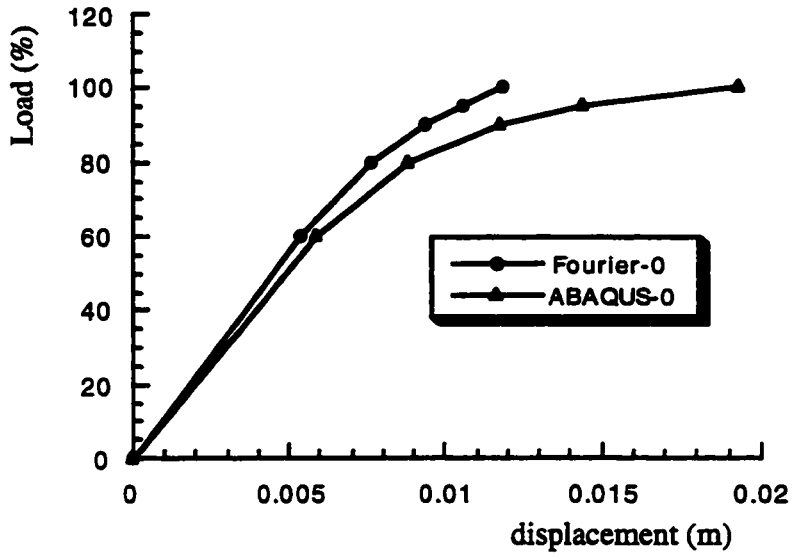

Fig. 5.38 Load vs. Displacement for Extremely Non-symmetric Plastic Case at 0° Location of Free End

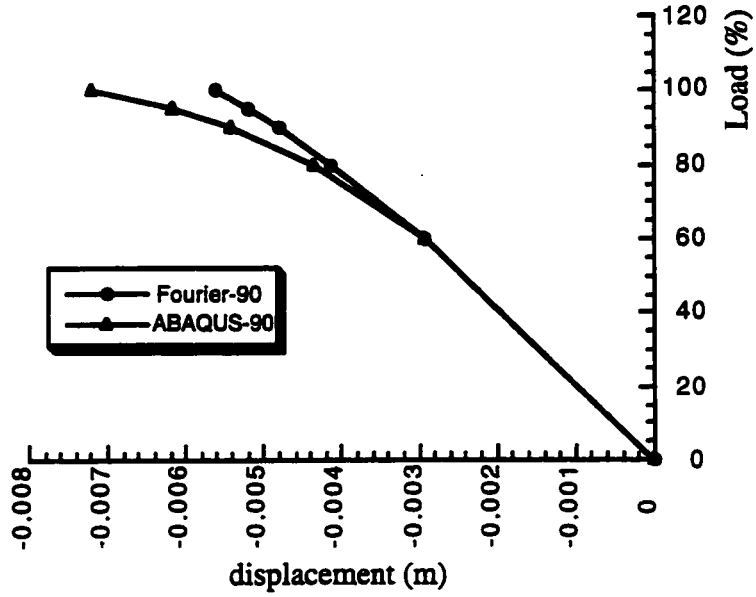

Fig. 5.39 Load vs. Displacement for Extremely Non-symmetric Plastic Case at 90° Location of Free End

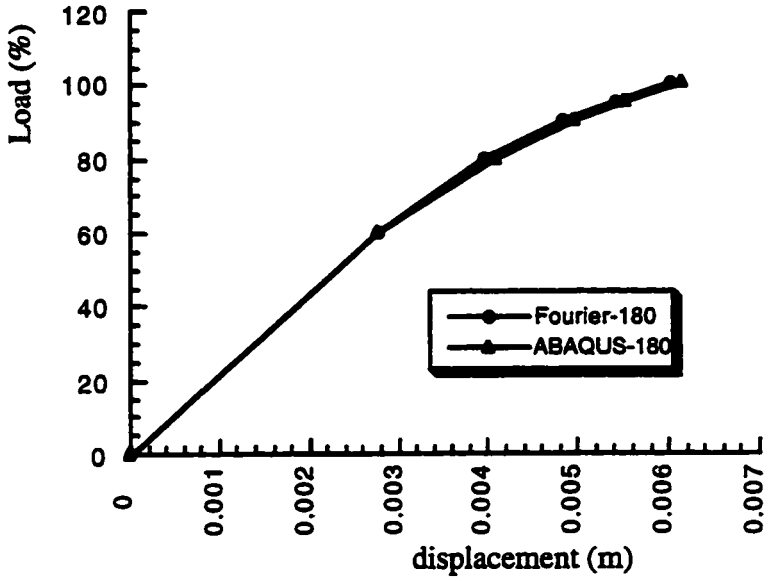

Fig. 5.40 Load vs. Displacement for Extremely Non-symmetric Plastic Case at 180° Location of Free End

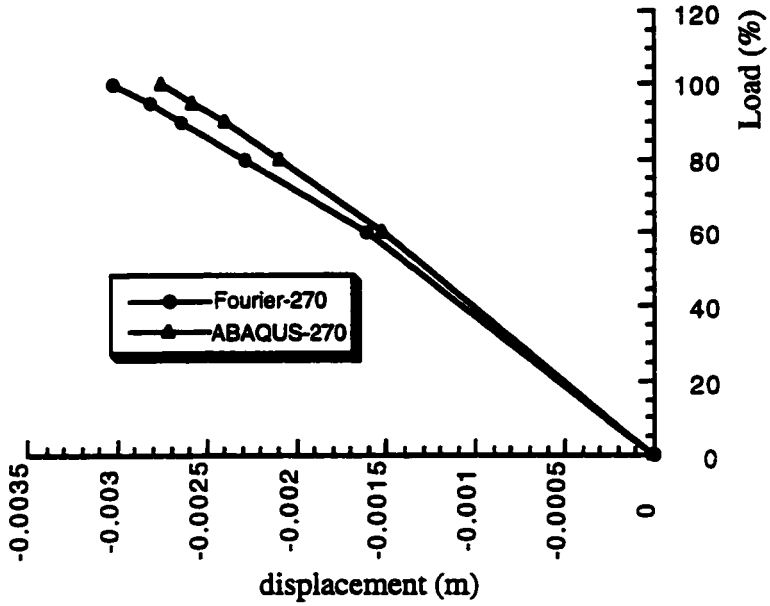

Fig. 5.41 Load vs. Displacement for Extremely Non-symmetric Plastic Case at 270° Location of Free End

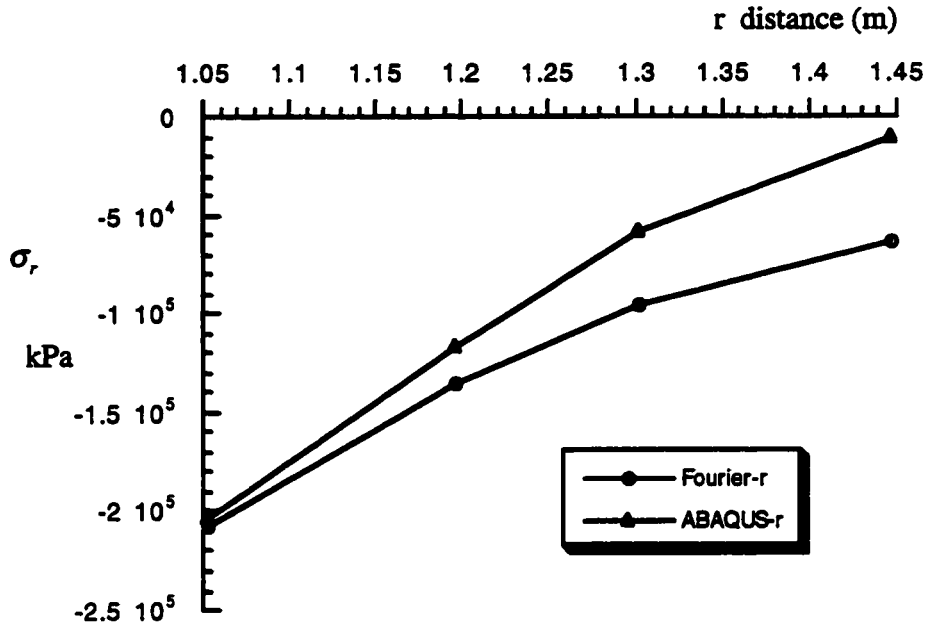

Fig. 5.42 Stress σ_r at 0° Location of Free End
Extremely Non-symmetric Load

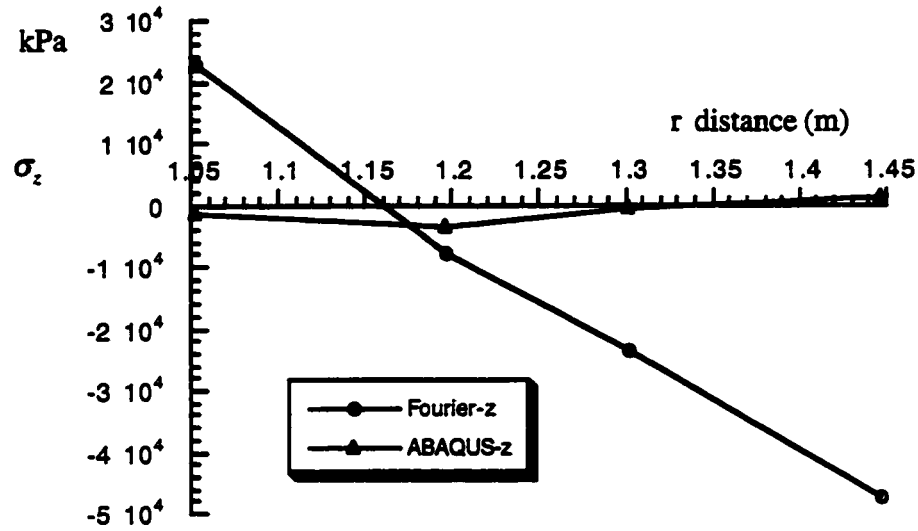

Fig. 5.43 Stress σ_z at 0° Location of Free End
Extremely Non-symmetric Load

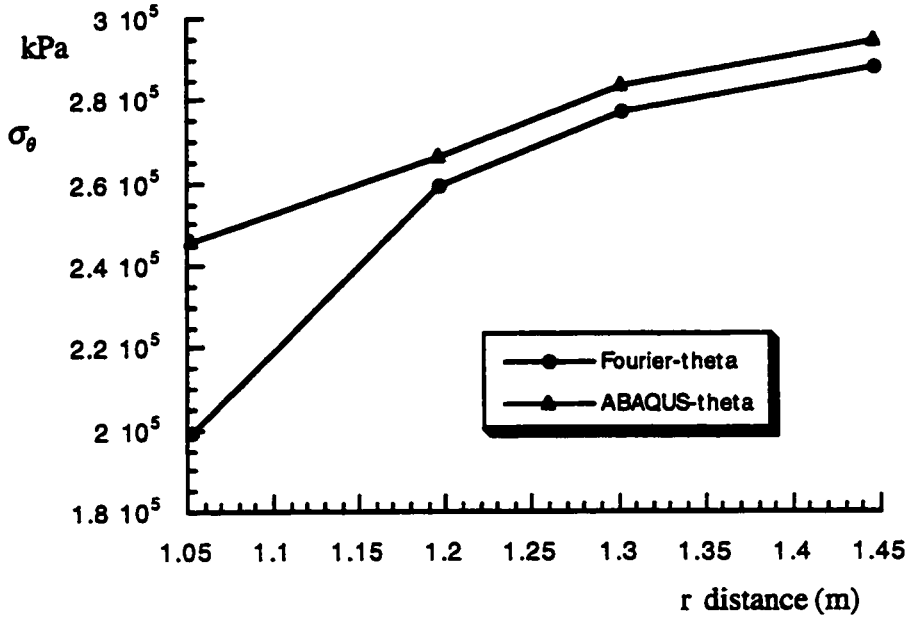

Fig. 5.44 Stress σ_θ at 0° Location of Free End
Extremely Non-symmetric Load

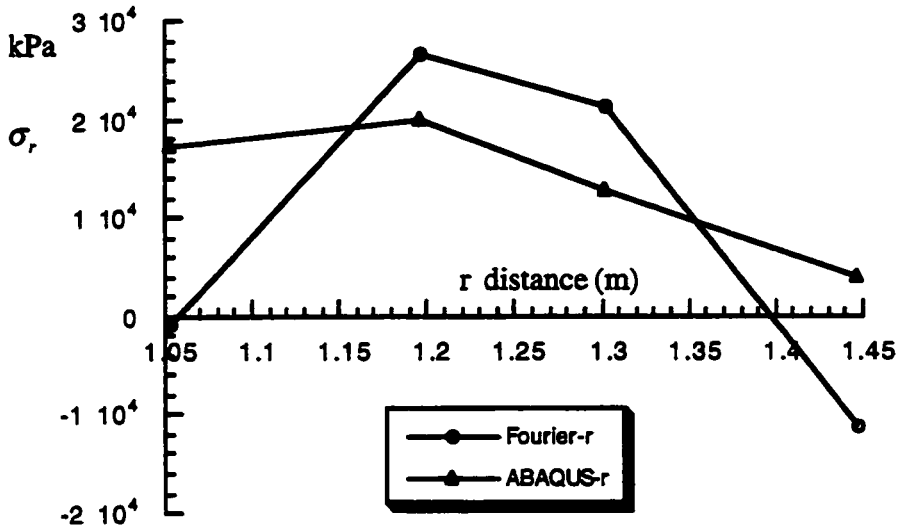

Fig. 5.45 Stress σ_r at 90° Location of Free End
Extremely Non-symmetric Load

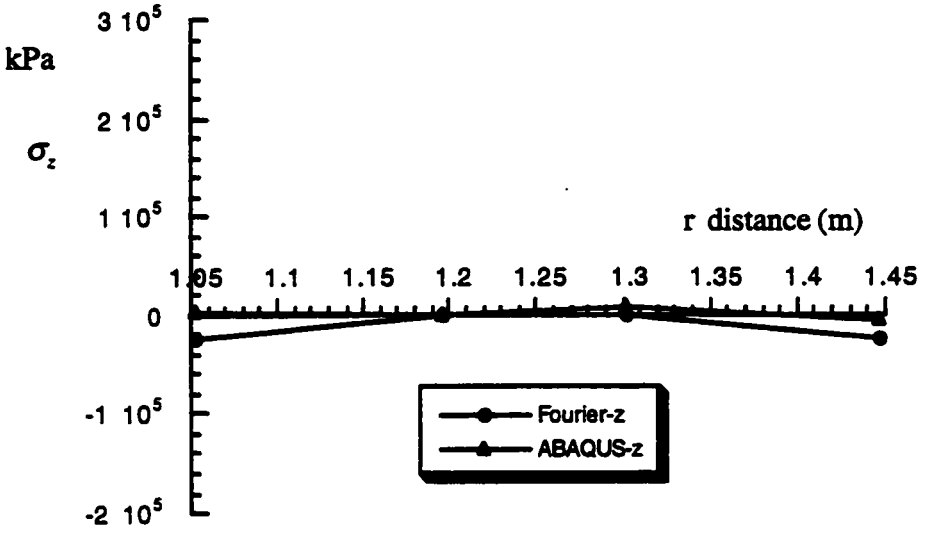

Fig. 5.46 Stress σ_z at 90° Location of Free End
Extremely Non-symmetric Load

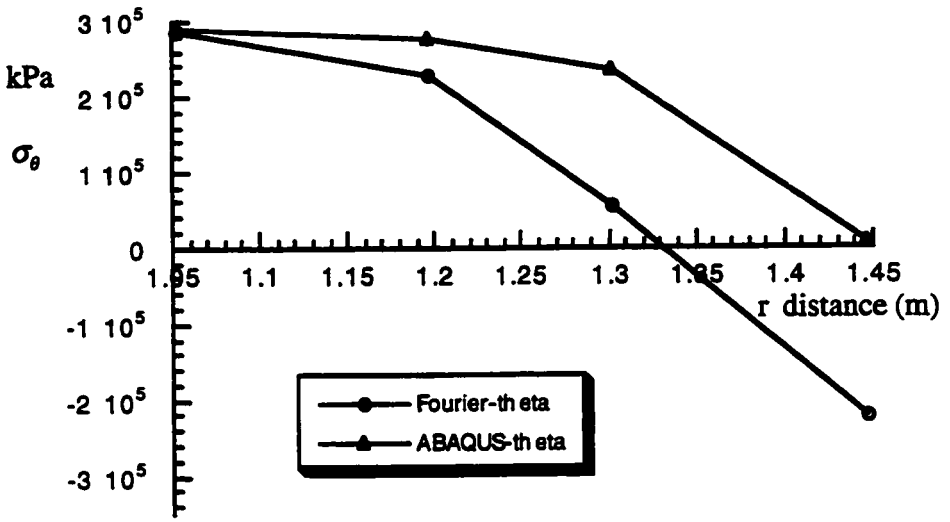

Fig. 5.47 Stressσ_θ at 90° Location of Free End
Extremely Non-symmetric Load

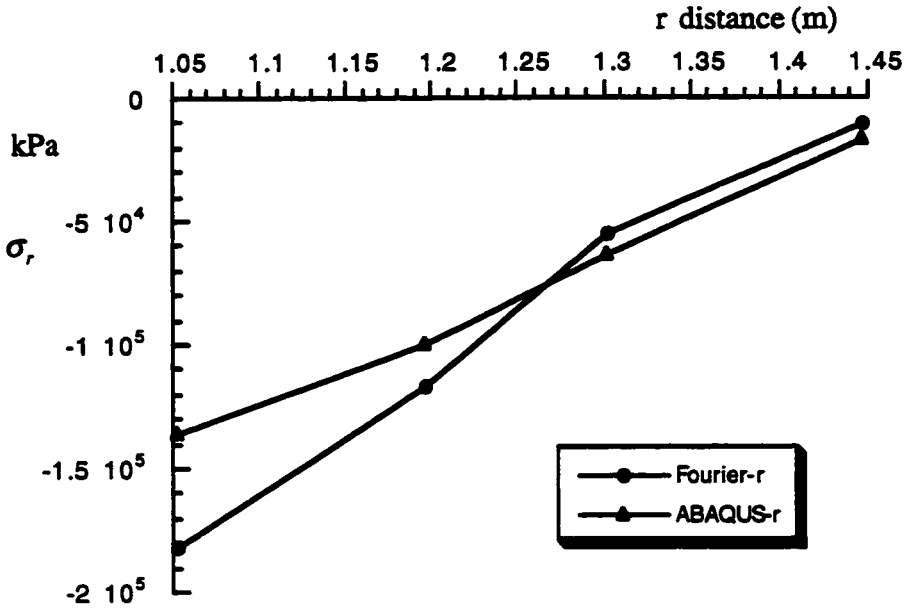

Fig. 5.48 Stress σ_r at 180° Location of Free End
Extremely Non-symmetric Load

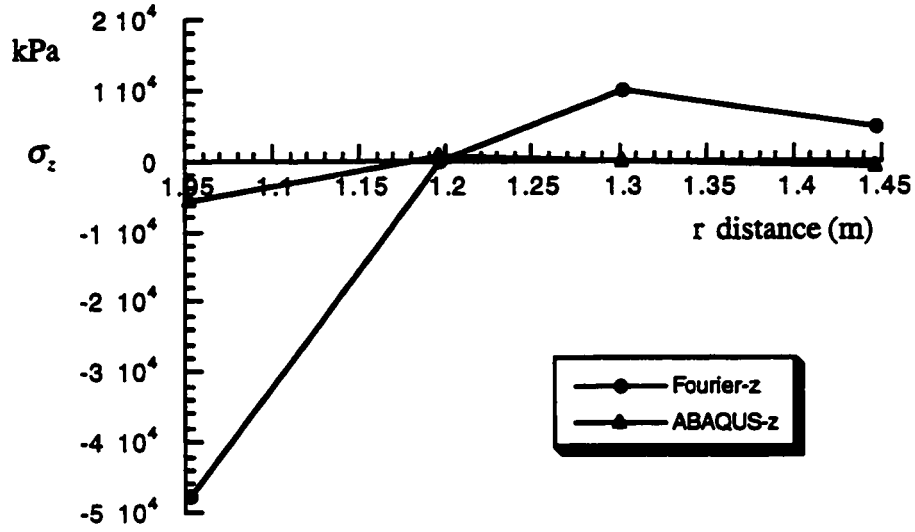

Fig. 5.49 Stress σ_z at 180° Location of Free End
Extremely Non-symmetric Load

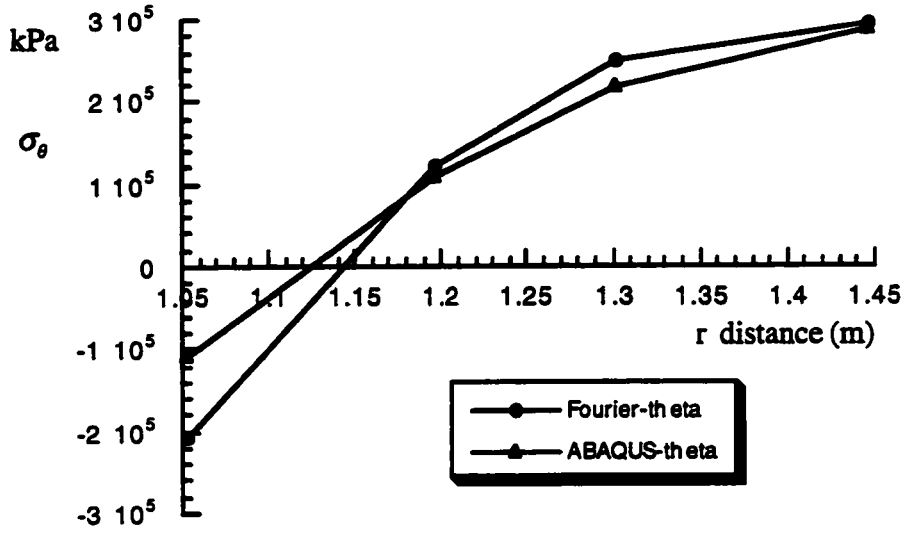

Fig. 5.50 Stress σ_θ at 180° Location of Free End
Extremely Non-symmetric Load

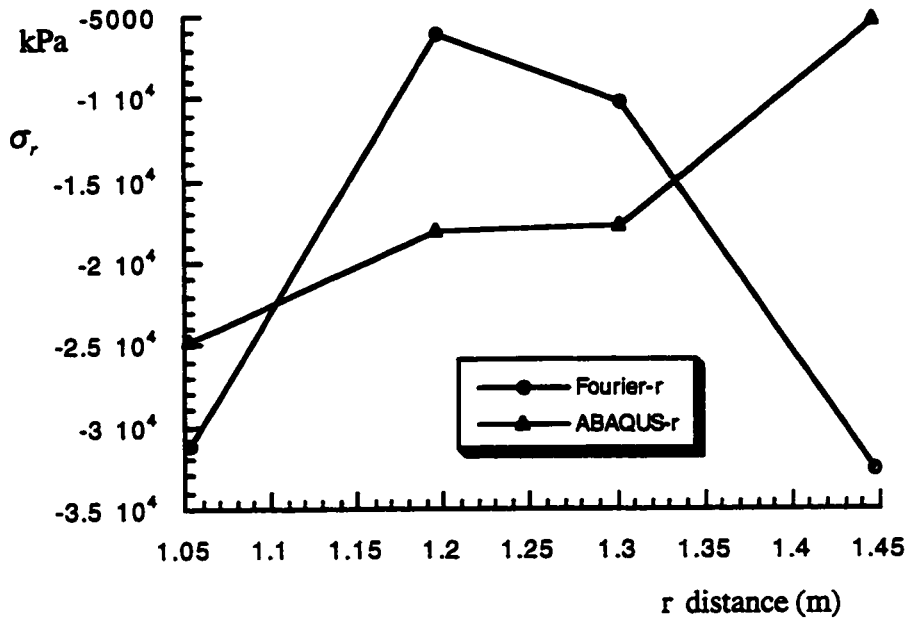

Fig. 5.51 Stress σ_r at 270° Location of Free End
Extremely Non-symmetric Load

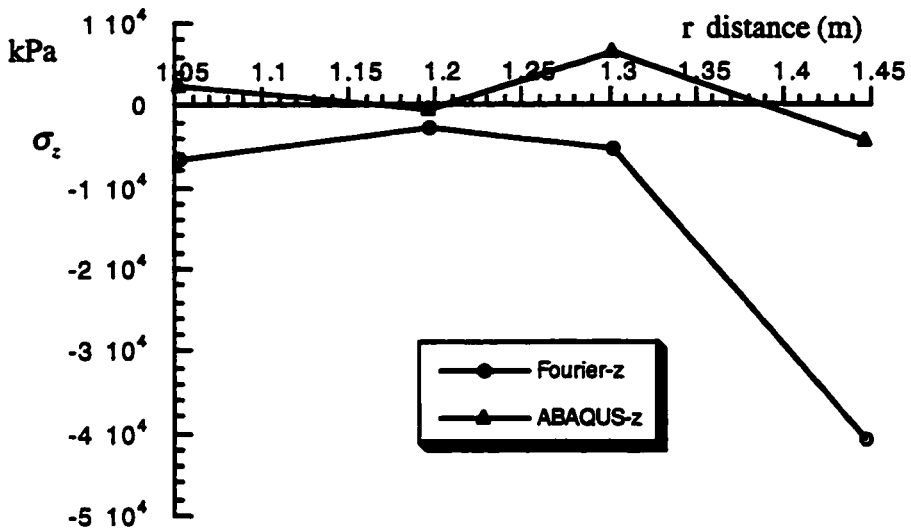

Fig. 5.52 Stress σ_z at 270° Location of Free End
Extremely Non-symmetric Load

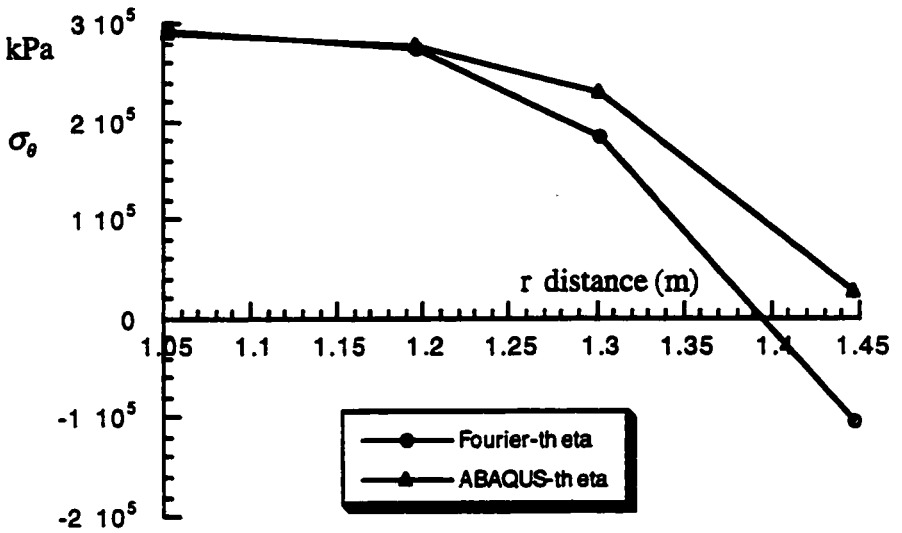

Fig. 5.53 Stress σ_θ at 270° Location of Free End
Extremely Non-symmetric Load

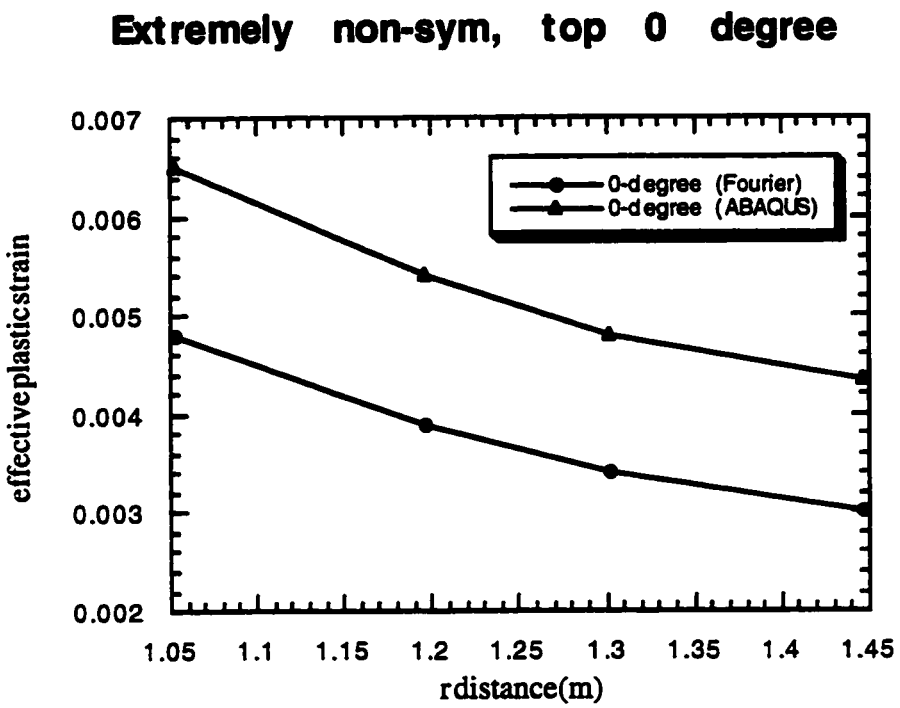

Fig. 5.54 Effective Plastic Strain at 0° Location of Free End
Extremely Non-symmetric Load

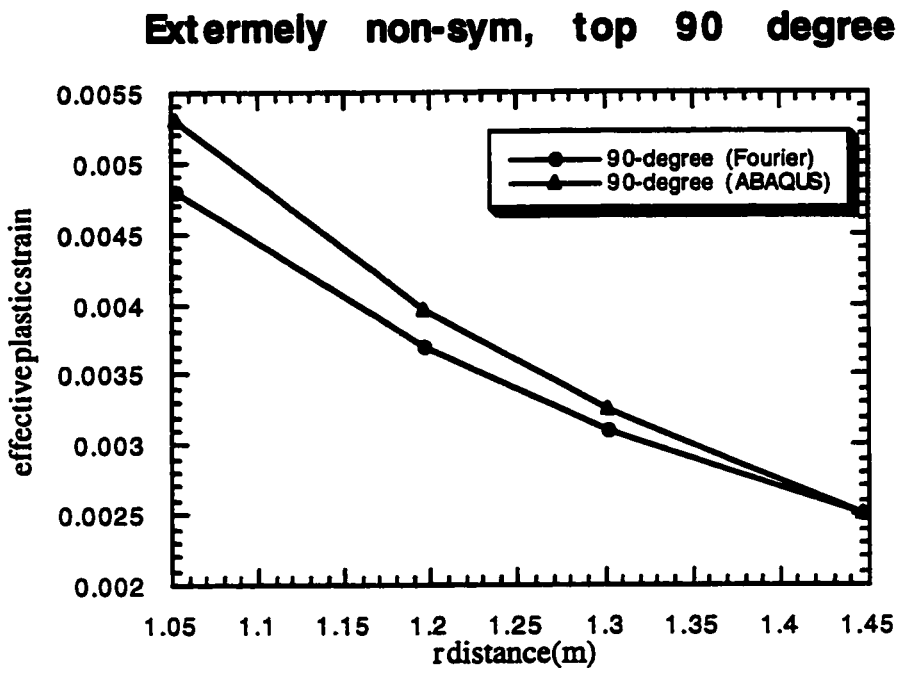

Fig. 5.55 Effective Plastic Strain at 90° Location of Free End
Extremely Non-symmetric Load

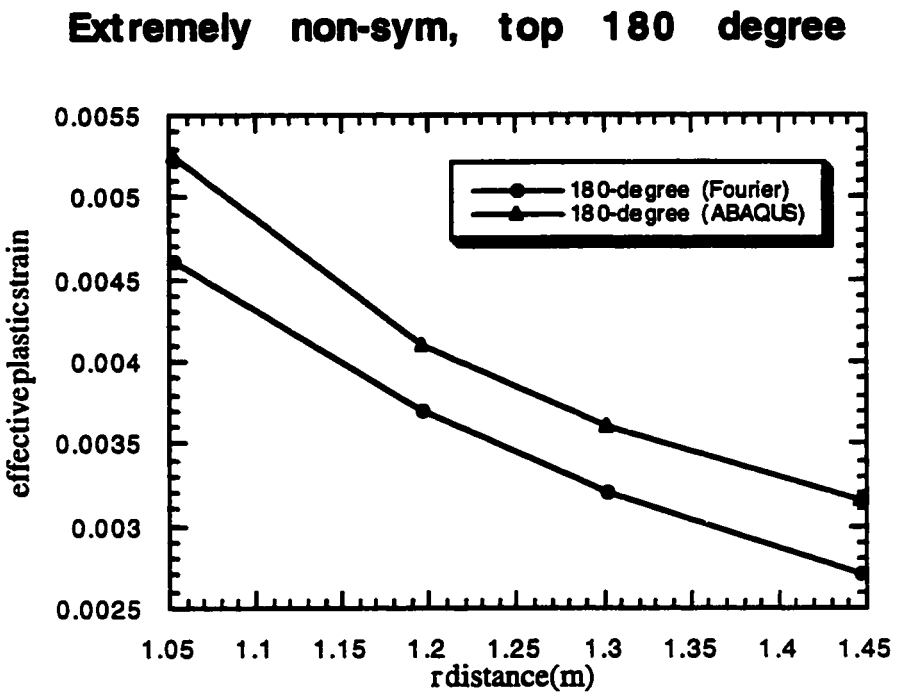

Fig. 5.56 Effective Plastic Strain at 180° Location of Free End
Extremely Non-symmetric Load

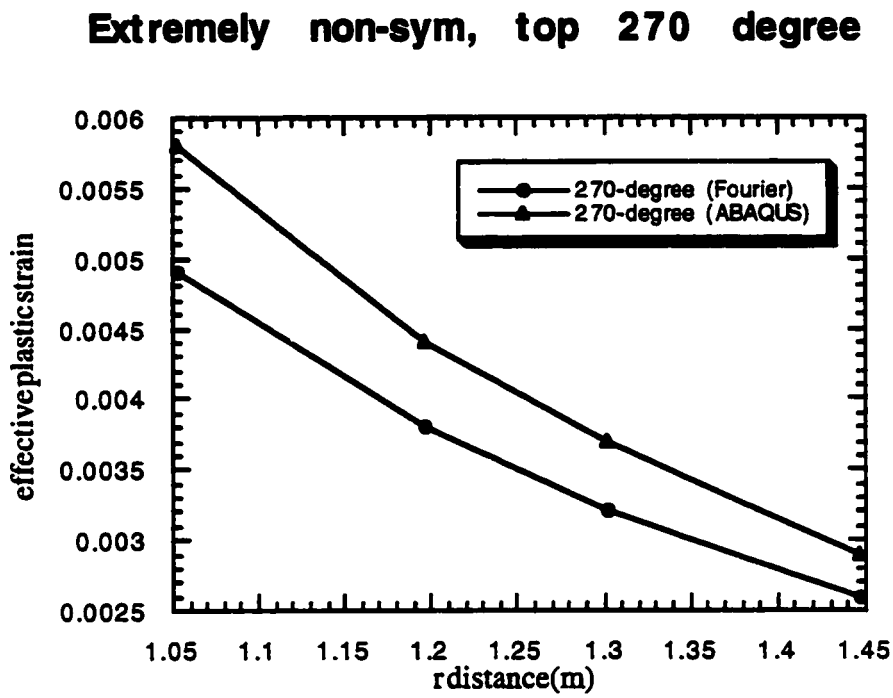

Fig. 5.57 Effective Plastic Strain at 270° Location of Free End
Extremely Non-symmetric Load

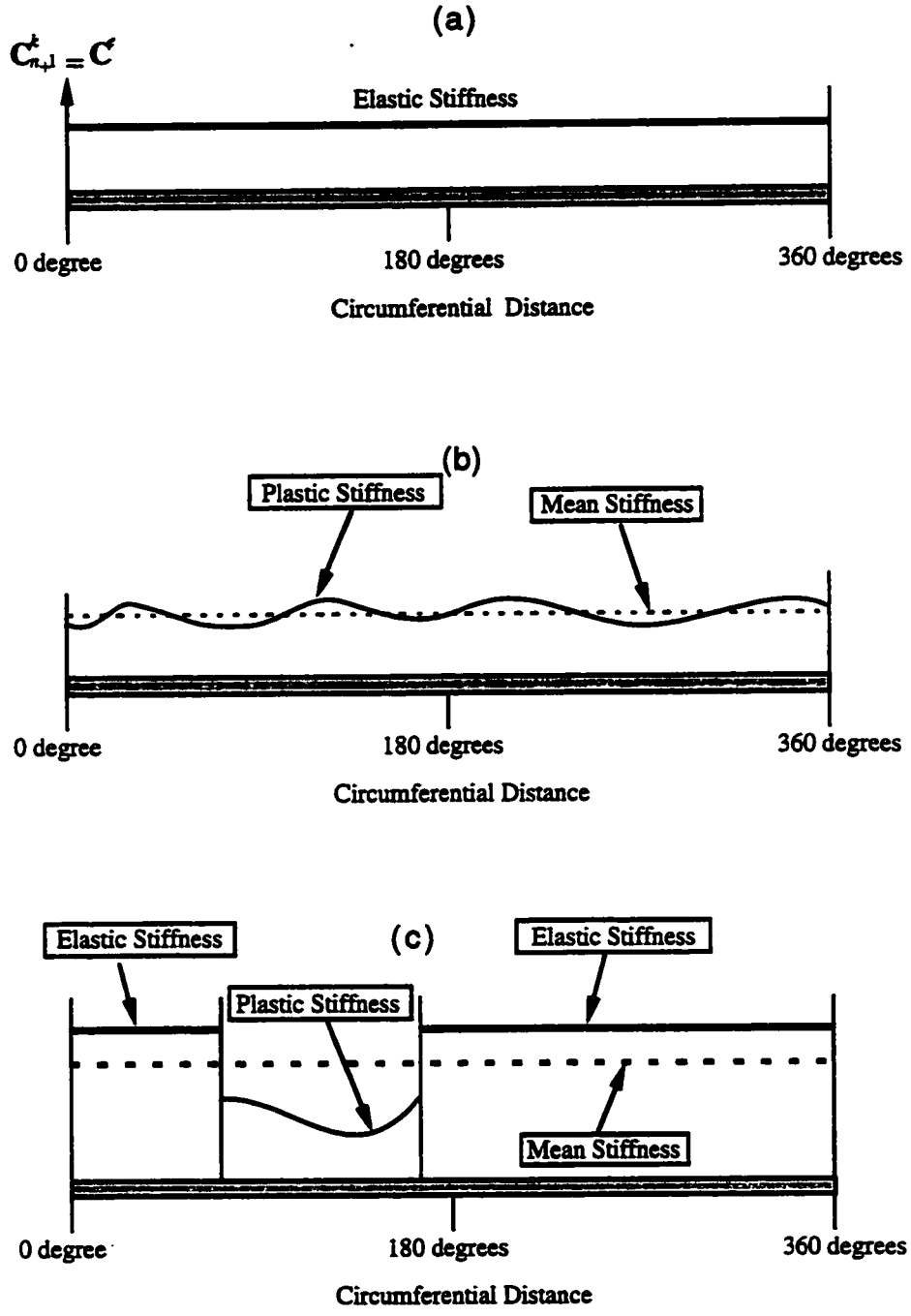

Fig. 5.58 Schematic Illustration of Mean Norm of Consistent Tangent Stiffness Scheme

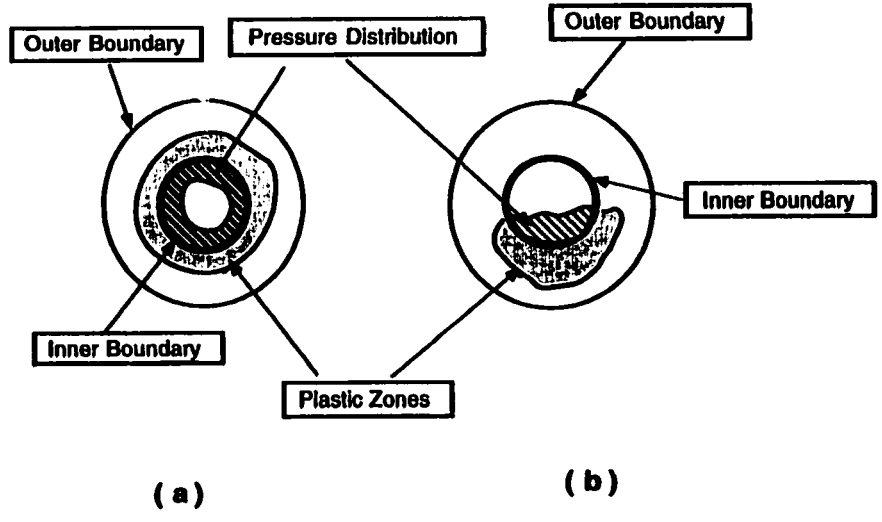

Fig. 5.59 Schematic View of Pressure Distributions and Plastic Zones

Chapter 6

SOIL-PIPELINE FROST HEAVE MODELLING

6.1 Introduction

The objective of this chapter is to explore the capabilities of the Fourier finite element model to analyze a soil-pipeline system which involves heat transfer and moisture migration phenomena. It is attempted to model the Caen (France) [6] laboratory experiment in which a small pipe (270mm in diameter), buried at a depth of 330mm, is subjected to loads from freezing soil made up of sand and silt. The schematic setup of the experiment with appropriate dimensions is shown in Fig. 6.1. The room temperature was kept at $-0.75°C$ while the pipe, carrying chilled gas at $-5°C$, ultimately froze the soil in its neighbourhood. The soil is composed of two different materials, namely SNEC sand and Caen silt which have largely different strengths and thermal conductivities. As a result of the differential freezing around the pipe, non-uniform movements and heave are induced at the surface of the soil. The computation of the resulting three-dimensional deformations is attempted.

The freezing of the soil underwent several stages as described in Rajani and Morgenstern [2] so that resulting deformations were incremental.

6.2 Finite Element Mesh

Figure 6.2 shows the layout of the aforementioned three-dimensional problem in which a pipe carrying chilled gas freezes the surrounding soil. The soil in the longitudinal section of the pipe is composed of two different materials, namely silt and sand with contrasting mechanical characteristics.

The Fourier finite element mesh used in the computations covers $9m$ of total pipe length with the radial, longitudinal, and circumferential directions denoted by r, z and θ. A typical $r-z$ plane is discretized by using eight-noded isoparametric finite elements. A total of 224 elements and 751 nodes were used with each node having three degrees of freedom. It is noted that considerably more elements and nodes would have been involved if a classical 3-D finite element mesh were to be used. The pipe is herein represented by thin elements and perfect bonding with the soil is assumed. An interface/contact element will be required for more refined calculations in future studies.

To capture the complete three-dimensional behaviour of the structure, it suffices to make several computations (so called harmonics) in the θ direction based on the two-dimensional finite element mesh shown in Fig. 6.2. Accordingly, computed displacements will have three components while stress and strains six independent components.

Thirty six planes ($np = 36$) were chosen in which the field variables T, θ_i, θ_l, P_i and P_l were determined from two-dimensional finite elements heat transfer and moisture migration calculations, see Fig. 6.3. Once the ice and liquid pressures were known for each of these planes, the thermal stresses emerged as $\boldsymbol{\sigma}^{th} = (P_i + P_l)\,\boldsymbol{\delta}$.

These are used to calculate the thermal loads $\mathbf{f}^m$ which enter into Eq. (3.54) such that

$$\mathbf{f}^m = \sum_{L=1}^{np} \left(\Delta\theta_L \int_r \int_z \mathbf{B}_m^T \boldsymbol{\sigma}_m^{th} r \, dz \, dr \right) \tag{6.1}$$

6.3 Boundary Conditions

6.3.1 Restrictions

With regards to fixity, all nodes on the right and left ends are fixed in z direction, but freed in the r and θ directions. Furthermore, in order to prevent rigid body modes, one node at each end was additionally restricted in the θ direction, see Fig. 6.2. All the remaining nodes along the external boundary and the internal side of the pipe are free in r, z and θ directions.

6.3.2 Thermal Boundary and Initial Conditions

For thermal boundary conditions, the right and left ends are assumed to be insulated boundaries in order to simulate an infinitely long pipe. The internal temperature of the pipe has a prescribed value of $-5°C$. Figure 6.4 shows the temperature distribution applied along the outside periphery of the finite element mesh as extracted from the work of Selvadurai [64] which dealt with the same case study. It is interesting to note that the temperature profile is symmetric about a vertical longitudinal cut of the pipe. The overall temperature distributions in the silt and sand around the pipe

appear to be mildly non-symmetric.

In the subsequent frost heave calculations, the initial temperature of the ground was assumed to be $0°C$.

6.3.3 Liquid Pressure Boundary Conditions

To simulate the evolution of frost bulb, the proper liquid pressure boundary condition has to be applied for the solution of Eq. (4.40). The liquid pressure boundary distribution used in this analysis is shown in Fig. 6.5. The upper semi-circle of the outside boundary defined by A, B, C, D, and E, has zero liquid pressure because all the pore water in this region is frozen. The liquid pressure along the lower semi-circle of the outside boundary is calculated according a certain capillary pressure distribution. In fact, at the lowest point, L, the capillary pressure is $-\gamma_w h$ and varies linearly decreasing to zero along the height up to the centre altitude of the pipe. Here, h is the distance from the lowest point to the water table, which is $0.5m$ taken from Caen experiment setup.

6.4 Model Parameters

The frozen sand and silt were assumed to follow a Drucker-Prager elasto-plastic material model law with corresponding mechanical properties borrowed from the literature, Rajani and Morgenstern [2]. Table 6.1 summarizes the material parameters used in the simulation. In order to simplify the calculations, the pipe was assumed to behave as a von Mises material with elasto-plastic properties much higher than

Table 6.1: Fourier FE Model Parameters

Property	Silt	Sand	Pipe
$E\ (kPa)$	960	2820	2×10^8
ν	0.3	0.3	0.3
$\sigma_y\ (kPa)$	140	170	2×10^5
$\varphi\ (°)$	30	30	–
$\lambda\ (W/m/°C)$	0.65	2.2	43
$C\ (J/m^3/°C)$	10^6	1.5×10^6	3.7×10^6
$k\ (m^2/s/Pa)$	2.9×10^{-14}	8.7×10^{-14}	–
n_0	0.38	0.29	–

that of the soil.

6.5 Results

6.5.1 General View

Figure 6.6 shows the ground surface heave along the longitudinal direction. The dashed lines represent the original configuration while the curved solid lines show the deformed one. It is clear that deformations on the Caen silt side are more prominent that those on the side of the SNEC sand. This is due to the considerable difference in material properties of the two soils. Also, deformations are function of the ice pressure, unfrozen water pressure and temperature distributions which were computed from the moisture migration FEM program, see Figs. 6.14–6.33 and 6.41– 6.43. The maximum heave of the silt reaches $16.4cm$ which is very close to the $16.2cm$ measured in the Caen experiment. The hump associated to this maximum heave is a result of the underlying large yield zone. The yielding taking place near

the ends of the pipe is possibly due to end effects. The other hump which appears near the interface region corresponds to the different frost loads existing in the two soils. The SNEC sand side has an almost uniform displacement of $2.5cm$, because it is stiffer and thus deforms elastically. It is worth noting that the surface heave shown in Fig. 6.6 corresponds to the superposition of both the surface and bottom radial displacements. This is necessary because the lower portion of the soil and the bottom of the tank are constrained to any downward displacement. Hence, all the calculated downward displacements have to be superposed onto the upper ones. Figure 6.6 also shows the soil-pipe system at steady state with a major part of the silt soil yielding. Here, the steady state refers to the condition at which both the temperature and frost heave have reached their ultimate values and remain constant. It takes sixteen iterations for the system to reach a mechanical equilibrium state. It is reminded here that, in general, the shape of the surface heave profile largely depends on a number of factors. These are: heat transfer/moisture migration induced loads, thermal coefficient of expansion, strength contrasts between silt and sand materials, and to some extent, soil-pipe interaction which, in this case, was omitted.

The yield zone distributions are graphically shown in Fig. 6.7. Extensive soil yielding occurred in the silt zone for section $a - a$, due to the sharp differential heave. Both the pipe and the surrounding soil are subjected to considerable shear stresses and strains. Since the pipe was modelled as a stiff member with very limited interaction with the adjacent soil, very high stresses built up in the pipe. If some degree of interaction was allowed by the introduction of contact elements, considerably lower pipe stresses would have been obtained due to the allowance of slip, and

hence enhancement of plastic yielding at the pipe-soil interface.

Figure 6.8 shows the cross sectional deformation of different pipe sections. In section $a-a$. This deformation does not include the rigid upward movement of the pipe, which means that the dashed original pipe position has moved upwards about $9cm$, seen from the left end of Fig. 6.6. The largest deformation of $6.2mm$ is also near the end restrictions, because more yield zone for the silt occurred in this area.

Figure 6.9 shows the plan view of the deformed pipeline along the longitudinal direction. Since the load and geometry are symmetric with respect to the vertical plane, the same symmetry is reflected in the displacements. The three-dimensional view of the ground surface clearly shows that most deformations take place in the silt zone with a maximum heave of $16.4cm$, see Fig. 6.10.

The plot of number of iterations as a function of out of balance residual force is given in Fig. 6.11. Since a Newton-Raphson scheme coupled with a consistent tangent operator (see Chapter 3) is used in the model, quadratic convergence rate should be expected. However, the results obtained in this analysis do not exactly reflect this expectation. There are two main reasons to explain this shortcoming here: firstly, the integration for the load term along circumferential direction θ is approximated by the summation of a series of sectors; secondly, when the material undergoes plastic deformations, the consistent tangential operator, $\overline{C}$, is approximated by the average value along the circumferential direction θ. One notices that in the first four iterations, see Table 6.2, the convergence appears to show an oscillating trend which dies out very rapidly at subsequent iterations. The total number of iteration was sixteen which is still considered as very acceptable in plasticity computations. It is

Table 6.2: Convergence Rate

No.	Residual	No.	Residual	No.	Residual	No.	Residual
1	2.19×10^{1}	5	3.13×10^{2}	9	6.37×10^{-1}	13	8.76×10^{-3}
2	4.30×10^{2}	6	1.63×10^{2}	10	3.47×10^{-1}	14	2.39×10^{-3}
3	2.86×10^{2}	7	3.10×10^{1}	11	4.73×10^{-2}	15	5.01×10^{-4}
4	4.06×10^{2}	8	4.05×10^{0}	12	5.67×10^{-3}	16	8.00×10^{-7}

also important to underscore the efficiency of the computations as the CPU time consumed on a Pentium PC/100 for running the analysis was about twenty five (25) minutes for calculating five harmonics. Table 6.2 gives the corresponding data to Fig. 6.11.

Figure 6.12 gives the comparison of the rate of convergence towards the 3-D solutions for the cases involving one harmonic and five harmonics. One can see that there is not too much difference between the ground surface heave computed for these two cases. This is mainly because the temperature induced load distribution does not vary much along the circumferential direction as discussed in detail for a mildly non-symmetric load case in Chapter 5. The results for the other harmonic cases (two, three, and four) are located between the one and five harmonic cases. Generally, four to five harmonics would be sufficient enough for addressing most loading conditions. In this example, five harmonics were sufficient to describe the three-dimensional aspect and asymmetry of the problem.

Figure 6.13 shows the surface heave value comparisons of the 'start' case, $t =$ 2 *hours*, to the 'end' (stable or steady) case, $t = 33$ *hours*. The 'start' case is the first time step at which the response is still elastic and the 'end' case is the fifteenth time step at which elasto-plastic behaviour occurs. It does not take too

many time steps to reach steady state, because the heat capacities of both soils are somewhat low, see [2]. Due to the scarcity of related information in the literature, these low heat capacities were the only best approximations. In the real practical case it is expected that the steady state will usually take much longer time. If the heat capacities for both soils are chosen reasonably, the proposed model will capture the actual procedure accordingly.

6.5.2 Analysis of Ice Pressure Evolution

At the beginning of the simulation (the initial state), the upper half of the soil-pipe system is considered to be in a frozen state. Therefore, ice bulb evolution only occurs in the lower half of the soil-pipe system due to suction and capillary effects mainly prevalent in the lower half of soil-pipe system. The capillary water pressure is assumed to increase with the height from the surface of source water table up to the bottom of the model boundary. Then, the capillary water pressure decreases from the bottom of the model boundary up to the interface of the lower half and upper half of the pipe. The above mentioned capillary water pressure distribution is shown in Fig. 6.5. Under the capillary water pressure, the water from the source water table will be sucked upward. This process results in more water aggregation to the frozen fringe so that the ice fringe will gradually expand with further cooling taking place as time passes by.

The numerical results of the simulation regarding the ice pressure evolution in the longitudinal direction is given in Figs. 6.14–6.33. Five typical sections of the soil-pipe system are investigated at locations of 190°, 210°, 230°, 250°, and 270° with

angle measured counterclockwise, see Fig. 5.1. Note that the axis $o-y$ is the only axis of symmetry. For each of these five sections, four time stations are examined. The four time stations are 2 hours, 4 hours, 6 hours, and 33 hours after the beginning of the initial state. These four time stations correspond to time step 1, time step 2, time step 3, and time step 15 (the last time step). The time step is the iteration time step used when solving Eq. (4.40). The results given in Figs. 6.14−6.33 reveal that the convergence rate to the steady state is very fast because the result at time step 3 is very close the that of time step 15, which is the last time step and the steady state. Generally the results computed at time step 1 of all the five sections have some oscillations especially in the region near the bottom of the model boundary. One possible reason for the oscillation may be attributed to the high capillary water pressure gradient at the bottom of the model boundary. Another possible reason may be due to the low heat capacities used in the two soils. The slight oscillation can be seen in time step 2 of these five sections. However, with the time increase, from time step 3 onwards, the oscillation vanishes very quickly.

Another important fact needs to be addressed. As shown in Figs. 6.14– 6.33, the ice bulb evolution on the silt side is much faster than that on the sand side. This is because of the different properties of the two materials. However, the overall numerical results obtained in this model agreed very well with the Caen experiment.

Figure 6.34 shows a schematic demonstration of the ice bulb evolution in the cross-sectional direction. It can be seen that the ice bulb expands with time. At the last time step, the ice bulb approaches the boundary of the model and steady state is reached. Again, because the ice bulb evolution converges very fast, the situation at

time step 3 (only 6 hours after the beginning of the initial state) is very close to the situation at steady state. This is because some parameters, such as heat capacity, were intentionally chosen so that the heat conduction process converges very quickly to save computational effort. It is important to note that only the steady state results are of interest in the calculations and not the manner in which one achieves them.

6.5.3 Stress Distribution

Figures 6.35–6.40 show selected stress distributions for some sections at the steady state. Generally, from these figures it can be seen that the stress in the silt side is larger than that in the sand side due to the contrast in material properties. The stress in the vicinity of pipe is more concentrated than that further away from it. This is because the soils near the pipe are closely bound to the pipe which is also much stiffer than the surrounding soil. If contact elements were introduced in the model, this effect would have been smoothened out significantly. Because the structure and the load are symmetric about the vertical central plane, only half structure is investigated. For example, the situation in the 180° section is the same as that in the 0° section.

6.5.4 Temperature Distribution

At steady state, the temperature distributions for typical sections are shown in Figs. 6.41–6.43. The temperature and load distributions are closely related. The colder

the temperature in the soil, the larger the ice pressure load will be in that soil and this effect can be clearly seen on the silt side. Also, due to the symmetry of the structure and load conditions, only half of the structure is being investigated.

6.6 Conclusion

This study shows that classical Fourier finite elements can be extended in order to address material non-linearities such as plasticity. The modelling of a buried pipe subjected to a freezing soil illustrates the viability of the method when it is supplemented with coupled heat transfer/moisture migration calculations. The soil heave profiles obtained in the numerical analysis are consistent with experimental findings for similar configurations. Also, the evolution of the frost bulb has been captured. It would be interesting to study the sensitivity of the results with regards to the inclusion of soil-pipe interface mechanism.

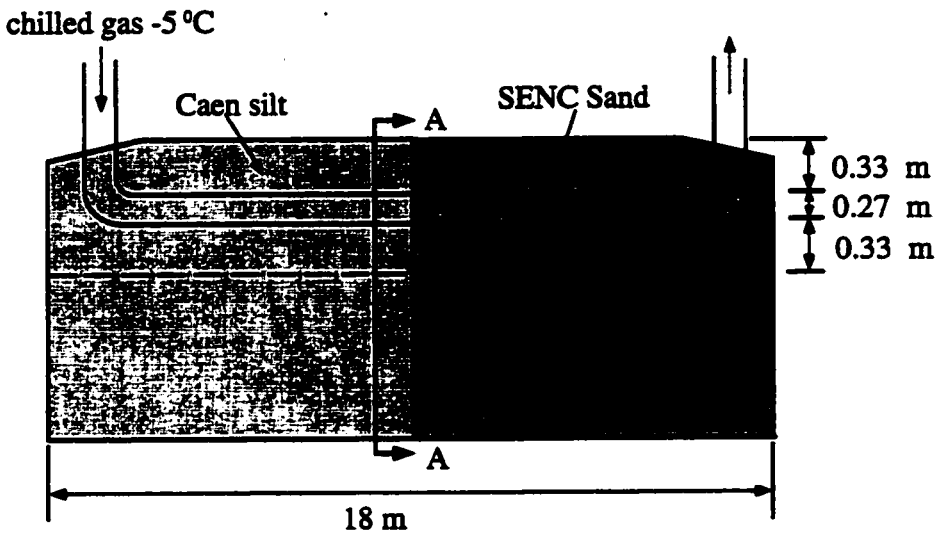

(a) Longitudinal section

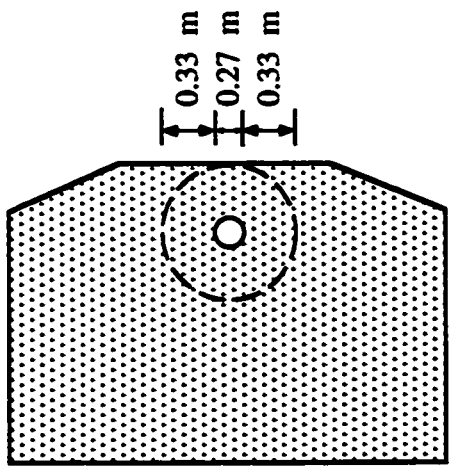

(b) Cross-section A-A

Fig. 6.1 Caen Experiment Facility (not to scale)

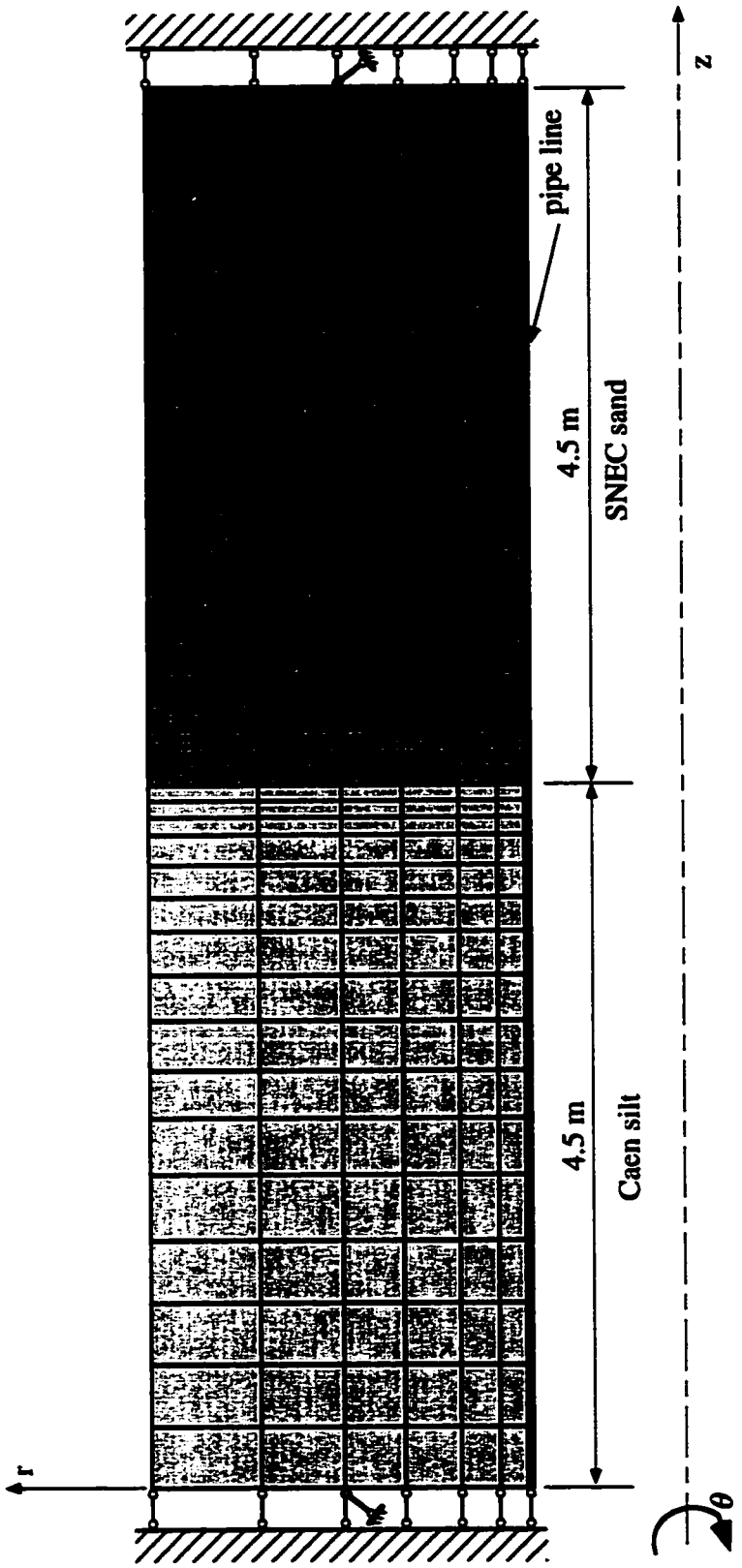

Fig. 6.2 Finite Element Mesh in a Typical r-z Plane

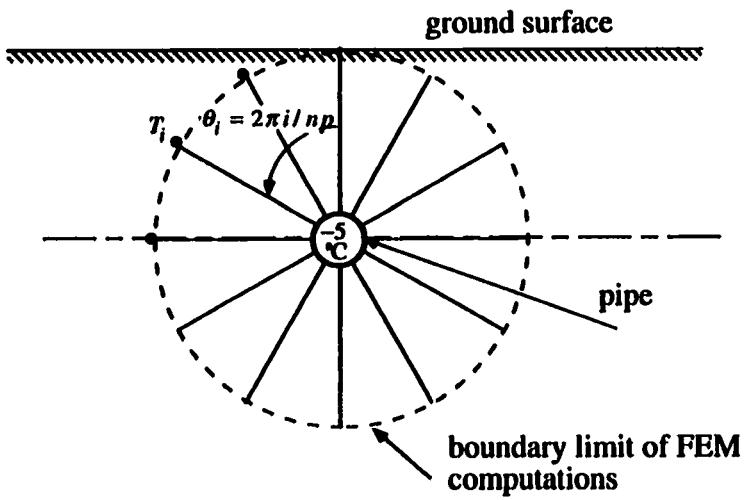

T(pipe) = $-5^0 C$

FEM mesh for plane i

np= number of sections used to discretize temperature field

np= 36 in this study

Fig. 6.3 Sections to Determine Initial Stress Load

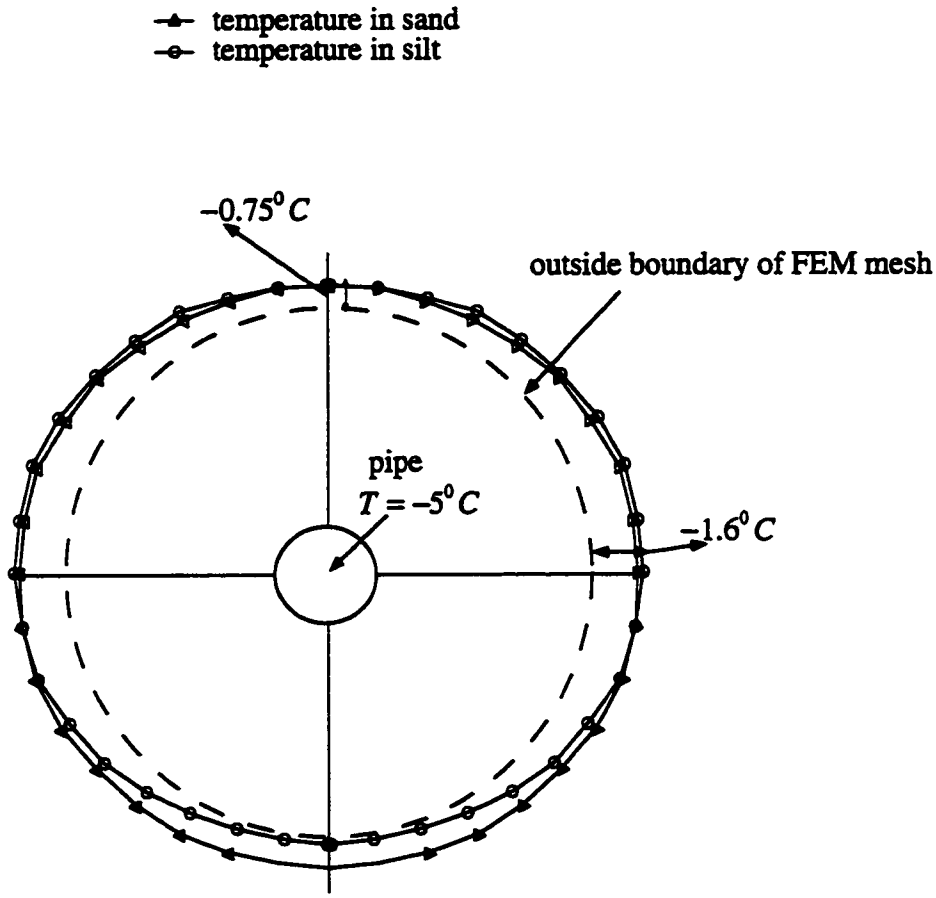

Fig. 6.4 Temperature Distribution on the Outside Boundary of the FEM Mesh

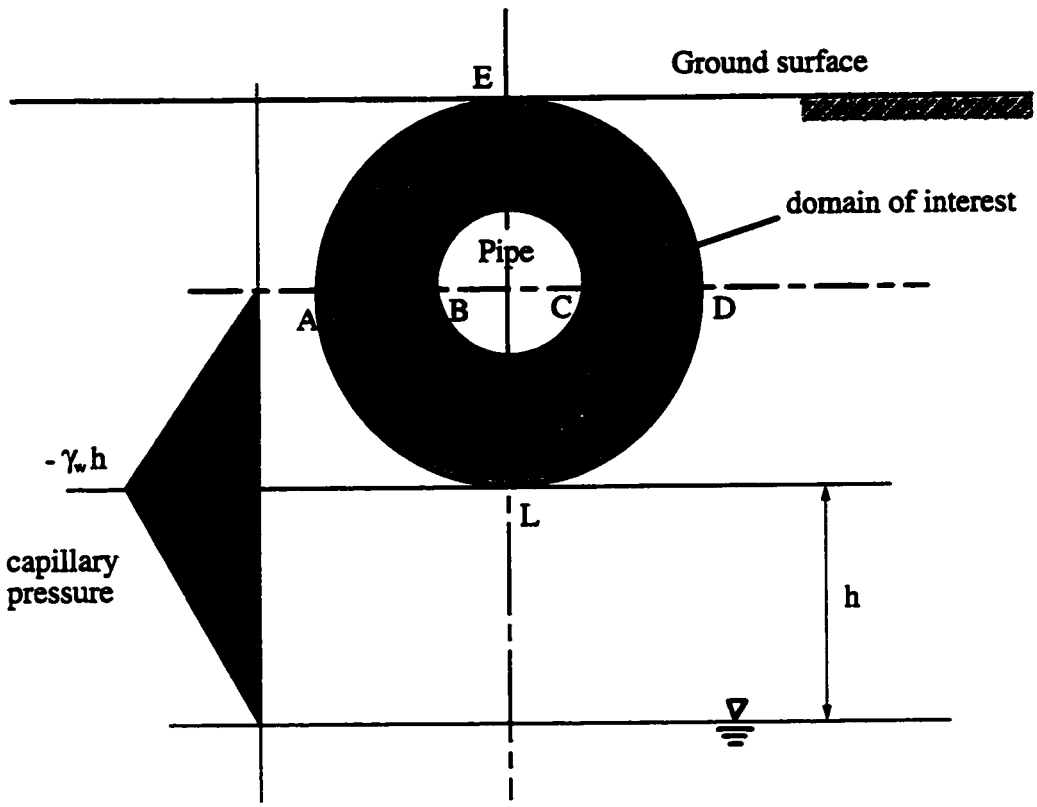

Fig. 6.5 Liquid Pressure Boundary Conditions

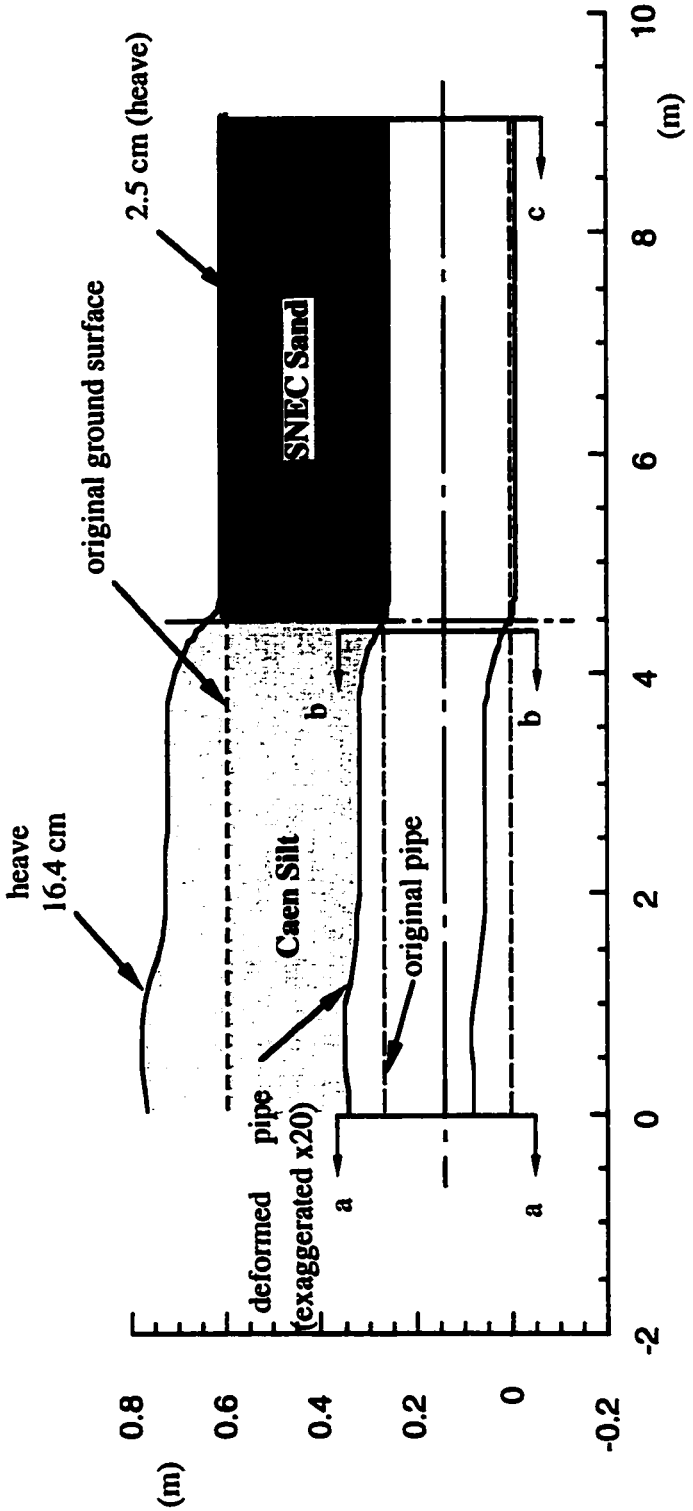

Fig. 6.6 Soil Profile and Associated Deformations in the Logitudinal Section

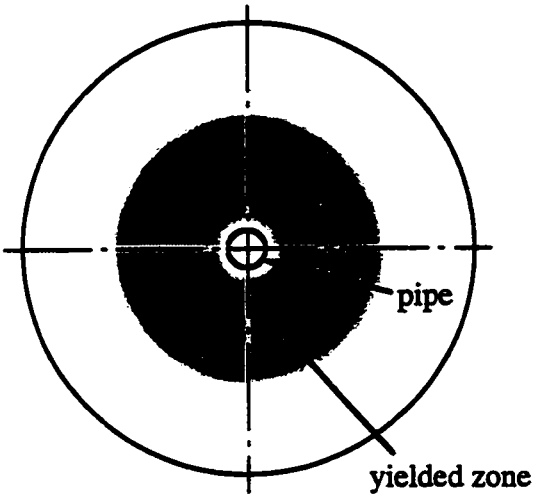

(a) yield zone (section a-a)

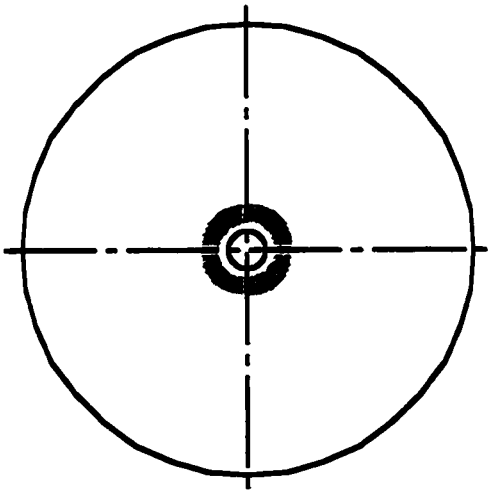

(b) yield zone (section b-b)

Fig. 6.7 Yield Zones at Different Sections

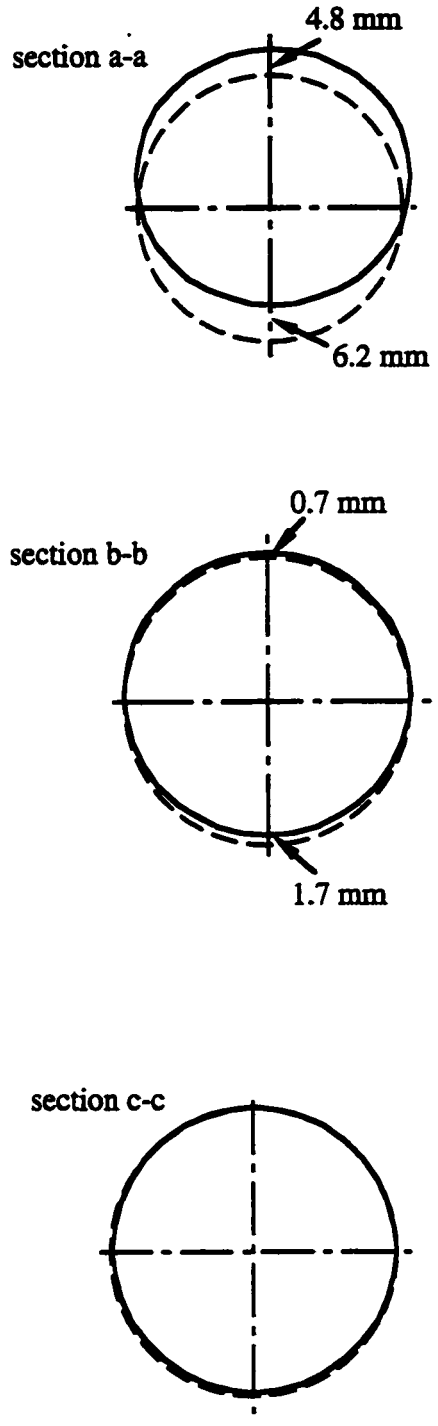

Fig. 6.8 Pipe Movement at Different Sections

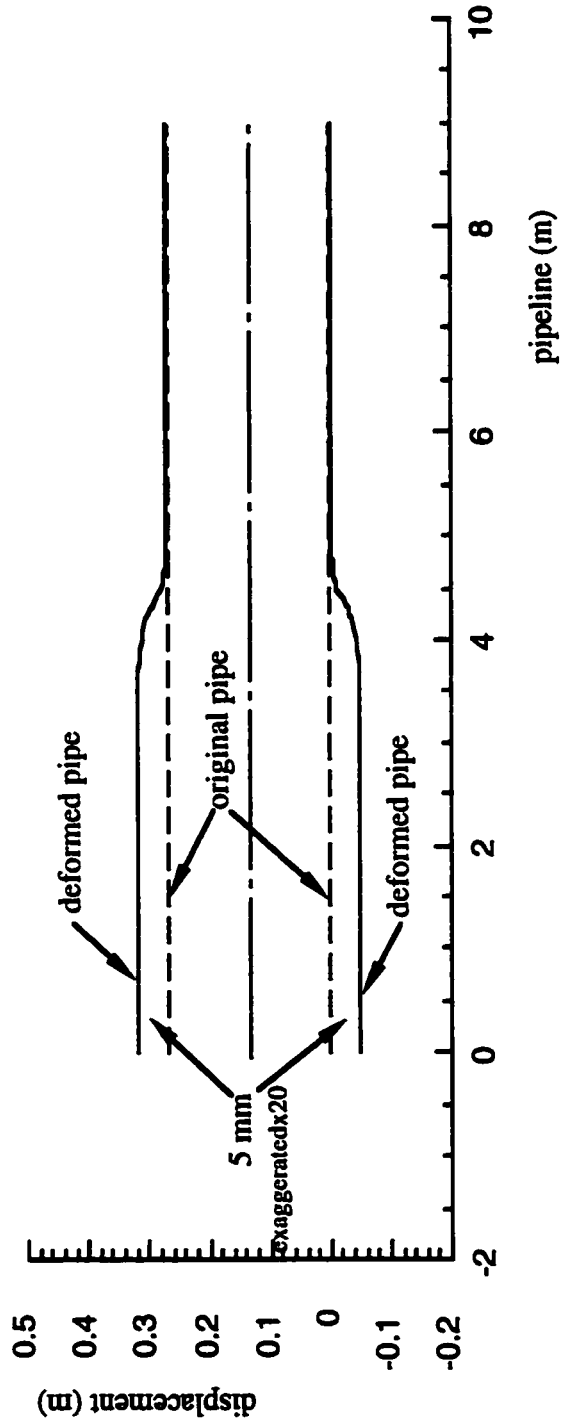

Fig. 6.9 Plan View of Deformed Pipe

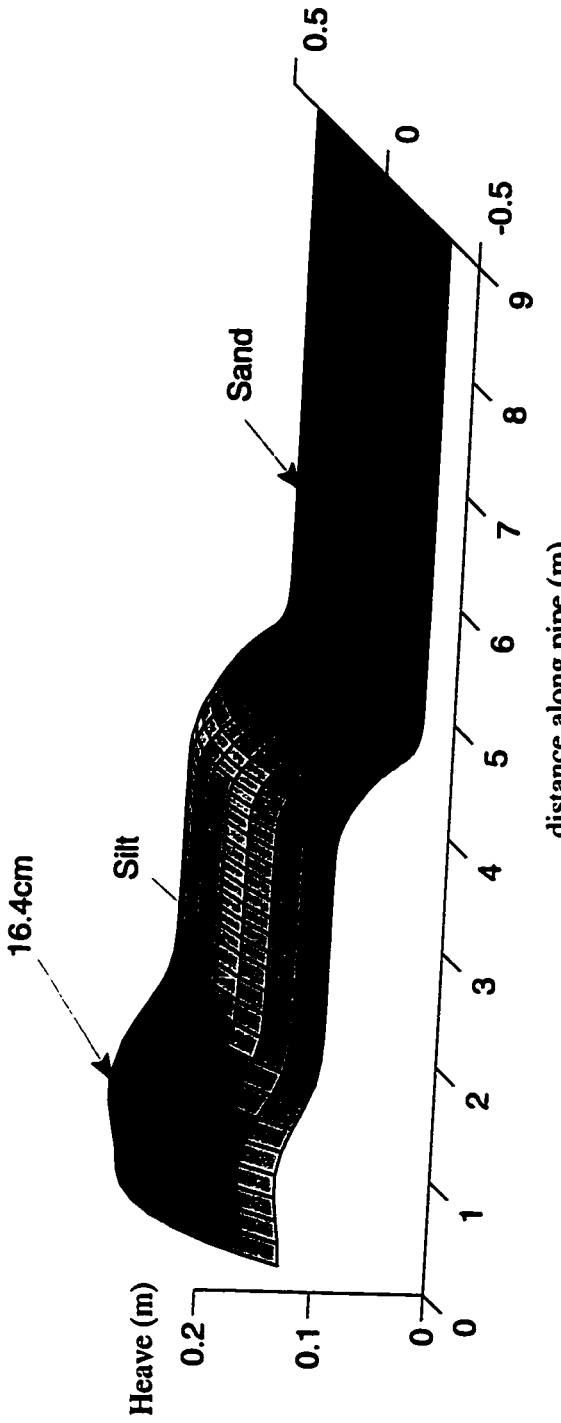

Fig. 6.10 3-D View of Surface Heave

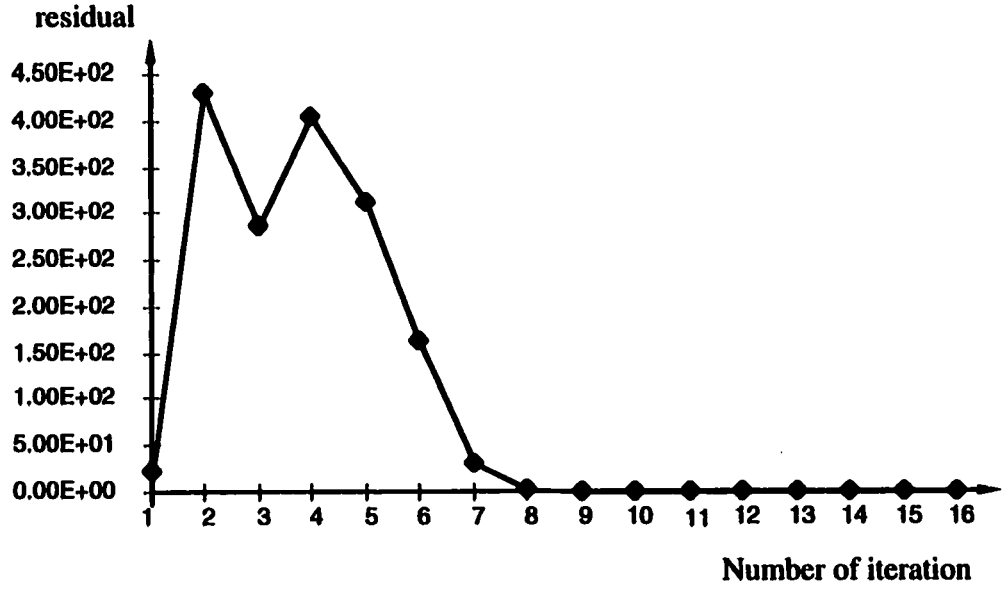

Fig. 6.11 Evolution of Residual with Number of Equilibrium Iterations

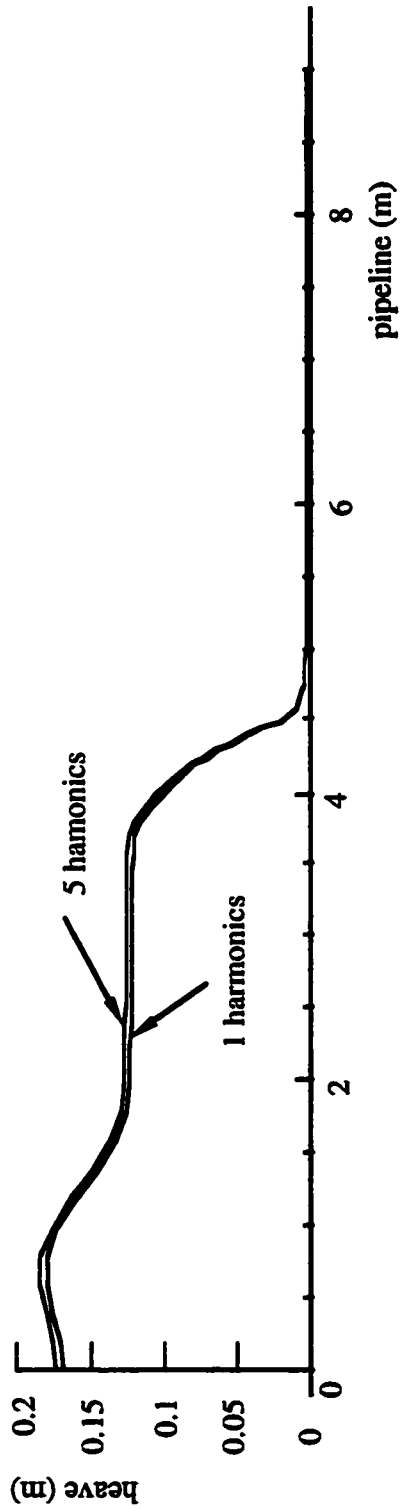

Fig. 6.12 Convergence Rate Respect to Number of Harmonics

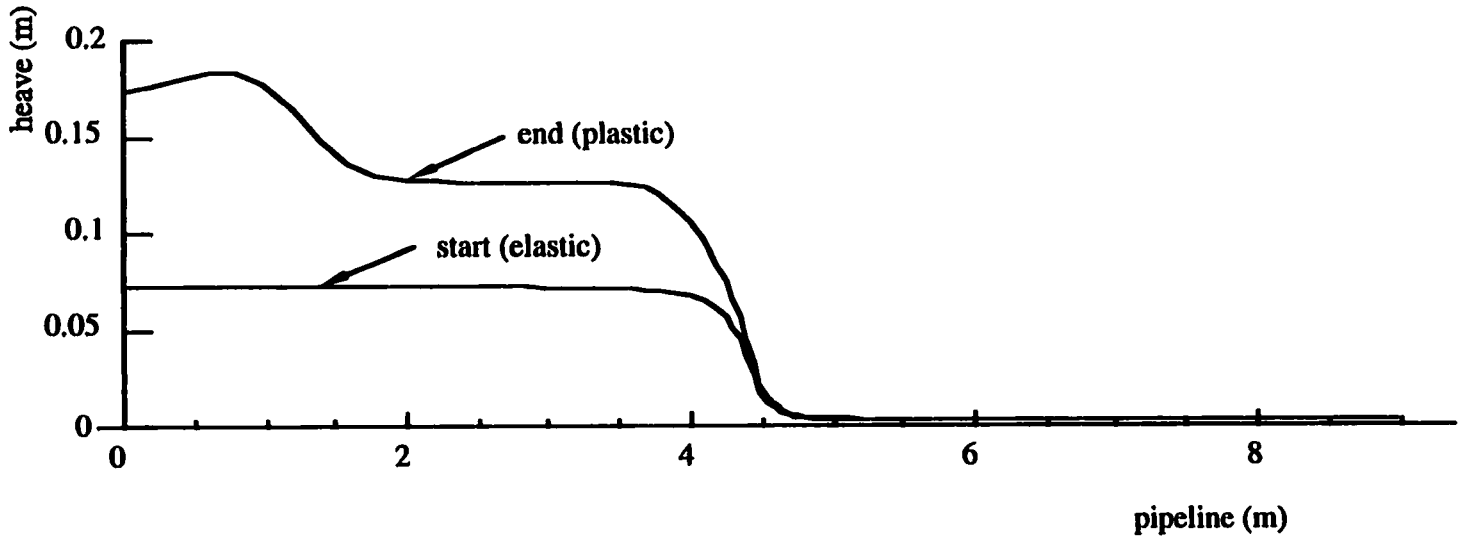

Fig. 6.13 Comparison between Elastic and Plastic Heave

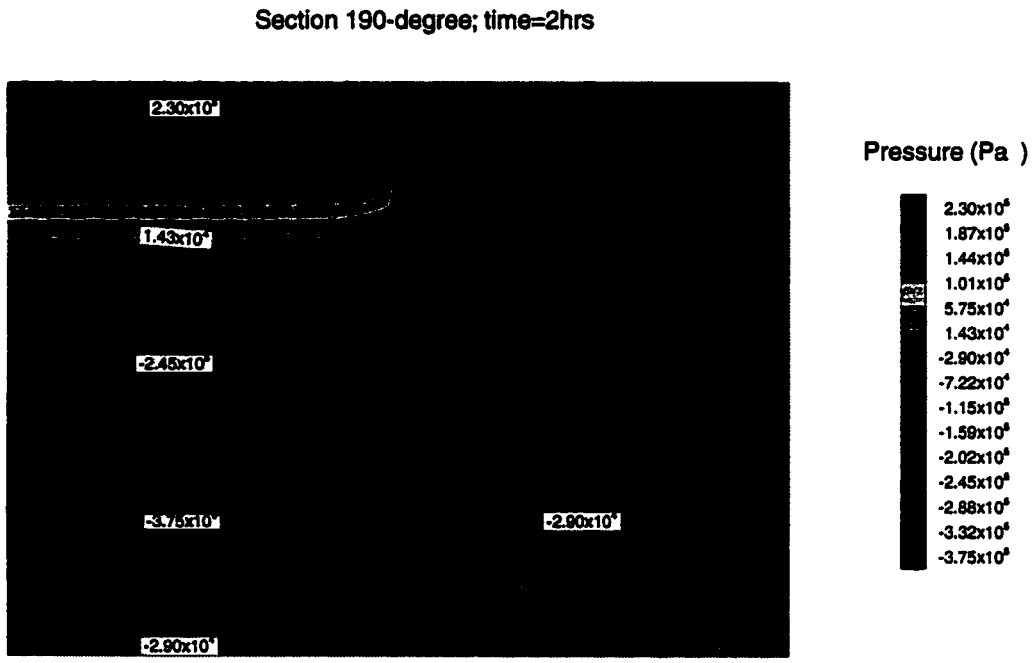

Fig. 6.14 Ice Pressure Evolution at Section 190 Degree; 1st Time Step

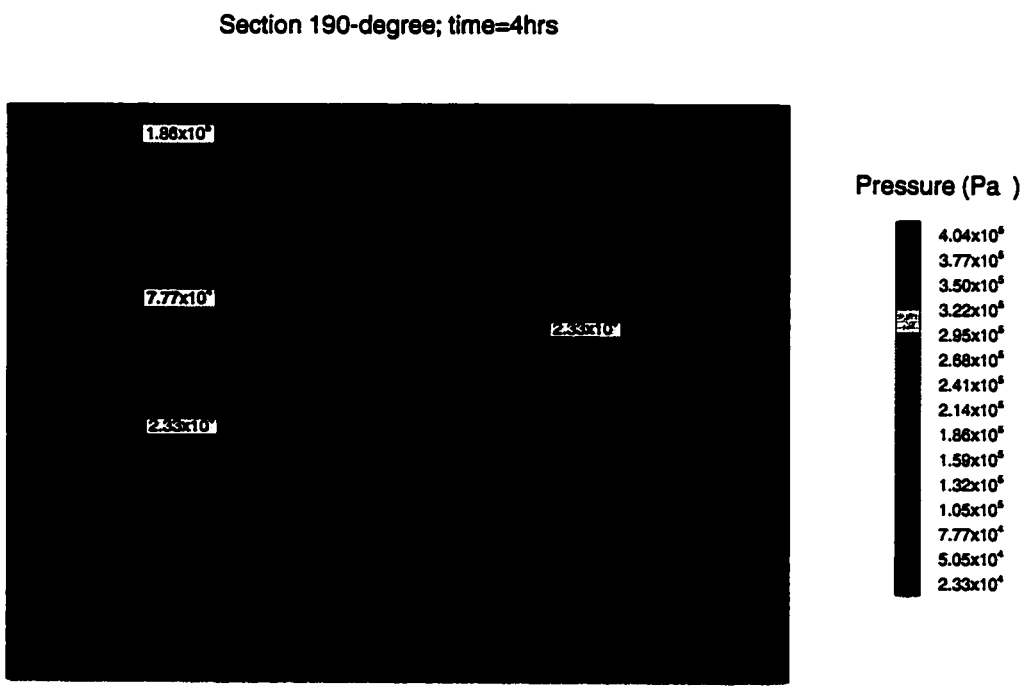

Fig. 6.15 Ice Pressure Evolution at Section 190 Degree; 2nd Time Step

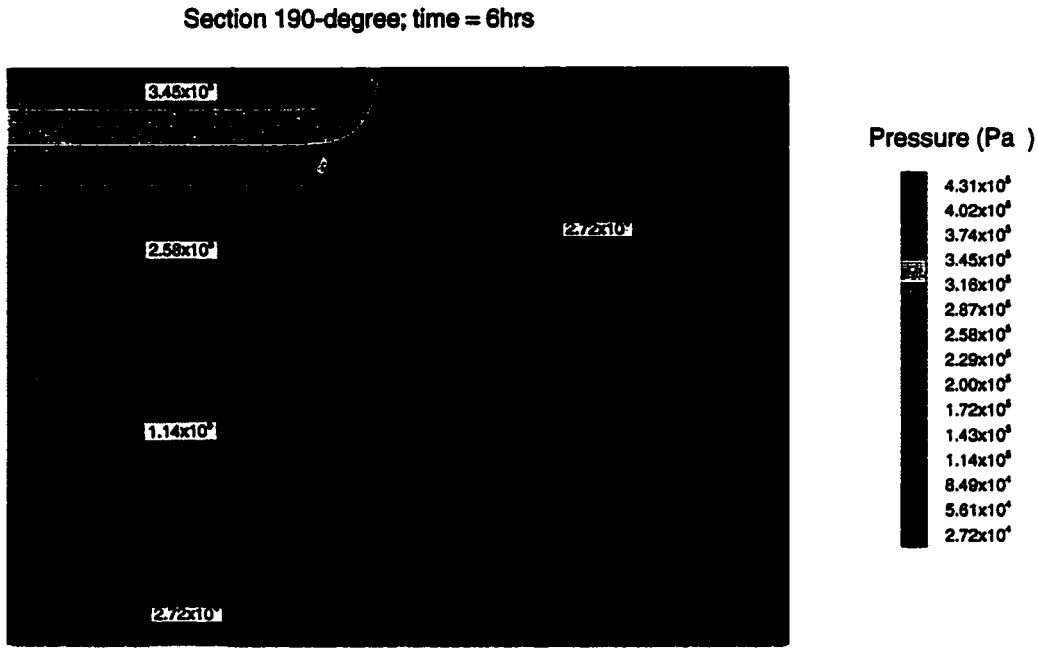

Fig. 6.16 Ice Pressure Evolution at Section 190 Degree; 3rd Time Step

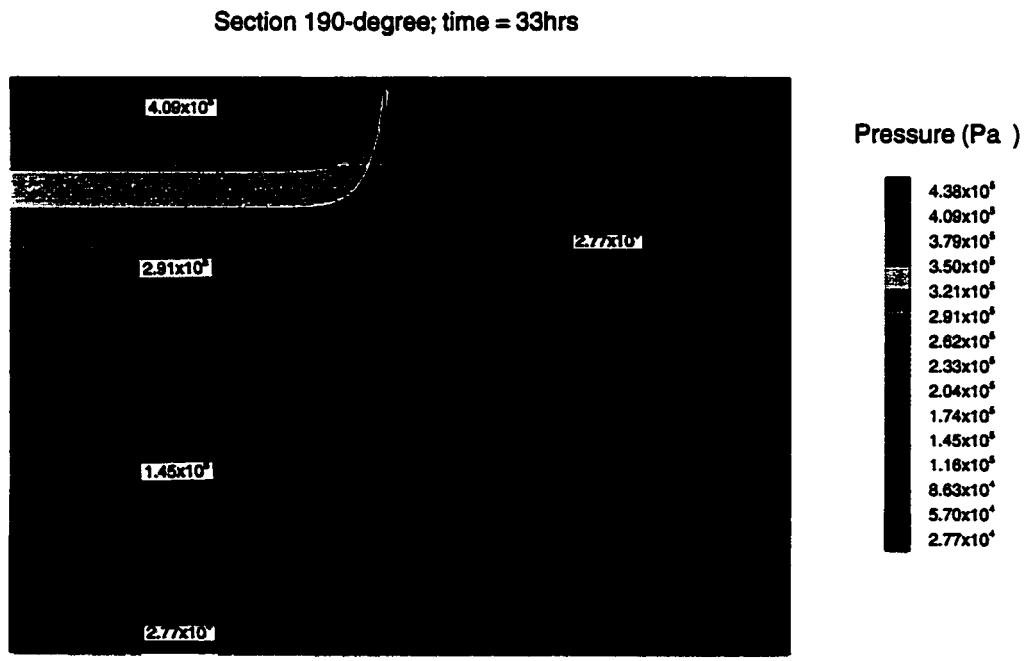

Fig. 6.17 Ice Pressure Evolution at Section 190 Degree; 15th Time Step

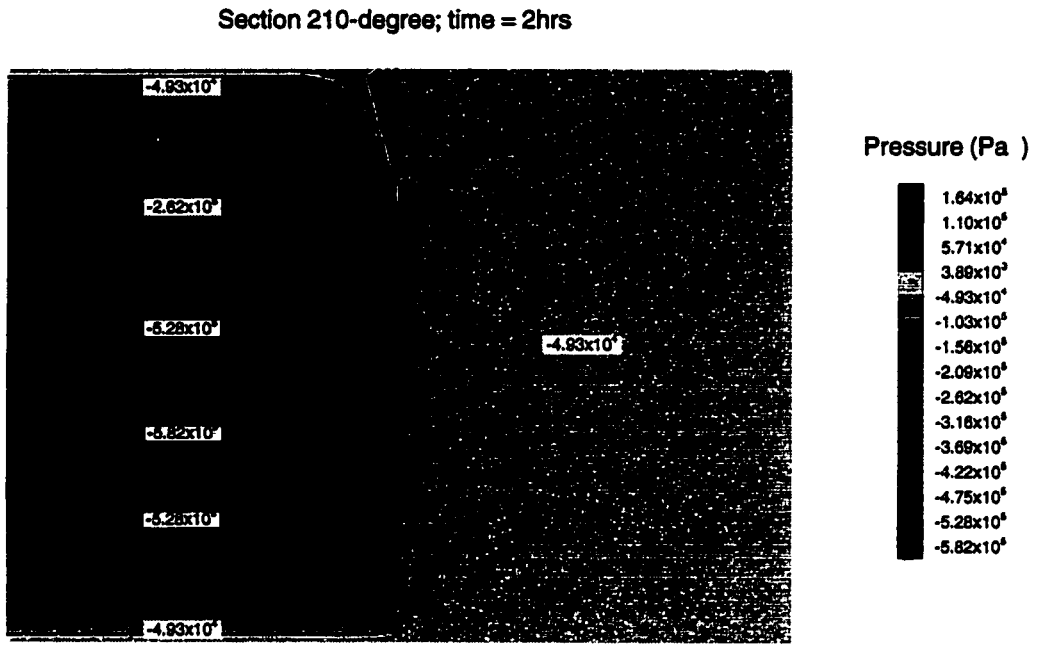

Fig. 6.18 Ice Pressure Evolution at Section 210 Degree; 1st Time Step

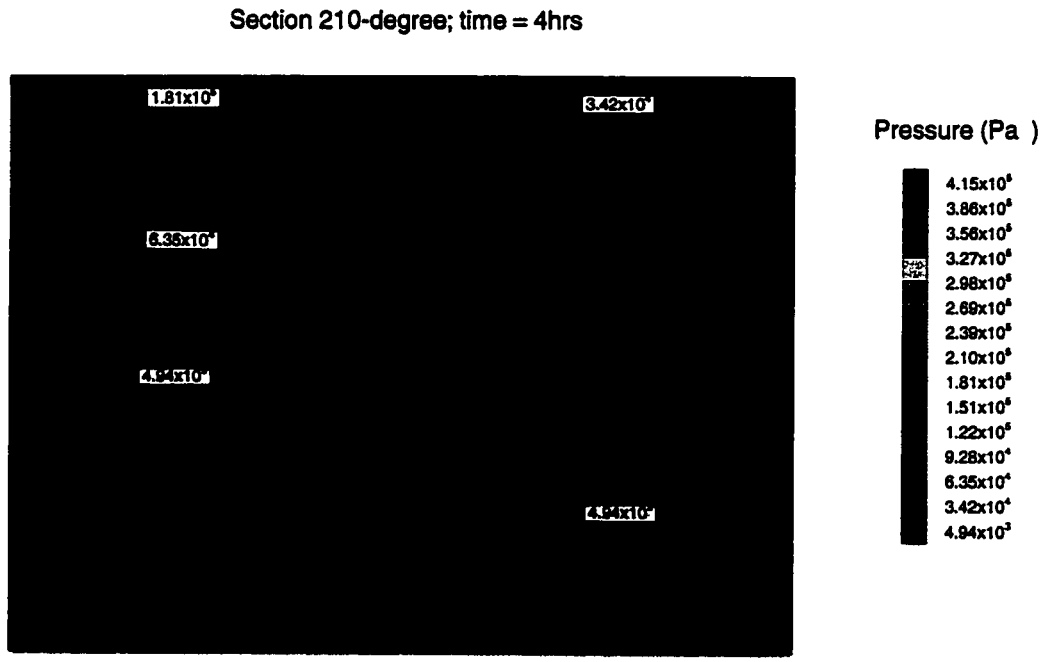

Fig. 6.19 Ice Pressure Evolution at Section 210 Degree; 2nd Time Step

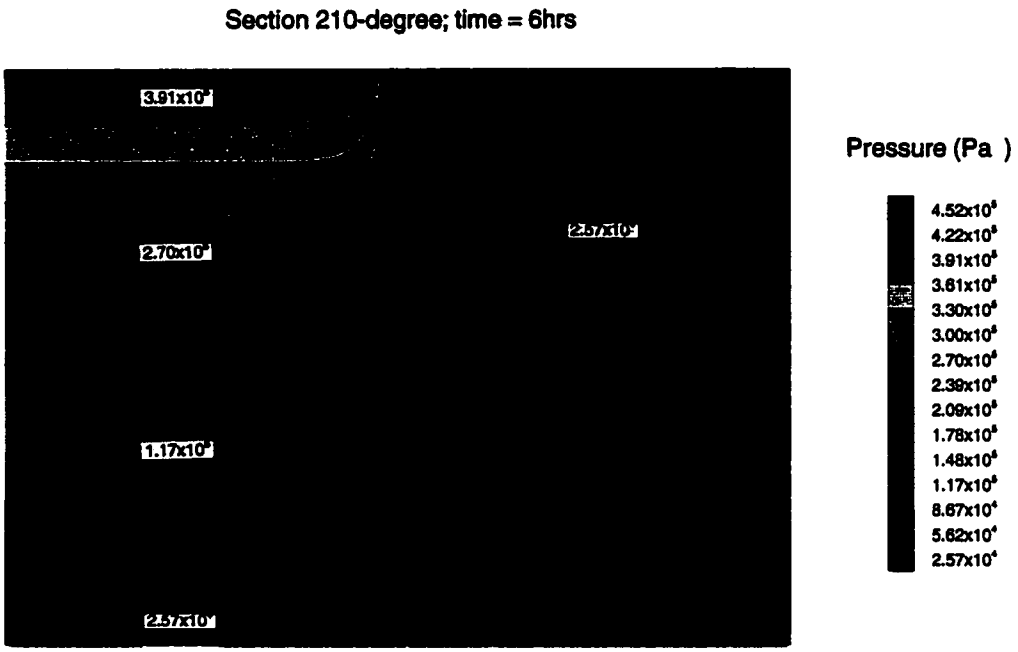

Fig. 6.20 Ice Pressure Evolution at Section 210 Degree; 3rd Time Step

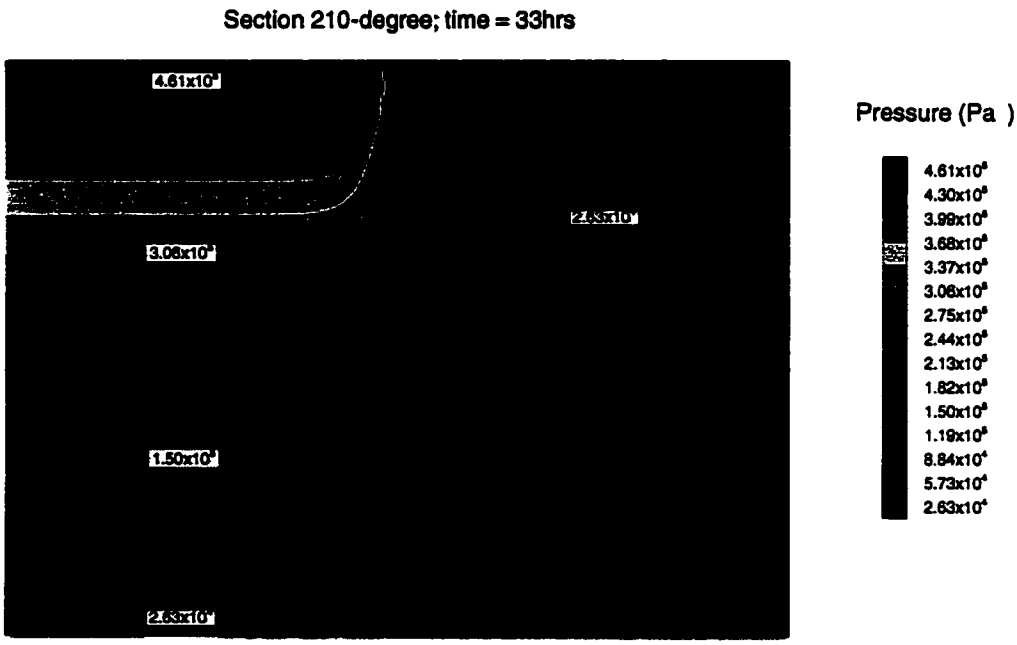

Fig. 6.21 Ice Pressure Evolution at Section 210 Degree; 15th Time Step

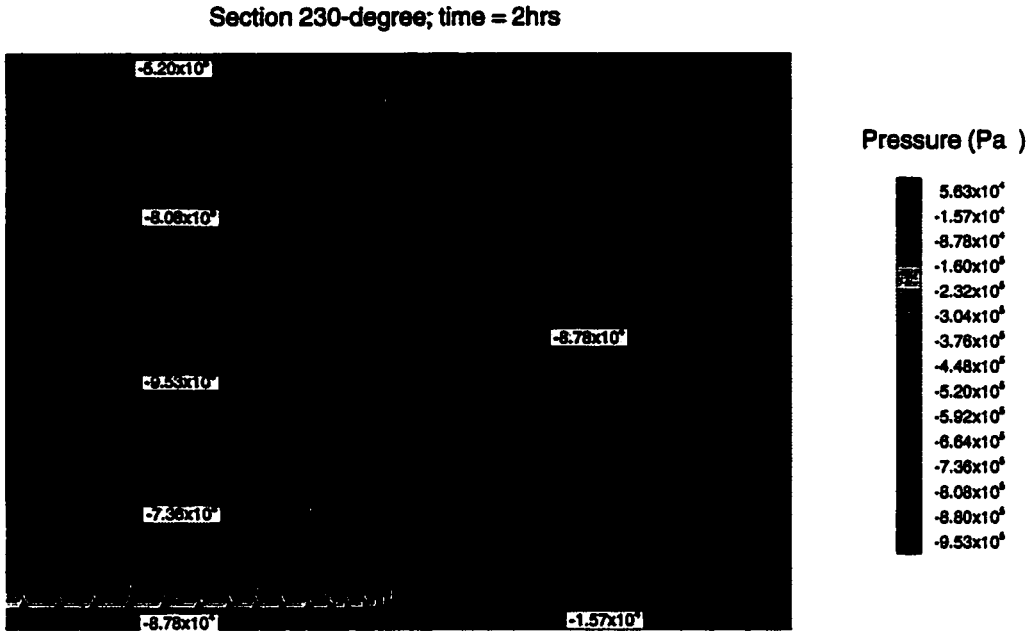

Fig. 6.22 Ice Pressure Evolution at Section 230 Degree; 1st Time Step

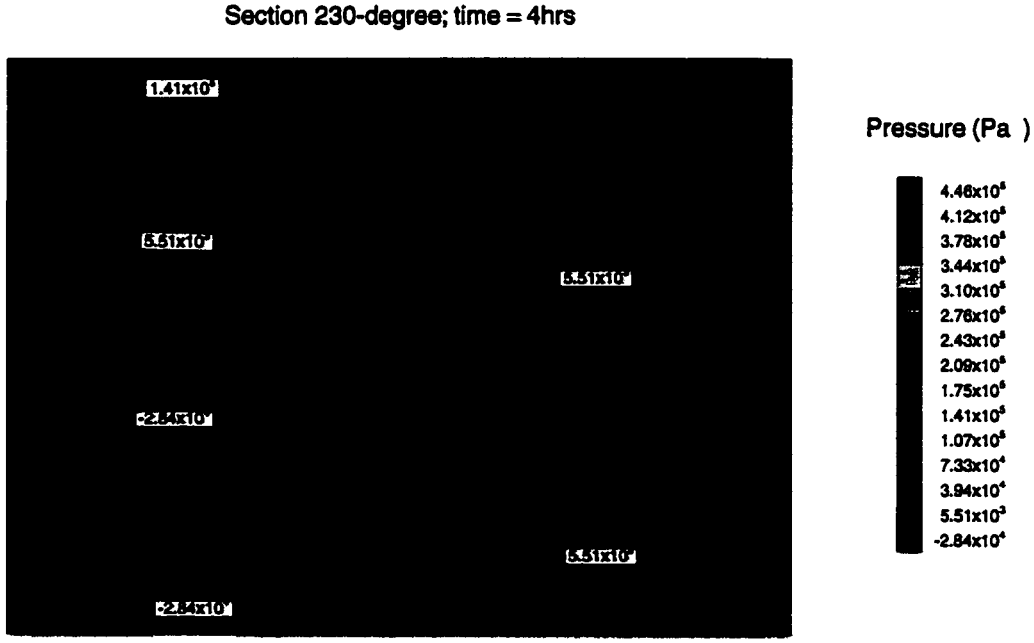

Fig. 6.23 Ice Pressure Evolution at Section 230 Degree; 2nd Time Step

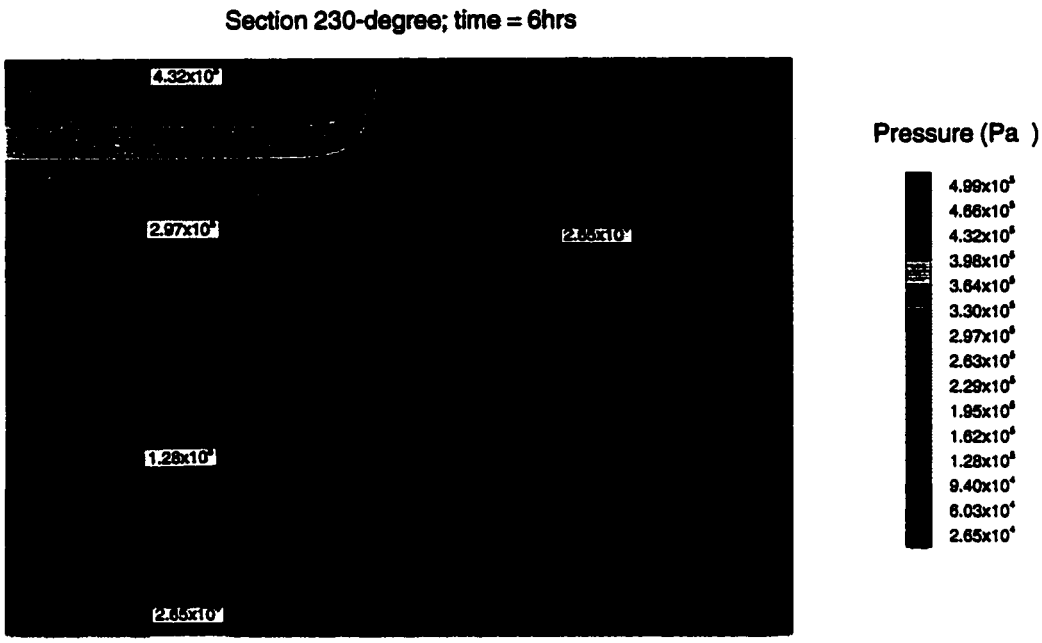

Fig. 6.24 Ice Pressure Evolution at Section 230 Degree; 3rd Time Step

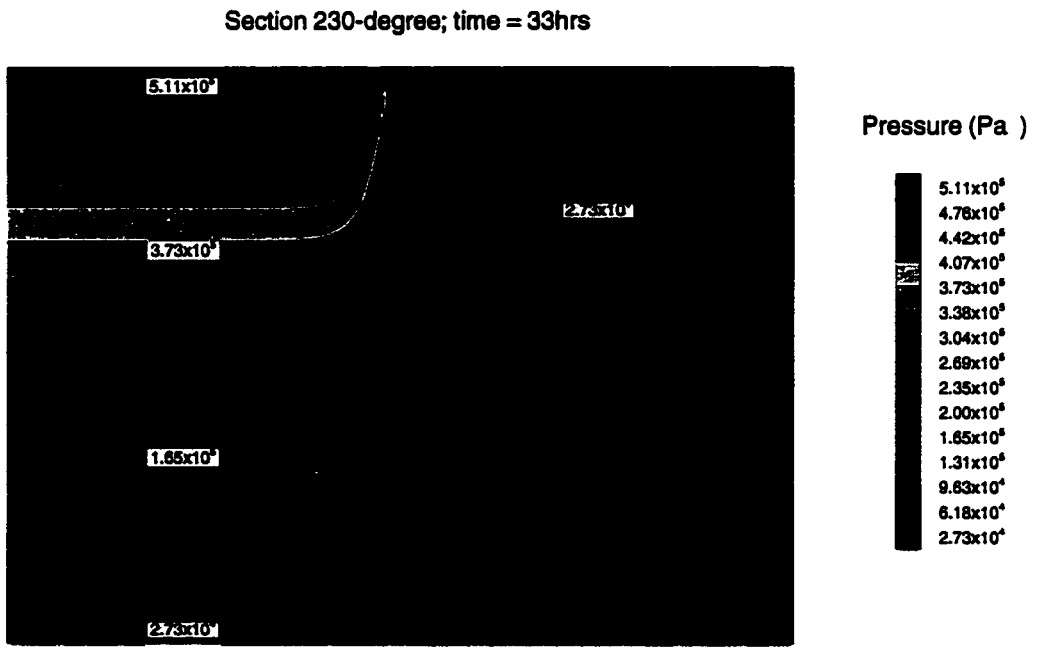

Fig. 6.25 Ice Pressure Evolution at Section 230 Degree; 15th Time Step

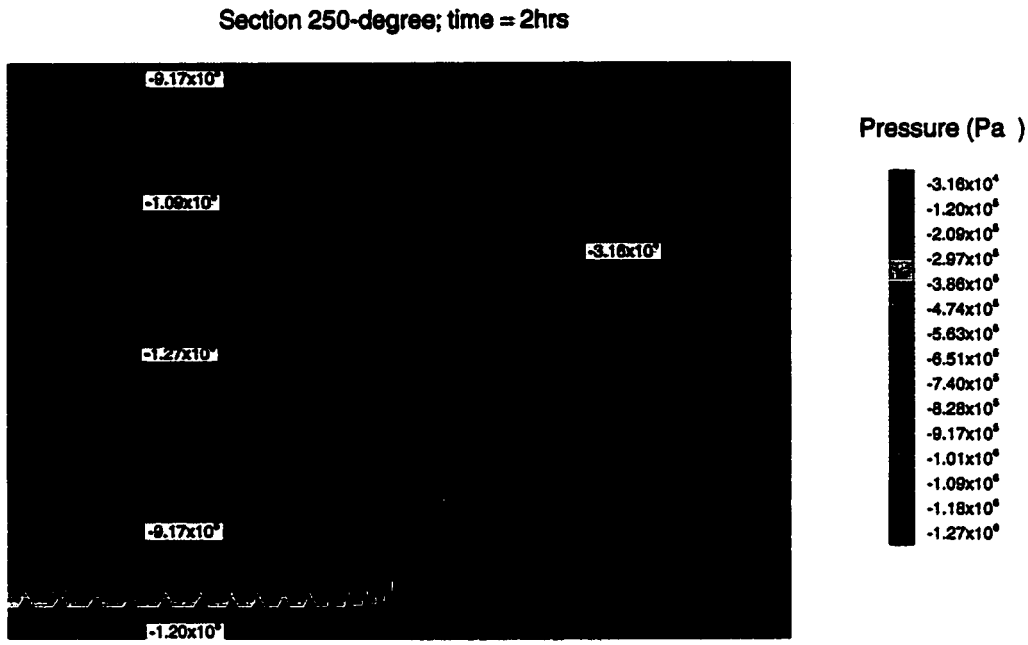

Fig. 6.26 Ice Pressure Evolution at Section 250 Degree; 1st Time Step

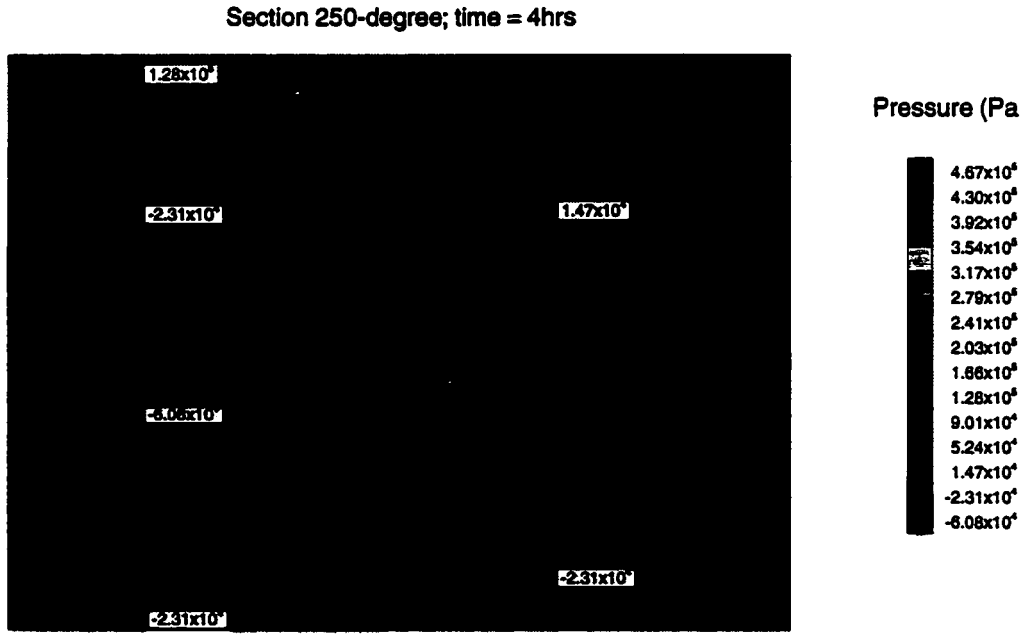

Fig. 6.27 Ice Pressure Evolution at Section 250 Degree; 2nd Time Step

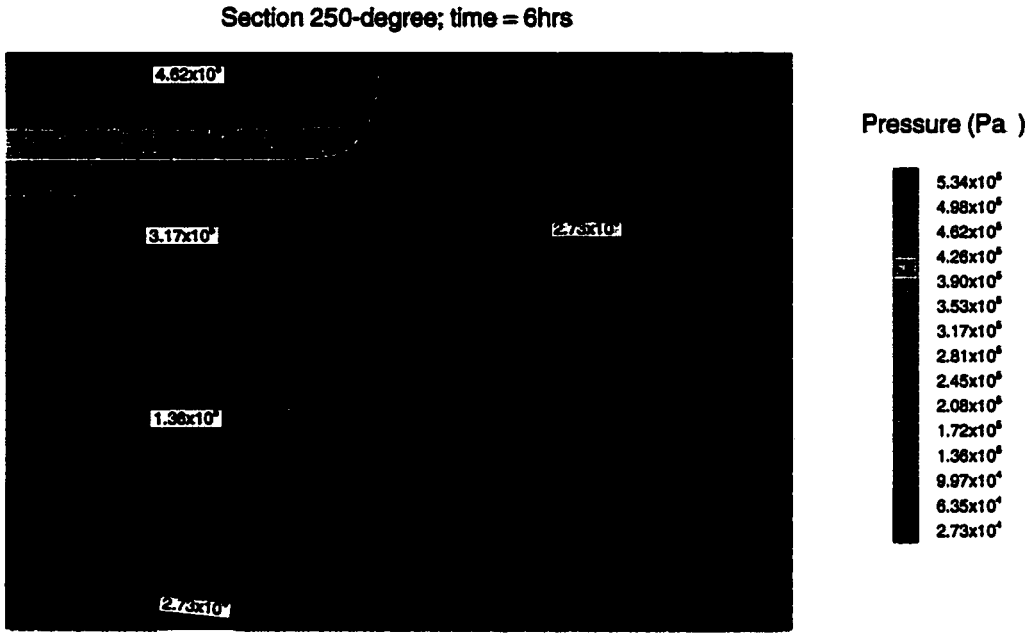

Fig. 6.28 Ice Pressure Evolution at Section 250 Degree; 3rd Time Step

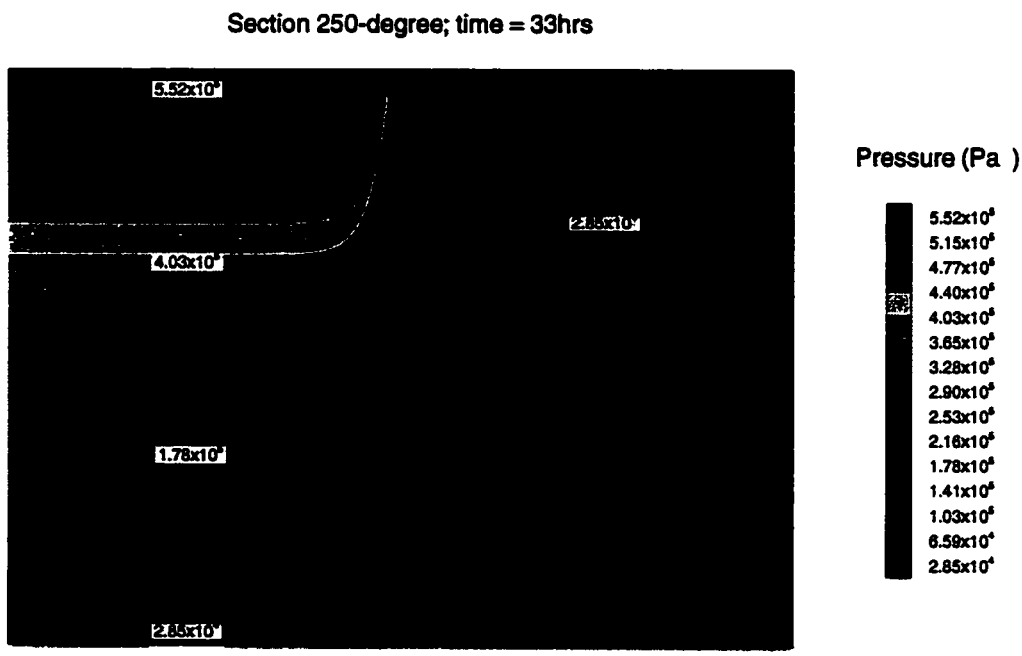

Fig. 6.29 Ice Pressure Evolution at Section 250 Degree; 15th Time Step

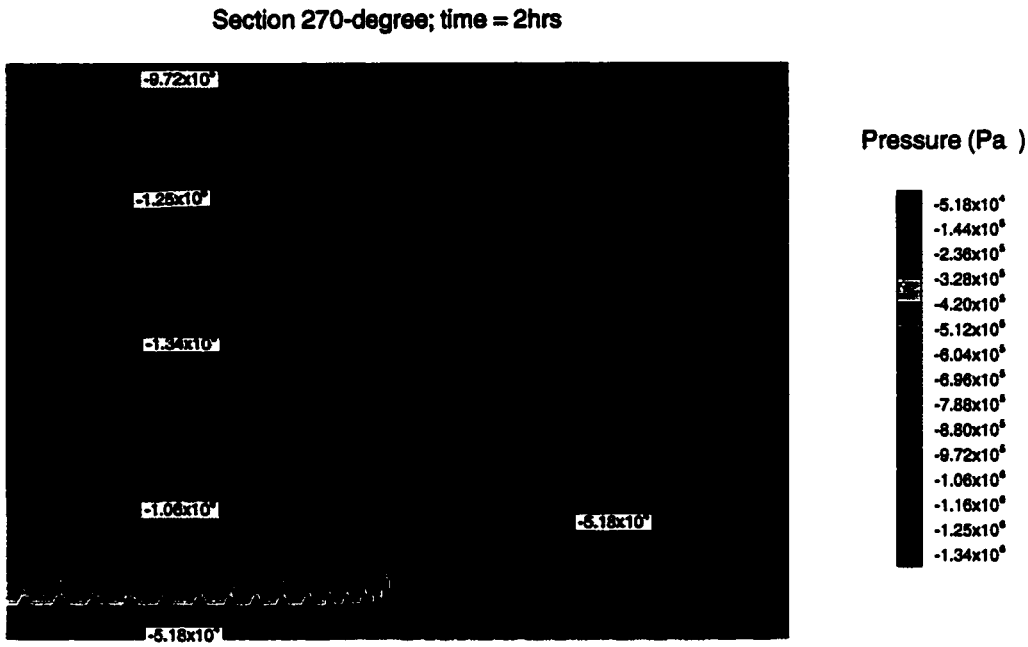

Fig. 6.30 Ice Pressure Evolution at Section 270 Degree; 1st Time Step

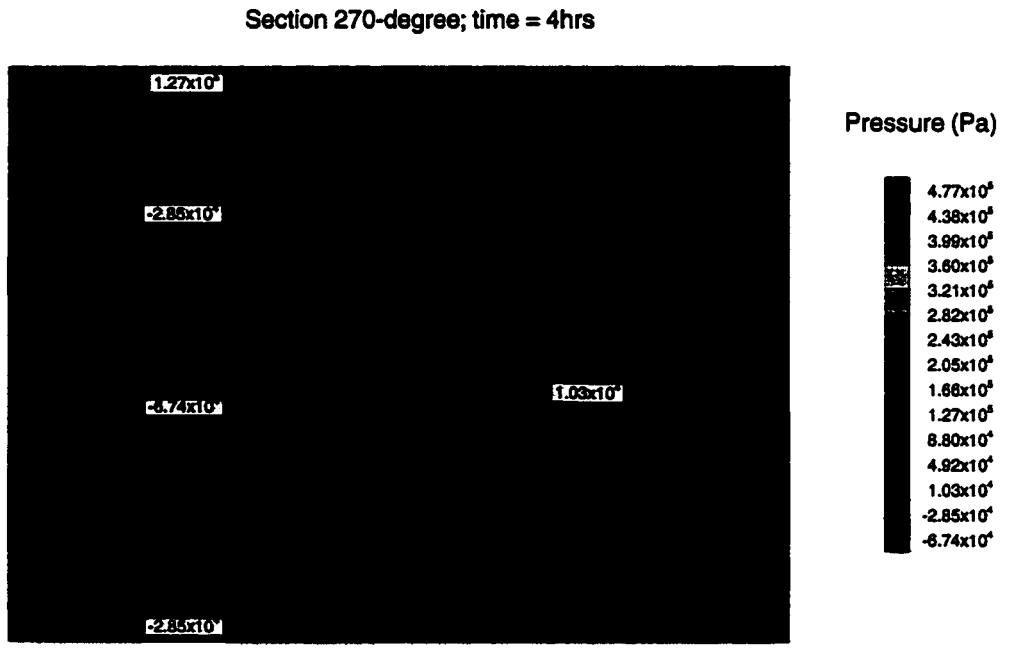

Fig. 6.31 Ice Pressure Evolution at Section 270 Degree; 2nd Time Step

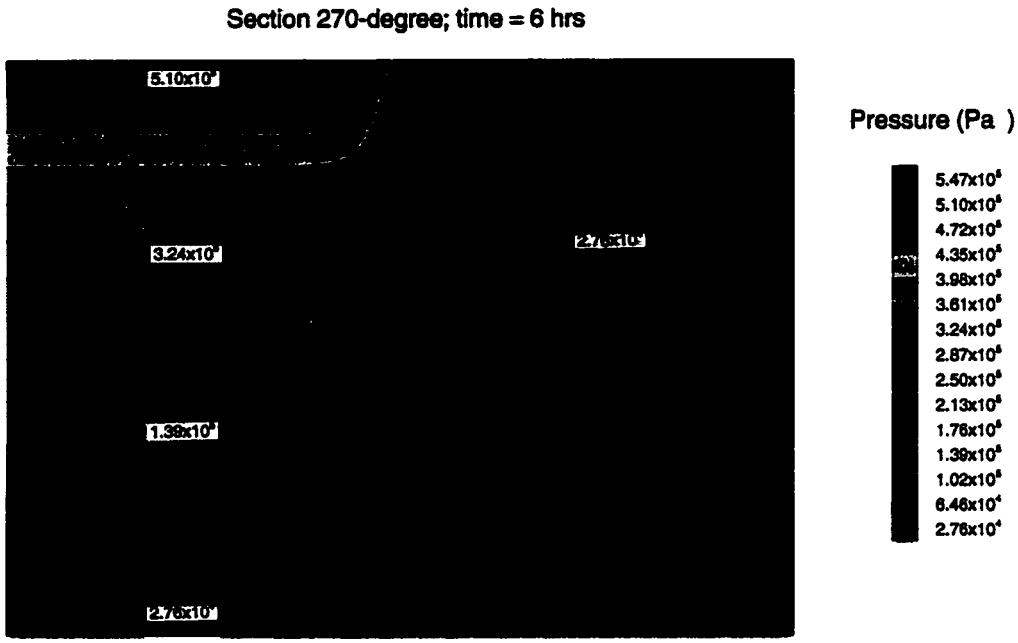

Fig. 6.32 Ice Pressure Evolution at Section 270 Degree; 3rd Time Step

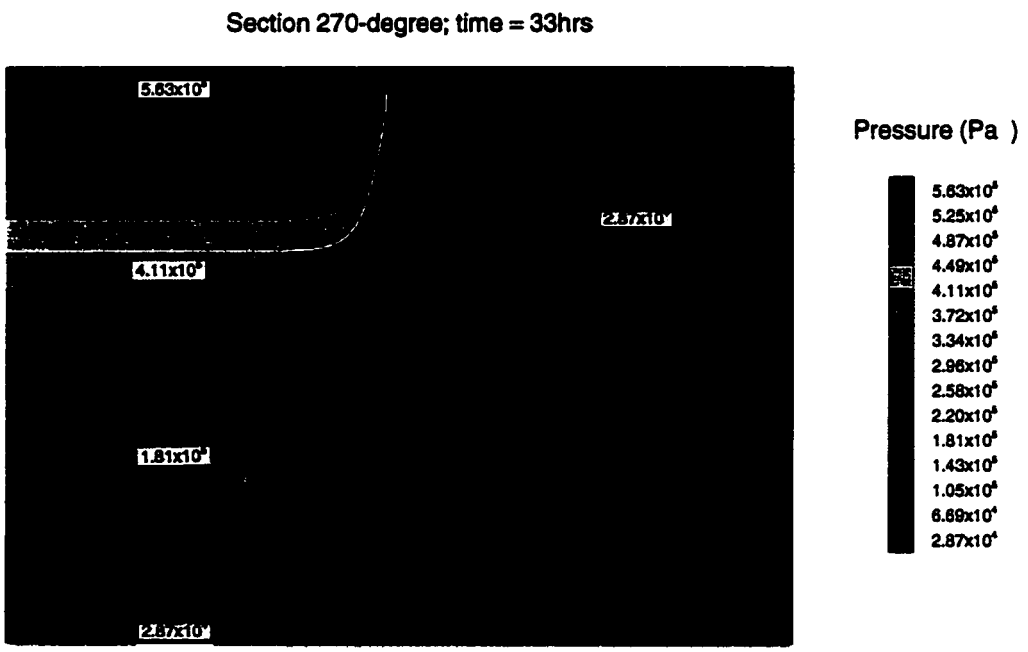

Fig. 6.33 Ice Pressure Evolution at Section 270 Degree; 15th Time Step

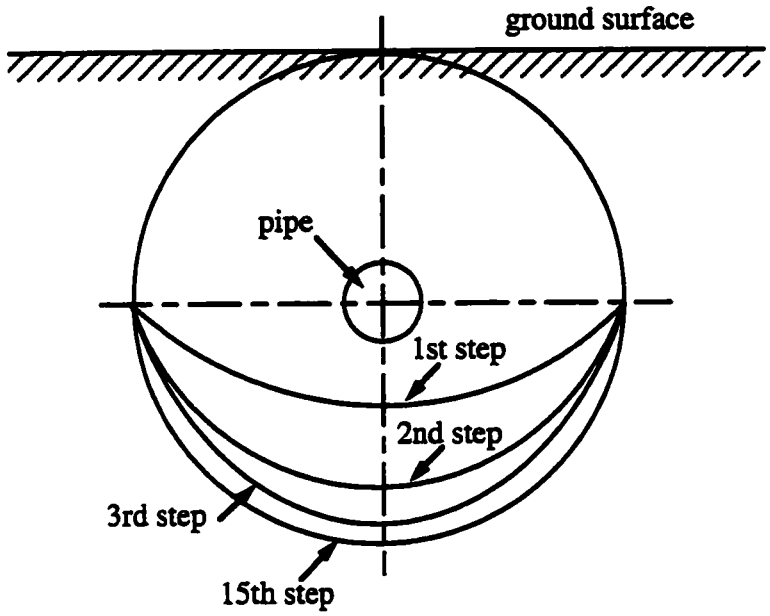

Fig. 6.34 Schematic Demonstration of Ice Bulb Evolution

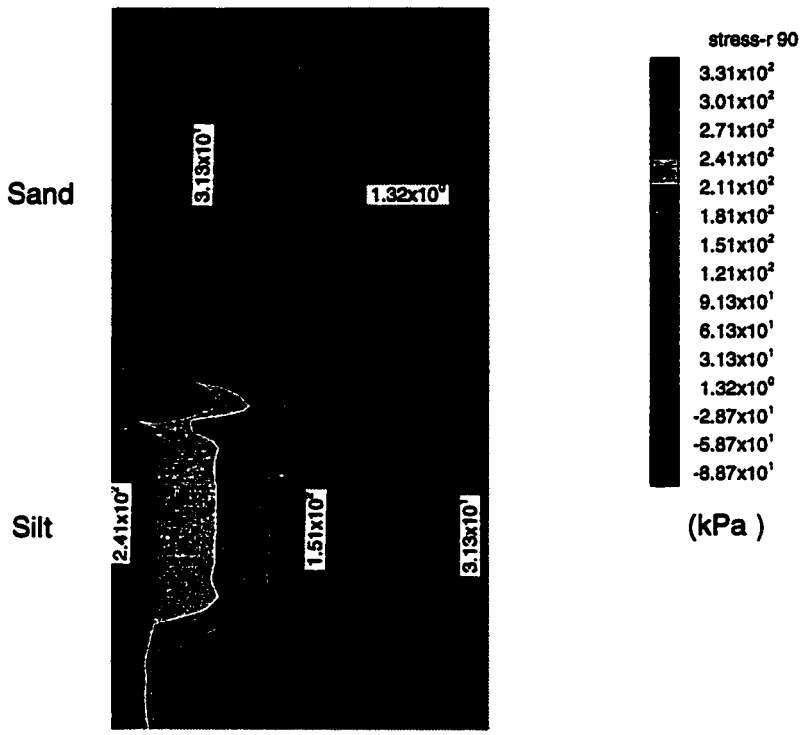

Fig. 6.35 Stress-r at 90 Degree Section; Steady State

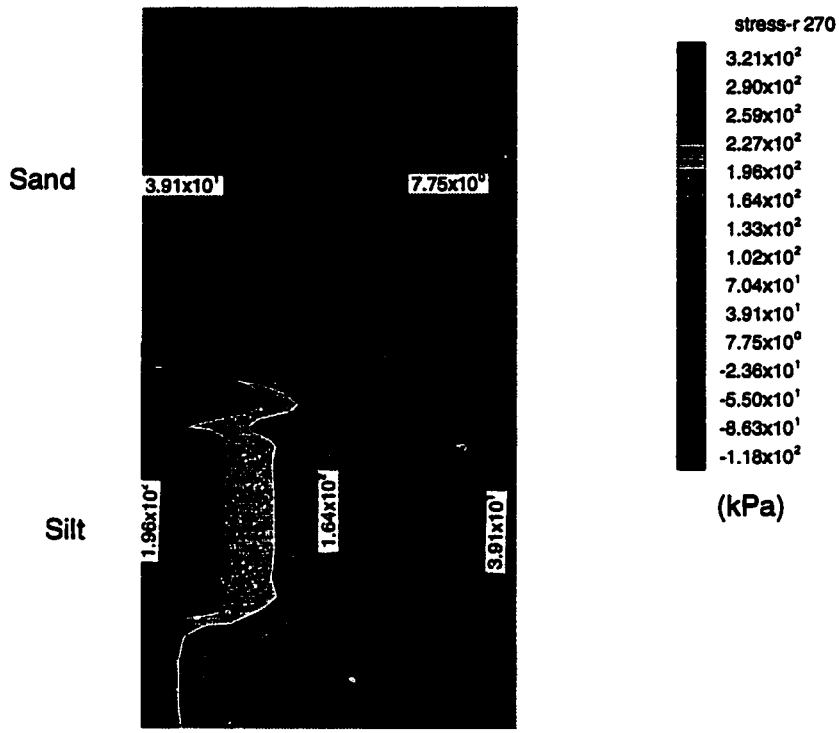

Fig 6.36 Stress-r at 270 Degree Section; Steady State

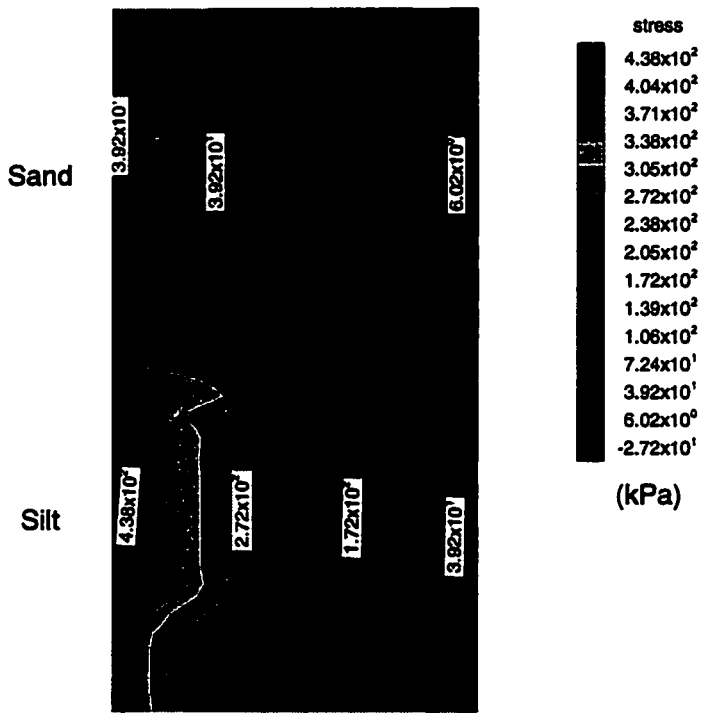

Fig. 6.37 Stress-r at 0 Degree Section; Steady State

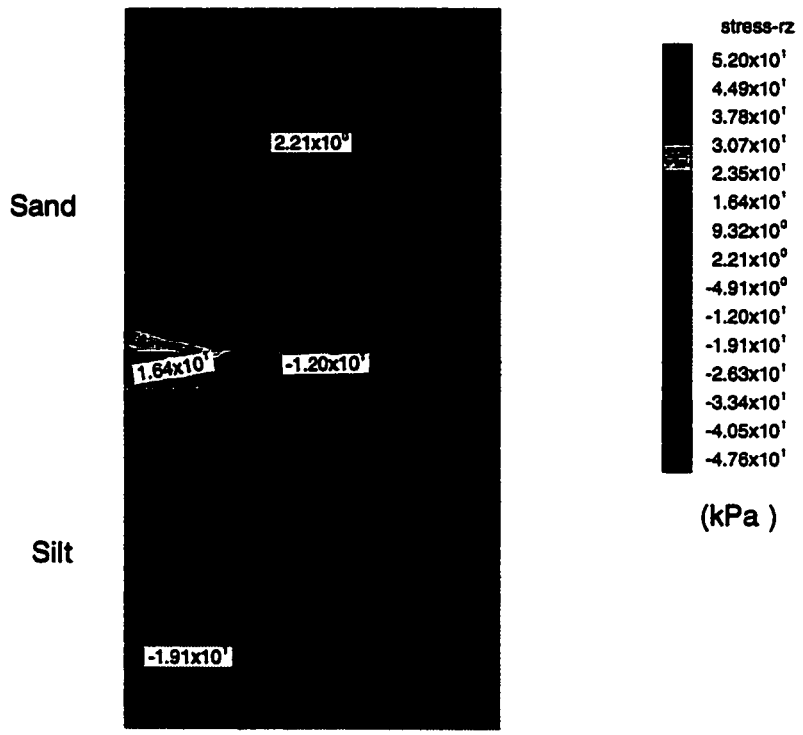

Fig. 6.38 Stress-rz at 0 Degree Section; Steady State

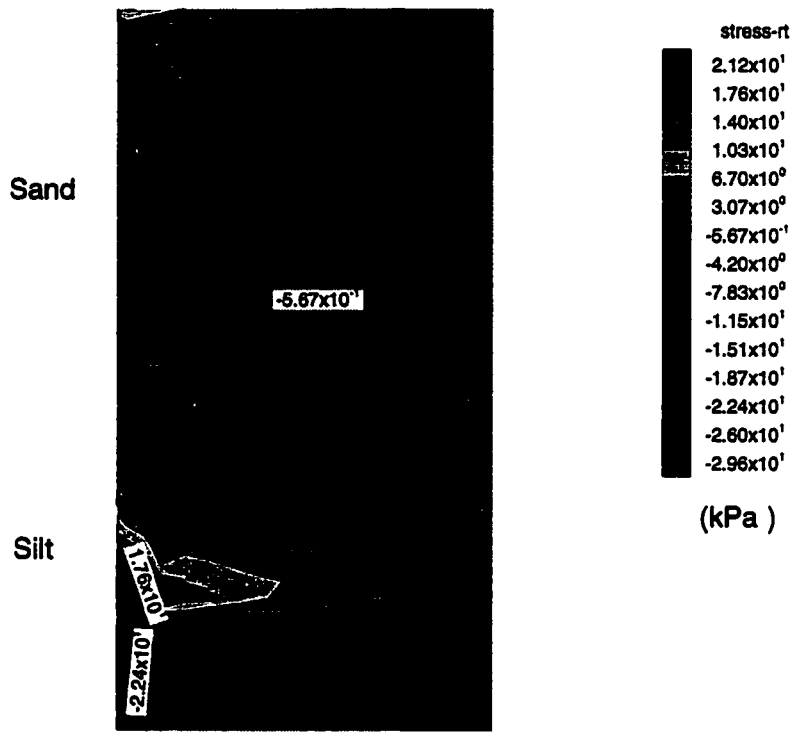

Fig. 6.39 Stress-rt at 0 Degree Section; Steady State

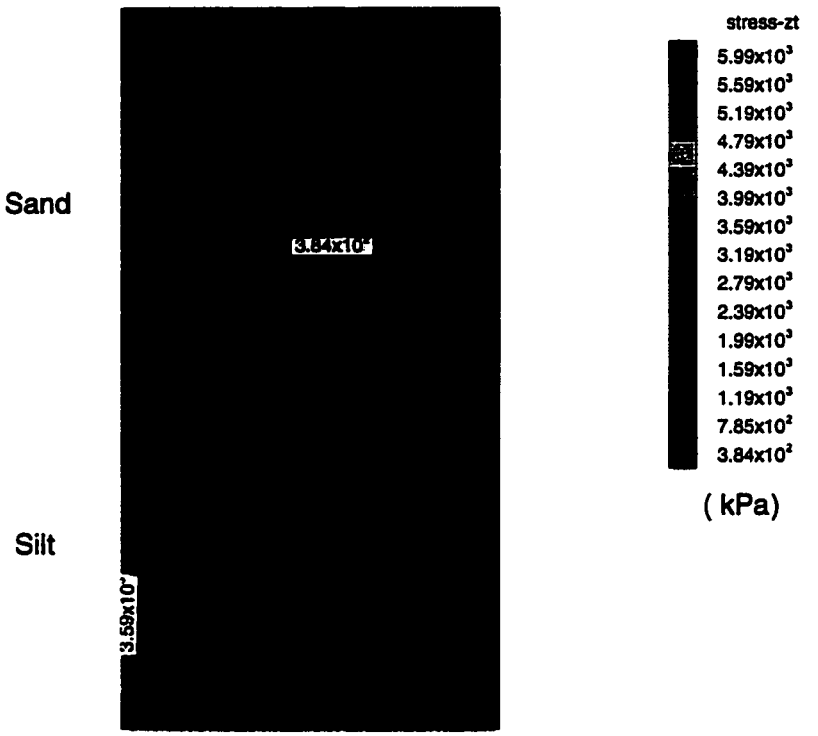

Fig. 6.40 Stress-zt at 0 Degree Section; Steady State

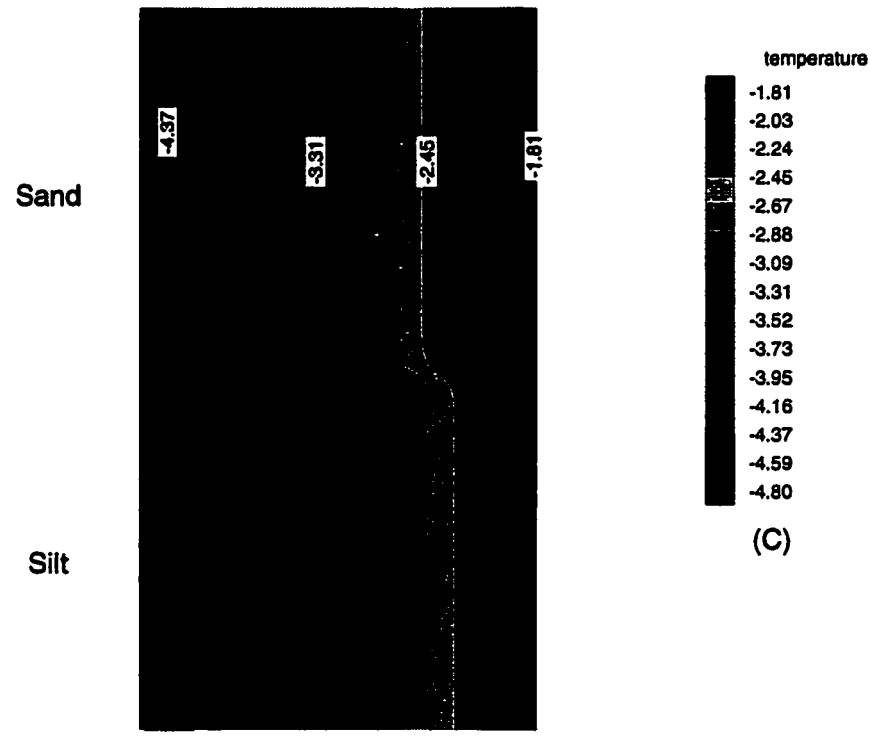

Fig. 6.41 Temperature Distribution at 0 Degree Section; Steady State

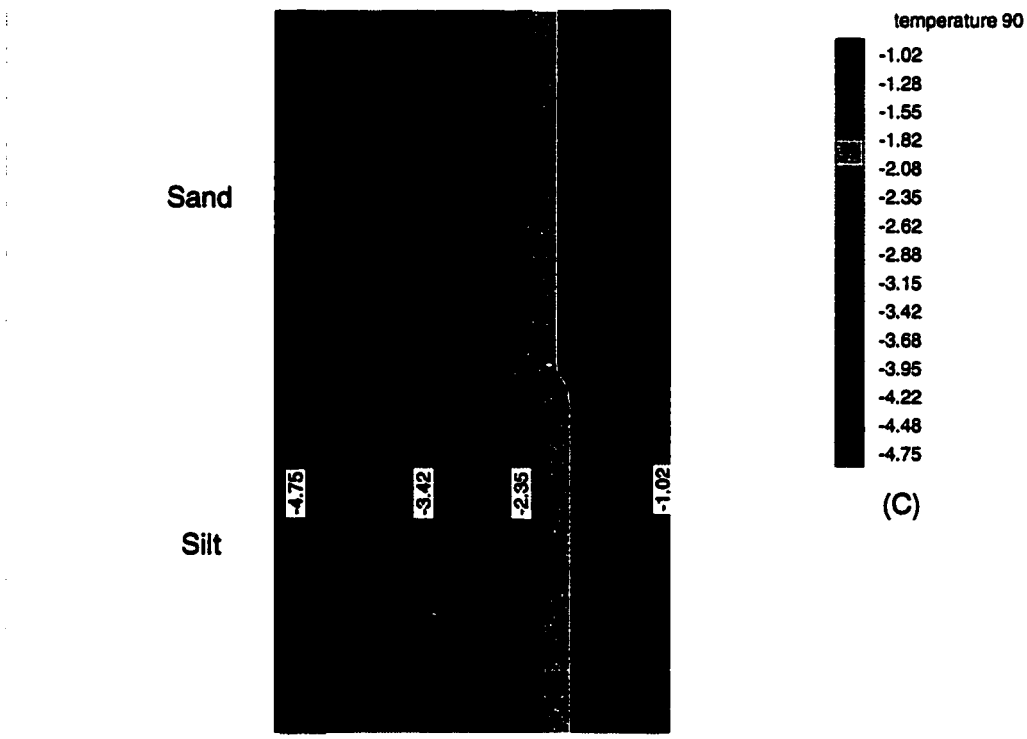

Fig. 6.42 Temperature Distribution at 90 Degree Section; Steady State

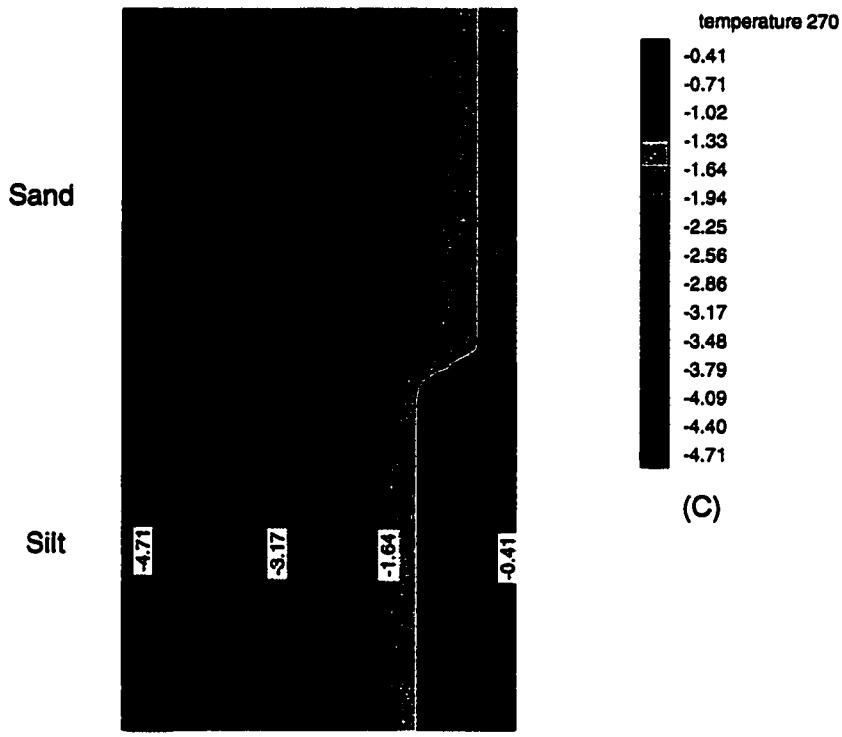

Fig. 6.43 Temperature Distribution at 270 Degree Section; Steady State

Chapter 7

CONCLUSIONS AND SUGGESTIONS FOR FUTURE WORK

7.1 Conclusions

The major conclusions which result from the work presented in this thesis are as follows:

1. The Fourier finite element model developed in this thesis has proved to be a viable tool for 3-D solutions which involve non-linear calculations. The main advantage of this method lies in the fact that 3-D computations are achieved from a series of 2-D calculations.

2. A consistent tangent modulus first introduced by Simo and Taylor [48] has been adopted for Fourier finite element calculations in this thesis. This framework ensures quadratic convergence of Newton method during the iteration for the determination of global equilibrium of the structure.

3. An algorithm has been devised for handling non-linear material behaviour in the Fourier finite element method without losing the decoupled nature of the global stiffness matrix. This is achieved by defining an average consistent

tangent modulus calculated from values obtained in each plane in the circumferential direction. Therefore, the integrals representing stiffness do not involve constitutive terms dependent on the circumferential direction. Hence, harmonics can be calculated independently with respect to each other.

4. Within the non-linear regime, the iteration procedure for the equilibrium of the system has to be taken care of. At each loading step, convergence of the entire global equilibrium system must be reached by considering all contributions from each harmonic. This is not done by just checking equilibrium conditions for each harmonic individually, but by using accumulated stress values based on contributions from each harmonic. Therefore, the accumulated stresses can be used to calculate the corresponding internal loads which are then checked against the applied external load level at the current loading step.

5. The quadratic convergence of the global equilibrium equations is almost preserved for the Fourier finite element method devised in the previous item. This has been verified in the numerical example which took only sixteen iterations to converge within a tight tolerance.

6. Few harmonics were necessary to describe the non-symmetry of the loads and the three-dimensional response of the structure. For the case studied in this thesis, five harmonics were usually needed with results not varying significantly after the third harmonic. Therefore, the computational effort was considerably less than that for a true 3-D problem, especially one involving plasticity calculations.

7. In comparison to the Caen experiment results, the model satisfactorily captures the surface heave and soil deformations, except for the pipe deflection due to the absence of soil-pipe interaction element.

8. The coupled heat transfer-moisture migration problem has been effectively solved by means of implicit finite elements. Again, non-linearities in the equations have been addressed using a consistent tangent operator which ensures quadratic convergence.

9. Two FORTRAN codes (over 6,000 lines) were mainly written by the author, (i) Fourier FEM for the stress analysis and (ii) a heat transfer-moisture migration FEM program. These two programs run separately; the liquid/ice pressure fields are determined first and used as load input in the Fourier FEM program.

7.2 Suggestions for Future Work

The following points need to be addressed in pursuit of future work.

- The soil-structure interaction aspect of the problem needs to be implemented in the present model.

- Large shift which results from deflection of the flexible pipe must be included so that more realistic results may be obtained.

- The Fourier finite element method as described in this thesis may have to be revised so that the above aspects may be integrated successfully. For example,

when applied to the non-linear regime, coupled terms of harmonics should be taken into account instead of eliminating them by using the mean of the consistent tangent modulus in the circumferential direction. This modification as described in section 3.3 algorithm for coupling terms will result in large increase of computational effort which may still be very economical compared to a true 3-D finite element model.

- An alternative solution may be found by expanding the Fourier terms in the longitudinal direction instead of the circumferential direction. Coupled terms should still be included since non-linearities and difference in material properties may occur in the longitudinal direction.

- Consideration may also be given to the development of classical 3-D finite element models, especially if contact elements are to be introduced.

- The interaction between ice and liquid pressures as described by Clapeyron equation gives unreasonable results in this study. Further theoretical work is necessary in this area.

- The coupling of the stress analysis (Fourier finite element model) with heat transfer/moisture migration was not done implicitly as computations for each component were done separately. Ideally, to check the level of coupling, the volume changes computed in the stress analysis must be compatible with those calculated in the thermal analysis. If these are not the same, new volume changes must be computed iteratively until mass balance is satisfied between the two models, i.e stress and thermal.

Bibliography

[1] Winkler, E. (1867). Die Lehre Von der Elastizitat. *und Festigkeit, Dominicus, Prague.*

[2] Rajani, B., and Morgenstern, N. (1994). Comparison of predicted and observed responses of pipeline to differential frost heave. *Canadian Geotechnical Journal, 31*, 803-816.

[3] Rajani, B., and Morgenstern, N. (1993). Uplift of model steel pipelines embedded in polycrystalline ice. *Canadian Geotechnical Journal, 30*, 441-454.

[4] Rajani, B., and Morgenstern, N. (1992). Behavior of a semi-infinite beam in a creeping medium. *Canadian Geotechnical Journal, 29*, 779-788.

[5] Ladanyi, B. (1972). An engineering theory of creep of frozen soils. *Canadian Geotechnical Journal, 9*, 63-80.

[6] Geotechnical Science Laboratories (1989). Canada-France pipeline-ground freezing experiment. *Report IR-58, Geotechnical Science Laboratories, Carleton University, Ottawa.*

[7] Ng, C.F., Pyrah, I.C., and Anderson, W.F. (1994). Lateral soil restraint of a pipeline. *Numerical Methods in Geotechnical Engineering, Smith (ed.), Balkema, Rotterdam, ISBN 90 5410 5100*, 215-220.

[8] Rajani, B., Zhan, C., and Kuraoka, S. (1996). Pipe-soil interaction analysis of jointed water mains. *Canadian Geotechnical Journal, 33*, 393-404.

[9] A.P.S. Selvadurai (1979). Elastic analysis of soil-foundation interaction. *Elsevier Scientific Publishing Company, ISBN 0-444-41663-3,* 28-38.

[10] Nixon, J.F., Morgenstern, N.R., and Reesor, S.N. (1983). Frost heave-pipeline interaction using continuum mechanics. *Canadian Geotechnical Journal, 20,* 251-261.

[11] Lewis, Roland W., and Sze Wah K. (1988). A finite element simulation of frost heave in soils. *5th International Symposium on Ground Freezing, Jones & Holden (eds), Nalkema, Rotterdam. ISBN 90 6191 8243* , 73-80.

[12] Svec, Otto J. (1989). A new concept of frost-heave characteristics of soils. *Cold Regions Science and Technology, 16,* 271-279.

[13] Penner, E. (1986). Aspects of ice lens growth in soils. *Cold Regions Science and Technology, 13,* 91-100.

[14] Konrad, J.-M. (1989). Influence of cooling rate on the temperature of ice lens formation in clayey silts. *Cold Regions Science and Technology, 16,* 25-36.

[15] Konrad, J.-M. and Morgenstern, N.R. (1982). Effects of applied pressure on freezing soils. *Canadian Geotechnical Journal 31,* 494-505.

[16] Smith, S.L. and Williams, P.J. (1995). Ice lens formation at a silt-sand interface. *Canadian Geotechnical Journal, 32,* 488-495.

[17] Shen, Mu, and Ladanyi, Branko (1987). Modelling of coupled heat, moisture and stress field in freezing soil. *Cold Regions Science and Technology,* 14, 237-246.

[18] Shen, Mu, and Ladanyi, B. (1991). Soil-Pipe interaction during frost heaving around a buried chilled pipeline. *Proceedings of the 6th Int. Specialty Conference hosted by US Army, Cold Regions Engineering, Sheraton North Country Inn, West Lebanon, NH, Feb. 26-28*, 11-21.

[19] Ladanyi, B, and Shen, Mu (1993). Freezing pressure development on a buried chilled pipeline. *Frost in Geotechnical Engineering, Phukan (ed.) Balkema, Rotterdam, ISBN 90 5410 3191*, 23-33.

[20] Sheppard, Marsha I., Kay, B.D., and Loch, J.P.G. (1978). Development and testing of computer model for heat and mass flow in freezing soils. *Proceedings of the 3rd International Conference on Permafrost*, 76-81.

[21] Kay, B.D. and Groenevelt, P.H. (1974). On the interaction of water and heat transport in frozen and unfrozen soils: I. Basic theory; The vapor phase. *Soil Science Society of America Proceedings, Vol. 38*, 395-400.

[22] Fremond, M. and Mikkola, M. (1991). Thermomechanical modelling of freezing soil. *Ground Freezing 91, Yu & Wang (eds), Balkema, Rotterdam.* 17-24.

[23] Selvadurai, A.P.S. (1992). Computational modelling of pipelines at discontinuous frost heave zones. *Numerical Models in Geomechanics, Pande & pietruszczak (eds), Balkema, Rotterdam, ISBN 90 5410 0885*, 645-659.

[24] Nixon, J.F. (1987). Thermally induced heave beneath chilled pipelines in frozen ground. *Canadian Geotechnical Journal 24*, 260-266.

[25] Rajani, B. and Zhan, C. (1996). On the estimation of frost loads. *Canadian Geotechnical Journal, 33*, 629-641.

[26] Williams, P.J. (1968). Experimental determination of apparent specific heats of frozen soils. *Norwegian Geotechnical Institute, Publication No. 72, Properties and Behaviour of Freezing Soils*, 1-10.

[27] Williams, P.J. (1968). Unfrozen water content of frozen soils and soil moisture suction. *Norwegian Geotechnical Institute, Publication No. 72, Properties and Behaviour of Freezing Soils*, 11-26.

[28] Williams, P.J. (1968). Suction and its effects in unfrozen water of frozen soils. *Norwegian Geotechnical Institute, Publication No. 72, Properties and Behaviour of Freezing Soils*, 27-35.

[29] Williams, P.J. (1968). Unfrozen water in frozen soils: pore size-freezing temperature-pressure relationship. *Norwegian Geotechnical Institute, Publication No. 72, Properties and Behaviour of Freezing Soils*, 37-48.

[30] Williams, P.J. (1968). Pore pressures at a penetrating frost line and their prediction. *Norwegian Geotechnical Institute, Publication No. 72, Properties and Behaviour of Freezing Soils*, 51-72.

[31] Williams, P.J. (1968). The nature of freezing soil and its field behavior. *Norwegian Geotechnical Institute, Publication No. 72, Properties and Behaviour of Freezing Soils*, 91-119.

[32] Wilson, E. L. (1965). Structural analysis of the axisymmetric solids. *AIAA Journal, 3*, 2269-2274.

[33] Percy, J.H., Pian, T.H.H., Klein, S., and Navaratna, D.R (1965). Application of matrix displacement method to linear elastic analysis of shells of revolution. *AIAA Journal, 3*, 2138-2245.

[34] Stricklin, J.A., Navaratna, D.R., and Pian, T.H.H. (1966). Improvements on the analysis of shells of revolution by the matrix displacement method. *AIAA Journal, Vol. 4, No.11*, 2069-2072.

[35] Stricklin, J.A., Martinez, J.E., Tillerson, J.R., Hong, J.H., and Haisler, W.E. (1971). Nonlinear dynamic analysis of shells of revolution by matrix displacement method. *AIAA Journal, Vol. 9, No. 4* , 629-636.

[36] Wunferlich, W., Cramer, H., and Obrecht, H. (1985). Application of ring elements in the nonlinear analysis of shells of revolution under nonaxisymmetric loading. *Computer Methods in Applied Mechanics and Engineering, 51*, 259-275.

[37] Danielson, K.T., and Tielking, J.T. (1993). Fourier continuum finite elements for large deformation problems. *Computers & Structures, Vol. 49, No. 1*, 133-147.

[38] Winnicki, L.A.and Zienkiewicz, O.C. (1979). Plastic (or visco-plastic) behavior of axisymmetric bodies subjected to non-symmetric loading—semi-analytical finite element solution. *International Journal for Numerical Methods in Engineering, Vol. 14*, 1399-1412.

[39] Owen, D. R. J. and Hinton, E. (1980). Finite elements in plasticity: Theory and Practice. *Pineridge Press Limited.*

[40] Kay, S. and Griffiths, D.V. (1991). Finite element analysis of skirts for gravity base structures. *Proceedings of the 10th European Conference on Soil Mechanis and Foundation Engineering, Florence, Vol. 1*, 233-236.

[41] Hinton, E. and Owen, D. R.J. (1979). An introduction to finite element computations. *Pineridge Press Limited*, 307-318.

[42] Cheung, Y. K. (1976). Finite strip method in structural analysis, *Pergamon Press, Oxford.*

[43] Runesson, K.R. and Booker, J.R. (1982). Efficient finite element analysis of consolidation. *Proceedings of the 4th International Conference on Numerical Methods in Geomechanics, Edmonton, Canada*, 395-364.

[44] Runesson, K.R. and Booker, J.R. (1983). Finite element analysis of elasto-plastic layered soil using discrete Fourier series expansion. *International Journal of Numerical Methods in Engineering, 19*, 473-478.

[45] Moore, I.D. and Booker, J.R. (1982). A circular boundary element for the analysis of deep underground openings. *Proceedings of the 4th International Conference on Numerical Methods in Geomechanics, Edmonton, Canada*, 53-60.

[46] Lai, J.Y. and Brooker J.R. (1991). Application of discrete Fourier series to the finite element stress analysis of axi-symmetric solids. *International Journal for Numerical Methods in Engineering, Vol. 31*, 619-647.

[47] ABAQUS/Standard, User's Manual, *Vol. I*, 3.3.5-1–3.3.5-6.

[48] Simo, J.C. and Taylor, R.L. (1985). Consistent tangent operators for rate-independent elastoplasticity. *Computer Methods in Applied Mechanics and Engineering, 48*, 101-118.

[49] Wan, R.G. (1992). Implicit integration algorithm for Hoek-Brown elastic-plastic model. *Computers and Geotechnics, 14*, 149-177.

[50] Wilson, E.A. and Parsons, B. (1970). Finite element analysis of elastic contact problems using differential displacements. *International Journal for Numerical Methods in Engineering, Vol. 2*, 384-395.

[51] Goodman, R. E., Taylor R. L., and Brekka, T. L. (1968). A model for the mechanics of jointed rocks. *ASCE, Journal of Soil Mechanics and Foundation Engineering. Vol. 94 SM3*, 637-659.

[52] Chan, C.H. and Tuba, I.S. (1971a). A finite element method for contact problems of solid bodies: I. Theory and validation. *International Journal for Mechanical Science, Vol. 13*, 615-625.

[53] Chan, C.H. and Tuba, I.S. (1971b). A finite element method for contact problems of solid bodies: Application to turbine blade fastenings. *International Journal for Mechanical Science, Vol. 13*, 627-639.

[54] Francavilla, A. and Zienkiewicz, O.C. (1975). A note on numerical computation of elastic contact problems. *International Journal for Numerical Methods in Engineering, Vol. 9*, 913-924.

[55] Bathe, K. and Chaudhary, A. (1985). A solution method for planar and axisymmetric contact problems. *International Journal for Numerical Methods in Engineering, Vol. 21*, 65-88.

[56] Peric, D. and Owen, D.R.J. (1992). Computational model for 3-D contact problems with friction based on the penalty method. *International Journal for Numerical Methods in Engineering, Vol. 35*, 1289-1309.

[57] Ju, S.H. and Rowlands, R.E. (1995). A new symmetric contact stiffness matrix for frictional contact problems. *Computers and Structures, Vol.54, No.2*, 289-301.

[58] Cescotto, S. and Charlier, R. (1992). Frictioncal contact finite elements based on mixed variational principles. *International Journal for Numerical Methods in Engineering, Vol. 36*, 1681-1701.

[59] Lee, J.S., Pande, G.N., and Pietruszczak (1992). A joint element based on a homogenization technique. *Numerical Models in Geomechanics, Pande & Pietruszczak (eds.), Balkema, Rotterdam, ISBN 90 5410 088*, 249-258.

[60] Lews,G. N. and Randall, M. (1961). Thermodynamics. *2nd Edition, revised by K. S. Pitzer and L. Brewer, New York: McGraw-Hill.*

[61] Anderson, D. M., and Morgenstern, N. R. (1973). Physics, chemistry, and mechanics of frozen ground: A review. *Proceedings, 2nd International Conference on Permafrost, Yakutsk, U.S.S.R., North America Contribution*, 257-288.

[62] Fortier, R., Allard, M., and Sheriff, F. (1996). Field Estimation of Water-Ice Phase Composition of Permafrost Samples using a Calorimetric Method, *Canadian Geotechnical Journal.* 33, 355-362

[63] Andersland, B., and Ladanyi, B. (1994). An Introduction to frozen ground engineering. *Chapman and Hall, New York*, 122.

[64] Selvadurai, A.P.S. (1994). Development of pipe-soil interaction models for frost heave or thaw settlement analysis at discontinuous frost heave zones. *Final Report Submitted to the National Energy Board of Canada, DSS Contract No. 84084-3-0215/02-XSH.*

TEST TARGET (QA-3)

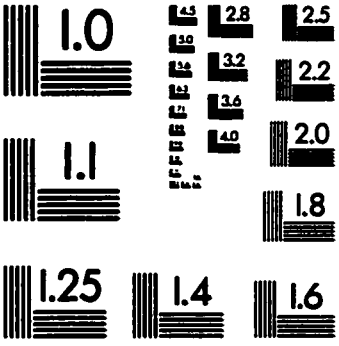

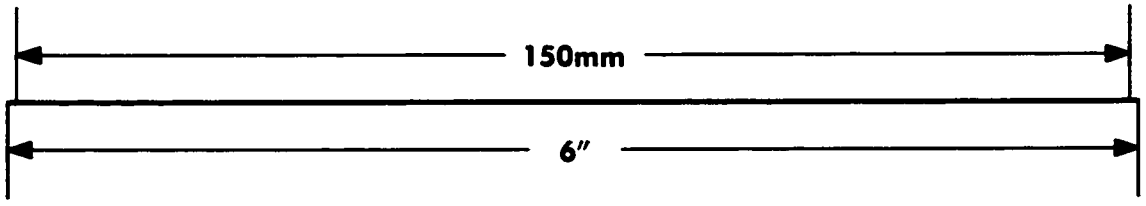

APPLIED IMAGE, Inc
1653 East Main Street
Rochester, NY 14609 USA
Phone: 716/482-0300
Fax: 716/288-5989